

Magnetic Resonance Spectroscopy: Quantitative Analysis of Brain Metabolites and Macromolecules

Dissertation

der Mathematisch-Naturwissenschaftlichen Fakultät
der Eberhard Karls Universität Tübingen
zur Erlangung des Grades eines
Doktors der Naturwissenschaften
(Dr. rer. nat.)

vorgelegt von
Tamás Borbáth
aus Braşov, Rumänien

Tübingen
2021

Gedruckt mit Genehmigung der Mathematisch-Naturwissenschaftlichen Fakultät der
Eberhard Karls Universität Tübingen.

Tag der mündlichen Qualifikation:

17.05.2021

Dekan:

Prof. Dr. Thilo Stehle

1. Berichterstatter:

Prof. Dr. Anke Henning

2. Berichterstatter:

Prof. Dr. Oliver Kohlbacher

Erklärung:

Ich erkläre, dass ich die zur Promotion eingereichte Arbeit mit dem Titel:

“Magnetic Resonance Spectroscopy: Quantitative Analysis of Brain Metabolites and Macromolecules“

selbständig verfasst, nur die angegebenen Quellen und Hilfsmittel benutzt und wörtlich oder inhaltlich übernommene Stellen als solche gekennzeichnet habe. Ich versichere an Eides statt, dass diese Angaben wahr sind und dass ich nichts verschwiegen habe. Mir ist bekannt, dass die falsche Abgabe einer Versicherung an Eides statt mit Freiheitsstrafe bis zu drei Jahren oder mit Geldstrafe bestraft wird.

I hereby declare that I have produced the work entitled:

“Magnetic Resonance Spectroscopy: Quantitative Analysis of Brain Metabolites and Macromolecules“

,submitted for the award of a doctorate, on my own (without external help), have used only the sources and aids indicated and have marked passages included from other works, whether verbatim or in content, as such. I swear upon oath that these statements are true and that I have not concealed anything. I am aware that making a false declaration under oath is punishable by a term of imprisonment of up to three years or by a fine.

Tübingen, den 27.01.2021
Datum

Unterschrift

Acknowledgements

This PhD thesis would not have been possible without the support of many people who gave me inspiration and motivation to conduct this work.

I am deeply grateful to my supervisor Prof. Anke Henning for giving me the opportunity to do this PhD project, for her guidance and excellent scientific inputs. Further, I would like to express the sincere appreciation to my co-supervisor Prof. Oliver Kohlbacher for his continuous support and for reading and evaluating this lengthy manuscript. I am also thankful to the board of examiners Prof. Fritz Schick and Prof. Peter Dayan for this thesis's assessment.

I am very grateful to all my former and current colleagues and friends at the Max Planck Institute, it was a pleasure to work with them, to discuss science and all other matters of life. I learned a lot from Ioannis about how to write a paper, but also how not to back-up your thesis; paper discussions were intense and enjoyable with Saipavitra, Andrew, Johanna. Endless phone calls and fun coding I had with Mark, Tabea and Patrik. I am lucky to have had such amazing colleagues: Ole, Theresia, Nikolai, Andi, Loreen, Sahar, Paul and Tingting. Sorry to all for being a too talkative and sometimes a too loud office mate.

Life was pleasant in Tübingen thanks to my flatmates and friends from DAAD Freundeskreis and many more. They provided a nice balance to all the hours spent with my research.

I also want to acknowledge the financial support from the European Union's CDS-QUAMRI grant. It was an honor to work with so many excellent partners within the EU-consortium. Thanks also to the logistic support of the Max Planck Institute: Tina, Mihai and all the administrative staff: these five years passed so smoothly thanks to you.

Finally, and most importantly, I would like to express my heartfelt thanks to my parents Zsuzsa and Áron, as well as my twin brother Áron for their support, through-out my whole life. Many thanks to my love Alexandra for proofreading this thesis and cheering me up all the time. My deepest gratitude to all four of them for enduring all my complaints, and for motivating me through-out the time of my PhD.

Abstract

Proton magnetic resonance spectroscopy (^1H -MRS) allows non-invasive quantification of the human brain's metabolism in vivo. ^1H -MRS measures the interaction of the ^1H -hydrogen isotope with oscillating electromagnetic fields in the presence of a strong electromagnetic field. The measured MRS signal of the ^1H -hydrogen atoms reflects the concentration of the metabolites present in the tissue. Metabolites are small molecules reflecting the metabolism.

Each ^1H -hydrogen atom present in a metabolite has a specific resonance frequency, which depends on the chemical structure of the metabolite. The ensemble of the resonance frequencies of all metabolites present in the measured tissue creates the MRS signal. The MRS signal is Fourier transformed, producing an MRS spectrum, where each resonance frequency appears as a distinct peak. The most abundant molecule in the human tissue is water. The resonance frequency of water is suppressed in ^1H -MRS to permit the quantification of other metabolites, which are present with significantly lower concentrations. In the MRS spectrum, protons with lower resonance frequencies than water form the upfield spectrum, whereas protons with higher resonance frequencies form the downfield spectrum.

This work focused on the modelling of the MRS spectrum. The first part is focused on the accurate determination of metabolite concentrations.

The upfield spectrum contains most brain metabolites of clinical interest. However, there is a severe spectral overlap between the metabolite resonances, and therefore dedicated software calculates the contributions of individual metabolites. The modelling of the individual metabolite contributions to the measured spectrum is referred to as spectral fitting. Through this spectral fitting, the metabolite concentrations needed for clinical diagnostics are determined.

The most significant overlap in MRS spectra originates from the signals underlying the metabolite resonances, referred to as the macromolecular spectrum. The macromolecular spectrum contains the resonance frequencies of protons in proteins and peptides, which have a slightly faster signal decay than the smaller molecules (metabolites).

Other contributors to the spectral overlap are residuals of the not entirely suppressed water signal or lipid signals originating from outside the volume of interest. A spline baseline is typically used in the fitting software to model these contributors.

This work firstly investigated the impacts of different macromolecular spectra and spline baselines used in spectral fitting. Significant effects in the quantified metabolite concentrations were noticed, when the spline baseline flexibility was altered in the community “gold standard” software, LCModel. Therefore, the newly developed fitting algorithm proposed in this work, ProFit-v3, incorporates an automatic adaptive baseline flexibility determination. The ProFit-v3 software was then systematically evaluated to different perturbations and baseline effects. The quantified concentrations were compared to the ground truth (when known) and the LCModel software results.

The second part of this work focuses on the modelling of the less investigated regions of the MRS spectrum.

The downfield spectrum contains many resonance peaks unassigned to metabolite contributions. In this work, downfield spectral peaks were used to quantify intracellular pH. Additionally, for all downfield peaks T_2 relaxation times, peak linewidths, and concentrations were calculated. Lastly, based on the quantified peak properties combined with previous literature measurements, the contributing molecules to the downfield peaks were assigned.

The macromolecular spectrum was attributed by previous literature to contributions of amino acids in proteins and peptides, based on in vitro measurement of dialyzed cytosol. Moreover, the resonance frequencies of protein amino acids have been extensively collected into a protein database by the NMR community. Hence, this work proposes a modelling approach to quantify the in vivo measured macromolecular spectrum to individual amino acids.

In conclusion, the investigation results and the proposed fitting software ProFit-v3 from this work should lead to improved quantification of ^1H -MRS spectra. Lastly, the peak assignments in the downfield spectra and the proposed amino acid model promises possible future biomarkers for disease.

Zusammenfassung

Die Protonen-Magnetresonanzspektroskopie (^1H -MRS) ermöglicht die nichtinvasive in vivo Quantifizierung des Metabolismus im menschlichen Gehirn. In der ^1H -MRS wird die Interaktion zwischen einem in ein starkes elektromagnetisches Feld platziertes ^1H -Wasserstoffisotop und einem oszillierenden elektromagnetischen Feld gemessen. Die gemessenen MRS-Signale der ^1H -Wasserstoffatome spiegeln die Konzentration der in dem Gewebe enthaltenen Metaboliten wieder.

Jedes ^1H -Wasserstoffatom in einem Metaboliten hat eine spezifische Resonanzfrequenz, die von der chemischen Struktur des Metaboliten abhängt. Die Gesamtheit der Resonanzfrequenzen aller Metaboliten in dem gemessenen Gewebe generiert das MRS-Signal. Durch die Fourier-Transformation dieses MRS-Signals entsteht ein MRS-Spektrum mit Spektrallinien, die den enthaltenen Resonanzfrequenzen entsprechen. Wasser ist das häufigste Molekül im menschlichen Gewebe. Um Metaboliten mit signifikant geringeren Konzentrationen quantifizieren zu können, wird in der MRS das Wassersignal unterdrückt. Wasserstoffatome mit einer niedrigeren Resonanzfrequenz als Wasser bilden das sogenannte „Upfield-Spektrum“, während die Wasserstoffatome mit einer höheren Resonanzfrequenz das „Downfield-Spektrum“ bilden.

Das „Upfield-Spektrum“ enthält die Spektrallinien der meisten klinisch relevanten Metaboliten, ist aber von einer starken spektralen Überlagerung geprägt. Deshalb müssen die Anteile der einzelnen Metaboliten im Gesamtspektrum durch eine spezielle Software berechnet werden. Die Modellierung der einzelnen Beiträge der Metaboliten zu dem gemessenen Spektrum nennt man spektrales Fitting. Mithilfe des spektralen Fitting werden die für die klinische Diagnostik relevanten Metabolitenkonzentrationen bestimmt. Diese Doktorarbeit fokussiert sich auf die Modellierung des MRS-Spektrums. Der erste Teil beschäftigt sich mit der akkuraten Quantifizierung der Metabolitenkonzentrationen. Die signifikanteste spektrale Überlagerung im MRS entsteht durch Signale, die unter den Spektrallinien der Metaboliten liegen und die als makromolekulares Spektrum bezeichnet werden. Das makromolekulare Spektrum besteht aus den Resonanzfrequenzen der Protonen von Proteinen und Peptiden, deren MRS-Signal schneller zerfällt als das der kleineren Moleküle (Metaboliten).

Zusätzlich tragen zu der spektralen Überlagerung nicht ausreichend unterdrückte Wassersignale, sowie Signale von Fettmolekülen, die sich von außerhalb des gemessenen Volumens in das Spektrum reinfalten bei. Diese unerwünschten Signale werden im spektralen Fitting typischerweise durch Spline-Grundlinien modelliert.

In dieser Arbeit wird untersucht, wie sich verschiedene makromolekulare Spektren und Spline-Grundlinien auf das spektrale Fitting auswirken. Änderungen der Flexibilität an der Spline-Grundlinie im LCModel (am häufigsten genutzte MRS-Software) führen zu signifikant unterschiedlichen Metabolitenkonzentrationen. Deshalb wurde in dem für diese Arbeit neuentwickelten, spektralen Fitting-Algorithmus ProFit-v3 eine automatische Erkennung der notwendigen Flexibilität der Spline-Grundlinie etabliert. Die ProFit-v3 Software wurde danach systematisch auf verschiedene Perturbationen und Grundlinien getestet. Die quantifizierten Konzentrationen wurden mit den wahren Konzentrationen (falls bekannt) und mit den Ergebnissen der LCModel Software verglichen.

Der zweite Teil dieser Arbeit untersucht neue Modellierungsmöglichkeiten für zwei weniger untersuchte Bereiche des MRS-Spektrums.

Das „Downfield-Spektrum“ enthält mehrere Spektrallinien, die noch keinen Metaboliten zugeordnet werden konnten. In dieser Arbeit wurde der intrazelluläre pH-Wert durch Downfield-Spektrallinien bestimmt. Im Weiteren wurden für alle Downfield-Spektrallinien T_2 Relaxationszeiten, spektrale Linienbreiten und Konzentrationen berechnet. Zuletzt wurden die entsprechenden Metaboliten anhand der quantifizierten Eigenschaften und Messungen aus vorliegender Literatur zu den Spektrallinien zugeordnet.

Vorherige Literatur ordnet das makromolekulare Spektrum Beiträge der Aminosäuren aus Proteinen und Peptiden zu. Zusätzlich wurden die Resonanzfrequenzen der Aminosäuren in Proteinen umfangreich von der NMR-Gemeinschaft in Proteindatenbanken gesammelt. Daher wird in dieser Arbeit ein Modellierungsverfahren vorgestellt, um die in vivo gemessenen makromolekularen Spektren als Kontribution einzelner Aminosäuren zu quantifizieren.

Insgesamt konnte gezeigt werden, dass die Forschungsergebnisse und die vorgestellte ProFit-v3 Fitting Software zur Verbesserung der MRS Quantifizierung beitragen. Die Zuordnung von Metaboliten im „Downfield-Spektrum“ und das Modell zur Quantifizierung von Aminosäuren können als zukünftige Biomarker für Krankheiten dienen.

CONTENTS

ACKNOWLEDGEMENTS	IV
ABSTRACT	V
ZUSAMMENFASSUNG	VII
1 INTRODUCTION	1
1.1 MAGNETIC RESONANCE	1
1.1.1 <i>NMR phenomenon</i>	1
1.1.2 <i>T₁ and T₂ Relaxation and chemical exchange</i>	5
1.2 METABOLITE SPECTRUM	8
1.2.1 <i>J-coupling</i>	9
1.2.2 <i>J-evolution</i>	10
1.2.3 <i>Spectral line-shape</i>	10
1.3 MRS DATA ACQUISITION	13
1.4 BRAIN METABOLITES	14
1.5 SPECTRAL FITTING	15
1.6 CONCENTRATION QUANTIFICATION	18
1.7 ULTRA-HIGH-FIELD MRS	20
1.8 THE MOTIVATION OF THE THESIS	22
~ PART A ~ IMPROVED SPECTRAL FITTING – METABOLITE QUANTIFICATION	24
2 IMPROVED SPECTRAL FITTING – SPLINE BASELINES AND MACROMOLECULES	25
2.1 INTRODUCTION	25
2.2 METHODS	27
2.2.1 <i>Technical Description, Coil Configuration, and Subjects</i>	27
2.2.2 <i>Data Acquisition</i>	27
2.2.3 <i>MRS Data Analysis</i>	29
2.2.4 <i>MRS Data Quantification Settings</i>	29
2.2.5 <i>MRS Data Quantification</i>	30
2.3 RESULTS	34
2.1 DISCUSSION	39
3 IMPROVED SPECTRAL FITTING – PROFIT	44
3.1 INTRODUCTION	44
3.2 THEORY – PROFIT-V3 ALGORITHM	45

3.2.1	<i>Magnetic resonance spectroscopy model</i>	45
3.2.2	<i>ProFit-v3 algorithm</i>	47
3.3	METHODS.....	52
3.3.1	<i>Simulated spectra</i>	54
3.3.2	<i>In vivo spectra</i>	57
3.3.3	<i>ProFit-v3 preprocessing</i>	57
3.3.4	<i>Evaluation of fit results</i>	57
3.3.5	<i>Comparison of cost functions</i>	59
3.4	RESULTS.....	59
3.1	DISCUSSION.....	63
3.2	CONCLUSION.....	71
~ PART B ~ NOVEL SPECTRAL MODELS – QUANTIFICATION OF DOWNFIELD PEAKS AND MACROMOLECULES		73
4	NOVEL SPECTRAL MODELS – DOWNFIELD SPECTRA.....	74
4.1	INTRODUCTION.....	74
4.2	METHODS.....	76
4.2.1	<i>Technical Description and Subjects</i>	76
4.2.2	<i>Data Acquisition</i>	77
4.2.3	<i>Data preprocessing</i>	78
4.2.4	<i>Fitting</i>	78
4.2.5	<i>pH estimation</i>	79
4.2.6	<i>T₂ relaxation</i>	82
4.2.7	<i>Linewidth calculations</i>	82
4.2.8	<i>Concentrations</i>	84
4.3	RESULTS.....	84
4.3.1	<i>Fitting</i>	84
4.3.2	<i>T₂ relaxation</i>	87
4.3.3	<i>Linewidth calculations</i>	88
4.3.4	<i>Concentrations</i>	91
4.1	DISCUSSION.....	93
4.1.1	<i>Spectral Quality</i>	93
4.1.2	<i>Fitting</i>	93
4.1.3	<i>pH estimation</i>	94
4.1.4	<i>T₂ relaxation</i>	94
4.1.5	<i>Linewidth calculations</i>	95

4.1.6	Concentrations and Peak Assignments	96
4.2	CONCLUSION	98
5	NOVEL SPECTRAL MODELS – DOWNFIELD PEAK ASSIGNMENTS	100
5.1	LINE BROADENING ANALYSIS DUE TO CHEMICAL EXCHANGE RATES	105
5.2	NAA AND ITS J-COUPLED ANALYSIS	110
5.3	HOMOCARNOSINE (HCS)	113
5.4	CREATINE (Cr) AND PHOSPHOCREATINE (PCr)	114
5.5	NICOTINAMIDE ADENINE DINUCLEOTIDE (NAD ⁺)	115
5.6	ADENOSINE TRIPHOSPHATE (ATP)	117
5.7	N-ACETYL ASPARTYL GLUTAMATE (NAAG)	118
5.8	GLUCOSE, A-ANOMER (GLC)	118
5.9	GLUTAMINE (GLN)	119
5.10	HISTIDINE (HIST)	120
5.11	HISTAMINE	121
5.12	UREA	121
5.13	GLUTATHIONE (GSH),	122
5.14	OTHER AMIDES AND AMINO ACIDS OF MACROMOLECULES	123
5.15	SUMMARY OF DOWNFIELD PEAK ASSIGNMENTS	124
6	NOVEL SPECTRAL MODELS – AMINO ACID MODEL	126
6.1	MOTIVATION	126
6.1.1	<i>Linewidth analysis of upfield singlets and effects of the B₀ shimming</i>	127
6.1.2	<i>The residual linewidth of the macromolecular peaks</i>	129
6.1.3	<i>NMR spectra of cytosol</i>	130
6.2	METHODS	132
6.3	RESULTS	135
6.1	DISCUSSION	136
6.2	CONCLUSION	140
7	CONCLUSION AND OUTLOOK	141
8	ABBREVIATIONS	143
9	CURRICULUM VITAE	145
10	LIST OF PUBLICATIONS	147
10.1	PUBLICATIONS INCLUDED IN THIS DOCTORAL THESIS	147

10.2	PUBLICATIONS NOT INCLUDED IN THIS THESIS	148
11	STATEMENT OF CONTRIBUTIONS.....	151
	BIBLIOGRAPHY.....	155
	APPENDIX A.....	170
	APPENDIX B.....	172

1 Introduction

This chapter aims to provide the reader with basic knowledge of Magnetic resonance spectroscopy (MRS). While this chapter explains the most important fundamentals, which help understand the research work presented in the chapters following, it is far from complete. A full explanation of the entire MRS physics and basics of computer science, biochemistry, physics, mathematics are beyond the reach of this manuscript, and the reader is assumed to be knowledgeable about these natural science fundamentals and may refer to the textbooks of de Graaf² and Keeler³ for extensive explanations of MRS. The chapter is concluded with the motivation for the scientific work presented in this thesis.

1.1 Magnetic resonance

MRS is a non-invasive methodology used to quantify tissue metabolite concentrations in vivo in several different organs in the human body: muscle, liver, heart, prostate. However, MRS is most widely used in examining the human brain⁴, which is also the focus of this thesis.

MRS is based on the same physical phenomenon and similar measurement techniques as nuclear magnetic resonance spectroscopy (NMR). Even if the two methods are very similar, measurements in vivo are abbreviated as MRS. In contrast, measurements performed in chemistry to derive the chemical composition of samples in vitro, are abbreviated as NMR. The differentiation between these two terms is also used throughout this thesis.

1.1.1 NMR phenomenon

The NMR physical phenomenon relies on the nuclear spin of the neutrons and protons composing an atom. If the number of protons and/or the number of neutrons in an isotope is odd, then the isotope can undergo NMR. Multiple isotopes are detectable through NMR and MRS: the hydrogen isotopes ^1H (proton) and ^2H (deuterium), the carbon isotope ^{13}C , the phosphorus isotope ^{31}P . However, the most commonly investigated isotope is ^1H , due to the high natural abundance of this isotope and hydrogen being ubiquitous in organic

tissue due to its high water content. The research results in this thesis are focused on MRS and NMR based observation of the ^1H isotope; hence often the term ^1H -MRS will be used to describe proton MRS.

When placed in a static strong magnetic field (B_0) the proton spin orients itself to the direction of the magnetic field. Through the shielding created by the electron orbital an inverse magnetic field (B_{inv}) is induced (see Figure 1.1). Hence, the investigated proton will observe a $B_{eff} = B_0 - B_{inv}$ magnetic field, the magnitude of which will depend on the intensity of the shielding created by the electron orbital⁵. The B_{eff} is sometimes also written as $B_{eff} = B_0(1 - \sigma)$, where σ represents the shielding constant.

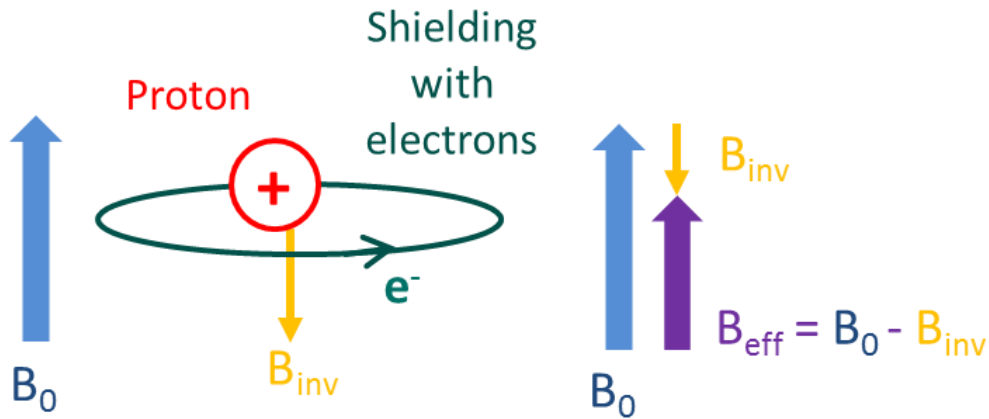


Figure 1.1: Schematic of a proton in a B_0 magnetic field. The electron shielding introduces an inverse magnetic field, decreasing the effective magnetic field (B_{eff}) observed by the proton.

The orientation of the spin can be aligned with the external B_0 field, named “spin-up” state, or opposing the external field, named “spin-down” state (see Figure 1.2). The energy difference (ΔE) between the spin states is known as the Zeeman effect and is dependent on the Planck’s constant h and the resonance frequency f_0 (see Eq. 1.1a).

$$\Delta E = hf_0 \quad \text{Eq. 1.1a}$$

This energy gap also scales with the magnetic field, and is described by the Zeeman equation:

$$\Delta E = \gamma h B_{eff} \quad \text{Eq. 1.1b}$$

where γ is the gyromagnetic ratio equal to 42.58 Mhz/Tesla for the ^1H nucleus.

Combining the Eq. 1.1a and Eq. 1.1b we get the Larmor equation in Eq. 1.1c.

$$f_0 = \gamma B_{eff} \quad \text{Eq. 1.1c}$$

Summarizing, the previous equations, a more shielded proton will result in a larger B_{inv} , and hence a decreased in B_{eff} , a decrease in ΔE and a decrease in f_0 .

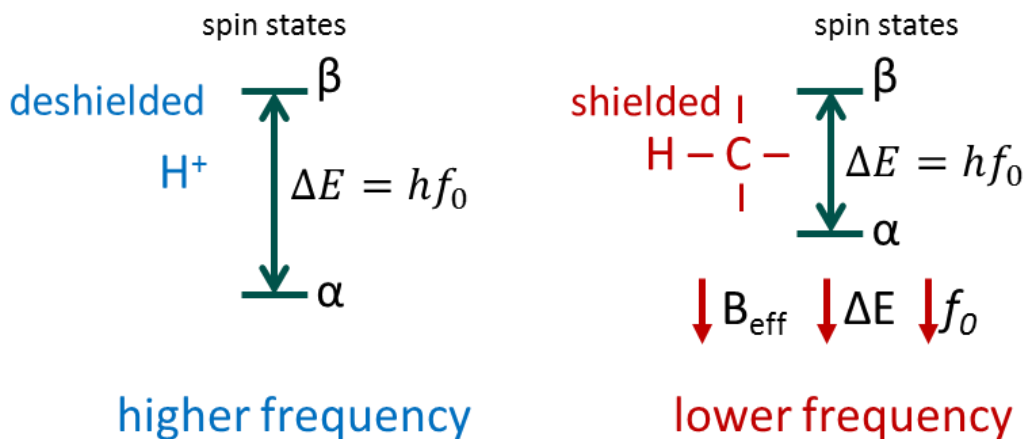


Figure 1.2: The energy difference (ΔE) between the spin states: “spin-up” state β and “spin-down” state α is depicted for protons in different shielding environments. Shielded protons will have a smaller ΔE , then deshielded or less shielded protons, due to the decrease in B_{eff} . This in turn leads to a lower resonance frequency f_0 .

To measure the signals from a spin system, an oscillating magnetic field with the resonance frequency f_0 is used to excite the spins. Following the excitation, the spin will return to its original energy state while emitting an electromagnetic signal reflecting the energy difference ΔE . This signal has the characteristic resonance frequency f_0 . The excitation frequencies are in the radio-frequency (RF) range; hence the pulses and the coils are called RF pulses and RF coils. The electromagnetic signal response of the spin system is decaying at a given rate and is called free-induction-decay (FID). The FID is a vector of complex numbers, which when Fourier transformed, creates a spectrum with a peak appearing at the resonance frequency f_0 of the nucleus (see top row of Figure 1.3).

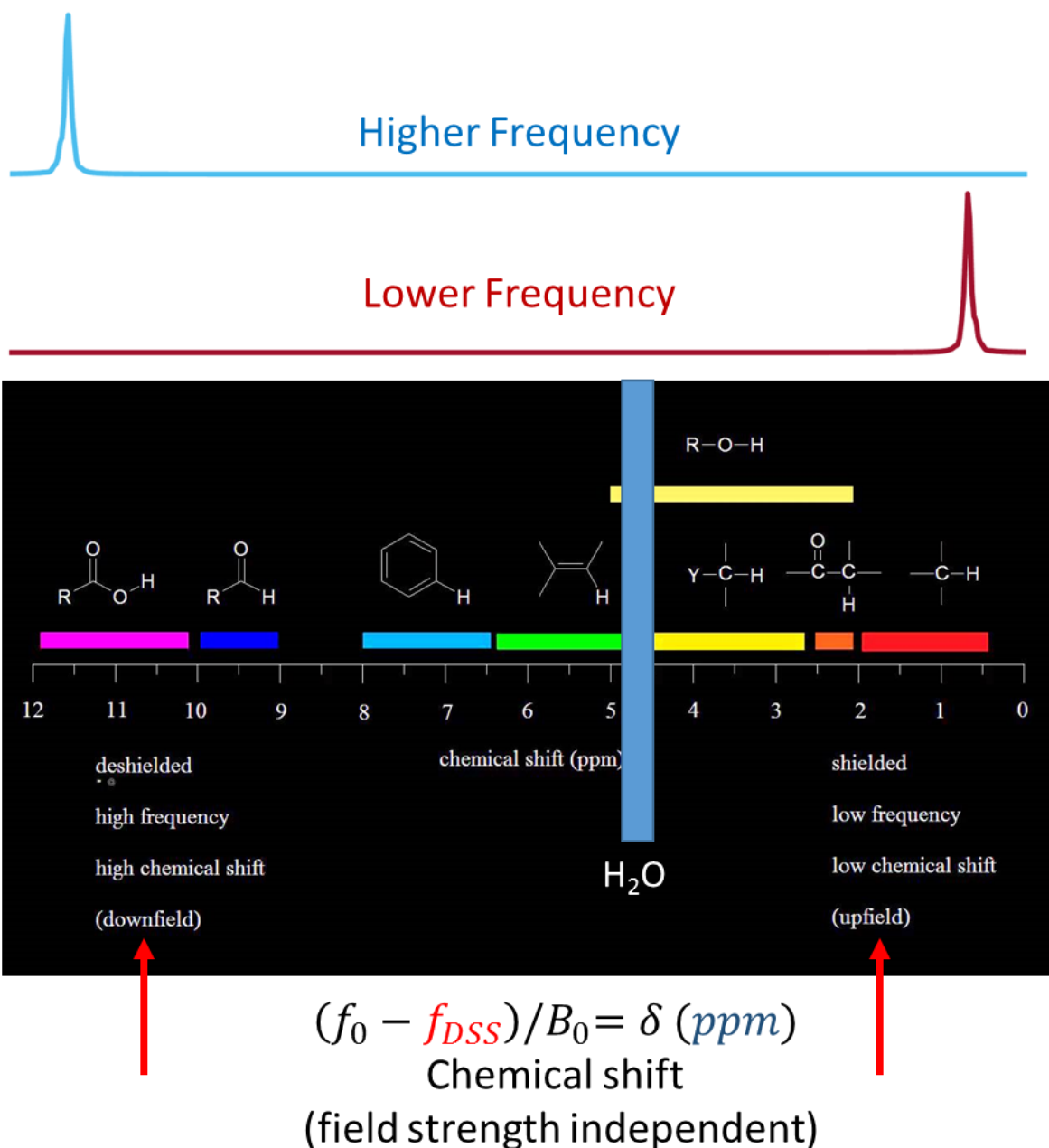


Figure 1.3: The field strength independent chemical shift axes is shown. The two upper traces exemplify the spectra of the unshielded and shielded protons from Figure 1.2, depicting low and high resonance frequencies. The general shielding effects of the protons based on their location in the chemical structure is shown in the black area above the axes. The blue bar is depicting the resonance frequency of the water protons (hydrogen atoms). The red arrows highlight the terms upfield and downfield, which are used with respect to the water resonance frequency. Courtesy of American Medical Colleges and Khan Academy, www.khanacademy.org (CC BY-NC-SA 3.0)

The precise resonance frequency f_0 of a nucleus depends on the shielding created by the electron orbitals surrounding it. The chemical bonds influence the electron orbitals within a molecule; hence different molecules create different shielding effects. These lead further to peaks in the spectrum with different resonance frequencies f_0 , which allows the differentiation between metabolites.

To have a B_0 field independent frequency axes for the resonance frequencies, Eq. 1.2 is used.

$$(f_0 - f_{DSS})/B_0 = \delta \quad \text{Eq. 1.2}$$

f_{DSS} is the resonance frequency of 2,2-dimethyl-2-silapentane-5-sulfonate (DSS), and δ stands for the chemical shift, expressed in terms of parts-per-million (ppm). The chemical shift axis is plotted in reverse by convention⁶. The example of deshielded and shielded protons resulting in lower and higher frequencies from Figure 1.2 are depicted after the Fourier transformation of their respective FIDs in the top rows of Figure 1.3.

Figure 1.3 also shows the typical chemical shifts of protons in different chemical compounds depending on the shielding created by the electron orbital related to the respective chemical structure. The most abundant molecule in vivo is water, which has its chemical shift at 4.66 ppm and is depicted with the blue bar in Figure 1.3. The spectrum on the right-hand side of the water signal contains lower chemical shifts (with lower resonance frequencies) and forms the so-called “upfield” spectrum. In contrast, higher chemical shifts (higher resonance frequencies), on the left-hand side of the water signal are forming the so-called “downfield” spectrum (see the red arrows in Figure 1.3).

In this thesis, chapters 2 and 3 are focusing on the upfield spectrum, while chapters 4 and 5 on the downfield spectrum. Chapter 6 is looking at the simultaneous handling of both the upfield and downfield spectrum to create a quantification model for amino acids.

1.1.2 T_1 and T_2 Relaxation and chemical exchange

In MRS larger volumes of tissue are measured (for the spectra presented in this thesis the voxel size was generally $2 \times 2 \times 2 \text{ cm}^3$). Hence, this volume contains several spins: we denote n_α the population of the spins in the low energy state and n_β the population of the spins in the high energy state. All these spins $n = n_\alpha + n_\beta$ contribute to the net

magnetization vector (M_0) at thermal equilibrium with their energy difference $\Delta E = hf_0$ as follows:

$$M_0 = \frac{\gamma h}{2\pi} \cdot \frac{n\Delta E}{4kT} \quad \text{Eq. 1.3a}$$

where k is the Boltzmann constant and T is the absolute temperature.

To measure all these spins in MRS, multiple RF pulses are used, referred to as RF pulse sequences. These MRS pulse sequences usually flip the spins by a 90° RF pulse (excitation pulse) from their equilibrium magnetization (M_0) parallel to the B_0 magnetic field, into a transverse plane. The created transverse component of the magnetization is denoted as M_{xy} . The spins will decay back to the M_0 magnetization by a rate of the T_1 relaxation time (also called longitudinal relaxation time).

For MRS equally important is the T_2 relaxation time (also called transverse relaxation or spin-spin relaxation). This phenomenon is depicted in Figure 1.4, which shows, that the spins interact with each other and try to minimize the magnitude of their joint M_{xy} magnetization by spreading out (dephasing) their magnetizations in the XY plane. This phenomenon is widely used in MRS when applying spin-echo sequences, which flip by 180° the dephasing signal of the spins. The previously (before the 180° pulse) dephasing spins will continue their motion and get rephased with their magnetization pointing in the opposite direction ($-M_{xy}$). This rephased signal is called a spin-echo and is centered at the so-called echo-time (TE). The relationship between the T_2 relaxation time and the TE is used in chapter 4 to measure T_2 relaxation times at the B_0 field strength of 9.4 T.

Multiple factors contribute to the T_2 relaxation: microscopic magnetic susceptibility differences, dipole-dipole interaction, chemical shift anisotropy, molecular translation, fluid flow, J-coupling, chemical exchange. These effects lead to large variations of T_2 relaxation times. For MRS measurements and quantification, as far as possible, the metabolite T_2 relaxation times should be considered. These are specific to the magnetic field strength B_0 , the tissue, the brain region and the sequence. In the human brain, tissue-specific relaxation times are determined for grey-matter (GM), white matter (WM), and cerebrospinal fluid (CSF). For abundant metabolites with multiple peaks, T_2 relaxation times specific to the individual subparts of the molecule (moieties) are used. For example, to determine the T_2 relaxation times of N-acetylaspartate (NAA) it is split into its acetyl

moiety with the proton resonances of $^2\text{CH}_3$ and its aspartyl moiety which includes the protons from ^2CH and $^3\text{CH}_2$. Further, the NH proton is treated separately (the structure of the NAA molecule and its properties are presented in chapter 1.2 and Figure 1.6).

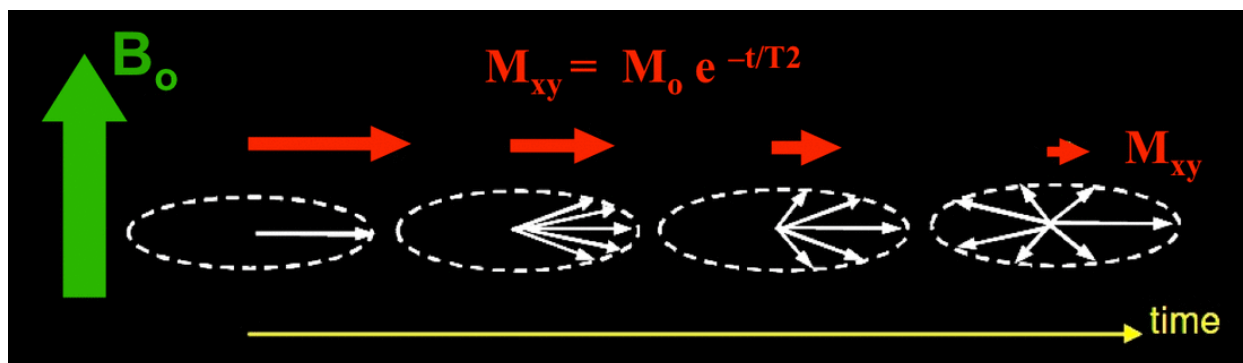


Figure 1.4: A symbolic depiction of the T_2 relaxation, where the magnetization of the spins in the transverse plane (M_{xy}) decreases exponentially with the time constant T_2 . The spins forming the original full magnetization (M_0) parallel with the B_0 plane, when flipped into the transverse plane interact with one another to get back into an equilibrium state. Courtesy of Allen D. Elster, MRIquestions.com

Metabolites bound to tissue membranes or constrained by solid structures, such as bones, have T_2 relaxation times in the order of nanoseconds and are referred to as MR-invisible. Molecules which are freely moving in a liquid are generally detectable, and their T_2 relaxation time also depends on the size of the molecule. Smaller molecules (metabolites) have longer relaxation times than larger molecules, and hence are more prominent in MRS spectra at long TE. Large molecules, such as peptides and proteins, are referred to as macromolecules (MM) in MRS. These MMs have shorter T_2 relaxation times due to their bulky nature. Their influence on the quantification of small metabolites' concentrations is discussed in chapter 2, while chapter 6 presents a characterization of these MMs themselves.

In chapter 6, the measured T_2^{eff} relaxation times of MMs are mentioned. These T_2 relaxation times also include the unknown J-evolution effects (will be explained in section 1.2.2) for the macromolecular peaks.

Hydrogen atoms of an amide ($-\text{NH}$) or hydroxyl ($-\text{OH}$) group of a molecule in an aqueous solution can transfer their nucleus to a water molecule. This nucleus transfer is referred to as chemical exchange and is depicted in Figure 1.5. The chemical exchange occurs

with the exchange rate k . When measuring T_2 relaxation times of protons undergoing chemical exchange their T_2 relaxation time will appear shorter.

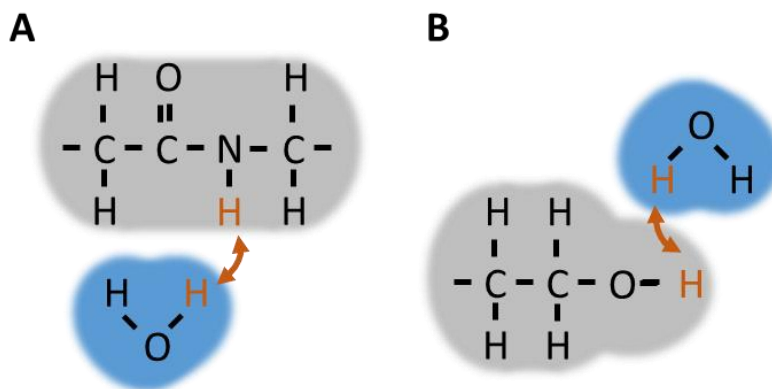


Figure 1.5: A. Chemical exchange between an amide ($-NH$) group of a macromolecule and water. B: Chemical exchange between a hydroxyl ($-OH$) group of a molecule and water. The exchanging protons are highlighted in orange.

In chapter 4, T_2^{app} values are measured for the downfield spectrum, which include unknown J-evolution effects, but also the chemical exchange effects with water. These are corrected for the water exchange effects and presented as T_2^{corr} , see subchapter 4.2.6. The results of the T_2^{app} measurements will be further used in elaborating peak assignments in chapter 5 and 6; while in subchapter 5.1 more elaborated theoretical aspects of the chemical exchange are detailed.

1.2 Metabolite spectrum

The properties of the spectral appearance of a metabolite are exemplified in this subchapter based on the most prominent metabolite in the healthy human brain, N-acetylaspartate (NAA). Other metabolites present in the human brain and measurable by MRS are enumerated in subchapter 1.4.

Protons shielded in a chemically equivalent environment have identical resonance frequencies, and their spectral peak will scale with the number of protons contributing to it. For example, the 2CH_3 group of NAA has three equivalent protons, which form a singlet at 2.008 ppm⁷ with the amplitude being 3 times as high as for a single proton (see dark green arrows in Figure 1.6). As a reference peak, the DSS peak, at 0 ppm was simulated with the amplitude 1 (see red arrow in Figure 1.6).

1.2.1 J-coupling

If there are two adjacent protons with chemical bonds between them, an electron-mediated interaction occurs, which leads to the phenomenon known as J-coupling. If the proton with the resonance frequency f_H ($\Delta E = hf_H$) interacts with only one additional proton with a different chemical shielding and resonance frequency f_C ($\Delta E = hf_C$), two additional energy states are created. These four energy states lead to energy differences of $\Delta E = h\left(f_H \pm \frac{J}{2}\right)$ and $\Delta E = h\left(f_C \pm \frac{J}{2}\right)$, where J is the J-coupling constant defining the interaction between the two spins. This splitting of the energy levels leads to both spectral peaks at f_H and f_C splitting in two. These are called doublets. A doublet is exemplified in Figure 1.6 through the NH resonance of NAA, resonating at 7.891 ppm (see the light green arrows in the figure). The NH proton interacts only with the ^2CH proton and the J-coupling constant of 6.4 Hz between the two protons⁷ means that in the spectra the peaks of the doublet will appear at a distance of 6.4 Hz. J-coupling constants are B_0 field strength independent.

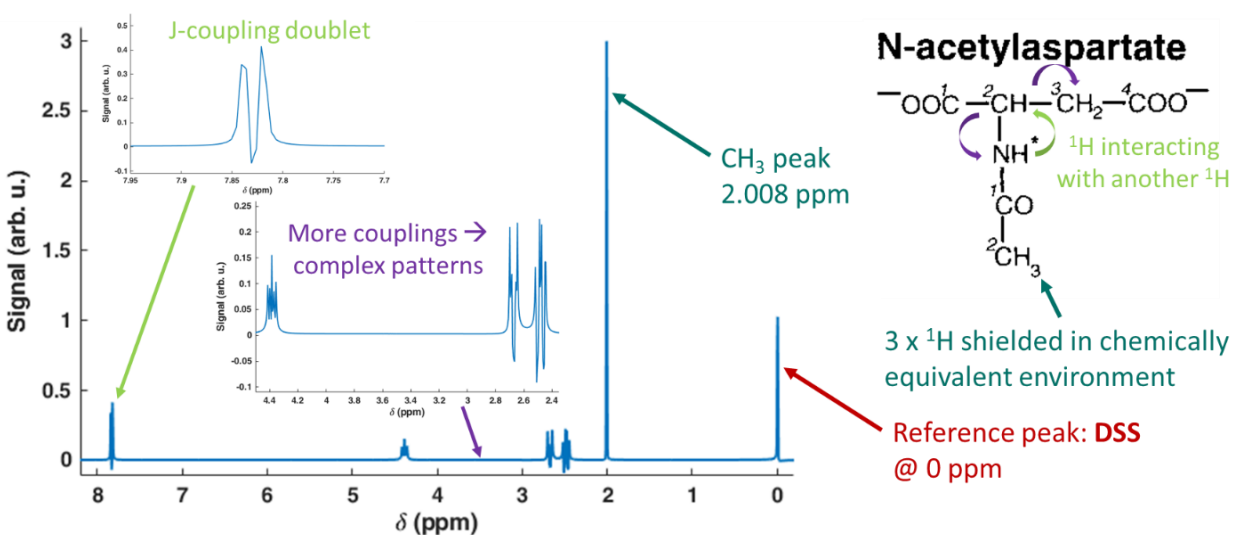


Figure 1.6: The spectral appearance of N-acetylaspartate is depicted. The chemical structure is displayed on the right, with colored arrows pointing to different protons and J-coupling interactions. Their corresponding peaks are marked with the same colored arrows in the spectrum. The peak at 0 ppm is a simulation of the added DSS resonance, and its peak is used as a frequency reference.

If there are multiple J-couplings for a given proton, this will result in the appearance of triplets or multiplets in the spectrum. These have a more complex pattern, as shown for the ^2CH and $^3\text{CH}_2$ protons of NAA and highlighted in purple in Figure 1.6.

If there is no J-coupling present, like for the $^2\text{CH}_3$ of NAA, the peak in the spectrum is called a singlet. Independently, whether we have a singlet or a J-coupled peak, the area under the curve will still be equivalent to the number of protons contributing.

The scaling effect of the contributing protons to a single resonance frequency as exemplified for the $^2\text{CH}_3$ peak of NAA is similar to the metabolite concentration's scaling effect within a measured volume. All the contributing protons are summed up macroscopically for the given volume and thereby scale the metabolite peaks. For instance, if NAA is measured in a solution with the double concentration, also the entire spectrum will be scaled by a factor two.

An individual spectrum of a metabolite, like the one shown in Figure 1.6, can be simulated using the known chemical shifts and J-coupling constants. The sequence parameters of the MRS acquisition are applied to these simulations. Such simulated spectra are referred to as spectral basis sets, and when used in equations, these will be denoted as β_k .

1.2.2 J-evolution

For the coupled spin systems (see examples in Figure 1.6), the spin interactions also lead to the so-called J-evolution, shown in Figure 1.7. The spectral peaks start to invert, with a full inversion achieved at $TE = 1/J$, while at $TE = 2 * 1/J$ the peaks of the coupled resonances will point upwards again.

Chemical shifts and J-couplings are measurable constants for the protons of a metabolite. Therefore, these chemical shifts and J-coupling constants are used for the peak assignments in chapters 5 and 6, with a more detailed example on J-evolution presented in the subchapter 5.2.

1.2.3 Spectral line-shape

MRS spectra are acquired from larger volumes of interests (voxels) through localization procedures created by MRS pulse sequences. While ideally, the static magnetic field (B_0) should be homogeneous in this voxel, this is never the case in vivo. The B_0 inhomogeneity

can be “macroscopic (intervoxel, which is constant across a voxel) or microscopic (changing within a voxel)”⁸. Macroscopic inhomogeneities can originate from tissue-tissue or air-tissue boundaries (magnetic susceptibilities can be very different) or fluid motion or the deoxyhemoglobin in tiny veins. Microscopic inhomogeneities are caused by local paramagnetic effects, blood products or iron content present in the voxel⁸. To achieve a more homogeneous B_0 field, a method called shimming is applied, which creates additional local magnetic fields to compensate the inhomogeneities. However, some effects will persist, and these inhomogeneity effects are referred to as microscopic and macroscopic susceptibility effects.

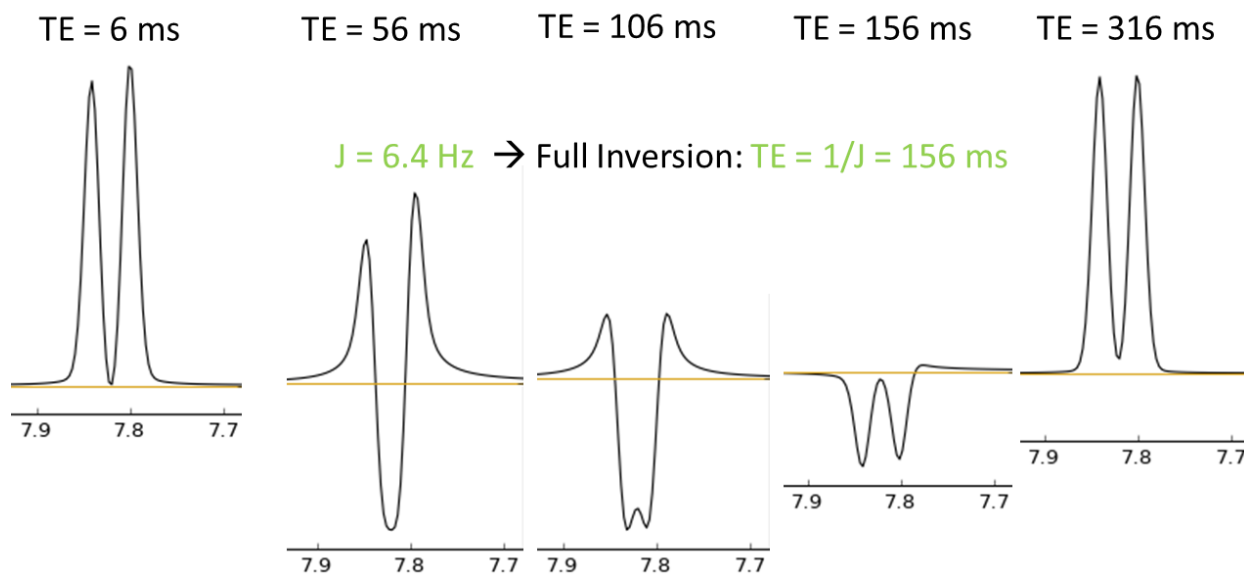


Figure 1.7: The J -evolution in relationship with the duration of the TEs is exemplified for the NH proton of NAA. Full inversion is achieved at $TE = 1/J$, in the current example at 156 ms.

The microscopic and macroscopic susceptibility effects lead to a faster decaying FID than predicted by the T_2 relaxation times and is referred to as T_2^* relaxation. The T_2^* value is also a characteristic of the peaks in the spectrum, creating a Lorentzian line broadening of the peaks, defined as $\nu_e = \frac{1}{\pi T_2^*}$. In the absence of a measured T_2^* , the measured T_2 relaxation time is used for the linewidth approximation ($\nu_e = \frac{1}{\pi T_2}$). In chapters 3 and 4 of this thesis the T_2^{app} values were used.

The inhomogeneous B_0 within the voxel leads to changes in resonance frequencies impacting all metabolites identically³. This inhomogeneous B_0 makes the all spectral

peaks appearing broader. Assuming that the B_0 inhomogeneities have a close to Gaussian distribution, the associated broadening effects are characterized in MRS by a Gaussian line-broadening factor ν_g . The combination of the Lorentzian and Gaussian line-broadening is referred to as the Voigt line shape.

Applying these Gaussian and Lorentzian line broadening factors to a simulated ideal spectrum (β_k), the signal equation of the spectrum (\hat{y}) can be written as:

$$\hat{y} = \beta_k \cdot \exp[-\nu_{e,k}\pi(TE + \mathbf{t})] \cdot \exp\left[\frac{(\nu_g\pi\mathbf{t})^2}{4\ln(2)}\right] \quad \text{Eq. 1.4}$$

where TE is the echo-time, and \mathbf{t} is the acquisition time vector.

The spectral appearance resulting from applying the respective line broadening factors for the brain metabolite NAA is shown in Figure 1.8. Please note, that while the peak at 2.008 gets broader and the amplitude decreases, it maintains the singlet appearance. On the other hand, the line broadening effects smooth out coupled peaks between 2.4 and 2.7 ppm, and several spectral features are not distinguishable anymore.

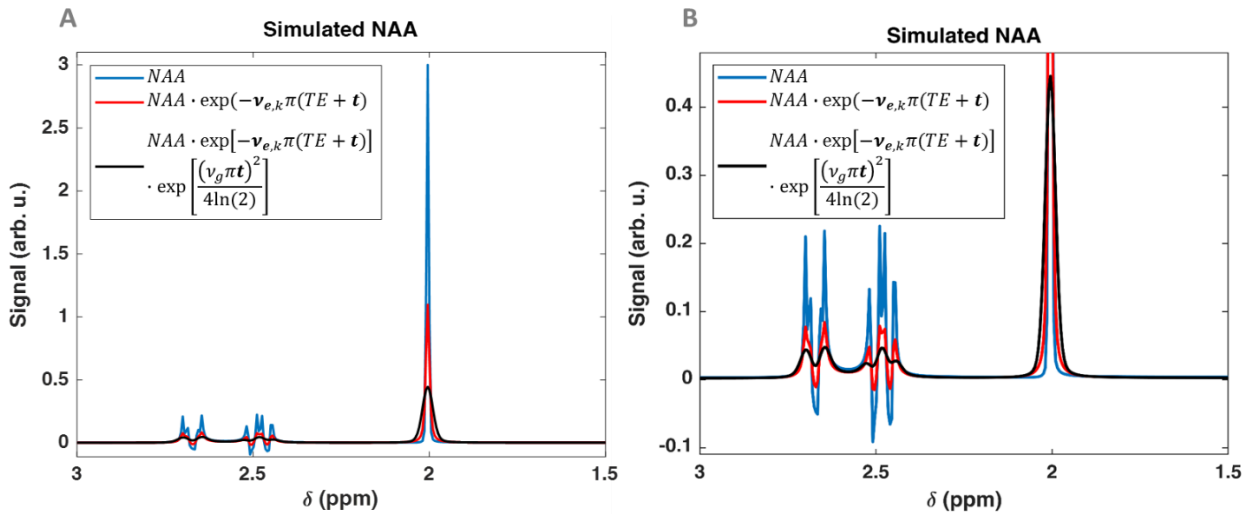


Figure 1.8: The *in vivo* line broadening effects for the Lorentzian parameter $\nu_{e,k}$ and the Gaussian parameter ν_g are shown on the NAA spectrum simulated for ideal conditions. Subfigure B shows the zoomed-in version of subfigure A. While the singlet lineshape is well maintained at 2.008 ppm, the spectral pattern of the coupled spin systems between 2.4 and 2.7 ppm are smoothed out. The top of the 2.008 ppm peak is not shown, but the singlet appearance is maintained.

Additional effects on the spectra are phase or frequency shift errors. Zeroth-order phase errors (φ_0) originate from the coil and the acquisition chain, while the first-order phase errors (φ_1) are caused by the timing of the acquisition sequence. Frequency shift errors can be global (ω_{global}) or local ($\omega_{local,k}$). Global frequency errors originate from acquisition or post-processing errors. The local frequency shift errors are specific to an individual peak or metabolite. The metabolite's chemical shielding and resonance frequencies are affected differently from local temperature, pH or other ion changes. Moreover, these changes may occur in a single cell compartment, impacting only some metabolites. Examples of phase and frequency errors are shown in chapter 3 in Figure 3.3. A metabolite, which is part of a larger molecule will have a slightly shifted resonance frequency caused by the change in shielding due to the rest of the molecule, which is an effect discussed in subchapter 6.1.2.

1.3 MRS Data Acquisition

MRS spectra are acquired using a sequence of RF pulses, which create the localization of the spectra to the desired voxel. In this work, spin-echo sequences are used, which refocus the dephasing spins described in section 1.1.2 and Figure 1.4. The used spin-echo sequence is a semi-LASER sequence⁹, which achieves improved signal-to-noise ratio (SNR) by applying so-called adiabatic-full-passage (AFP) 180° refocusing pulses. The most dominant peak in MRS spectra is the water signal, which is around 10,000 times higher than those of the rest of the metabolites. To allow the identification and quantification of the metabolite peaks, MRS pulse sequences suppress the water signal through the saturation of water resonance frequency, before the localizing RF excitation pulses^{10,11}.

The downfield spectrum contains several peaks, which exchange their protons with the water signal. The saturation pulses used to suppress the water signal also lead to the suppression of these downfield peaks.

The recently developed technique of metabolite-cycling⁹ (MC), suppresses the water signal while avoiding the saturation of it. It is achieved by using a subtraction scheme, and metabolite-cycling pulses. Metabolite-cycling pulses selectively invert in subsequent acquisitions only the upfield or downfield metabolite spectrum, while not exciting the water

signal. This MC technique, avoiding the perturbation of the water signal makes the peaks exchanging with water in the downfield spectrum measurable¹².

An insufficient suppression of the water signal or an imperfect metabolite-cycling will lead to residual water signal artefacts present in the spectrum.

1.4 Brain metabolites

In the following, the most abundant brain metabolites and their role¹³ are enumerated.

Water is the most abundant molecule present in the human brain, its concentration being several orders of magnitude higher than those of all other metabolites. Hence, the water signal is used for internal concentration referencing (see subchapter 1.6). On the other hand, water suppression methods mentioned in subchapter 1.3 are used to measure the metabolite spectra. Water creates the aqueous environment in which all the metabolic processes take place.

N-acetylaspartate (**NAA**) is the most prominent metabolite of healthy brain spectra with concentrations of around 10-13 mmol/kg, and it was also used to exemplify spectral properties in this chapter. NAA has been used as a marker of neuronal density, and its main role is assumed to be osmoregulation.

Adenosine triphosphate (**ATP**) is the primary source of free energy for the molecular processes and is present in the brain with concentrations of around 2.4-3 mmol/kg. To produce ATP, the brain cells use the energy freed from glucose (**Glc**) by glycolysis. Lactate (**Lac**) is the end-product of anaerobic glycolysis.

Brain cells use aerobic glycolysis to produce the most abundant excitatory neurotransmitters glutamate (**Glu**). Glu, together with glutamine (**Gln**) create the Glu-Gln neurotransmitter cycle. Other excitatory neurotransmitters include aspartate (**Asp**) and N-acetylaspartylglutamate (**NAAG**). The inhibitory neurotransmitters measurable with MRS are γ -aminobutyric acid (**GABA**) and glycine (**Gly/Glyc**). Gly also acts as an antioxidant. However, glutathione (**GSH**) is the most important antioxidant present in the brain.

Another source of energy is created by the energy buffer between creatine (**Cr**) and phosphocreatine (**PCr**). The chemical shift differences between the methyl (CH₃) and

methylene (CH₂) protons of Cr and PCr is small, and therefore the total creatine (**tCr**) signal is often used in MRS.

Albeit present in lower concentrations than NAA and tCr, choline compounds form a prominent peak at 3.2 ppm due to nine protons (CH₃)₃ contributing to this singlet peak. The choline compounds are phosphocholine (**PCho**), glycerophosphocholine (**GPC**). These together are referred to as total choline (**tCho**).

Myo-inositol (**mi**), scyllo-inositol (**Scy**) are sugars present in the brain, with their exact function unknown, but they are believed to be mainly osmoregulators.

Finally, the proteins and peptides present in the brain form the macromolecular spectrum (**MM spectrum**). Alternative namings present in literature and this manuscript to the MM spectrum are MM baseline or just macromolecules.

1.5 Spectral Fitting

MRS fitting is the algorithmic processing step modelling the individual metabolite and the MM spectrum contributions using their basis spectra (β_k) to a measured spectrum. This modelling quantifies the individual metabolite concentrations found in the measured voxel.

The most important MRS aspect is that the individual metabolite spectra scale linearly with their respective metabolite concentrations. The signal amplitude of all the spectrum (independent of the individual metabolite concentrations) scales with several factors, such as coil impedance, coil loading, signal receive chain and amplifiers. However, if the concentration of a molecule can be determined, this can be used to reference all other metabolite concentrations. Generally, this referencing is done by assuming a constant tissue water content (see subchapter 1.6) and acquiring a water reference spectrum in addition to the water suppressed metabolite spectrum.

While the peak amplitude of the metabolite basis set β_k can additionally change due to the line-shape effects (as discussed in section 1.2.3 and Figure 1.6), the area under the peak will always reflect proportionally the metabolite concentration within the measured voxel.

For any measured voxel, all the metabolites present in that voxel and excited by the RF pulses will contribute to the spectrum in an intensity weighted manner according to their

respective concentrations. An example of such a spectrum is shown in Figure 1.9 in the blue top line. The lines below show the contributing factors to the spectrum: the macromolecular spectrum (MM Spec.), the individual metabolites, the fit residual, and the spline baseline (Baseline). All the individual metabolite basis sets, but also the MM spectrum are scaled by their respective concentrations in the measured voxel. Simultaneously, their line-shape reflects the broadening effects described in section 1.2.3 and Figure 1.8.

MRS fitting solves an optimization problem that finds the best spectral model of the measured spectrum while minimizing the fit residual. In Figure 1.9 the example of a fitted spectrum (denoted “Fit”) for an in vivo measured spectrum (denoted “Data”) is shown in the top two overlapped lines in red and blue, respectively.

In vivo spectra besides the metabolites, for which chemical shifts and coupling constants have been measured^{7,14}, also contains the MM spectrum and the baseline components highlighted with green arrows in Figure 1.9. As mentioned in section 1.1.2, the MM spectrum is composed of large molecules, such as peptides and proteins, which have shorter T_2 relaxation times than the other metabolites. The baseline component is used for fitting artefacts stemming from experimental imperfections such as residual water signals, lipid contaminations or rarely other very low content metabolite signals, which cannot be modelled otherwise. Notably, these contributions are approximated by splines¹⁵⁻¹⁷. The influence of the MM spectrum and spline baselines, on the spectral fitting is investigated in chapter 2.

MRS fitting is a very ill-posed problem. Multiple metabolites contribute in the same spectral region (at similar chemical shifts), which is called spectral overlap (see Figure 1.9). The differentiation between the contributing metabolites relies on the small differences in chemical shifts and J-coupling properties, which may be masked by the broad linewidths achieved in vivo. Additionally, multiple parameters characterize a spectrum, as shown in section 1.2.3, but fully expressed by the Eq. 3.1 in chapter 3. These can create several local minima for the minimization problem used in fitting. While the fitting algorithm minimizes the fit residual, the modelling results may not correspond to the physiological ground truth. More importantly, physiological variations of a few

percent serve as disease markers^{4,18} or markers of the brain metabolism¹⁹⁻²², and these should be differentiated correctly by the fitting algorithms.

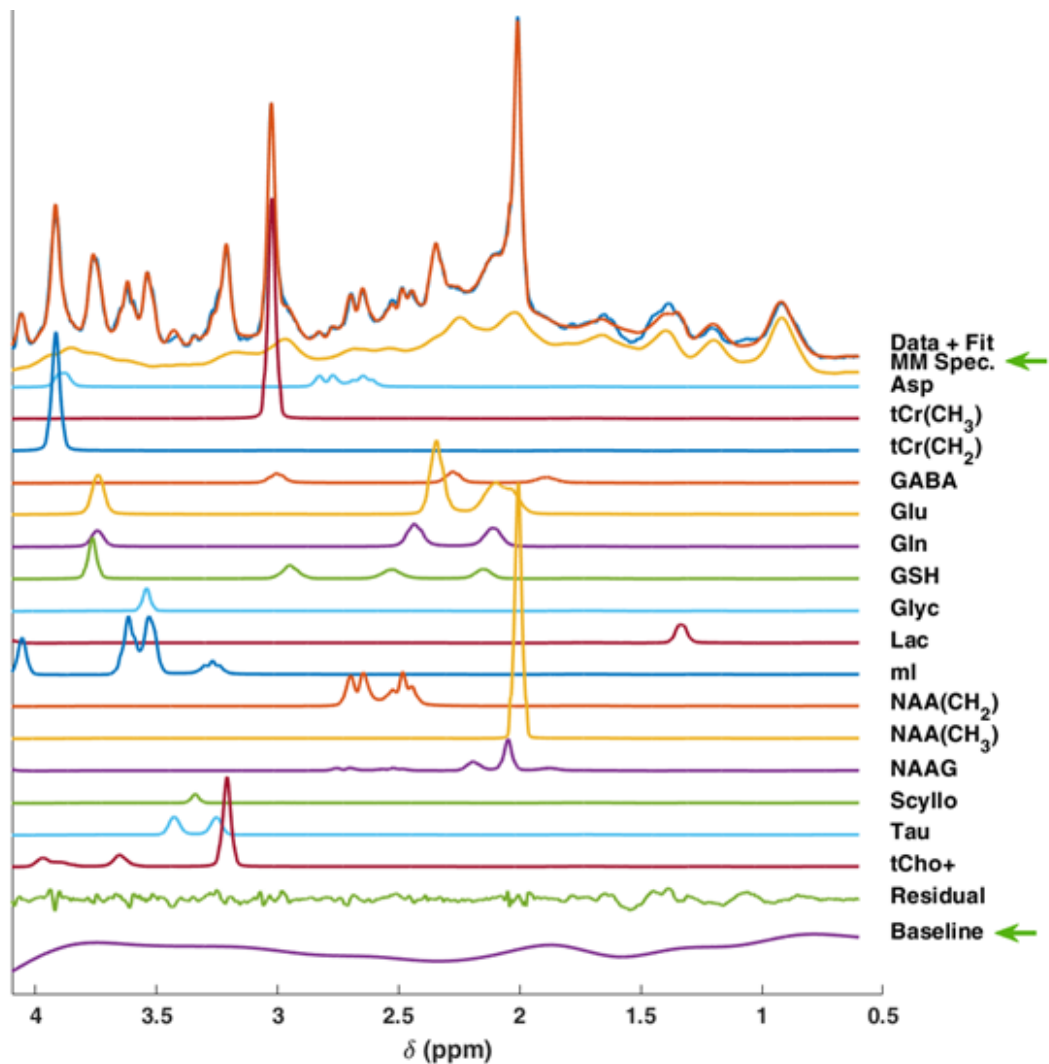


Figure 1.9: Sample spectrum (top blue line “Data”) with the fit (top red line “Fit”) is shown. The individual contributing metabolites are shown in the lines below. The last two lines, show the residual of the fitting (in green) and the fitted spline baseline (in purple). The green arrows point to the contribution of the macromolecular spectrum (MM Spec.) and the spline baseline (Baseline). Abbreviations: Macromolecular spectrum (MM Spec.), aspartate (Asp), total creatine – 3.9 singlet [$tCr(CH_2)$], total creatine – 3.0 singlet [$tCr(CH_3)$], γ -aminobutyric acid (GABA), glutamate (Glu), glutamine (Gln), glutathione (GSH), glycine (Glyc), myo-inositol (ml), N-acetylaspartate – acetyl moiety [$NAA(CH_3)$], N-acetylaspartate – aspartyl moiety [$NAA(CH_2)$], N-acetylaspartylglutamate (NAAG), scyllo-inositol (Scy), taurine (Tau), lactate (Lac) and combined phosphocholine, glycerophosphocholine and phosphoethanolamine molecules (tCho+).

1.6 Concentration Quantification

Text and tables in this subchapter were adapted with minor modifications from our work previously published in the Supporting Information of:

Giapitzakis IA*, **Borbath T***, Murali-Manohar S, Avdievich N, Henning A. “Investigation of the influence of macromolecules and spline baseline in the fitting model of human brain spectra at 9.4 T”. *Magnetic resonance in medicine*, 2019;81(2):746-758.

Borbath T*, Murali-Manohar S*, Wright AM, Henning A. “In vivo characterization of downfield peaks at 9.4 T: T₂ relaxation times, quantification, pH estimation, and assignments.” *Magnetic resonance in medicine*, 2020.

The presented equations are adaptations from Gasparovic et al.¹ to the work of this thesis.

Fitted concentrations have to be scaled to quantitative units to allow their comparison across different research and clinical sites, which may use MR scanners from different vendors. The most widely used method is the scaling of the metabolite concentrations by using the internal water reference, where the unsuppressed water signal is measured in the same voxel as the metabolites. Concentrations in mmol/kg (mmolal) and mmol/L (mmolar) are derived by applying corrections for the fractional tissue composition as well as T₁ and T₂ corrections for both the water and the metabolite signals.

Hence, for the present works, additionally acquired high-resolution MP2RAGE images were segmented into WM, GM and CSF using Statistical Parametric Mapping 12 software (Wellcome Trust Centre for Neuroimaging, London, UK; www.fil.ion.ucl.ac.uk/spm). The tissue compositions were calculated using an in-house written Python (v3.7) script.

The internal water reference method was used to calculate the concentrations of the resonances in mmol per kilogram of solvent (millimolal (mmol/kg)). The concentration quantification formula given by Gasparovic et al.,¹ was used as follows:

Concentrations in mmol/kg (mmolal)

$$[M]_{mmolal} = [M]_{obs} \times conc_{pure_H2O} \times \frac{2}{1 + F_s} \times \frac{(f_{GM} \times R_{H2O_GM} + f_{WM} \times R_{H2O_WM} + f_{CSF} \times R_{H2O_CSF})}{(1 - f_{CSF}) \times R_M} \quad \text{Eq. 1.5}$$

$$\text{where } f_y = \frac{f_{y_vol} \times a_y}{f_{GM_vol} \times a_{GM} + f_{WM_vol} \times a_{WM} + f_{CSF_vol} \times a_{CSF}}$$

where y corresponds to either GM, WM or CSF; f_{y_vol} is the fraction of the respective tissue type determined by segmentation; a_{GM} , a_{WM} , a_{CSF} (78%, 65%, 97% respectively) are the relative densities of MR-visible water for the given tissue type; The molal concentration of water in metabolite solution is 55510 mmoles/kg and is denoted by $conc_{pure_H2O}$.

Concentrations in mmol/L (mmolar)

$$[M]_{mmolar} = [M]_{obs} \times conc_{pure_{H2O}} \times \frac{2}{1 + F_s} \times \frac{(f_{GM_vol} \times a_{GM} \times R_{H2O_GM} + f_{WM_vol} \times a_{WM} \times R_{H2O_WM} + f_{CSF_vol} \times a_{CSF} \times R_{H2O_CSF})}{(1 - f_{CSF}) \times R_M} \quad \text{Eq. 1.6}$$

Where f_{y_vol} is the fraction of the respective tissue type determined by segmentation; a_{GM} , a_{WM} , a_{CSF} (78%, 65%, 97% respectively) are the relative densities of MR-visible water for the given tissue type; The molar concentration of water is 55126 mM and is denoted by $conc_{pure_H2O}$.

For both cases (mmolal and mmolar concentrations), $R_{H2O_y} = \exp\left[-\frac{TE}{T2_{H2O_y}}\right] \left[1 - \exp\left[-\frac{TR}{T1_{H2O_y}}\right]\right]$ is the relaxation correction factor for each water compartment y . $T1_{H2O_y}$ and $T2_{H2O_y}$ are the T_1 and T_2 relaxation times of water in the compartment y . $R_M = \exp\left[-\frac{TE}{T2_{M_ave}}\right] \left[1 - \exp\left[-\frac{TR}{T1_{M_ave}}\right]\right]$ is the relaxation correction term for metabolites. The denominator $1 - f_{CSF}$ was implemented for partial-volume correction. The factor $\frac{2}{1+F_s}$ was introduced to correct for the multiplication of even-numbered acquisitions with the scaling factor (F_s), originating from the metabolite-cycling data processing. $[M]_{obs}$ is the concentration obtained from LCModel, which is divided by the preset value of 40873 (the developer used this value to give a rough correction for metabolite concentrations not corrected with tissue fractions and relaxations as described above).

For known metabolites, all protons are included in the basis set simulations (which adjusts the peak scaling accordingly). However, for all the unassigned peaks from chapters 4 and 5, a single proton contribution is assumed, and these concentrations are named proton density in these chapters.

1.7 Ultra-high-field MRS

Advancements in magnetic resonance engineering permitted the development of higher B_0 field strengths MRI scanners. Human brain MRS measurements are currently possible with field strengths of 7 T²³ or 9.4 T^{9,24}, while for rat brain measurements up to 17.2 T²⁵ were achieved. Clinical MRIs operate currently at 3 T; however, in 2017, Siemens CE and FDA certified a 7 T human MRI system. MRI field strengths of ≥ 7 T are referred to as ultra-high field (UHF) scanners, and they will be the focus of this thesis. The measured spectra all originate from a Siemens Magnetom 9.4 T whole-body MRI system.

UHF strengths have the advantages of a better spectral dispersion (resonance frequencies of the same metabolite signals are further apart on a Hz scale), see Eq. 1.2, and an increase in signal-to-noise ratio (SNR)²⁶. While MRS spectra and MRS fitting benefit from these advantages, the disadvantages include larger B_0 inhomogeneities and shorter T_2 relaxation times. The B_0 inhomogeneities at UHFs induce broader peaks in terms of Hz (not in terms of chemical shifts in ppm), which conceal J-splitting patterns (see Figure 1.8 and Figure 1.9). Some J-splitting patterns are better visible or more pronounced at lower field strengths.

Because of the shorter T_2 relaxation times at UHF, short TE sequences are preferred to acquire in vivo spectra. T_2 relaxation times of metabolites are decreasing faster than those of the MM spectrum²⁷. On the one hand, at 3 T metabolites²⁸ have T_2 relaxation times in the range of 75 to 350 ms, while macromolecules²⁹ relax in 14 to 43 ms. On the other hand, at 9.4 T metabolite relaxation times of 45 to 110 ms and MM relaxation times of 15 to 37 ms were measured³⁰. Hence, the MM spectrum contributes more significantly to the measured spectra in vivo at 9.4 T, which was an additional motivation for the investigations performed in chapter 2.

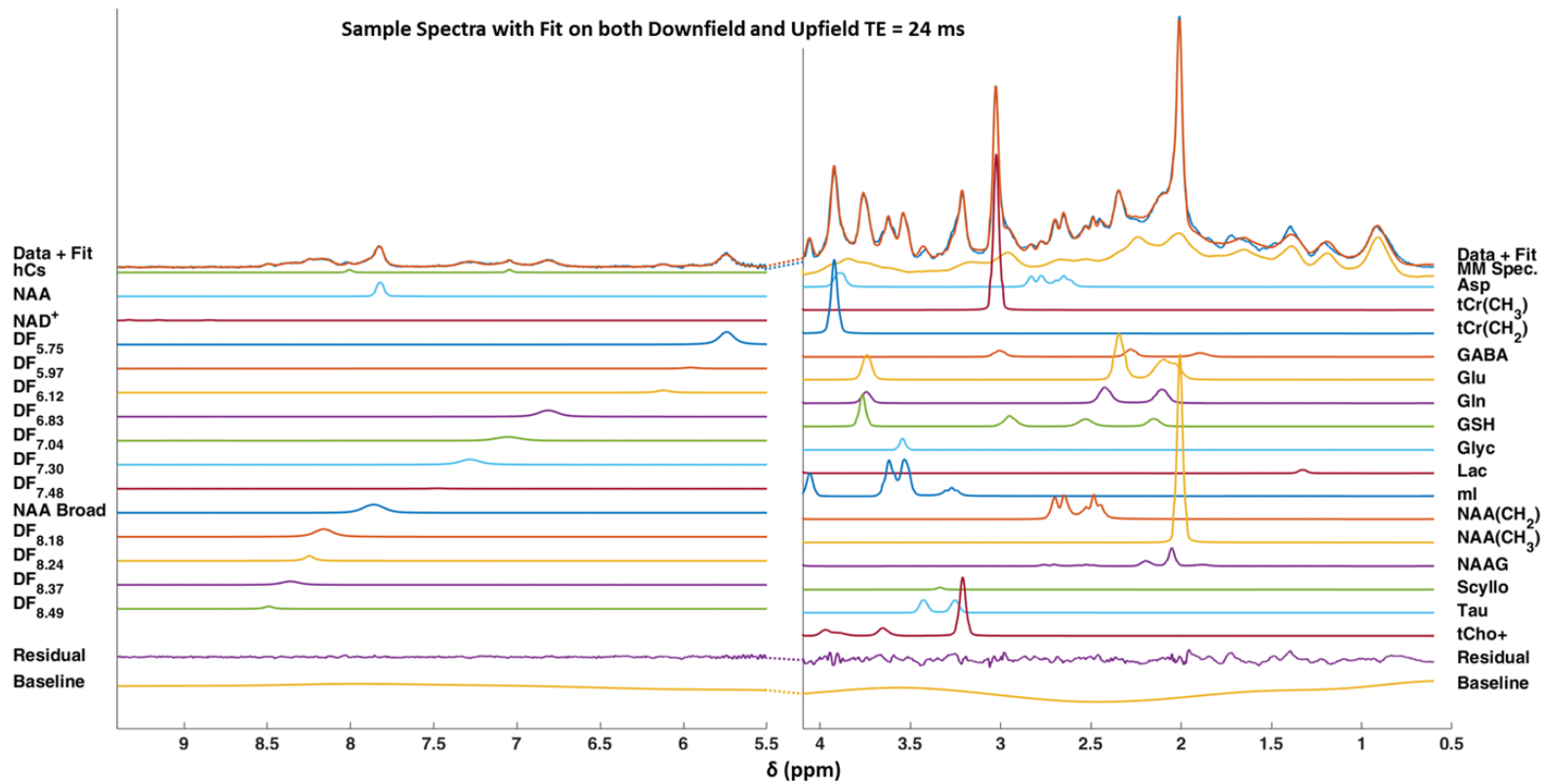


Figure 1.10: The sample spectrum where both the downfield and the upfield spectra were fit together. This fitting approach was used in chapter 4 for fitting the downfield spectrum because the fitting software estimates the metabolite lineshape more correctly when also the upfield spectrum is used.

1.8 The motivation of the thesis

The previous subchapters explained how the basics of magnetic resonance spectroscopy relate to the clinically relevant metabolite concentrations in mmol/L or mmol/kg units. Key to the clinical relevance is making metabolite concentration quantifiable with high accuracy and precision to detect small disease-induced changes of a few percent.

Thus [Part A](#) of this thesis focuses on the accurate and precise fitting of the MRS spectra. The golden standard software for fitting spectra in MRS is the commercial software LCModel. The sensitivity of this LCModel software to changes in the MM spectrum and the spline baseline is investigated in the following chapter 2.

The lack of open-source spectral fitting software, lead to the development of the new open-source fitting algorithm ProFit-v3, presented in chapter 3. Due to the improved spectral resolution and a smaller difference in T_2 relaxation times between metabolites and macromolecules at UHFs, the MM spectra have to be handled more carefully at UHF (see results in chapter 2). More importantly, the spline baseline flexibility set manually in LCModel seems to impact the quantified metabolite concentrations. Both of these problems were considered for the development of ProFit-v3, which has an automatic baseline stiffness determination for fitting built-in. The quantified results of ProFit-v3 are extensively validated for simulated and in vivo spectra, with the objective to adhere to the physiological ground truth. Furthermore, the fitting results are compared to the LCModel fits.

[Part B](#) of this thesis explores novel spectral modelling approaches of the downfield spectrum and the MM spectrum. UHF measurements with the recently developed MRS sequences permitted the disentanglement of the metabolic information contained in these downfield and MM spectra.

The downfield spectrum contains many peaks which are unassigned to a metabolite. For these peaks, no basis sets with known J-coupling constants and chemical shifts could be simulated and were modelled as Voigt lines by the fitting software. An example, where the downfield peaks are fitted as Voigt lines, while metabolite basis sets for the upfield spectrum were used, is shown in Figure 1.10. Fitting the upfield and the downfield spectrum simultaneously has proven to improve the downfield fitting (see chapter 4).

In chapter 4 a series of downfield spectra are used to measure for the first time the T_2 relaxation times of individual downfield peaks at 9.4 T, to estimate the pH value and to derive T_2 relaxation corrected proton densities of the peaks. These new results, together with the information of the fitted linewidths, previous results of T_1 relaxation times and chemical exchange rates were used to derive possible new downfield metabolite peak assignments. These assignments are discussed briefly in subchapter 4.1.6 and extensively in chapter 5.

Lastly, the improved spectral separation at UHF and linewidth characterizations of the MM spectrum³⁰ and the downfield spectrum (results from chapters 4 and 5) lead to the amino acid fit model presented in chapter 6. While the MM spectrum was previously described as composed of the amino acid contributions of peptides and proteins^{31,32}, the method shown in chapter 6, is the first attempt to create a fitting model to characterize the MM spectrum as individual amino acid contributions.

~ PART A ~

Improved Spectral Fitting – Metabolite Quantification

2 Improved Spectral Fitting – Spline Baselines and Macromolecules

Text and figures in this chapter were adapted with minor modifications from our work previously published in (some of the supporting information material from these publications is not shown):

Giapitzakis IA*, **Borbath T***, Murali-Manohar S, Avdievich N, Henning A. “Investigation of the influence of macromolecules and spline baseline in the fitting model of human brain spectra at 9.4 T”. *Magnetic resonance in medicine*, 2019;81(2):746-758.

Parts of this chapter were also published in:

Borbath T, Giapitzakis IA, Henning A. “The influence of the macromolecular and spline Baselines on Quantification Results at 9.4 T”, *University Hospital Tuebingen’s Workshop on Proton MR Spectroscopy in Neuroradiological Diagnostics*, 2018, Tuebingen, Germany

Borbáth T, Giapitzakis I, Murali Manohar S, Henning A. “Do macromolecular and spline baselines affect the metabolite quantification at 9.4T?”, *Proc. of the 34th Annual Meeting of the European Society for Magnetic Resonance in Medicine and Biology*, 2017, Barcelona, Spain.

2.1 Introduction

The introduction of ultra-high field (UHF) scanners (≥ 7 T) enables a higher SNR and an increase of spectral resolution due to the higher chemical shift dispersion. Proton magnetic resonance spectroscopy (^1H -MRS) studies at 9.4 T reported concentrations of 18 metabolites from spectra acquired from the occipital lobe (OccL) of the human brain^{9,24}. The performance of MRS studies in OccL at UHF is facilitated from the achievement of high excitation profiles (B_1^+) in this brain region, by partial volume arrays, and its distance (~ 30 - 40 mm) from the surface of the skull. In contrast, in deeper brain locations such as the anterior cingulate cortex or medial parietal lobe, a sufficiently high B_1^+ is more difficult to achieve due to the decreased transmission efficiency at UHF in more distant locations^{33,34}.

The advantages of UHF for ^1H -MRS have been also used to investigate the macromolecule signals (MM) on MRS spectra, as well as, their handling on metabolite quantification³⁵⁻³⁸. Due to their short transverse relaxation times (T_2), MM appear in ^1H -

MRS spectra as broad peaks, which underlie the narrow and higher intensity peaks from other metabolites. Consequently, MM can influence the precision and the accuracy of metabolite quantification due to very broad underlying peaks. This effect becomes even more severe in the case of short echo times (TE) due to the more pronounced presence of MM^{36,39}. At low static magnetic fields, MM in ¹H-MRS spectra can be sufficiently handled by different fitting software such as LCModel, using simulated macromolecule resonances^{40,41}, and polynomial functions (e.g. splines) for addressing additional broad peaks which are not included in the fitting model. These polynomial functions, named hereafter spline baseline, is designed “to account for a wide variety of unpredictable complications, including: (1) artifacts in the data; (2) substances not present in the Basis Set of model metabolite spectra; (3) substances possibly in the Basis Set, but with abnormally short T₂ times; (4) inaccuracies in the simulated models for the highly variable lipid and macromolecule signals; (5) incomplete water suppression”¹⁵. Particularly in LCModel⁴², there is one parameter called “dkntmn”, which is defined as the minimum allowed spacing between spline knots, and which controls the stiffness of the spline baseline. This value is set to a default value of 0.15. The effect of the parameter dkntmn was first addressed by Pfeuffer et al.,⁴³ for processing rat brain spectra from 9.4 T. However, its influence on the quantification of human brain UHF spectra has not been fully investigated.

At higher magnetic fields, for the handling of the macromolecular peaks, an experimentally measured macromolecular basis set (MMB) is to be included in the fitting model due to the higher frequency resolution³⁸. Current studies at UHF demonstrated that a general MMB might be adequate for the quantification of the metabolites of single-voxel ¹H-MRS spectra from different brain regions since no significant differences in macromolecular components of the various regions were detected^{36,37}. Interestingly, a recent study at 9.4 T³⁵ characterized the MMB of the human brain in two different regions (occipital lobe and left parietal lobe) and demonstrated that the higher spectral resolution enabled the detection of two new macromolecular peaks.

For this study, ¹H-MRS spectra from the left parietal lobe (IPL) of the human brain were acquired from eight healthy volunteers at 9.4 T using metabolite-cycled semi-LASER (MC-semi-LASER)⁹ for the first time. Then, the IPL data along with OcCL spectra, acquired

from the same volunteers in another study⁹, were quantified and the influence of the inclusion of experimentally measured MMBs from both regions³⁵ in the fitting model, was evaluated. Furthermore, the effect of the stiffness of the additionally fitted spline baseline on the resulting concentrations of the metabolites was investigated.

2.2 Methods

2.2.1 Technical Description, Coil Configuration, and Subjects

All measurements were performed on a Siemens 9.4T whole-body MRI scanner (Erlangen, Germany) equipped with an SC72 gradient system. The experiments were performed using a home-built proton coil with eight transmit and sixteen receive channels^{44,45}. To obtain high Tx fields for the excitation of a voxel within the occipital and left parietal lobe, only 2-3 coil elements adjacent to the region of interest (ROI) were used for transmission. For this purpose, a 2-way and an unbalanced 3-way Wilkinson splitter were used which enabled driving of different coil elements as it is described in references^{9,35}. The coil was tuned and matched for each volunteer individually before beginning the experiment. Eight healthy volunteers (six male and two female, age: 29 ± 4 years) participated in this study. Written informed consent was given by all subjects prior to the examination and the study had been approved by the local ethics board.

2.2.2 Data Acquisition

2D FLASH images (in-plane resolution: $0.7 \times 0.7 \text{ mm}^2$, slice thickness: 3.5 mm, 25 slices, TE/ TR: 9 ms/ 472 ms, flip angle: 25°) were acquired in three orientations (axial, sagittal and coronal) to facilitate the later placement of spectroscopic voxels. A 3D MPRAGE scan (isotropic voxel 1 mm^3 , TE/ TI/ TR: 4.2 ms/ 900 ms/ 2300 ms, flip angle: 9°)⁴⁶ was also acquired at 3 T (Siemens Prisma). The 3D MPRAGE images were used for the performance of image segmentation (please see MRS Data Quantification section 2.2.5). A spectroscopy voxel ($2 \times 2 \times 2 \text{ cm}^3$) was placed in a mixed gray matter (GM) and white matter area (WM) in the IPL (mainly WM) using the appropriate coil configuration as described previously³⁵. The OccL data used in this paper were acquired during a previous study⁹. First and second order B_0 shimming was performed using FASTE(ST)MAP⁴⁷ and voxel-based power calibration was executed⁴⁸. Next, localized ^1H -MRS spectra using

MC-semi-LASER with a TE of 24 ms⁹ were acquired from each volunteer (Figure 2.1). The TR used among different volunteers varied from 6000 ms to 7800 ms to ensure specific absorption rate within acceptable limits. The spectra were acquired with 4096 time-points, an 8 kHz receive-bandwidth, and acquisition time of 512 ms. The transmit reference frequency for the localization pulses of MC-semi-LASER was set at 2.3 ppm to reduce the chemical shift displacement error relative to the water-based MR image (measured with water on resonance at 4.7 ppm) and minimize lipid excitation. In particular, the bandwidth of the slice selection pulse, as well as, of the adiabatic refocusing pulses in semi-LASER was about 8 kHz resulting in a chemical shift displacement error of 5% per ppm for each voxel dimension. Neither water pre-saturation (WS) nor outer volume suppression (OVS) was applied.

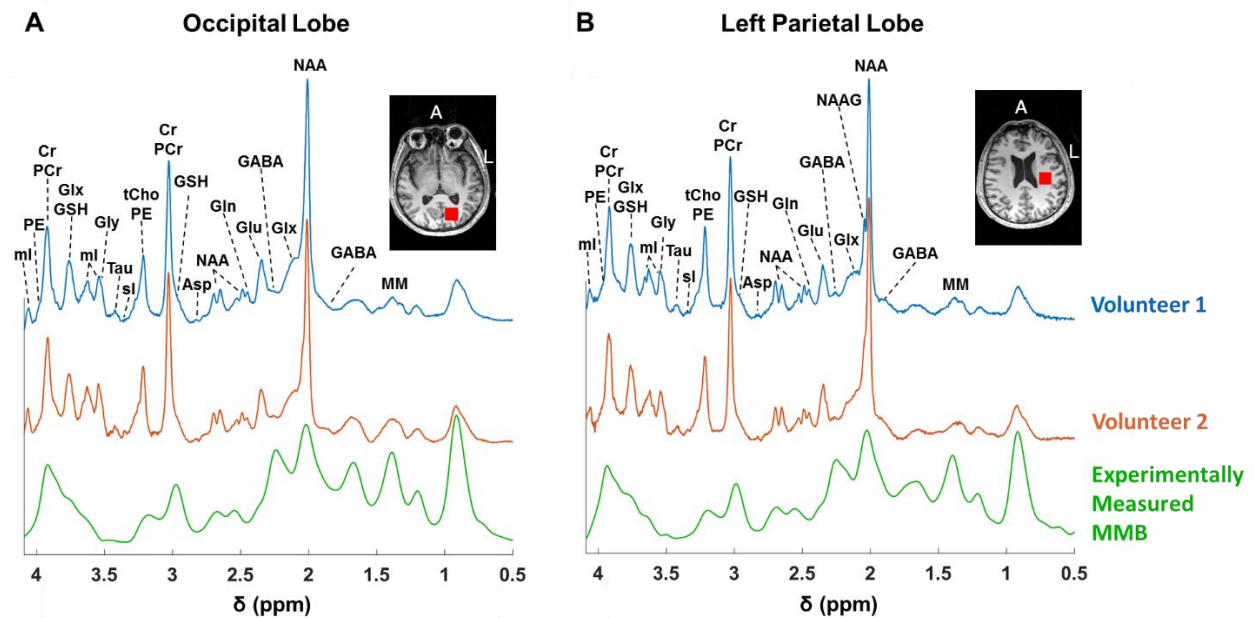


Figure 2.1: Sample spectra acquired from two volunteers (blue and red lines) using MC-semiLASER from a voxel (2 x 2 x 2 cm³) placed in the occipital lobe (left) and left parietal lobe (right). The quality of the data for both brain regions is high and several metabolites can be observed. The green spectrum indicates the corresponding experimentally measured MMB. Acquired spectra from both brain regions were reproducible among different volunteers with minimal lipid contamination. The inlays display the 3D MPRAGE image acquired from the same volunteer at 3 T. The tissue segmentation was performed based on these images.

Finally, to avoid any influence of the MC pulses on metabolite quantification, water reference signals (NEX: 16) were measured with semi-LASER (TE: 24ms) without MC and WS, with the same TR used for the acquisition of the metabolite spectra.

2.2.3 MRS Data Analysis

The acquired MC-semi-LASER raw data were analyzed with an in-house written MATLAB software (v. 2016a, The Mathworks, USA). The metabolite MRS data were processed using the following processing steps as described previously⁹: 1) Frequency and phase alignment. 2) Metabolite-cycling subtraction. 3) Averaging. 4) Zero-order phase and eddy current correction using the phase information of the water signal ref. 5) Coil channel combination using a singular value decomposition method. 6) A Hankel Singular Value Decomposition⁴⁹ technique was applied to remove the residual water uniformly from all the spectra since some metabolite spectra presented a small residual water peak. 7) Finally, truncation of FIDs at 250 ms.

Full-width half maximum (FWHM) and SNR of the water peak were calculated using the real part of the metabolite-cycled water spectrum. SNR was measured using the noise variation calculated as the standard deviation of 500 points from -5 to -3ppm.

For the acquisition of the MMBs, both in OccL and IPL regions (Figure 2.1, green spectra), the MC-semi-LASER sequence (TE: 24 ms, TR: 10000 ms) was combined with a double inversion recovery technique with optimized adiabatic inversion pulses and times ($T_{Inv1} = 2360$ ms, $T_{Inv2} = 625$ ms). For more details regarding the acquisition, as well as, the post-processing procedure for the creation of MMB please refer to the study of Giapitzakis IA. et al³⁵.

2.2.4 MRS Data Quantification Settings

The preprocessed metabolite spectra were fitted with LCModel-v6.3 and a basis set, consisting of 19 metabolites simulated using the PyGAMMA software⁵⁰ and published chemical shift and coupling constants^{51,52} as described in reference ⁹. Regarding the handling of macromolecular peaks in the metabolite spectra, four different processing protocols were used and evaluated:

For OccL and IPL data, experimentally measured MMBs acquired from OccL and IPL respectively³⁵, were included in the model (Figure 2.2 A and B). LCModel dkntmn parameter, which controls the stiffness of the spline, was set to 1.

For OccL data, an experimentally measured MMB acquired from IPL, and for IPL data an experimentally measured MMB from OccL (Figure 2.2 C and D) were used. LCModel dkntmn parameter was set to 1.

Likewise (a), however, in this case, the number of knots in the fitted spline in LCModel (dkntmn parameter), varied from 0.15 to 1 to investigate its influence on the quantification results (Figure 2.3), since in several spectroscopy studies (e.g., references⁵³⁻⁵⁶), the used dkntmn value lies in this range. The motivation of the selected range of dkntmn value was the evaluation of different cases, starting from 0.15 (low stiffness), which is the default value in LCModel, up to 1 (high stiffness). Empirically, it has been observed that no significant change occurs in the stiffness of the spline baseline for values higher than 1 and for this reason higher values were not evaluated in this study.

Data were fitted with the default settings of LCModel (Version 6.3), in which simulated fourteen Voigt lines^{15,42}, are utilized for the handling of macromolecular and lipid resonances instead of experimentally acquired MMBs (Figure 2.4). For more information regarding the default simulated Voigt lines used in LCModel, for the simulation of lipids and MM peaks, please refer to LCModel manual. The LCModel dkntmn value was not set to a specific value, hence LCModel uses the default value of dkntmn = 0.15.

The controls files (.control) used in LCModel for the processing protocols (a), (b), (c) and (d) are provided in Appendix A.

2.2.5 MRS Data Quantification

First, the content of gray matter (GM), white matter (WM) and cerebrospinal fluid (CSF) in the voxel of interest, both in OccL and in IPL, were calculated in percentage using an in-house written MATLAB script applying the segmentation algorithm from SPM8 (Institute of Neurology, University College London) based on the 3T MPRAGE images, as described previously³⁵.

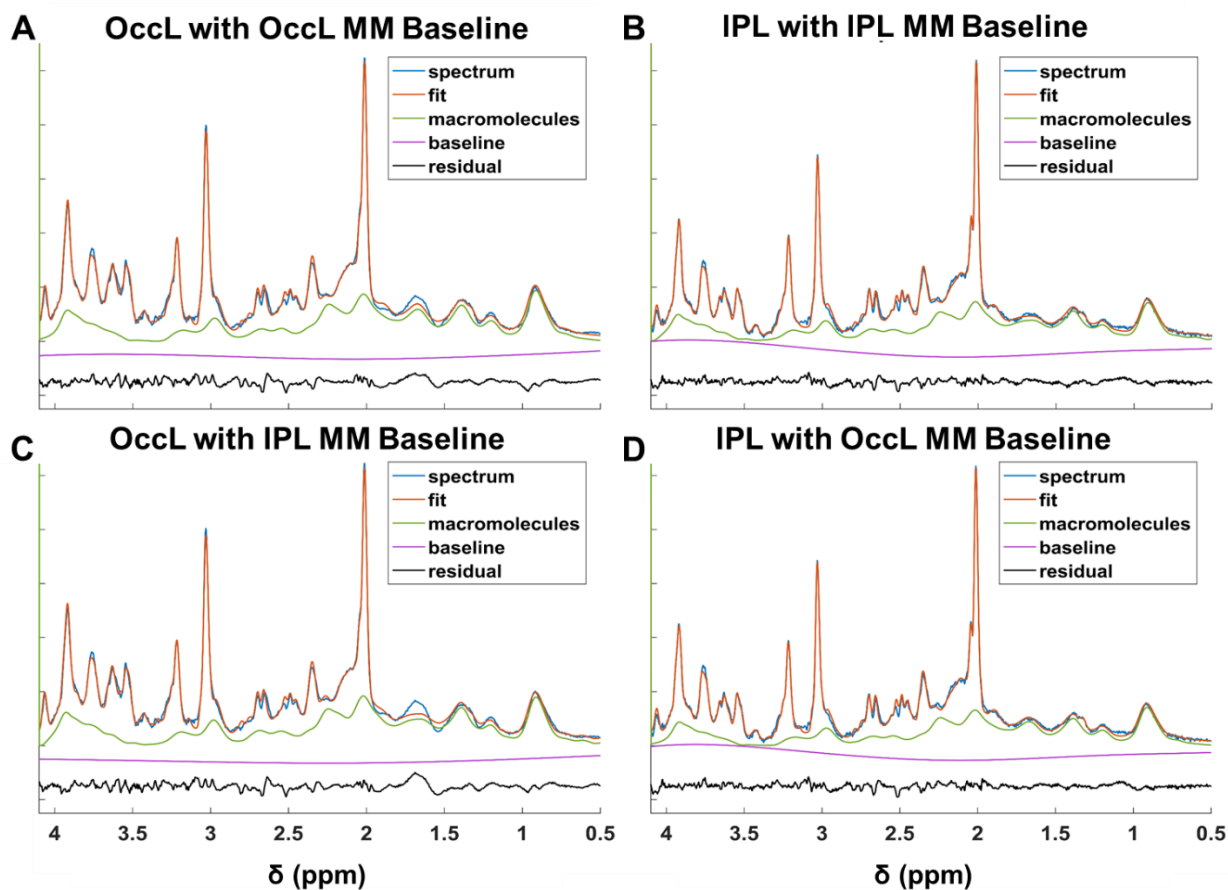


Figure 2.2: LCMoDel quantification results using an experimentally measured macromolecular basis sets (MMB) in the fitting model and a spline baseline with $dkntmn = 1$ A) Fitting results of an occipital lobe (OccL) spectrum with an experimentally measured MMB acquired from the same brain region. B) Fitting results of left parietal lobe (IPL) spectrum with an experimentally measured MMB acquired from the same brain region. C) Fitting results of an OccL spectrum with an experimentally measured MMB acquired from IPL. D) Fitting results of IPL spectrum with an experimentally measured MMB acquired from OccL. Note: the fitted baseline has been subtracted from the presented spectrum, fit and macromolecular basis set data.

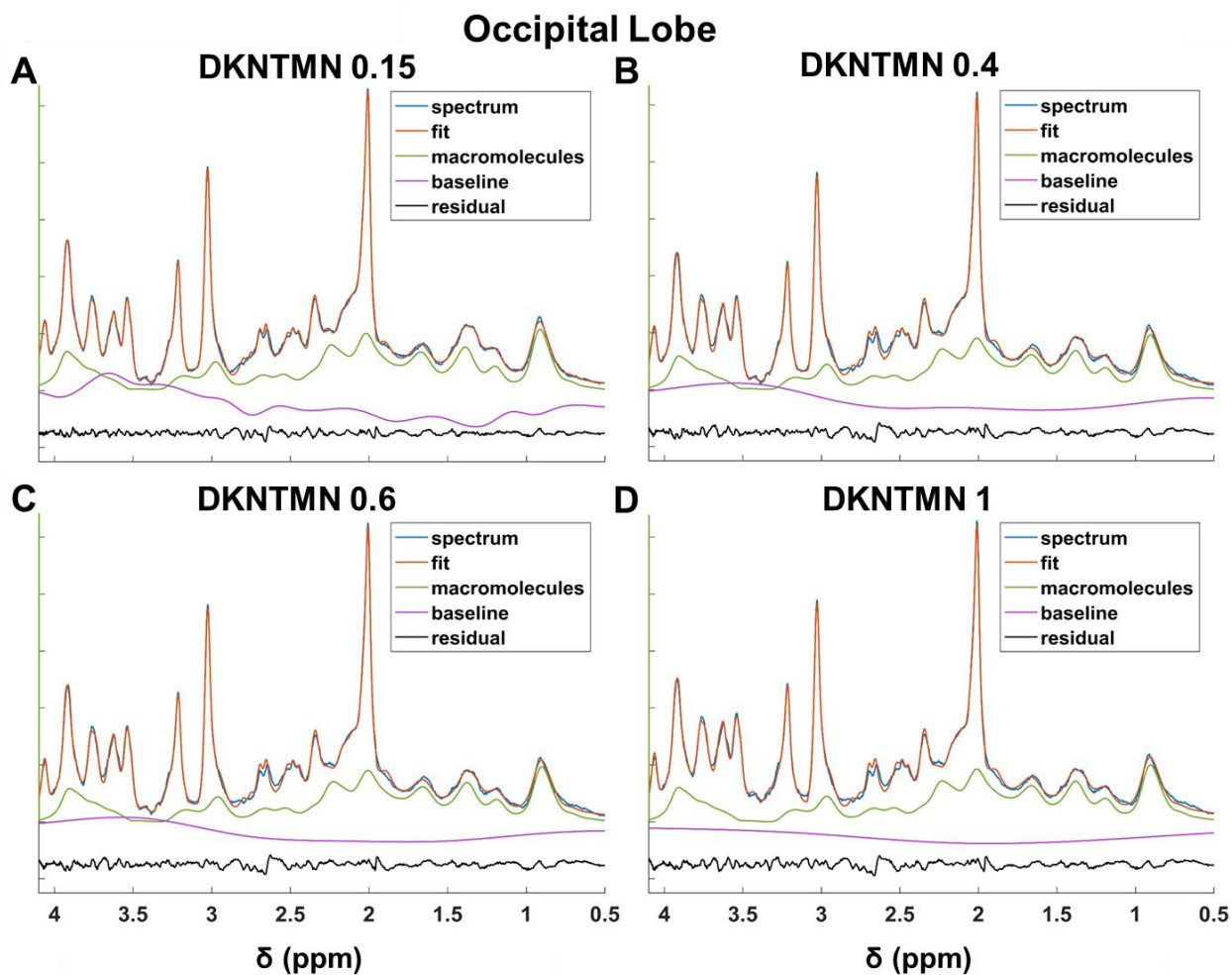


Figure 2.3: LCMoDel quantification results of an occipital lobe sample spectra using experimentally measured MMB acquired from OccL for different degrees of stiffness of the spline baseline ($dkntmn = 0.15$, the default value of LCMoDel; 0.4; 0.6 and 1). The higher the number of knots in the spline baseline (i.e., smaller $dkntmn$ value) the higher the flexibility of the spline baseline. Note: the fitted baseline has been subtracted from the presented spectrum, fit and macromolecular basis set data.

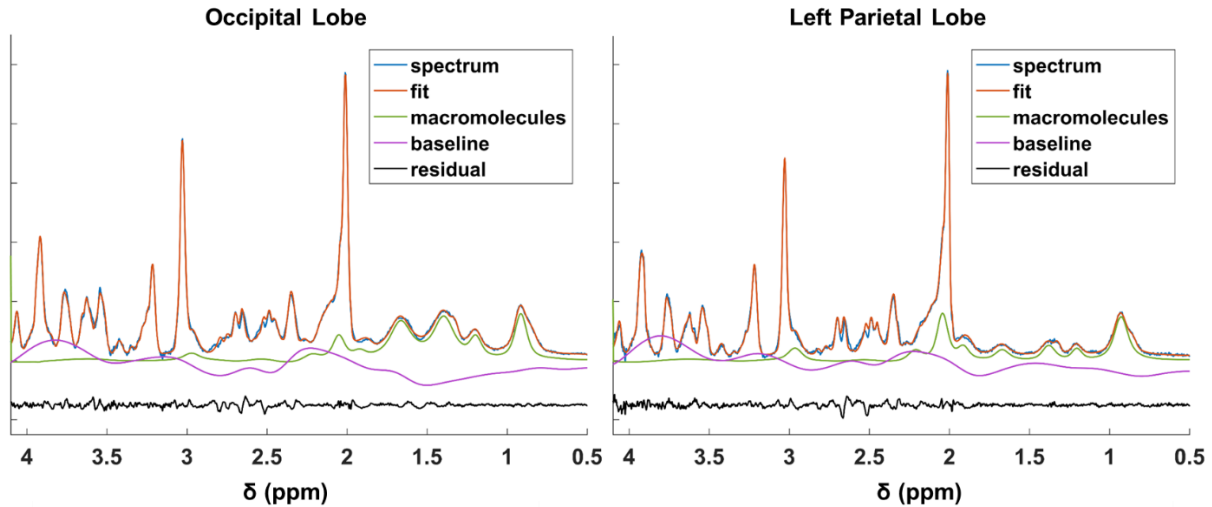


Figure 2.4: LCMoDel quantification results of an occipital lobe (left) and left parietal lobe (right) sample spectra using the default settings of LCMoDel in which the macromolecular components are fitted using simulated Voigt-shaped peaks. Note: the fitted baseline has been subtracted from the presented spectrum, fit and macromolecular basis set data.

The water signal from the respective voxel was used as the internal concentration reference for the metabolite quantification. The metabolite concentrations were calculated both in mmolar (mmoles per tissue volume) and in mmolal (mmoles of solute dissolved per weight of solvent) according to reference ⁵⁷, including corrections for the T_1 and T_2 relaxation times of the water in the different compartments and the approximation of metabolite relaxation times. In particular, for the T_2 (77 ms) and T_1 (1516 ms) relaxation times of the metabolites, the average values from reference ²⁴ were used. The T_1 relaxation times of different water tissues at 9.4 T (GM: 2000 ms, WM: 1300 ms and CSF: 4000 ms) were taken from Hagberg et al.⁵⁸ The assumption for the T_2 relaxation times of water at 9.4 T (GM: 45 ms, WM: 37 ms and CSF: 311 ms) was made utilizing published values from human brain measured with a stimulated echo acquisition mode (STEAM) sequence at 7 T⁵⁹, since to the best of our knowledge values were not yet available for 9.4 T, at the time of preparing this chapter.

The before mentioned water T_2 relaxation times were chosen since these were the closest match to in-house preliminary T_2 water relaxation times measured at 9.4 T with the same sequence as used for this study (MC-semiLASER). For these preliminary T_2 relaxation calculations voxels were placed in a GM rich area (68.7±2.5 % GM, 25.9±4.3 % WM and

5.2±2.6 % CSF) within the occipital lobe, and the measured average water T₂ relaxation time was around 48ms.

For more information regarding the metabolite quantification procedure, please refer to the subchapter 1.6. Relaxation times of water in different tissue types at 9.4 T were taken from Hagberg et al.,⁵⁸ see Table 2.1.

Table 2.1: Water relaxation times in the human brain at 9.4 T from Hagberg et al.⁵⁸.

Water Relaxation Times	T ₁ [ms]	T ₂ [ms]
GM	2120	37
WM	1400	30
CSF	4800	181

No exclusion criteria based on CRLB values were used in the calculation of metabolite concentrations to avoid biased estimations⁶⁰.

Statistical hypothesis testing was performed within MATLAB using a two-tailed non-parametric rank test (Wilcoxon signed rank test for equal and matched sample size). The False Discovery Rate (FDR) as described by Benjami & Yekutieli⁶¹ using $q = 0.1$ was used to conceptualize the rate of type I errors when using multiple comparisons. Additionally, the effect size was measured using Cohen's d for paired samples (calculated as the difference of the average values divided by the standard deviation of the differences)^{62,63}.

2.3 Results

The average SNR of the water peak for OccL data was almost double in comparison to the IPL spectra, while the average linewidths were 18.5±1.5 Hz and 17.5±2.5 Hz, respectively. Acquired spectra from both brain regions were reproducible among different volunteers with minimal lipid contamination (Figure 2.1). No significant differences in the spectral patterns between OccL and IPL were observed after visual inspection, except the splitting of N-Acetylaspartate (NAA) and N-Acetylaspartylglutamate (NAAG) peaks at ~2 ppm in IPL (Figure 2.1).

Quantification results, expressed in mmoles of solute dissolved per weight of solvent (mmolal), with processing protocol (a) for both OccL and IPL data, did not show any statistically significant difference after false discovery rate correction (Table 2.2).

Table 2.2: Concentrations expressed in mmolal (moles of solute dissolved per weight of solvent) and mmolar (moles per tissue volume) units, and CRLBs for metabolites in the occipital and the left parietal lobe.

Metabolite	Occipital Lobe ¹			Left Parietal Lobe ²		
	mmolal ³	mmolar ³	CRLB ³ (%)	mmolal ³	mmolar ³	CRLB ³ (%)
NAA	12.8 ± 0.9	8.9 ± 0.7	1.4 ± 0.5	11.8 ± 1.0	7.9 ± 0.7	1.8 ± 0.7
tCr	11.2 ± 0.6	7.8 ± 0.5	1.3 ± 0.5	9.5 ± 0.9	6.4 ± 0.6	1.4 ± 0.7
tCho	1.5 ± 0.2	1.1 ± 0.2	4.3 ± 1.7	2.0 ± 0.2	1.3 ± 0.2	3.1 ± 0.8
NAAG	1.5 ± 0.2	1.0 ± 0.2	8.1 ± 1.8	1.7 ± 0.4	1.1 ± 0.3	6.4 ± 2.4
ml	9.2 ± 0.8	6.4 ± 0.5	2.3 ± 0.5	7.1 ± 1.3	4.7 ± 0.9	3.1 ± 1.6
sl	0.6 ± 0.3	0.4 ± 0.2	8.3 ± 2.5	0.4 ± 0.3	0.2 ± 0.2	18.0 ± 9.1
GABA	1.2 ± 0.3	0.8 ± 0.2	12.8 ± 5.1	1.3 ± 0.7	0.8 ± 0.4	15.3 ± 11.2
Gln	2.8 ± 0.4	1.9 ± 0.3	5.4 ± 1.6	2.6 ± 0.5	1.7 ± 0.4	6.9 ± 2.9
Glu	9.5 ± 1.0	6.7 ± 0.8	2.1 ± 0.4	8.7 ± 0.6	5.8 ± 0.4	2.4 ± 1.1
Gly	2.6 ± 0.5	1.8 ± 0.3	7.0 ± 1.1	2.1 ± 0.4	1.4 ± 0.3	9.3 ± 4.0
Glc	3.4 ± 1.0	2.4 ± 0.7	10.6 ± 9.9	2.0 ± 1.2	1.3 ± 0.8	24.0 ± 26.3
GSH	2.7 ± 0.2	1.9 ± 0.1	3.8 ± 0.7	2.3 ± 0.3	1.5 ± 0.2	5.1 ± 3.2
Asp	3.2 ± 0.7	2.3 ± 0.5	8.3 ± 2.3	2.2 ± 1.1	1.5 ± 0.8	14.0 ± 3.5
Lac	1.0 ± 0.9	0.7 ± 0.6	20.2 ± 13.7	0.6 ± 0.4	0.4 ± 0.3	23.2 ± 17.4
PE	2.1 ± 0.7	1.5 ± 0.5	13.1 ± 10.3	1.1 ± 0.4	0.7 ± 0.3	19.3 ± 6.4
Tau	1.1 ± 0.7	0.8 ± 0.5	19.5 ± 13.2	1.6 ± 1.1	1.1 ± 0.7	12.0 ± 3.7

1: Average water compartment fractions in occipital lobe; WM: 56.2%, GM: 40.1%, CSF: 3.7%.

2: Average water compartment fractions in left parietal lobe; WM 80.1%, GM: 17.9%; CSF: 1.9%.

3: Expressed as mean value ± standard deviation (n=8).

However, trends toward significance ($P < 0.05$, not FDR corrected) were shown for total creatine (tCr) with 14% difference of the mean values between OccL and IPL, total choline (tCho) with 35% difference, myo-Inositol (ml) with 23% difference, glucose (Glc) with 36% difference, glutathione (GSH) with 16% difference, and phosphorylethanolamine (PE) with 51%. In general, concentrations were higher for metabolites in OccL than IPL. Comparison between numeric values of metabolite concentrations, expressed in mmolal and mmolar (Table 2.2), show that numeric values expressed in mmolal were about 50% higher than expressed in mmolar. For the majority of the metabolites, the Cramer Rao

Lower Bounds (CRLBs) were below 20%, except for lactate (Lac) and Glc in IPL spectra. Generally, CRLBs for OccL metabolites were lower than for IPL due to the higher SNR.

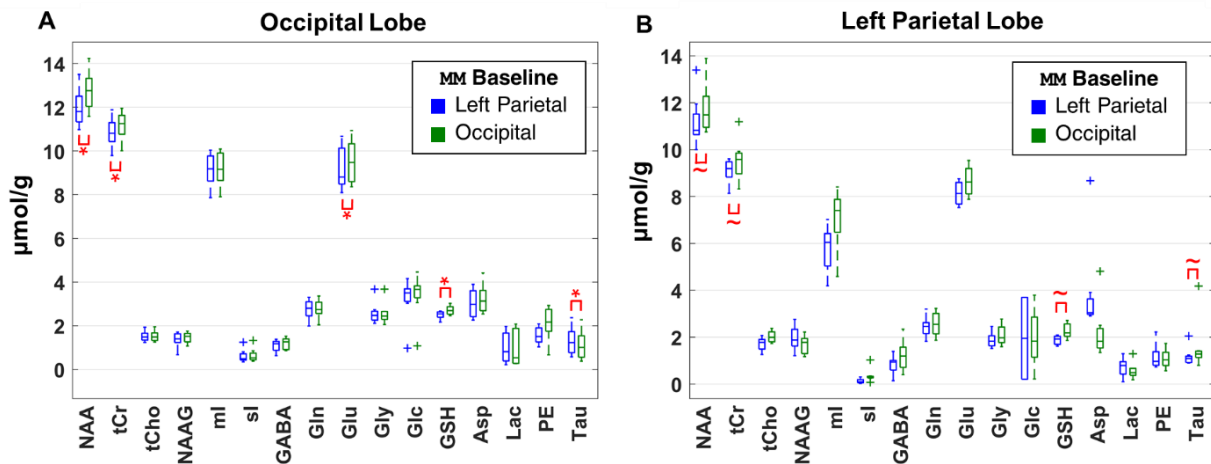


Figure 2.5: Concentrations of metabolites, corrected for relaxation, in the occipital lobe (left) and left parietal lobe (right), expressed in mmolal ($\mu\text{mol/g}$) units. Spectra from both brain regions were quantified using an experimentally measured MMB acquired from occipital lobe (green boxes) and left parietal lobe (blue boxes) within the processing protocol. Horizontal lines inside the boxes indicate median values (50% quartile), whereas the bottom and top box boundaries illustrate 25% and 75% quartiles, respectively. Crosses (+) show outliers. Differences ($P < 0.01$) between quantification with processing protocol (a) and (b) classified by the FDR as true positives are illustrated with red asterisks (*) for, while possible false positives with a red tilde (~).

Quantification results with processing protocol (b) compared to (a) (see MRS Data Quantification Settings in Methods), demonstrated statistically significant differences in some of the metabolite levels of OccL spectra when an experimentally measured MMB from another region was included in the fitting model (Figure 2.5 A). Very large effect size ($d > 1.2$) were found for the differences ($P < 0.01$, FDR corrected) of NAA, tCr, GSH and taurine (Tau), and a large effect size ($d > 0.8$) was found for glutamate (Glu) for the OccL data compared to processing protocol (a) (red asterisk in Figure 2.5 B). The IPL spectra showed only trends towards statistical significant differences ($P < 0.01$, not FDR corrected), for some of the metabolite levels using the same protocol comparison (red tilde in Figure 2.5). The differences were found for NAA, tCr, GSH, and Tau and were classified as possible false positives after FDR. The changes for both lobes of the mean concentration values for NAA and tCr were less than 6% and 3%, respectively. However,

the changes for Tau were greater, 10% and 17% for OccL and IPL, respectively. The average change of the mean values for all the metabolites that demonstrated statistical difference ($P < 0.01$, not FDR corrected) was 7%.

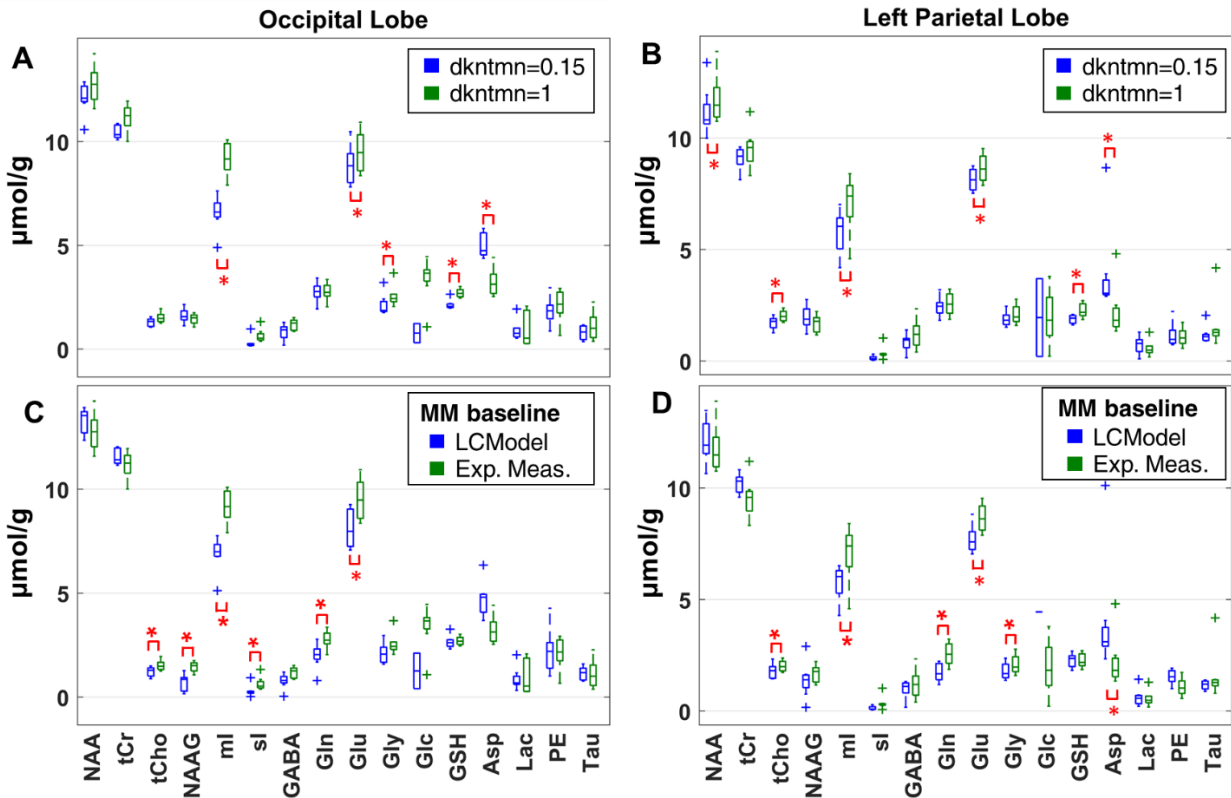


Figure 2.6: (A and B) Concentrations of metabolites ($\mu\text{mol/g}$) for both brain regions for a different degree of stiffness of the spline baseline ($dkntmn = 0.15$ and $dkntmn = 1$), by controlling LCMoel parameter $dkntmn$ (processing protocol (c)). A larger number of knots in the spline (smaller $dkntmn$ number) resulted in a more flexible baseline. (C and D) Quantification of the metabolites of occipital and left parietal lobe with the simulated MMB of LCMoel (processing protocol (d); blue) and using an experimentally measured MMB from the corresponding brain region (green). Horizontal lines inside the boxes indicate median values (50% quartile), whereas the bottom and top box boundaries illustrate 25% and 75% quartiles, respectively. Crosses (+) show outliers. Red asterisks (*) illustrate differences ($P < 0.01$, FDR corrected).

Figure 2.6 (Panel: A and B) illustrates concentrations of metabolites for both brain regions derived for a different degree of stiffness of the spline baseline, by controlling LCMoel parameter $dkntmn$. Statistically significant differences ($P < 0.01$; FDR corrected) with a very large ($d > 1.2$) to huge ($d > 2$) effect size between spline baseline with $dkntmn = 1$

and $dkntmn = 0.15$, was observed for several metabolites for both brain locations. In particular, an average change of 18%, 6%, 17% and 55% were found for ml, Glu, GSH, and aspartate (Asp), respectively. Additionally, changes of 5% and 15% were observed for NAA and tCho in the IPL spectra, and 17% in glycine (Gly) in the Occ spectra, respectively. The average change of the mean values for all the metabolites that demonstrated statistically significant difference ($P < 0.01$, FDR corrected) was 24%. An illustrative comparison of the concentration levels for several degrees of stiffness of the spline configuration are shown in Figure 2.7.

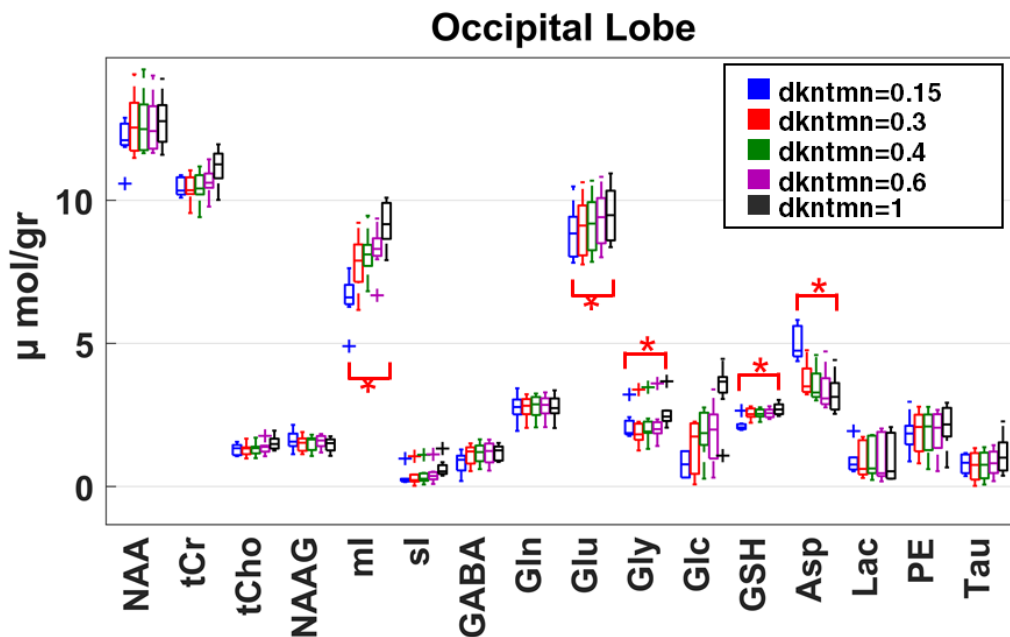


Figure 2.7: Boxplots showing the comparison of the concentrations of metabolites ($\mu\text{mol/g}$) for the occipital lobe in case of manipulating the degree of stiffness of the spline baseline (processing protocol (c)) by controlling LCMoel parameter $dkntmn$ (set to 0.15, 0.3, 0.4, 0.6 and 1).

Quantification of the metabolites with the default settings of LCMoel (processing protocol (d)), which resemble simulated MM peaks, manifested statistically significant difference ($P < 0.01$, FDR corrected) in comparison with metabolite levels calculated with inclusion of experimentally measured MMB in the fitting model (processing protocol (a)). In particular, differences of above 15% with a very large ($d > 1.2$) to huge ($d > 2$) effect size in the quantification of metabolite levels for both brain regions between the two fitting protocols were observed for ml and glutamine (Gln) concentrations, and above 10% for tCho and Glu in both brain regions, and Gly and Asp in IPL (Figure 2.6 Panels C and D).

It is noteworthy that for SI and NAAG the alterations of the concentrations between the two processing protocols were more than 100% for the OccL. The average change of the mean values for all the metabolites that demonstrated statistically significant difference ($P < 0.01$, FDR corrected) was 42%.

Figure 2.8 demonstrates the spline baseline fitting results and the corresponding fitted MMBs for all volunteers for the different processing protocols. For processing protocols (a) and (b), the resulting spline baselines which were highly constrained by the `dkntmn` set to 1, were flat among all the volunteers without obvious differences, and the MM fits were highly reproducible. Contrarily, for processing protocols (c) and (d), and especially for case (d), the fitted spline baselines were quite distorted with large deviations across volunteers in the frequency regions from 1 ppm to 2 ppm, and from 3 ppm to 4 ppm. Additionally, the deviation of the corresponding fitted macromolecular components in (d) was large in these spectral regions as well.

2.1 Discussion

Fitting with the default settings of LCModel had significant influence in the resulting spline baselines leading to large deviations both in the concentrations and fitted macromolecular components. A high number of knots in the spline resulted in a non-flat baseline, which potentially leads to quantification errors. Interestingly, the interchange of macromolecular basis sets between OccL and IPL spectra had less influence on the quantification results compared to the default LCModel settings.

The coil setup, as described in reference ⁶⁴, allowed the acquisition of high-quality spectra from OccL and IPL. The reported average FWHM of water in IPL data was in agreement with the reported linewidth of the water peak in spectra acquired from OccL at 9.4 T using MC-semi-LASER⁹. Moreover, spectra from both OccL and IPL manifested minimal lipid contamination, even though OVS was not applied. This minimal lipid contamination was because of the high bandwidth of the refocusing adiabatic full passage pulses (~8 kHz) in semi-LASER, leading to reduced chemical shift displacement errors, as well as, the fact that refocusing adiabatic full passage pulses typically have much less unwanted excitation at the edges and outside of the slice in comparison to amplitude modulated RF pulses^{9,65}.

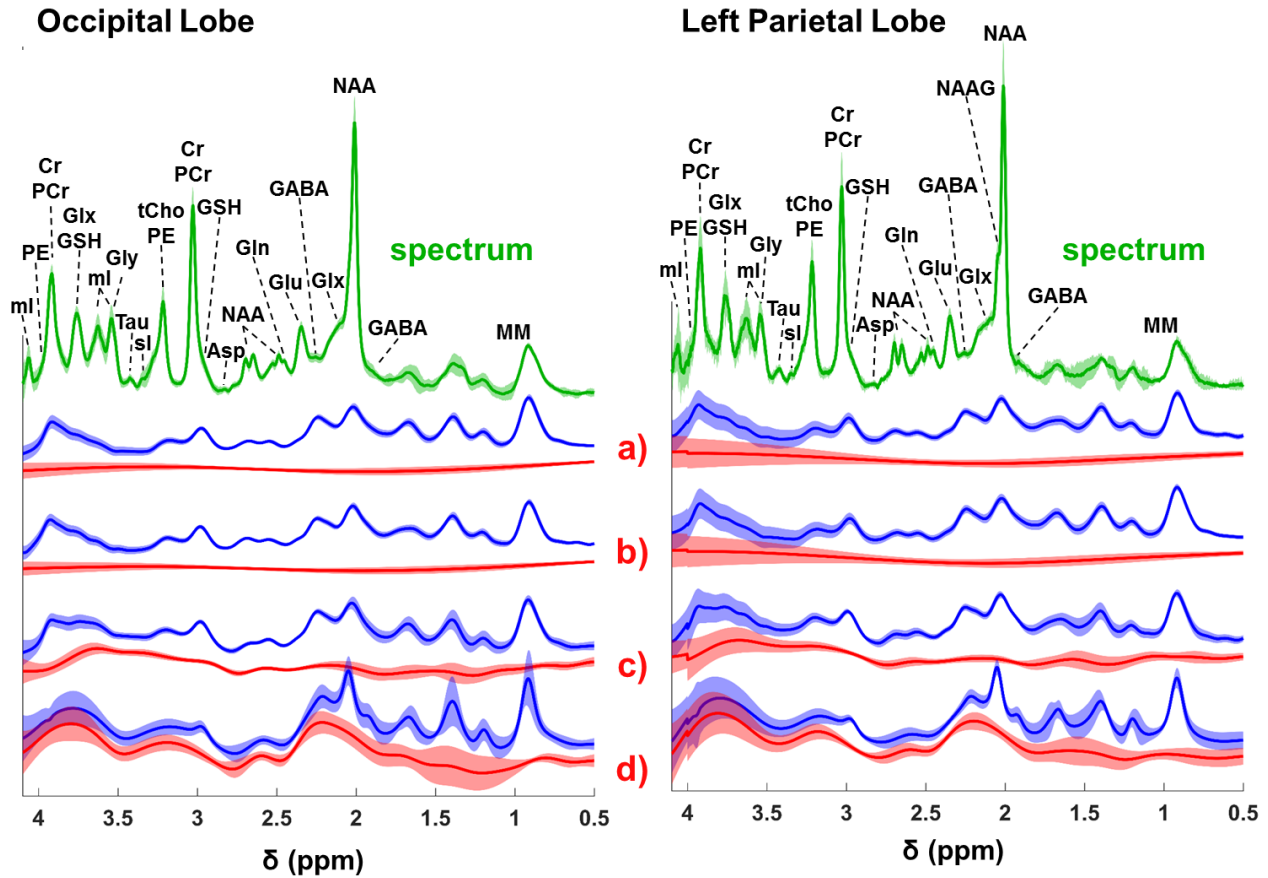


Figure 2.8: Spectra (green), spline baseline fitting results (red) and the corresponding fitted MMBs with spline baseline (blue) for all the volunteers for occipital lobe (left) and left parietal lobe (right) data for the different processing protocols: (a), (b), (c) and (d). Processing protocol (a), (b) and (c) include a measured MMB in the basis set used for fitting. (a) and (c) use an MMB acquired in the corresponding region, while processing protocol (b) includes a measured MMB acquired from a different region, as stated in the MRS Data Quantification Settings section 2.2.4. Processing protocol (d) does not include a measured MMB, but uses Voigt lines to simulate macromolecular and lipid resonances. The *dkntmn* parameter, controlling the spline stiffness, was set for (a) and (b) to 1, while for (c) the *dkntmn* value of 0.15 was used. For processing protocol (d) *dkntmn* was not set, hence LCModel took the default value of 0.15. Bold lines indicate mean values ($n = 8$), whereas shadow areas represent the standard deviation. For case (d), the fitted baselines were quite distorted with large deviation across volunteers in the frequency regions from 1 ppm to 2 ppm, and 3 ppm to 4 ppm. Additionally, the deviation of the corresponding fitted macromolecular components in (d) was large in these spectral regions as well.

It is noteworthy that the SNR of the water resonance in OccL was almost double in comparison to the water resonance in IPL data. This observation was in agreement with the SNR map of the used RF coil⁶⁴, which demonstrated a higher SNR in the region of OccL in comparison to IPL (Fig. 5 in reference ⁶⁴). Consequently, both CRLBs and standard deviation of concentrations in OccL were lower for most of the metabolites compared to IPL (Table 2.2). Despite the SNR difference, the splitting of the NAA and NAAG peaks around 2 ppm was only observable in IPL, mainly due to the smaller linewidth and higher WM content since NAAG is higher in WM⁶⁶.

The reported concentration values in mmolal (mmoles of solute dissolved per weight of solvent) were about 50% higher than in mmolar (mmoles per tissue volume). This finding was expected since in the first case, different tissue water concentrations were included in the calculations, while in the second, the whole volume was considered to be solvent⁶⁷. Concentrations for OccL metabolites calculated with processing protocol (a) (Table 2.2) were in good agreement with other published values^{56,68,69}. In this study, small deviations, if any, can be explained from the fact that corrections for the fractions of the different water compartments (OccL: 40% GM and 56% WM; IPL: 18% GM and 80% WM) and T_2 relaxation of water tissues on 7 T values were included in the quantification. In the aforementioned studies ^{56,68,69} T_2 relaxation correction was not required due to the used ultra-short TE (6 and 7 ms, respectively).

Furthermore, metabolite concentrations of IPL were lower than the concentrations reported in reference ⁷⁰, which could be due to the overlapping peaks appearing at the field strength of 1.5 T, no inclusion of a macromolecular baseline, no corrections for tissue water content or T_2 relaxation times. Hence, no direct conclusion can be drawn. Since metabolites with coupled spins might have shorter T_2 relaxation times^{28,71}, the concentrations of these metabolites could be slightly underestimated with our calculations.

Even though there are published T_2 values for WM, GM, and CSF, acquired from the rat brain at 9.4 T⁷², they were not used in the current quantification calculations. The reason is that high deviation between the human and rat brain T_2 values are expected, which is also highlighted in the study of Deelchand et al.²⁴. Noteworthy, in this study the semi-LASER localization technique was used whose behavior is quite similar to the Carr-

Purcell mode⁷³ due to the four refocusing adiabatic full passage pulses⁷⁴⁻⁷⁶, which makes the T_2 relaxation times comparable to the used 7 T values from reference⁵⁹ measured with a STEAM sequence, which was also shown by our preliminary water T_2 relaxation times mentioned in the MRS Data Quantification section 2.2.5.

Generally, concentrations for most of the metabolites in OccL were higher than those in IPL. A tendency towards a significant difference ($P < 0.05$; not FDR corrected) was found for tCr, tCho, ml, Glc, GSH, and PE.

In particular, increased concentrations of tCr, ml and GSH and decreased concentrations of tCho, NAAG and Tau between OccL and IPL were observed. This finding is in agreement with the results of high-resolution MRSI studies^{77,78}.

In this study, a relatively small number of datasets ($n=8$) was used for the calculation of the metabolite concentrations, and the corrections for the T_1 and T_2 values of the water compartments were calculated in approximation. Moreover, a global T_2 (77 ms) and T_1 (1516 ms) were assumed for all the metabolites. Thus, slight underestimation and overestimation of concentrations are expected for metabolites with smaller and higher T_2 values, respectively.

The inclusion of an experimentally acquired MMB from another brain region seemed to affect the quantification results for some of the metabolites giving significant changes in concentration (Figure 2.5), but the resulting spline baselines constrained by the `dkntmn` parameter did not seem to change visually (Figure 2.8). Also, the changes in the concentration of the metabolites showing significance were less than 10%, except for Tau. In the study of Schaller B. et al³⁶, OccL spectra were quantified using a WM-rich MMB and a GM-rich MMB, and no significant changes in the metabolite concentrations between these two settings were observed. Both WM-rich and GM-rich MMBs were from the same brain region (OccL). However, in this study, the MMBs were acquired from different brain regions (OccL and IPL) which might explain the differences in the quantification results of Tau.

However, quantification with different degrees of stiffness in the spline baseline had a higher impact on the fitting results (Figure 2.6 A and B), as indicated by the larger mean change (24%) and the larger effect size. A larger number of knots in the spline baseline (smaller `dkntmn` number) resulted in a more flexible baseline. As a result, peaks in the

spectral area from 3.5 to 4 ppm were fitted by the spline baseline (Figure 2.8). A certain degree of flexibility in the spline baseline is required for the fit of peaks or artifacts which are not included in the fitting model. However, a highly flexible spline baseline ($dkntmn = 0.15$) can lead to overestimation or underestimation of metabolite concentrations. The results presented in Figure 2.7 show that there are linear and non-linear variabilities in the quantified metabolite concentrations depending on the $dkntmn$ parameter. For this purpose, an appropriate degree of stiffness for the spline baseline (in this case the value of the $dkntmn$ parameter) for the case of using an acquired experimentally MMB at UHF, should be derived using further studies for cross-validation. Therefore, a conclusion that a $dkntmn$ value of 1 should be used for LCModel quantifications cannot be drawn.

Similarly, fitting with the default settings of LCModel (d), where MM are fitted using simulated Voigt-shaped peaks, had significant influence in the resulting spline baselines leading to large deviations both in the concentration levels (Figure 2.6 C and D), with a mean change of 42%, and fitted macromolecular components (Figure 2.8) between different volunteers. Similar conclusions were shown for the rat brain at 14.1 T⁷⁹ and for the human brain at 1.5 T⁸⁰.

We realize that the number of datasets in this study is small and impact the statistical significance, hence interpretations might not be generalizable. However, the results indicated that the inclusion of the experimentally measured MMB in the fitting model can improve the quantification results as reflected both from the smaller deviation of concentrations among the volunteers (Figure 2.6 C and D), and the flat spline baselines (Figure 2.8). Regarding the stiffness of the baseline, a reliable conclusion could not be extracted from the current study since that would require additional datasets and simulations. However, it seems that a high number of knots in the spline baseline (i.e., a small $dkntmn$ number) results in a non-flat baseline (Figure 2.4), which potentially could lead to fitting ambiguity, overfitting, and thus, quantification errors; but further studies are required. Interestingly, the interchange of macromolecular basis sets between OcCL and IPL spectra had a lower influence on the quantification results compared to using the default LCModel settings.

3 Improved Spectral Fitting – PROFIT

Text and figures in this chapter were adapted with minor modifications from our work submitted to *Magnetic resonance in medicine*, 2021 (some of the supporting information material from this publications is not shown):

Borbath T, Dorst J, Murali-Manohar S, Wright AM, Henning A. “ProFit-v3 - a 1-D fitting software and open-source validation datasets.” *Magnetic resonance in medicine*, 2021

3.1 Introduction

Magnetic resonance spectroscopy (MRS) allows for the non-invasive detection of metabolites in the human brain which helps to determine diagnostic markers for neurological and psychiatric disorders and gives an insight into respective disease processes⁴. While MR-visible signal arises from different nuclei such as ^1H , ^2H , ^{13}C or ^{31}P , most common in clinical applications is the acquisition of ^1H MRS signal.

In vivo spectra acquired with ^1H MRS are a convolution of all ^1H MR-visible resonance lines of a comprehensive set of metabolites present in the volume of interest. Metabolite concentrations scale linearly with the area under the respective spectral peaks. In ^{31}P , ^{13}C or ^2H MRS spectra, most peaks are well separated, and hence the determination of the area under the spectral peaks is possible by either line integration or simple spectral modelling approaches⁸¹⁻⁸⁵. However ^1H -MRS suffers from severe spectral overlap and individual metabolite concentrations are hence calculated by more sophisticated spectral fitting software.

Accurate spectral quantification has long been a research interest, and hence, time-domain⁸⁶ and frequency-domain^{87,88} algorithms, as well as machine learning approaches⁸⁹ have been developed. The most widely used fitting algorithms, based on the number of citations for time-domain algorithms are AMARES⁹⁰, QUEST⁹¹, Tarquin⁹², AQSES⁹³, while the most cited frequency-domain methods include: LCModel¹⁵⁻¹⁷, MIDAS^{94,95}, ProFit^{96,97}, Vespa⁹⁸, and FitAid⁹⁹, or the newly developed AB-Fit¹⁰⁰ and Osprey¹⁰¹. However, the most widely used spectral fitting tool with more than 4000 citations and “gold standard” in the MRS community is the commercial LCModel software¹⁵⁻¹⁷.

The main aim of this project was to develop an alternative open-source spectral fitting software with high accuracy and precision for 1D ^1H spectra based on ProFit-v2⁹⁶, which has previously been developed to quantify 2D spectra. The accuracy and precision of the new open-source software was compared with the commercial LCModel software.

Testing the fit accuracy directly with in vivo spectra is impossible since the actual concentrations of the metabolites at the time of acquisition and hence the “ground truth” are not known. Hence, the accuracy of the software was tested utilizing simulated spectra mimicking in vivo conditions and respective data quality. To ensure accurate fitting of in vivo spectra all possible perturbations were simulated and systematically tested.

The underlying spline baseline contributions originating from experimental imperfections have been shown to impact spectral quantification^{102,103}. In this work, the estimation of the necessary spline smoothness is done through the previously published method by Wilson¹⁰⁰. This method was then systematically evaluated for simulated spectra with baseline contribution similar to data acquired in vivo to ensure accurate metabolite concentration estimates.

Fitting precision, on the other hand, has been evaluated using the above described simulated spectra as well as spectra acquired in vivo. Using different subsets of averages of acquired spectra test-retest spectra were created to evaluate the in vivo precision. With this manuscript, we provide the entire data set which should allow for systematic evaluations of other fitting software.

Complementary information can help in improving fitting accuracy, hence different cost functions were investigated, which combined both the frequency and the time-domain information of the spectra. Since in vivo ^1H -MRS spectra can be highly impacted by noise, different spectral filtering options in the preprocessing for fitting were also investigated.

3.2 Theory – ProFit-v3 Algorithm

3.2.1 Magnetic resonance spectroscopy model

MRS spectra can be described as a linear combination of the spectral pattern of the contributing metabolites. If the chemical shifts and coupling constants of all spins related to a number of K metabolites^{7,14} are known, a basis set β_k can be simulated for each

metabolite. These basis sets are simulated with sequence parameters used in the actual MRS acquisition, such as: pulse timings, pulse shapes, the acquisition bandwidth and the number of acquired spectral points. Hence, the resulting basis set $\boldsymbol{\beta}_k$ will reflect the complex spectral pattern of a spin system of a metabolite, particularly with matching J-evolution at longer echo times (TE).

Generally, a spectrum $\hat{\mathbf{y}}$ can be defined as the free-induction-decay in the time-domain with the following equation:

$$\hat{\mathbf{y}} = \left[\exp \left(i \frac{\pi \varphi_0}{180} - \frac{(\pi v_g \mathbf{t})^2}{4 \ln(2)} \right) \cdot \sum_k^K c_k \boldsymbol{\beta}_k \exp(-\pi v_{e,k} (TE + \mathbf{t}) + i 2\pi \omega_k \mathbf{t}) \right] \otimes \exp \left[i \frac{\pi \varphi_1}{180} (\boldsymbol{\delta}_{ppm} - \boldsymbol{\delta}_{ref}^I) \right]. \quad \text{Eq. 3.1}$$

Each metabolite, k , contributes with the concentration c_k to the full spectrum and is characterized by its specific Lorentzian line-shape parameter $v_{e,k}$, which depends on the metabolite transverse relaxation time, $T_{2,k}$ ($v_{e,k} = \frac{1}{\pi T_{2,k}^*} \approx \frac{1}{\pi T_{2,k}}$). Moreover, the spins experience microscopic and macroscopic magnetic-susceptibility effects, which are generally described by a globally applied Gaussian line-broadening factor v_g . This factor v_g can also partially compensate small differences between $\frac{1}{\pi T_{2,k}^*}$ and $\frac{1}{\pi T_{2,k}}$. The resonance frequency of each metabolite might be shifted by a factor $\omega_k = \omega_{local,k} + \omega_{global}$, where $\omega_{local,k}$ originates from the metabolite's environment from factors such as: pH (hydrogen ions), other ions or slight temperature differences; whereas the entire spectrum might be shifted by a factor ω_{global} due to subject motion or due to some post-processing step of the spectra after the acquisition. The MRS sequence timings lead to the zeroth- and first-order phase (φ_0, φ_1) of the spectrum. Lastly, the terms \mathbf{t} and $\boldsymbol{\delta}_{ppm}$ stand for the acquisition time and ppm vectors, $\boldsymbol{\delta}_{ref}^I$ the acquisition frequency, and \otimes is convolution in the time-domain (applied as a pointwise multiplication in the frequency-domain). For the vectors over all metabolites the bold notations \mathbf{c} , $\boldsymbol{\omega}$, $\boldsymbol{\omega}_{local}$, and \mathbf{v}_e will be used.

In vivo spectra with short TEs have significant contributions from macromolecules (MM), which are broad peaks mainly attributed to amino acids in peptides and proteins underlying the sharper metabolite peaks. To achieve accurate spectral fitting of the

metabolites resonance lines, an acquired or fully simulated MM spectral model should be added to the spectral basis set^{27,78,103-105}. Since the included MM spectrum is acquired in vivo, it automatically includes both the Lorentzian and Gaussian broadening factors and hence for the MM basis set vector the $v_{e,k}$ and v_g parameters should be set to zero.

MRS spectra originate from metabolites in aqueous solutions. Since water is generally not of interest, it is suppressed either through the acquisition sequence or additionally during post-processing. However, residual water signals might still be present in the spectra. Together with possible outer volume lipid contributions, these residual contaminations are characterized using a spline baseline underlying the metabolite spectrum in the frequency-domain (*baseline*).

Finally experimental spectra and especially spectra from in vivo measurements contain *noise*. Hence, the ideal time-domain spectrum \hat{y} is described under in vivo conditions as y , which includes the afore-mentioned spectral basis sets of all metabolites of interest and MM considering actual sequence parameters, a spline baseline model to model experimental imperfections and noise and is described in the frequency-domain ($\hat{Y} := fft(\hat{y})$) by Eq. 3.2.

$$\mathbf{Y} = \hat{\mathbf{Y}} + \mathbf{noise} + \mathbf{baseline} \quad \text{Eq. 3.2}$$

The above described spectral model is used in the ProFit-v3 spectral fitting algorithm itself in order to model in vivo spectra precisely. In this case, the noise as well as any feature of the spectrum that is not reflected by the comprehensive spectral model is represented by the fit residual \mathbf{R} (compare section 3.2.2.1).

In addition the spectral model was also used to simulate test data for the accuracy test of the fit algorithm. In that case macromolecular signal, a baseline distortion and noise is added to the linear combination of simulated spectral pattern of all metabolites to mimic in vivo spectral data quality (compare subchapter 3.3.1).

3.2.2 ProFit-v3 algorithm

3.2.2.1 Cost function

The aim of a spectral fitting algorithm is to adjust all parametric and non-parametric parts of the spectral model such that the fit residual \mathbf{R} is minimized.

Let the fit residual R be:

$$R = Y - \hat{Y} - Ba \quad \text{Eq. 3.3}$$

where Y is the measured spectrum and \hat{Y} is the fitted spectrum. Furthermore, to account for the *baseline* from Eq. 3.2 a vector of tensor splines B is introduced, which are scaled by the corresponding spline coefficients a .

For the ProFit-v3 algorithm, three different options for the cost function were defined and their results on spectral fitting investigated.

In the first case, the cost function R_1 is defined as the spectral fit residual in the frequency domain corresponding to a predefined frequency range of interest (*FOI*), typically 0.6 to 4.1 ppm:

$$R_1 = R[\delta_{ppm}(FOI)] \quad \text{Eq. 3.4a}$$

In the second case, the cost function R_2 is extended to include also the fit residual in the time-domain (Eq. 3.4b). Only the first points of the free-induction-decay are included before the signal decays into noise. The used truncation point (*truncPoint*) was calculated from the data, as the time-point when the FID signal fully decayed (signal amplitude is smaller than 1.15 times the noise standard deviation).

$$R_2 = \{R[\delta_{ppm}(FOI)] \quad R[t(1:truncPoint)]\} \quad \text{Eq. 3.4b}$$

In a third case, besides the above-mentioned components, an additional weighted spectral residual is added to the cost function R_3 (Eq. 3.4c). To minimize the fit residual only where the metabolite peaks contribute significantly and avoid scaling based on peak tails or minor contributions (less than 25% of the metabolite maximum absorption peak) the *weights* for the spectral residual are introduced (see Figure 3.1). Please note that each metabolite impacts the real (*Re*) part of the spectrum Y through its basis set β_k only at few chemical shifts significantly. These *weights* are calculated from the summation of the active metabolites at any given fitting iteration.

$$R_3 = \{R[\delta_{ppm}(FOI)] \quad R[t(1:truncPoint)] \quad R[\delta_{ppm}(FOI)] * \mathbf{weights}\},$$

where

$$\mathbf{weights} = \sum_k^K \{Re(\beta_k) > 0.25 * \max[Re(\beta_k)]\}$$

Eq. 3.4c

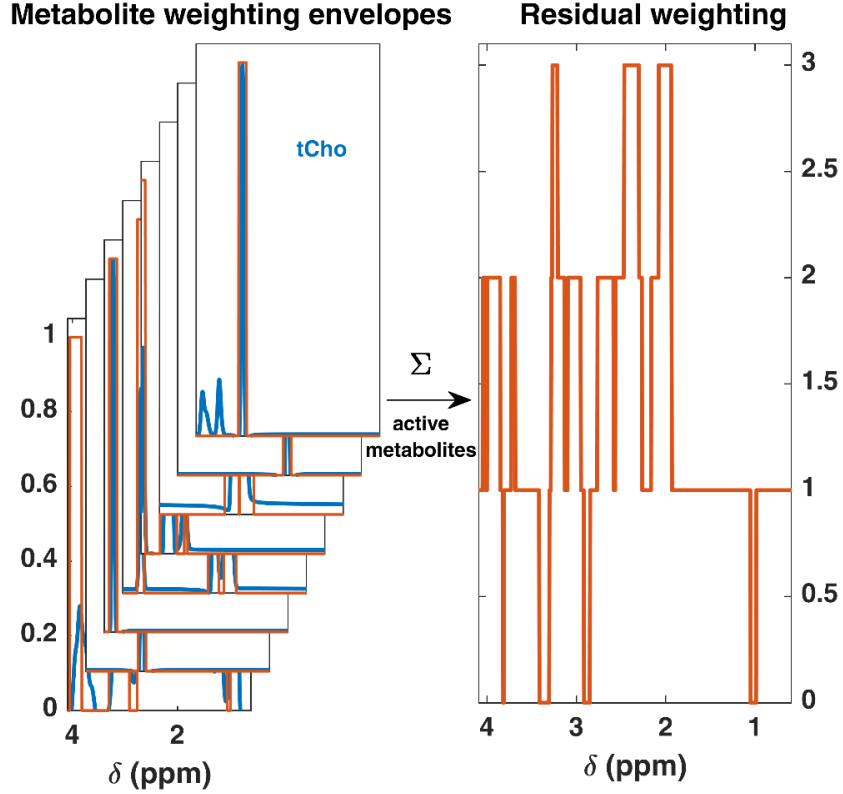


Figure 3.1: For the cost function R_3 a weighting of the spectral residual was introduced. The residual *weights* are calculated from the sum of the active metabolites at the given fit iteration. The metabolite weighting envelopes are displayed in red and are calculated according to Eq. 3.4c.

Using either of these three cost functions (R_x), the minimization problem to find the metabolite concentrations and other spectral parameters is expressed as:

$$\min_{c,a,\varphi_0,\varphi_1,v_e,v_g,\omega} \|R_x\|^2 + \lambda \|D\mathbf{a}\|^2. \quad \text{Eq. 3.5a}$$

To avoid over-fitting through the spline baseline, a regularization to assure smoothness is used, where λ is the regularization parameter and D the second-order difference operator expressed as:

$$D = \begin{bmatrix} 1 & -2 & 1 & 0 & 0 & \dots \\ 0 & 1 & -2 & 1 & 0 & \dots \\ 0 & 0 & 1 & -2 & 1 & \dots \\ \vdots & \vdots & \vdots & \vdots & \vdots & \ddots \end{bmatrix}. \quad \text{Eq. 3.5b}$$

All the minimizations are performed on both the real and the imaginary part of the data. The ProFit-v3 is based on ProFit-v2⁹⁶ and was coded in Matlab-R2019a. Multiple iteration steps (see section 3.2.2.3) are used to minimize the cost function R_x , for which the *lsqnonlin* optimization function with the trust-region-reflective algorithm was applied.

Within the *lsqnonlin* optimization, the metabolite concentrations c and spline coefficients a are determined through the *lsqlin* function. This combination of linear and non-linear optimizations were adapted from the previous ProFit versions^{96,97}.

3.2.2.2 Spline baseline estimation

The degree of spline baseline stiffness has been shown to influence metabolite concentrations substantially^{102,103}. To find the optimal regularization parameter λ for the spline baseline stiffness, Wilson¹⁰⁰ proposed the concept of the modified-Akaike's information criterion (*mAIC*). For this the matrix \mathbf{H} is defined using the matrix of the tensor spline vectors (\mathbf{B}) and the second-order difference operator \mathbf{D} :

$$\mathbf{H} = \begin{bmatrix} \mathbf{B} \\ \sqrt{\lambda} \cdot \mathbf{D} \end{bmatrix}^{-1} \begin{bmatrix} \mathbf{B} \\ 0 \end{bmatrix} \quad \text{Eq. 3.6a}$$

Afterwards, the effective dimension (ED), calculated from the trace of \mathbf{H} :

$$ED = \text{tr}(\mathbf{H}) \quad \text{Eq. 3.6b}$$

Using the ED , the number of data points n , and the arbitrary numeric parameter m , the *mAIC* is defined as:

$$mAIC = \ln \left[\|\mathbf{Y} - \hat{\mathbf{Y}}\|_2^2 \right] + 2m \cdot ED/n \quad \text{Eq. 3.6c}$$

Finally, the optimal spline baseline flexibility is found by choosing the minimum *mAIC* value over a series of possible λ regularization parameters; and hence also ED values. While Wilson set m to 5 to avoid overfitting of the 3T spectra, the optimal m value for 9.4T determined in this study was 15. We assume, that there is a field strength dependence of this user set parameter m . Identically, to the work of Wilson, 15 spline baselines per ppm constituting the matrix \mathbf{B} were defined.

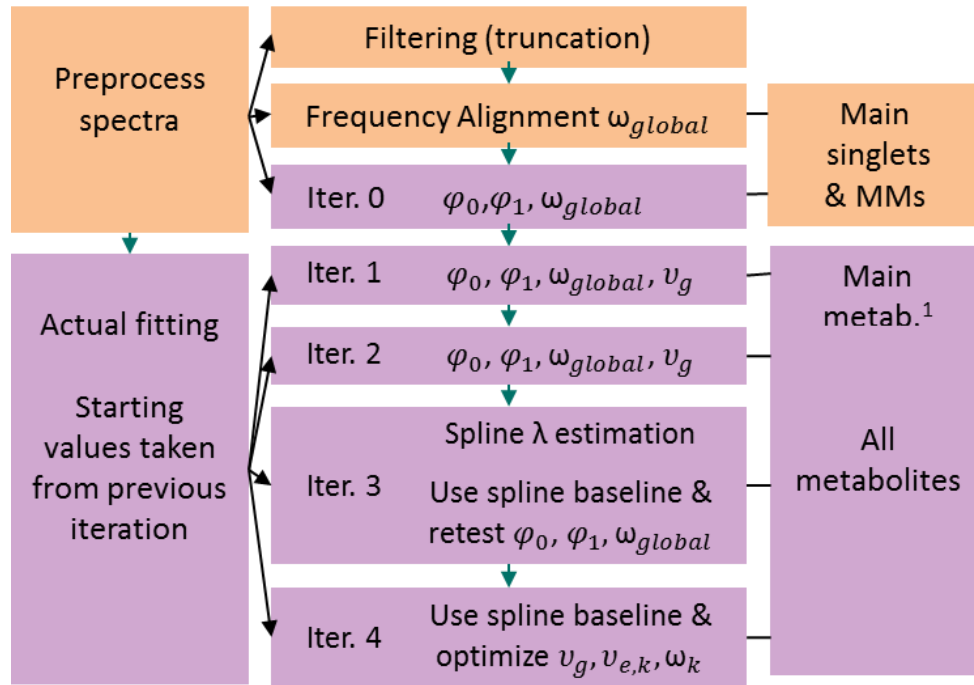
3.2.2.3 Iterations

The optimal solution to the minimization problem of Eq. 3.5a is found through multiple iterations. The ProFit-v3 spectral fitting software allows a flexible setting of the fitting iterations and constraints for the individual fitting steps through a single file.

In all iterations previously determined $T_{2,k}$ relaxation times are used for the determination of the initial values of the $v_{e,k}$ lineshape parameter. Since this study was performed using human brain spectra acquired at 9.4T, $T_{2,k}$ relaxation times from Murali-Manohar³⁰ were taken. Furthermore, since the measured MM spectrum includes already both a v_g and

$v_{e,k}$ broadening, these are fitted as a separate fixed global parameter and are set to 0 and 1, respectively.

To avoid overfitting and local minima solutions, which do not correspond to the physiological reality, first iterations aim to determine global parameters. In contrast, later iterations permit higher degrees of freedom for individual metabolite parameters. For the investigated data sets, the following settings with 1+4 iterations led to the best among the investigated solutions (see algorithmic steps depicted in Figure 3.2 and Table 3.1):



¹ Main metabolites: NAA, tCho, tCr, Glu, ml, MM spectrum

Figure 3.2: The ProFit-v3 algorithm is depicted with the successive optimization steps: first preprocessing steps affecting the spectrum to be fit and the fitting iterations optimizing the linear combination of the basis sets. Depending on the stage of the fitting, more metabolites are added, and additional local degrees of freedom are allowed while keeping the previously optimized global parameters.

Iteration 0: A well-phased and frequency corrected spectrum is crucial for fitting. Hence, a minimization is performed using Eq. 3.5a only considering the main metabolite singlets: N-acetylaspartate (NAA) acetyl moiety [NAA(CH₃)], total choline (tCho) [includes glycerophosphoryl-choline and phosphoryl-choline] together with phosphoethanolamine (PE) named tCho+, the tCr moieties tCr(CH₃) and tCr(CH₂) and the MM spectrum, while

keeping all parameters global and setting a zero baseline. The resulting φ_0 , φ_1 and ω_{global} values from iteration 0 are applied to correct the spectrum prior to the actual spectral fitting steps.

All further iterations adjust the basis sets to the spectrum and the solution of each iteration is used as a starting value for the following iteration.

Iteration 1: Additionally, to the main metabolites used in iteration 0, the following metabolites were set as active: aspartyl moiety of NAA [NAA(CH₂)], glutamate (Glu), and myo-inositol (ml). These are used to determine the global values of φ_0 , φ_1 , ω_{global} , and v_g .

Iteration 2: All metabolites are used to refine the φ_0 , φ_1 , ω_{global} , and v_g parameters.

Iteration 3: The spline baseline flexibility is determined as described in section 3.2.2.2 and Eq. 3.6c for each spectrum. In this spline estimation fitting procedure, the fitted parameters are highly constrained to the fit values from iteration 2. Using the determined λ , the spectrum is refitted with a spline baseline and the fitted values of φ_0 , φ_1 , and ω_{global} are fine-tuned by using less strict bounds for these three parameters, while keeping the parameters v_g , ω_{local} , and v_e more constrained.

Iteration 4: The final values of all parameters are determined in this step. Most significant changes include the permission of individual metabolites to have independent $v_{e,k}$ and ω_k , while allowing the v_g to be adjusted to the new parameters. The global φ_0 and φ_1 are more constrained in this step.

The fitting software will be freely available at <https://cde-quamri.eu> upon acceptance of the manuscript.

3.3 Methods

The ProFit-v3 fitting software underwent a comprehensive validation process. To evaluate the accuracy of the ProFit-v3 fitting software, spectra mimicking in vivo data quality and different perturbations characteristic for in vivo data were simulated (see section 3.3.1). These simulated data also gave insight into the precision of the fitting software. While the fitting accuracy cannot be tested using in vivo data, human brain spectra were used to further test the precision of the fitting algorithm (see section 3.3.2). The results of ProFit-v3 were also compared to those of LCModel V6.3-1L.

Table 3.1: Bounds for the individual parameters during the different fitting iterations (Iter.). Parameters may be adjusted globally to all metabolites or independently (indep.) for each metabolite.

	φ_0	φ_1	ω_k	v_g	$v_{e,k}$	MM. Spectrum	Spline baseline
Iter. 0	Global [-Inf Inf]	Global [-Inf Inf]	Global [-5 5]	Global [0 30]	[0, 6]	$v_{g,MM} = 0$ $v_{e,MM} = 1$ $\omega_{MM} = \omega_k$	0
Spectrum updated							
Fitting basis sets to spectrum							
Iter. 1	Global [-10,10]	Global [-5 5]	Global [-5 5]	Global [0 100]	std(T _{2,k})=0.01	$v_{g,MM} = 0$ $v_{e,MM} = 1$ $\omega_{MM} = \omega_k$	0
Iter. 2	Global [-2 2] + φ_0^{iter-1}	Global [-1.5 1.5] + φ_1^{iter-1}	Indep [-5 5] + ω_k^{iter-1}	Global [-5 5] + v_g^{iter-1}	std(T _{2,k})=0.1	$v_{g,MM} = 0$ $v_{e,MM} = 1$ $\omega_{MM} = \omega_k$	0
Iter. 3	Global [-15 15] + φ_0^{iter-1}	Global [-15 15] + φ_1^{iter-1}	Indep [-3 3] + ω_k^{iter-1}	Global [-2 2] + v_g^{iter-1}	std(T _{2,k})=0.05	$v_{g,MM} = 0$ $v_{e,MM} = 1$ $\omega_{MM} = [-0.2 0.2]$ + ω_{MM}^{iter-1}	mAIC calculation with chosen λ retest all values as described on the left
Iter. 4	Global [-0.1 0.1] + φ_0^{iter-1}	Global [-0.1 0.1] + φ_1^{iter-1}	Indep [-0.2 0.2] + ω_k^{iter-1}	Global [-5 5] + v_g^{iter-1}	std(T _{2,k})=1	$v_{g,MM} = 0$ $v_{e,MM} = 1$ $\omega_{MM} = [-0.2 0.2]$ + ω_{MM}^{iter-1}	use λ^{iter-1}

The spectral basis set that was used for all validation steps was simulated for a semi-LASER sequence¹⁰⁶ in Vespa⁹⁸ using real pulse shapes¹⁰⁷ and included the following metabolites, combined metabolites or metabolite moieties, as described in Murali-Manohar et al.³⁰: N-acetylaspartylglutamate (NAAG); γ -aminobutyric acid (GABA); aspartate (Asp); Glu; glutamine (Gln); glutathione (GSH); glycine (Gly); ml; scyllo-inositol (sl); lactate (Lac); and taurine (Tau); tCho+; finally the tCr(CH₃) and tCr(CH₂); and NAA(CH₃) and NAA(CH₂) moieties. Chemical shifts and coupling constants were taken from Govindaraju et al.^{7,14} and for GABA from Near et al.¹⁰⁸.

All the simulated and preprocessed in vivo data will be publicly available at <https://cde-quamri.eu> upon acceptance of the manuscript.

3.3.1 Simulated spectra

Simulated test data was created using Eq. 3.1, Eq. 3.2, and scan parameters of in vivo spectra acquired at 9.4T (TE = 24 ms, TR = 6 s, bandwidth = 8 kHz, 4096 points, excitation frequency $\delta_{ref}^O = 7.0$ ppm, acquisition frequency $\delta_{ref}^I = 4.66$ ppm). To match in vivo conditions best, concentrations in mmol/kg ($c_k^{mmol/kg}$) and $T_{2,k}$ relaxation times were taken from Murali-Manohar et al.³⁰ and the metabolite concentrations were then relaxation adjusted according to $c_k = c_k^{mmol/kg} / \exp\left[-\frac{TE}{T_{2,k}}\right]$. Respective relative intensity weightings were applied to the simulated spectral pattern of all above mentioned metabolites before their linear combination to yield the test spectra for the accuracy test.

To test the fit accuracy first default values for each parameter $\varphi_0, \varphi_1, \nu_g, \omega$ (ω_{global} and ω_{local}), ν_e , **noise**, and c were chosen. Then one parameter at a time was varied, while keeping all others at their default values. This way six different sets of 15 simulated spectra each were generated with defined minimum and maximum values for $\varphi_0, \varphi_1, \nu_g, \omega_{global}, \omega_{local}$, or ν_e (see Table 3.2). For **noise** 25 test cases were generated, whereas for c simulations 100 test cases were generated. Further, 16 different **baseline** simulations were created: 14 baselines were extracted from previous LCMModel fits and 2 additional baselines were created simulating a Gaussian lipid peak at 1.3 ppm, both in phase ($\varphi_0 = 0^\circ$) and out of phase ($\varphi_0 = 90^\circ$).

Table 3.2: The simulated parameters are summarized in this table. These include the following nine simulation setups: φ_0 , φ_1 , v_g , ω_{global} , ω_{local} , v_e , **noise**, **c**, and **baseline**. For every simulation, an x “Number of simulations” were performed with values ranging between the shown minimum and maximum values, while all the other parameters were left at the indicated default value. Concentration c_k and T_2 relaxation $T_{2,k}$ values were taken from Murali-Manohar et al.,³⁰. $rand(-1,1,k)$ stands for a random value between $[-1,1]$ for each parameter k . Abbreviations: φ_0 – zero order phase, φ_1 – first order phase, v_g – Gaussian broadening, ω_{global} – global frequency shift, $\omega_{local,k}$ – local frequency shift, $v_{e,k}$ – Lorentzian broadening, c_k – concentration, $T_{2,k}$ – T_2 relaxation time, k – k^{th} metabolite.

Parameters for the simulated spectra				
Parameters (units)	Default value	Minimum	Maximum	Number of simulations
φ_0 (degrees)	0	-35	35	15
φ_1 (degrees/ppm)	0	-17.5	17.5	15
v_g (Hz)	12	4	32	15
ω_{global} (Hz)	0	-17.5	17.5	15
$\omega_{local,k}$ (Hz)	0	$rand(-1,1,k) \cdot 0.75$	$rand(-1,1,k) \cdot 15$	15
$v_{e,k}$ (Hz) $\approx \frac{1}{\pi T_{2,k}(\text{ms})}$	Literature mean T_2 ³⁰	Literature mean T_2 + $rand(-1,1,k) \cdot 0.2 \cdot$ $std(T_2)$	Literature mean T_2 + $rand(-1,1,k) \cdot 2 \cdot$ $std(T_2)$	15
noise <-> SNR_{NAA}	158	13	207	25
c_k	Literature mean conc ³⁰	Literature mean conc + $rand(-1,1,k) \cdot 3.5 \cdot$ $std(\text{conc})$		100
baseline	0	14 extracted baselines from LCModel fits and simulation of lipid peak at 1.3 ppm with 0 and 90 degree φ_0		16

The SNR of the spectra (SNR_{NAA}) was defined for the NAA(CH₃) singlet using the real part of the spectrum and dividing the peak amplitude by the standard deviation of the noise between -4.0 and -1.0 ppm. The average SNR_{NAA} was around ~150. The series of simulated spectra are shown in Figure 3.3.

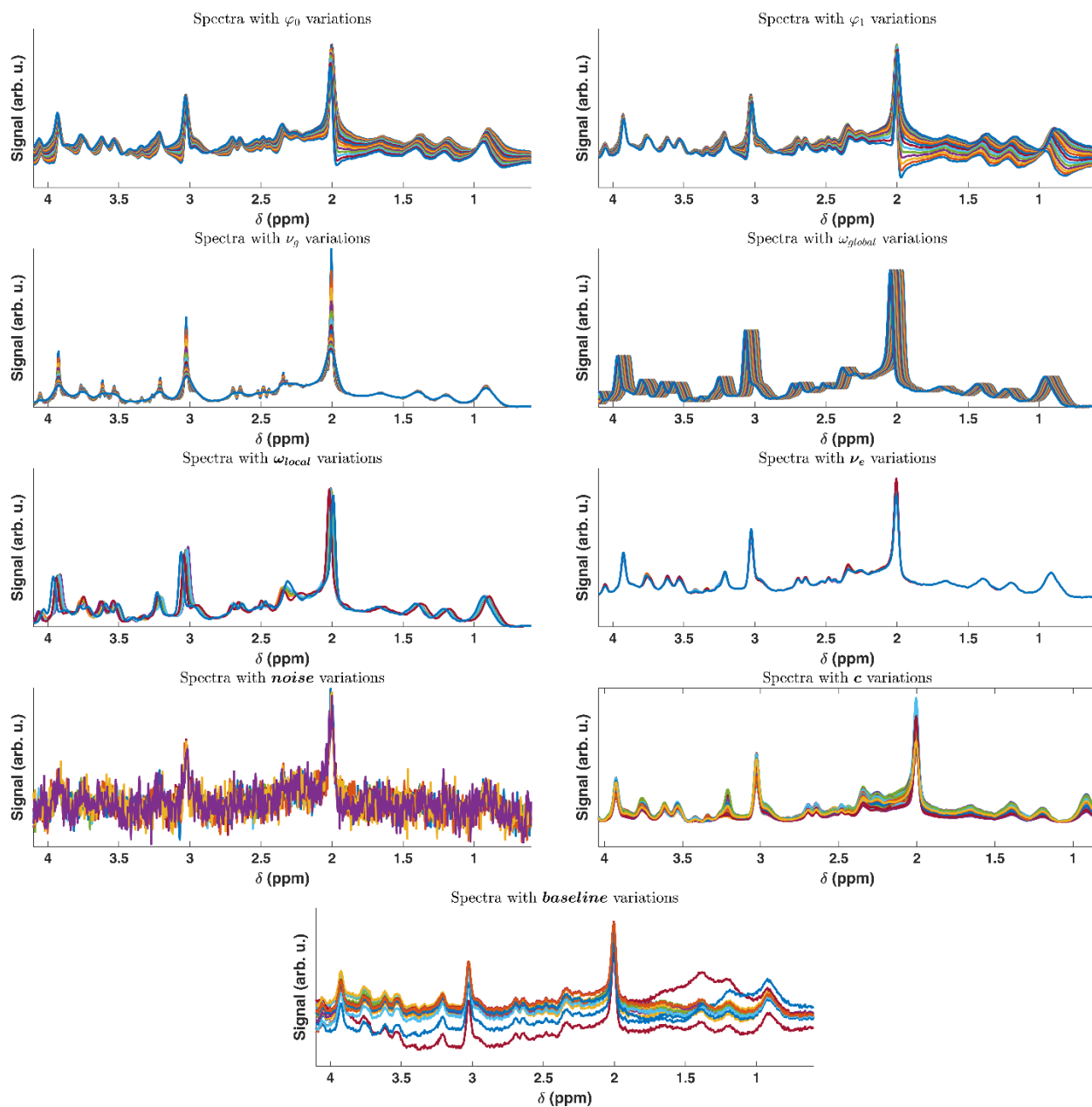


Figure 3.3: The series of simulated spectra are shown for the variations in φ_0 , φ_1 , ω_{local} , ω_{global} , c , ν_g , ν_e , **noise**, and **baseline**. For each simulation series all parameters were kept at the default values as described in Table 3.2, while varying only the parameter mentioned in the title. For the parameter in question the variation of the simulation included values as described by the minimum and maximum values shown in Table 3.2.

3.3.2 In vivo spectra

For the evaluation of the precision of the fitting software previously acquired metabolite-cycled semi-LASER spectra were used (see acquisition parameters in section 3.3.1). This data set was previously published in up-field³⁰ and downfield¹⁰⁹ T₂ studies. Voxels were positioned in the occipital lobe of the human brain at 9.4T (Siemens Magnetom 9.4T whole body MRI scanner) and measured in eleven healthy volunteers (27.8±1.9 years, three females). Data were preprocessed as described in Murali-Manohar et al.³⁰. For each subject, out of all available spectral averages (NEX = 96) subset spectra for test-retest procedure were created. To maintain the appropriate metabolite- and 16-step phase-cycling, two spectra with 32 averages each and two spectra with 64 averages each (combining phase-cycling blocks) were averaged per subject.

3.3.3 ProFit-v3 preprocessing

Before the actual ProFit-v3 fitting iterations, the MRS signal is enhanced through the spectral filtering, i.e. signal truncation, at the time-point when the FID decayed into the noise. Afterwards the spectrum is frequency aligned to the main metabolite singlets: NAA(CH₃), tCr(CH₃), tCr(CH₂), and tCho trimethyl moiety [tCho(CH₃)₃]. Frequency alignment is performed on the magnitude spectrum to avoid possible phasing errors.

3.3.4 Evaluation of fit results

As first step of the accuracy evaluation of ProFit-v3 the dependence of the fit accuracy for the fitted parameters $\varphi_0, \varphi_1, \nu_g, \omega, \mathbf{v}_e$, and \mathbf{c} on input parameter variations of the parameters $\varphi_0, \varphi_1, \nu_g, \omega_{global}, \omega_{local}, \mathbf{v}_e, \mathbf{noise}$, and **baseline** was investigated using simulated spectra. For global parameters φ_0, φ_1 , and ν_g the fitting errors were calculated by comparing the fitted value against the ground truth used during simulation of the spectra as:

$$\Delta param = (param_{simulated} - param_{fitted}) \quad \text{Eq. 3.7a}$$

whereas for parameter vectors \mathbf{c} , \mathbf{v}_e , and ω the fitting errors were calculated as:

$$|\overline{\Delta param}| = \text{mean}[abs(\mathbf{param}_{simulated} - \mathbf{param}_{fitted})] \quad \text{Eq. 3.7b}$$

where $param$ stands for any of the fitting parameters and abs is the absolute value.

As further step of the accuracy and precision evaluation the influence of parameter variations in the simulated input spectra on the accuracy of the concentration estimates was investigated and respective results from ProFit-v3 were compared against LCModel results. Both the LCModel and ProFit-v3 derived metabolite concentrations were normalized to the simulated tCr(CH₃) concentration. The concentration differences in percent ($c_k^{\%}$) induced by parameter variations of $\varphi_0, \varphi_1, v_g, \omega_{global}, \omega_{local}, v_e, noise$, and **baseline** were determined for each metabolite and both fitting software packages as follows:

$$c_k^{\%} = \frac{(c_k^{simulated} - c_k^{fitted})}{c_k^{simulated}} \cdot 100 \quad \text{Eq. 3.7c}$$

As final step of the accuracy evaluation and part of the precision evaluation the concentration c of the simulated spectra was varied and respective correlation plots between input and measured concentrations were created to investigate how accurately a range of low to high metabolite concentrations in the spectra are determined.

Bland-Altman plots¹¹⁰ were used for the precision analysis of the metabolite concentrations fitted for in vivo data. For this purpose we define, the concentration of the metabolite k and the subject i for the fit ($fits1$) and refit ($fits2$) as $c_{i,k}^{fits1}$ and $c_{i,k}^{fits2}$, respectively. $fits1$ represents the first set of the sub-spectra with 64 or 32 averages, whereas $fits2$ the second sub-spectra. The metabolite concentrations were normalized to the water reference. The Bland-Altman plots are calculated for changes of metabolite concentration in percent $c_{i,k}^{\%}$:

$$c_{i,k}^{\%} = \frac{(c_{i,k}^{fits2} - c_{i,k}^{fits1})}{\text{mean}(c_{i,k}^{fits1}, c_{i,k}^{fits2})} \cdot 100 \quad \text{Eq. 3.8a}$$

Reproducibility coefficients¹¹⁰ ($RPC_k^{\%}$) for the in vivo sub-spectra are also reported:

$$RPC_k^{\%} = 1.96 \cdot \text{std}_i(c_{i,k}^{\%}) \quad \text{Eq. 3.8b}$$

For comparison of the two fitting software packages and to investigate the influence of cost functions (R_x) in ProFit-v3 (see section 3.2.2.1) the averaged reproducibility coefficient was introduced $\overline{RPC_K^{\%}}$:

$$\overline{RPC_K^{\%}} = \text{mean}_K(RPC_k^{\%}) \quad \text{Eq. 3.8c}$$

This metric was evaluated for all metabolites $\overline{RPC}_{all}^{\%}$ or only the main metabolites $\overline{RPC}_{main}^{\%}$. All simulated and in vivo data used in accuracy and precision analyses were fitted with the same fit settings for both ProFit-v3 and LCModel, except when the different cost functions for ProFit-v3 were compared, see section 3.3.5.

3.3.5 Comparison of cost functions

The different cost functions (see section 3.2.2.1) were compared against each other. Eq. 3.7c and Eq. 3.8c were used for both simulated and in vivo results. For the in vivo results also the fit-quality numbers (FQN) are reported. The FQN is defined “as the ratio of the variance in the fit residual (in the fitted frequency or time range) divided by the variance for pure spectral noise”^{111,112}, see Eq. 3.9. Since several of the in vivo data in the current study have some small lipid contaminations, the FQN was calculated for following ppm ranges of the residue (FOI_{FQN}): $FOI_{FQN} = 0.6:4.1(\text{ppm})$ and $FOI_{FQN} = 1.95:4.1(\text{ppm})$.

$$FQN[FOI_{FQN}] = \frac{\text{var}\{R[\delta_{ppm}(FOI_{FQN})]\}}{\text{var}\{\text{noise}[\delta_{ppm}(-5:-1)]\}} \quad \text{Eq. 3.9}$$

A $FQN = 1$ indicates a perfect fit, whereas $FQN > 1$ indicates an underfitting.

For the comparison with LCModel, as well as for all the shown figures the R_3 cost function was used.

3.4 Results

The results of the *baseline* simulations are shown in Figure 3.4 to conceptualize the fit results of the spline baselines. These visualizations show both the input baselines and the fitted baselines by ProFit-v3 and LCModel with the corresponding residual. Furthermore, the estimation of the needed spline baseline flexibility is showcased through the *mAIC*-plots, where the minimum point of the *mAIC* line determines the used *ED* and hence λ .

The ProFit-v3 accuracy validation results for the systematic parameter changes are presented in Figure 3.5 and Figure 3.6. The six subplots in Figure 3.5 show the accuracy of each of the following fitted parameter $\varphi_0, \varphi_1, \nu_g, \omega, \nu_e$, and c in dependence of the input variance of the parameters $\varphi_0, \varphi_1, \nu_g, \omega_{global}, \omega_{local}, \nu_e, \text{noise}$, and *baseline* computed according to Eq. 3.7a and Eq. 3.7b, respectively.

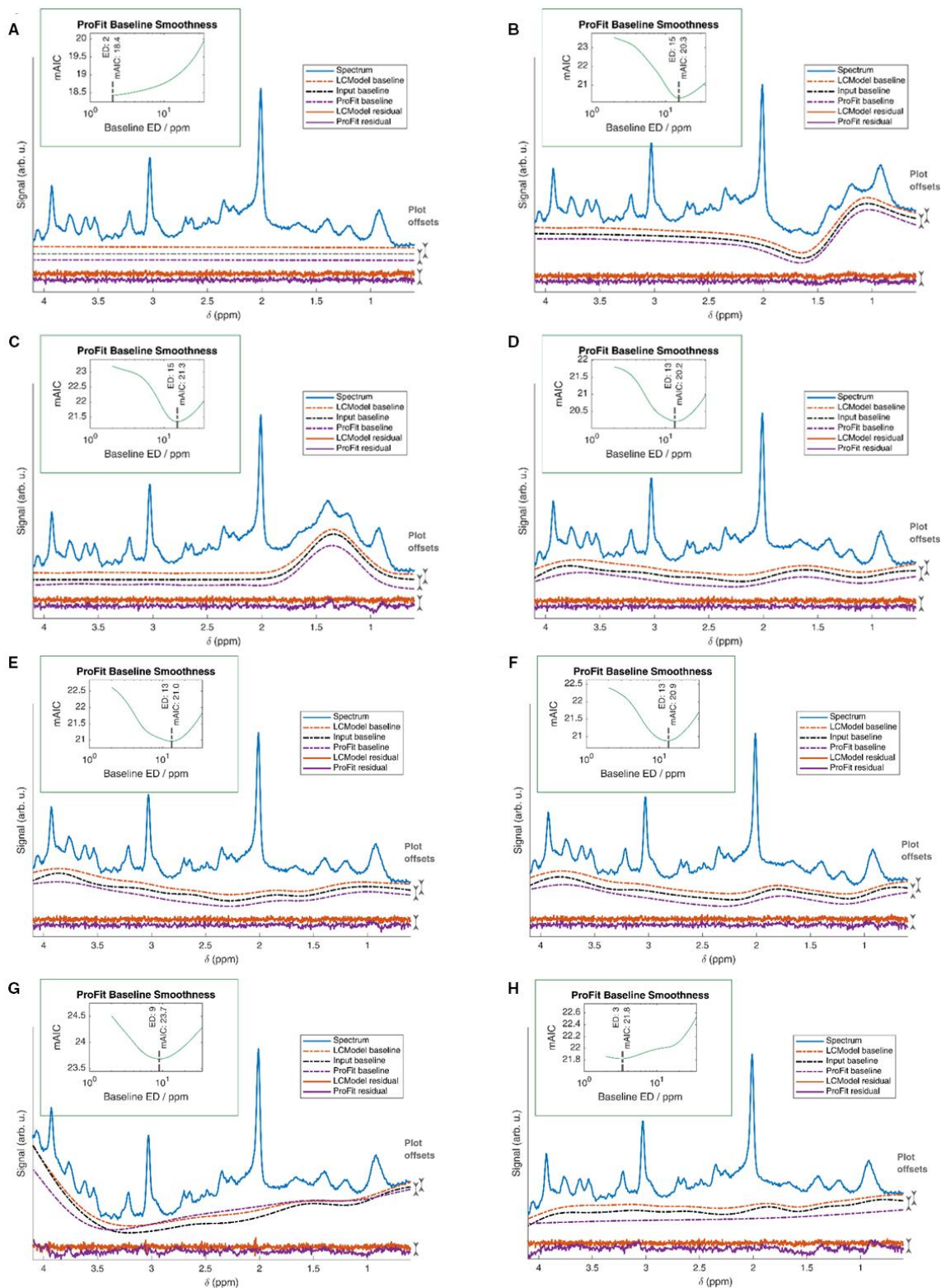


Figure 3.4: Fit results for the *baseline* simulation are shown. The blue line shows the input spectrum, while the black line indicates the input baseline. The fitted baselines (dashed lines) and the resulting residual (continuous lines at the bottom) are shown in red for LCMoDel and purple

for ProFit-v3. The plot offsets used for display purposes are indicated on the right of each subplot. Fitted baselines agree well with the simulated ones. Inlays show the $mAIC$ curves for the ProFit-v3 fitting. These spectra show a simulated zero baseline (A), an in phase ($\varphi_0 = 0^\circ$) (B) and an out of phase ($\varphi_0 = 90^\circ$) (C) lipid peak at 1.3 ppm, but also extracted baselines from a previous LCModel fit (D-H).

Noise and baseline variations influence the fit accuracy of most other parameters most, while also local frequency shifts ω_{local} and the ν_e line broadening has a negative impact on the accuracy of the concentration estimates.

The accuracy of metabolite concentration estimates in dependence on each of the above-mentioned parameter variations is summarized in Figure 3.6. These results are shown for both ProFit-v3 and LCModel. While the concentration results of ProFit-v3 are slightly more accurate (smaller deviation of the mean measured value from the ground truth), the LCModel results are more precise (smaller standard deviations).

The correlation plots created for the concentration variation simulations c in Figure 3.7 show that overall, both ProFit-v3 and LCModel determine the true variance of metabolite concentrations well. Metabolites corresponding to the most prominent spectral singlets are particularly well fitted, whereas metabolite concentrations derived from less prominent multiplets related to metabolites like Asp, GABA, GSH, Gly, NAAG, Tau and sl show slightly lower accuracy and precision.

Spectral fits with ProFit-v3 and LCModel for representative in vivo spectra are shown in Figure 3.8. The corresponding Bland-Altman plots for the metabolite concentration test-retest results according to Eq. 3.8a are showing the reproducibility of ProFit-v3 and LCModel in Figure 3.9. The reproducibility coefficients $RPC_k^{\%}$ and the summaries $\overline{RPC_{man}^{\%}}$ and $\overline{RPC_{all}^{\%}}$ are presented in Table 3.3.

A comparison of the cost functions R_x are shown in **Error! Reference source not found.** There is a minor improvement of accuracy and precision for simulated and in vivo data between R_1 and R_2 . There is however an improvement in all these metrics when using the R_3 cost function. Additionally, for the in vivo data the $FQN[FOI_{FQN}]$ are reported, where the use of the cost function R_3 leads to the with the smallest FQN for the lipid-free area, whereas it is the highest for the whole FOI_{FQN} .

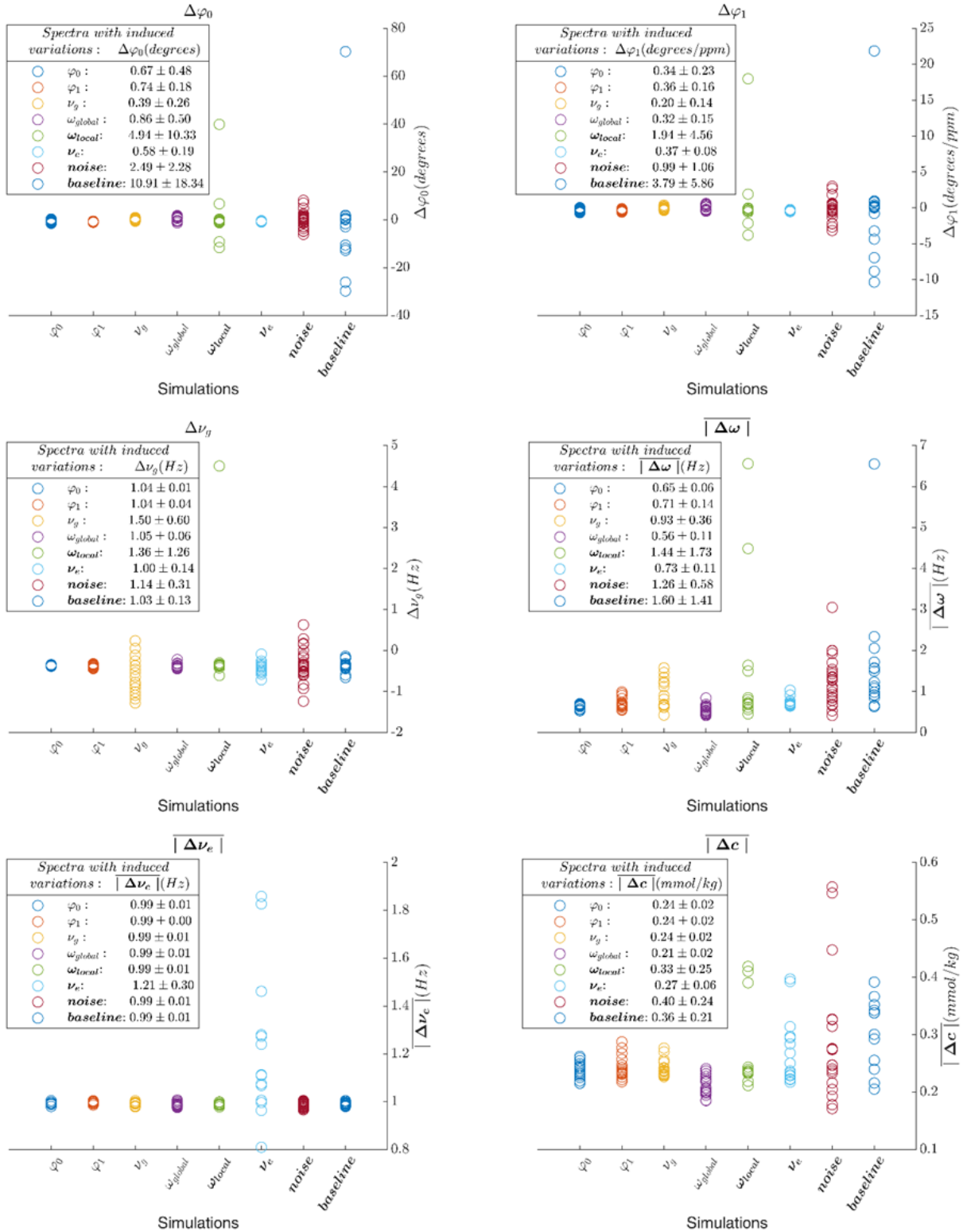


Figure 3.5: ProFit-v3 parameter evaluation of the parameter differences of φ_0 , φ_1 , ν_g , ω , ν_e , and c for the eight simulation setups with changes in φ_0 , φ_1 , ν_g , ω_{global} , ω_{local} , ν_e , **noise**, and **baseline**. The legends display for each simulation setup the mean and the standard deviation

between the simulations for the fitting parameter specified in the title. $\Delta\varphi_0$, $\Delta\varphi_1$ and $\Delta\nu_g$ are the differences between the fitted and the simulated values of φ_0 , φ_1 , ν_g , whereas $|\overline{\Delta\omega}|$, $|\overline{\Delta\nu_e}|$ and $|\overline{\Delta c}|$ are the mean absolute differences of the respective input parameters. The legends are displayed such, that no data point is covered.

The best accuracy and precision for both simulated and in vivo data was achieved using R_3 ; hence the figures and results from all the previous sections display these results.

3.1 Discussion

This work presents a newly developed spectral fitting software, ProFit-v3, and systematically evaluates its performance with respect to accuracy and precision of the fit results and against the MRS-community gold standard for spectral fitting LCModel. The ProFit-v3 software and the data sets are freely available.

As part of the accuracy test of the new fitting algorithm a systematic evaluation for all possible perturbations of ^1H -MRS spectra was performed. Analyzing ProFit-v3 for particular disturbances such as phase distortion, frequency shifts, baseline distortions, line broadening and noise, which mimicked in vivo conditions, allowed to conceptualize whether the fitting software is underperforming for a particular type of disturbance. The results displayed in Figure 3.5 and Figure 3.6 show that the newly developed ProFit-v3 fitting algorithm does not have systematic errors in determining the fitting parameters in general and the metabolite concentrations more specifically.

During the development of ProFit-v3 it was observed, that large phase and frequency shift distortions lead to fit uncertainty. Therefore, similarly to other spectral fitting packages^{15,100,101}, preprocessing steps for spectral fitting were introduced. Herein, frequency alignment and phase correction of the spectra was performed considering the multiple singlets in the magnitude spectra and using the main metabolites for an initial φ_0 and φ_1 correction. However, the 1-3 outliers produced by the $\omega_{local,k}$ simulations are for simulating $\omega_{local,k}$ of up to 9 or 15 Hz, which are mimicking rather unusual scenarios: the effects of temperature on the metabolite moieties, as measured by Wermter¹¹³ can be up to $7 \cdot 10^{-4}$ (ppm/K), or 0.28 (Hz/K) at 9.4T; the effects of pH or other ions are more significant, however only highly pH-sensitive metabolites such as homocarnosine has two resonances that shift by 7.7 Hz and 20 Hz for a 0.1 pH change^{109,114}.

Accuracy and precision analysis for concentration estimates from simulated spectra

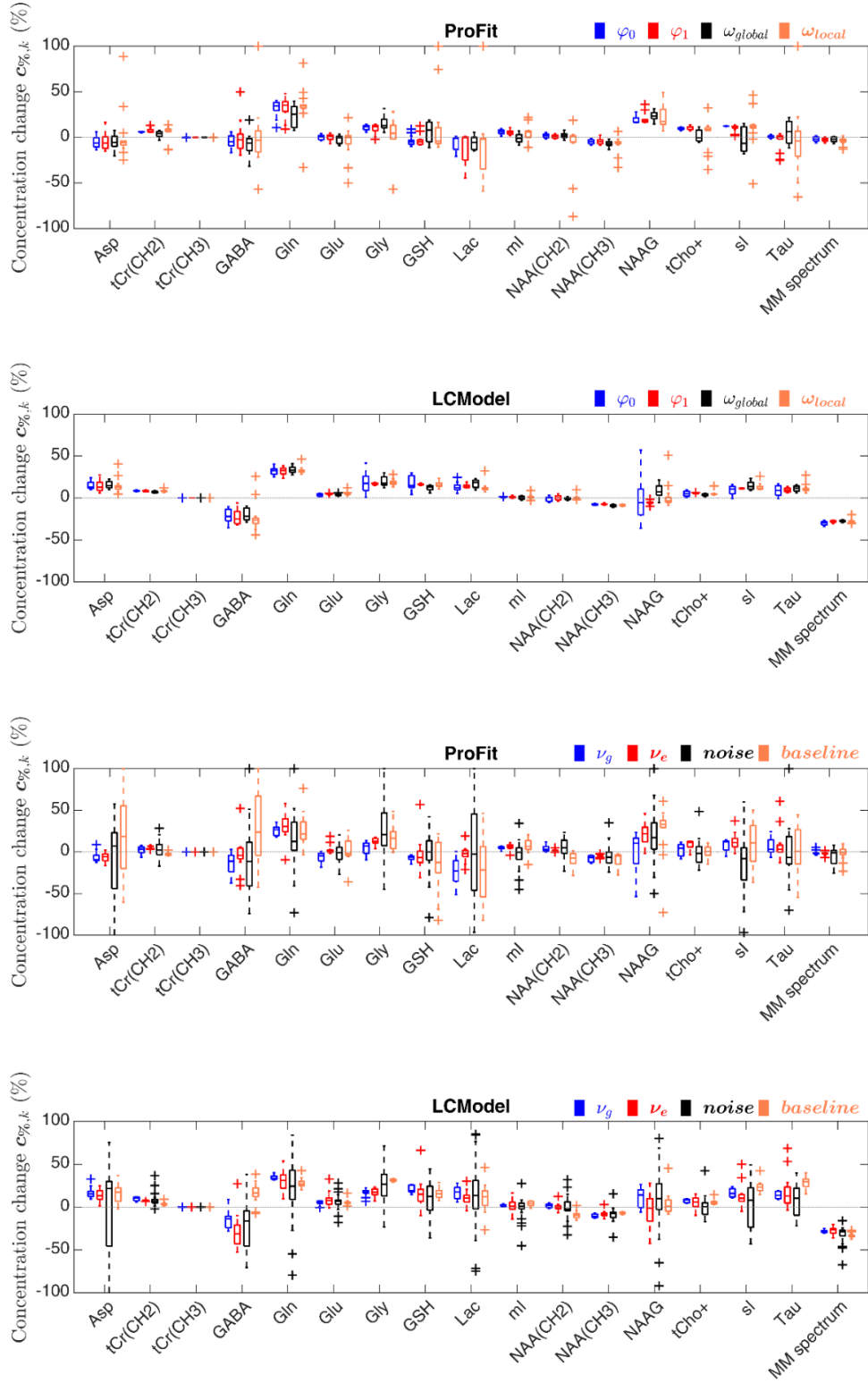


Figure 3.6: Boxplots of concentration changes in percent $c_k\%$ for each metabolite for the φ_0 , φ_1 , v_g , ω_{global} , ω_{local} , v_e , noise, and baseline simulations comparing ProFit-v3 and LCModel results.

Concentration estimates from simulated spectra

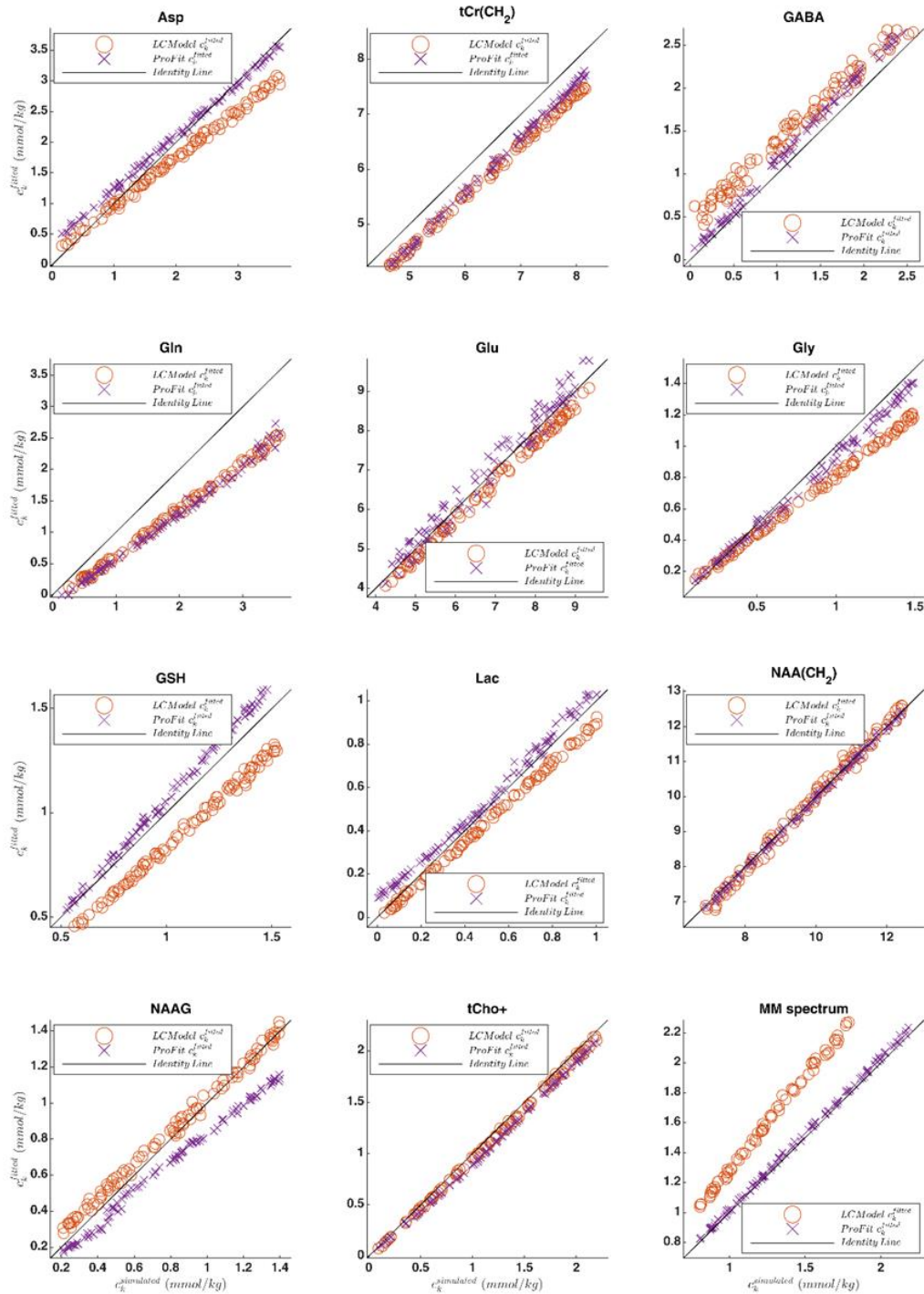


Figure 3.7: Correlation plots between the fitted and simulated metabolite concentrations are shown for both ProFit-v3 and LCMoDel fits. The identity line is shown in yellow. The plots show the following metabolites: Asp, tCr(CH₂), GABA, Gln, Glu, Gly, GSH, Lac, NAA(CH₂), NAAG, tCho+, and the MM spectrum. The correlation plots for the other metabolites are not shown.

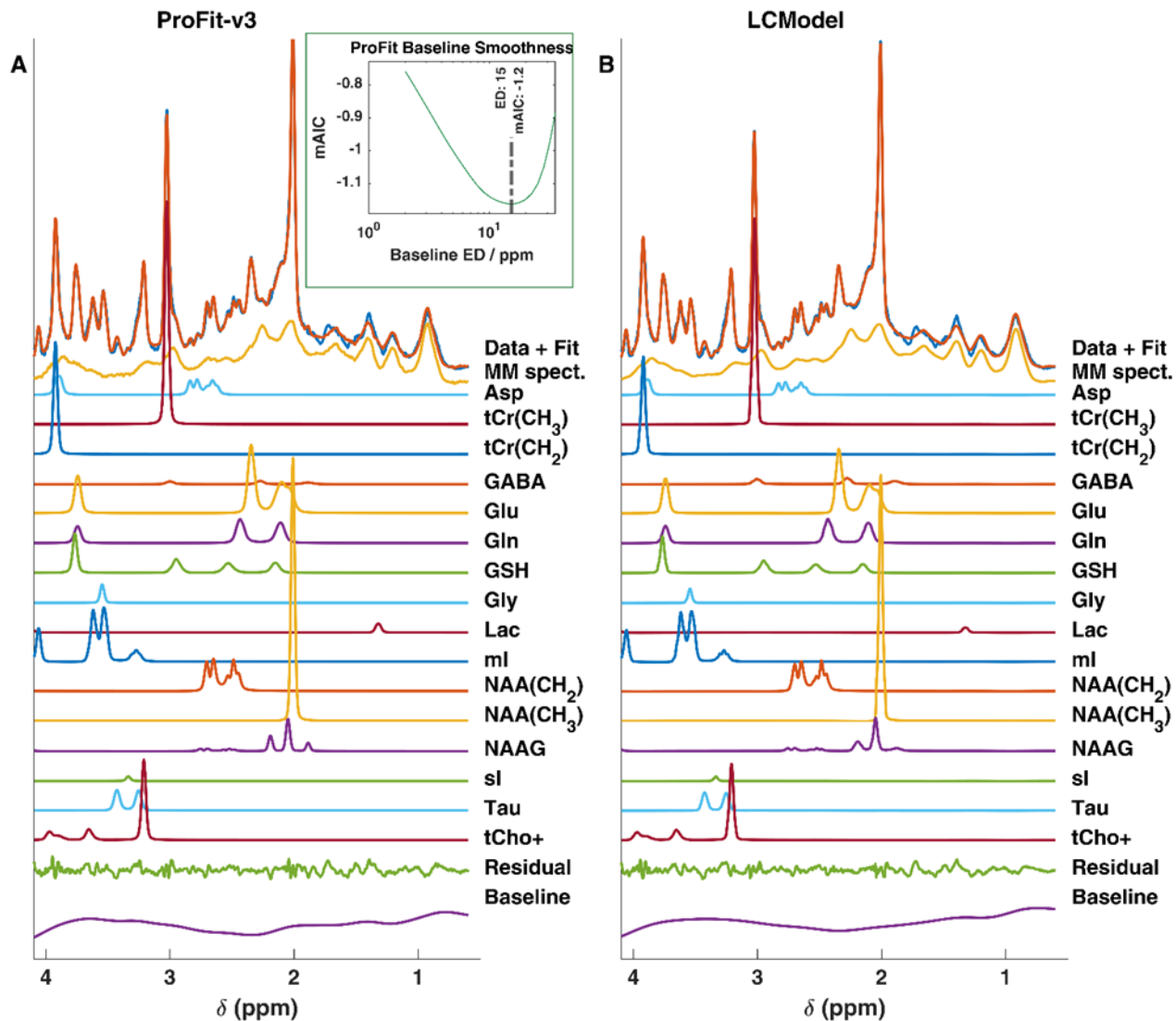


Figure 3.8: *In vivo* sub-spectra with 64 averages and metabolite fits for a sample subject. A: shows the fit results for ProFit-v3, while B: the fit results for LCModel. The inlay shows the *mAIC* curve, used for the determination of the regularization term λ , and hence, the smoothness of the spline baseline (purple line) used for ProFit-v3 fitting. That λ and effective dimension (ED) is chosen, for which the *mAIC* is minimal. Both the splines baseline and the residue from the two fitting software show similar characteristics. Minor lipids can be observed between 1.2 and 1.9 ppm.

Overall, ProFit-v3 had the highest uncertainty for fitting noisy spectra and spectra with large baseline distortions. Also previous publications using LCModel demonstrated that the fitted spline baseline can impact the fitted metabolite concentrations significantly^{102,103,115}.

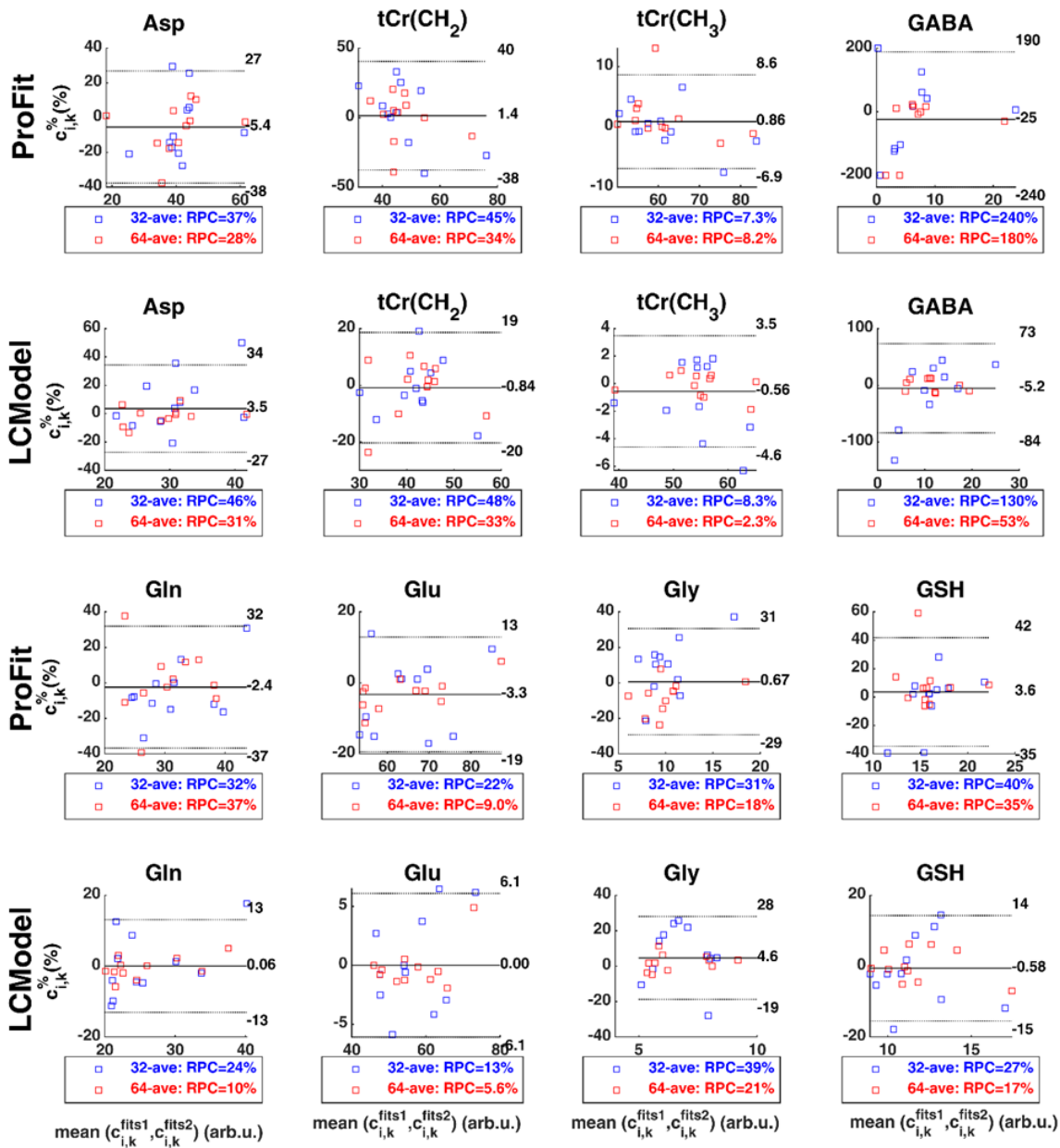


Figure 3.9: Bland-Altman plots shown for 8 out of the 17 fitted metabolites, odd rows showing the concentrations fitted with ProFit-v3, while the even rows show the results for LCMoDel. The individual scatter-points represent the fits and refitted concentrations for the eleven volunteers. One sub-spectra with 32 averages is compared against the other sub-spectra with 32 averages (blue circles). Similar comparison was made for the two 64 averages sub-spectra/subject (red circles). The labels report the calculated reproducibility coefficients ($RPC_k^{\%}$). The continuous horizontal line and number indicates the mean $c_{i,k}^{\%}$ error, while the dotted horizontal lines represent the reproducibility bounds, meaning the $\pm 1.96 \cdot \text{std}(c_{i,k}^{\%})$ values.

Table 3.3: The reproducibility coefficients $RPC_k^{\%}$ calculated for each metabolite given in percent. Additionally, the mean value of all the metabolites $\overline{RPC_{all}^{\%}}$ and mean of only the main metabolites (tCr(CH₃), tCr(CH₂), Glu, ml, NAA(CH₂), NAA(CH₃), tCho+) $\overline{RPC_{main}^{\%}}$ are presented. The columns show the results for ProFit-v3 and LCModel broken up for in vivo data comparisons when 32 or 64 averages were used.

In vivo spectra $RPC_k^{\%}(\%)$				
	ProFit-v3		LCModel	
	32 ave.	64 ave.	32 ave.	64 ave.
Asp	37	28	46	31
tCr(CH ₂)	45	34	48	33
tCr(CH ₃)	7	8	8	2
GABA	245	179	127	53
Gln	32	37	24	10
Glu	22	9	13	6
Gly	31	18	39	21
GSH	40	35	27	17
Lac	177	160	217	119
ml	18	13	13	10
NAA(CH ₂)	14	19	12	7
NAA(CH ₃)	15	8	10	3
NAAG	48	54	30	19
tCho+	10	9	15	9
sl	225	209	154	132
Tau	56	44	30	13
MM spectrum	12	14	15	13
$\overline{RPC_{main}^{\%}}$	19	14	17	10
$\overline{RPC_{all}^{\%}}$	61	52	49	29

For this reason, Wilson¹⁰⁰ proposed the AB-fit algorithm with automatic determination of the optimal spline smoothness through the modified-Akaike's information criterion. This method was also implemented into the ProFit-v3 software and subsequently evaluated on spline baselines extracted from previous LCModel fits. Comparing the simulated baselines with the fitted spline baselines, both LCModel and ProFit-v3 seems to model the simulated baselines well (Figure 3.4). The fitted splines did not pick up minor variations of the input spline baseline; however, as seen from the residual and the fitted concentrations, these seem to have little impact on the estimated concentrations.

Table 3.4: A comparison of the ProFit-v3 fit setups for different cost functions for simulated and in vivo data is shown. The cost functions: R_1 uses only the spectral residual, R_2 uses additionally the free-induction-decay, whereas R_3 includes additionally a weighted spectral residual based on the active metabolites. $\overline{|c_k^\%|_{all}}$ are the mean changes in concentration in percent compared to the simulated concentration. For in vivo data both the results for the 32 and the 64 averages fit-refits are reported. $\overline{RPC_{all}^\%}$ is the mean reproducibility coefficients ($RPC_k^\%$) over all metabolites. $\overline{RPC_{main}^\%}$ includes only the main metabolites (tCr(CH₃), tCr(CH₂), Glu, ml, NAA(CH₂), NAA(CH₃), tCho+, MM spectrum). For the in vivo data also the mean of the FQN's are reported for the two different ppm areas ($\overline{FQN[FOI_{FQN}]}$).

		R_1		R_2		R_3	
Simulated spectra $\overline{ c_k^\% _{all}}$							
Simulations with induced variations:	φ_0	8.5±4.3		8.5±4.3		7.5±3.8	
	φ_1	8.5±4.9		8.5±4.9		7.7±4.2	
	ω_{global}	6.9±7.1		6.9±7.1		6.9±6.8	
	ω_{local}	8.7±22.6		8.7±22.7		8.4±23.7	
	ν_g	8.2±6.2		8.2±6.2		7.3±7.5	
	ν_e	9.2±7.9		9.2±7.9		8.2±7.9	
	<i>noise</i>	9.8±33.8		9.8±33.8		9.6±34.0	
	<i>baseline</i>	10.8±21.0		10.8±20.9		12.6±33.9	
	<i>c</i>	13.4±19.8		13.3±19.8		12.7±22.3	
In vivo data $\overline{RPC_K^\%}$ and FQN							
		32	64	32	64	32	64
		ave.	ave.	ave.	ave.	ave.	ave.
$\overline{RPC_{main}^\%}$		21	17	23	17	19	14
$\overline{RPC_{all}^\%}$		62	49	61	47	61	52
$FQN[0.6:4.1 \text{ (ppm)}]$		25.1	44.1	25	44.1	34.1	54.5
$FQN[1.95:4.1 \text{ (ppm)}]$		21	36.8	21	36.8	20.3	33.2

On the other hand, some major baseline distortions such as major lipid peaks or significant water residues led to some structured noise for both fitting software (Figure 3.4 C and G). Overall the spline smoothness estimation through the $mAIC$ seems to work robustly, even though for one spectrum out of the 15 the $mAIC$ criterion estimated a stiffer than necessary spline baseline (Figure 3.4 H).

Correlation plots show that ProFit-v3 seems to be slightly more accurate than LCModel in determining the true underlying metabolite concentration variance for most metabolites or shows an equal accuracy performance. Especially MM are estimated more accurately by ProFit-v3, while ml and NAAG were the metabolites which were more accurately estimated by LCmodel (Figure 3.7). While ProFit-v3 performed better regarding the all-over accuracy of concentration estimates, LCModel performs better with respect to the precision of concentration estimates for noisy and strongly baseline distorted data.

For the in vivo data set performance, the ProFit-v3 fitted spectra matches the measured spectra well, and the fit residuals show minimal noise structure, similar to LCModel fits (Figure 3.8). However, the $mAIC$ curves tend to be slightly different in the reproducibility tests. The achieved in vivo reproducibility of ProFit-v3 is slightly worse than for the LCModel fits. While the main metabolites are comparably accurate ($\overline{RPC_{main}^{\%}} = 17\%$ for LCModel vs $\overline{RPC_{main}^{\%}} = 19\%$ for ProFit-v3), a higher discrepancy in precision is seen for the other metabolites ($\overline{RPC_{all}^{\%}} = 49\%$ for LCModel and $\overline{RPC_{all}^{\%}} = 61\%$ for ProFit-v3). These $\overline{RPC_K^{\%}}$ results were similar for both the 32 averages and the 64 averages test-retest setups.

Chong et al.⁹⁹ showed through their FiTAID fitting algorithm, that complementary information from a series of data can improve the fitting. In this study, only slight improvements were observed, when using a cost function that combined the time domain and frequency domain. Interestingly, a further improvement of the performance was observed upon the addition of **weights**. The best performing cost function R_3 has proven useful both in the optimization of the fit parameters more accurately early on, when fewer metabolites were included, but also in later iterations. The cost function is induced to apply a more accurate minimization at the most prominent parts of the metabolite, or where multiple metabolites are present. Most likely, the **weights** help avoiding over-fitting

due to lipid contaminations in spectral ranges of lower interest for the in vivo data. The optimization with R_3 seems to be less influenced by these, as it can be deduced from the smaller $FQN[1.95: 4.1ppm]$ versus the higher $FQN[0.6: 4.1ppm]$, compared to R_1 and R_2 . The goal of the current software development of ProFit-v3 was to keep the accuracy of the fitted results as high as possible while also maintaining high precision. Hence, it was chosen not to increase the precision artificially at the detriment of accuracy, for example, through enforced stiffer baselines or tighter bounds.

The current software version has the limitation of being optimized for 9.4 T human brain data and does not include non-Voigt lineshapes. However, in future, the ProFit-v3 algorithm could be extended by non-parametric lineshape modelling, and it could also be tested on other data sets, particularly for more clinically relevant field strengths. The extension to different data sets will be more straightforward since all fitting iterations and boundaries are defined through a single Matlab file.

Including a fitting software into a fully integrated MRS analysis pipeline is highly desirable. This would provide a more user-friendly software and make MRS data analysis clinically more widely applicable. And while the ProFit-v3 is not yet better than LCModel (developed for 30+ years already), it comes close to its performance and it being open-source an integration into other software packages will be possible. Lastly, open-source code should allow easier modifications to fit non-proton spectra^{116,117}, or fitting downfield spectra¹⁰⁹.

3.2 Conclusion

In this study, the new fitting algorithm ProFit-v3 is presented and systematically evaluated for its accuracy and precision using both simulated and in vivo data. The systematic evaluation with simulated data includes all spectral parameters which influence in vivo spectra. Special care was given to spline baselines, which have shown to impact spectral fitting significantly in previous literature^{27,102,103}. While simulated spectra were used for evaluating the fitting accuracy and precision, the fitting precision was also tested on in vivo spectra. Additionally, three different cost functions were compared against each other.

Lastly, the accuracy and precision of the developed ProFit-v3 algorithm were compared to the LCModel software. ProFit-v3 was slightly more accurate but somewhat less precise than LCModel on the data sets used for evaluation.

~ PART B ~

**Novel spectral models – Quantification of downfield peaks and
macromolecules**

4 Novel spectral models – Downfield spectra

Text and figures in this chapter were adapted with minor modifications from our work previously published in (some of the supporting information material from these publications is not shown):

Borbath T*, Murali-Manohar S*, Wright AM, Henning A. “In vivo characterization of downfield peaks at 9.4 T: T₂ relaxation times, quantification, pH estimation, and assignments.” *Magnetic resonance in medicine*, 2020

Parts of this chapter were also published in:

Murali Manohar S, **Borbath T**, Wright A, Henning A. “Characterization of Downfield Resonances and their T₂ Relaxation Times in Human Brain at 9.4 T.” *Proc. of the 27th Annual Meeting of the International Society for Magnetic Resonance in Medicine*, 2019, Montréal, QC, Canada.

Murali Manohar S, **Borbath T**, Fichtner N, Giapitzakis I, Zaldivar D, Kreis R, Henning A. “Estimation of T₂ Relaxation Times of Downfield Peaks in Human Brain at 9.4 T.” *Proc. of the 26th Annual Meeting of the International Society for Magnetic Resonance in Medicine*, 2018, Paris, France

4.1 Introduction

Proton magnetic resonance spectroscopy (¹H-MRS) allows for non-invasive detection and quantification of metabolites. The upfield ¹H spectrum (between 0.0 and 4.7 ppm) is well characterized and understood¹¹⁸. However, the downfield ¹H spectrum (between 4.7 and 10.0 ppm) poses a significant challenge to the MRS community as most resonances in this ppm range are low in signal-to-noise ratio (SNR), severely overlapped, and/or fast exchanging¹². Therefore, it remains less explored and most peaks remain unassigned.

Increased SNR and better peak separation are prime advantages of ultra-high field strengths, and could help tackle the challenges posed by downfield spectra. Non-water saturation techniques, such as metabolite-cycling¹¹⁹, are crucial to handle the challenge posed by chemical compounds which exchange protons with water^{12,120}. Utilizing these two complementary approaches, exploring downfield spectra was feasible, and the spectral assignment of the downfield peaks, which is of interest, was achievable.

T₁ and T₂ relaxation times and exchange rates at different field strengths^{12,120,121} play a pivotal role in guiding spectral assignment of the downfield peaks. Downfield resonances

have shorter T_2 relaxation times at 7 T¹²² compared to the more widely studied upfield metabolites¹¹⁸. At 9.4 T, they are expected to have even shorter T_2 relaxation times due to the B_0 dependence of T_2 relaxation times¹²³. Since T_2 relaxation times are measured by observing the exponential decay in echo time (TE) series spectra, a sequence that allows short TEs was chosen in this work. A previous study¹² used metabolite-cycled (MC) stimulated echo acquisition mode (STEAM). However, due to the improved SNR of semiLASER¹⁰⁶ compared to STEAM, the MC-semiLASER was preferred in the current study design.

A previous study¹² at 9.4 T characterized the T_1 relaxation times and the chemical exchange rates of downfield resonances and reported several peaks that reflect a chemical exchange of protons with water in the downfield metabolite spectrum. Chemical exchange saturation transfer (CEST) experiments also exploit the mechanism of chemical exchange, and the major exchange effects in Z-spectra are observed in the downfield proton spectral range. There are many exchangeable amide protons with resonances between 5.0 and 10.0 ppm. The CEST amide proton transfer (APT) signal has shown improved contrast between healthy and diseased tissue in diseases such as cancer or stroke¹²⁴⁻¹²⁶. The CEST amide signal has, however, a strong dependence on both the concentration of mobile amide protons and pH as demonstrated by simulations¹²⁷ and on rat brain metastasis¹²⁸. While a recent study¹²⁵ on human breast cancer found that “the concentration of mobile amide protons is the main contributor to the observed APT signal”, compared to pH, the contributions of the amide-CEST contrast require further investigation.

CEST shows a significant increase in contrast at ultra-high field¹²⁹. Recent CEST research is moving towards a more quantitative analysis, such as CEST MR-Fingerprinting^{130,131} or Bloch fitting¹³², where knowledge about amide T_2 relaxation times and pH values are crucial. Hence, the characterization of downfield spectra through ¹H-MRS including the amide resonances and assessing the achievable pH sensitivity at ultra-high field will also benefit the CEST community.

In ¹H-MRS only homocarnosine (hCs)¹¹⁴ and histidine (hist)¹³³ are reported to have pH-sensitive chemical shifts for their downfield imidazole rings: for hCs, the hCs_{Im-C4} at ~7.08 ppm and hCs_{Im-C2} at ~8.08 ppm; and for hist, the hist_{Im-C4} at ~7.06 ppm and hist_{Im-C2} at

~7.79 ppm. Measuring pH variations is useful as diseases such as glioblastoma not only change the concentration of a few metabolites in the brain⁴, but also cause variations in the tissue pH as shown in ³¹P phosphorus spectroscopy¹³⁴. Therefore, assessing the pH sensitivity in vivo with ¹H-MRS is of interest.

The primary goal of this study was to measure the apparent T_2 relaxation times (T_2^{app}) of the downfield resonances at 9.4 T. While T_2 relaxation times have been reported in a previous study at 7 T¹²² for resonances that do not undergo chemical exchange; this study aims at quantifying T_2^{app} also for the downfield resonances with protons exchangeable with water (15 peaks in total). These T_2^{app} relaxation times were further corrected for the previously reported exchange rates¹². Additionally, estimated tissue concentrations of molecules resonating downfield are reported after applying relaxation corrections. The linewidth ($\Delta\nu_{1/2}$) after accounting for T_2^{app} relaxation times and micro- and macro-susceptibility effects of the downfield peaks might indicate J-coupling or overlapping resonances. This quantitative linewidth characterization helped analyze the degree of spectral overlap, which along with the concentrations aided spectral assignments.

4.2 Methods

4.2.1 Technical Description and Subjects

Measurements were performed on eleven healthy volunteers (eight males, three females, age: 26 ± 3 years) on a 9.4 T Magnetom whole-body MRI scanner (Siemens Healthineers, Erlangen, Germany) using a home-built proton coil with 8 transmit and 16 receive channels¹³⁵. Single voxel MRS data were acquired in a gray-matter (GM) rich region within the occipital lobe. The coil was driven in surface mode by driving the bottom three channels of the coil using an unbalanced three-way Wilkinson splitter as previously described for 2D FLASH imaging and spectroscopy acquisitions¹⁰⁶. The local ethics board approved the study, and all subjects gave written informed consent before the examination.

4.2.2 Data Acquisition

Spectroscopy voxels of $2 \times 2 \times 2 \text{ cm}^3$ were positioned in the occipital lobe in a GM-rich region, facilitated by gradient-echo images acquired using a 2D FLASH sequence (in-plane resolution: $0.7 \times 0.7 \text{ mm}^2$, 20 slices, 3 mm slice thickness, Flip angle: 25° , TE = 9 ms, TR = 378 ms, acquisition time: 2:03 min, field-of-view: $197 \times 197 \text{ mm}$) along axial and sagittal orientations. FAST(EST)MAP¹³⁶ was used for B_0 shimming with the shim volume set to 150% of the volume of interest, followed by a voxel-based transmit (B_1) power calibration^{137,138}.

T_2^{app} measurements of the downfield resonances were performed by acquiring an echo time series using MC semi-LASER¹⁰⁶ (excitation pulse duration: 1.2 ms, refocusing pulse duration: 3.5 ms, TR: 6 s, NEX: 96). The echo times were non-linearly spaced (TE: 24, 32, 40, 52, 60 ms). The increase in TE was spread evenly across all timings (between the excitation pulse, refocusing pulses and the start of the data sampling); while the timing between the second and third refocusing pulse was kept at the minimum system specified ramp time. The 8 kHz bandwidth of both the excitation pulse and the adiabatic-full-passage pulse resulted in a chemical shift displacement error (CSDE) of 5% per ppm. The transmit reference frequency (ν_{ref}) was set at 7.0 ppm, which led to a CSDE of -7.5% for the 8.50 ppm peak. A 16-step phase-cycling was implemented to avoid contributions from other unwanted coherence pathways¹³⁹.

In order to use the internal water as a reference for estimated tissue concentration calculations of molecules, water reference signals were acquired with the same semi-LASER sequence (TE: 24 ms, ν_{ref} : 4.7 ppm) without metabolite-cycling. This was done in order to avoid any influence of MC pulses on the water signal due to the asymmetry of the MC pulse and localization differences due to the difference of ν_{ref} of 2.4 ppm in the metabolite spectral measurements and the water frequency.

The data used in the current study was also used for the Murali-Manohar³⁰ up-field metabolite T_2 study.

High-resolution MP2RAGE⁵⁸ images ($0.6 \times 0.6 \times 0.6 \text{ mm}^3$) were acquired using the same coil by driving radio-frequency power to all eight channels for five out of the eleven volunteers. These images were then segmented using SPM12¹⁴⁰ into GM, white matter

(WM), and cerebrospinal fluid (CSF) tissue probability maps for use in quantification of the estimated tissue concentrations of molecules.

4.2.3 Data preprocessing

Raw data were analyzed with in-house written software in Matlab (version 2016a, MathWorks, Natick, MA). The metabolite MRS data were processed as described previously^{106,141}. The following steps were used in the processing of the raw data: 1) truncation of free induction decays at 250 ms to get a better SNR for subsequent processing steps; 2) frequency and phase alignment; 3) metabolite-cycling subtraction; 4) averaging; 5) zero-order phase and eddy current correction using the phase information from the MC water signal; 6) coil channel combination using a singular value decomposition method; 7) peak alignment in the frequency domain to 3.028 ppm; 8) residual water removal using a Hankel singular value decomposition (HSVD) method; 9) reversing in the frequency domain the downfield spectra to positive magnetization while keeping the upfield spectra also positive 10) residual water removal using an HSVD method for the potential water residuals not handled in step 8; and 11) truncation of free induction decays at 200 ms as the signal decays by that time.

The SNR of the NAA downfield resonance was calculated using the real part of the spectrum dividing the peak amplitude by the standard deviation of the noise between -4.0 and -1.0 ppm.

4.2.4 Fitting

The metabolite basis set was simulated in Vespa (v0.9.3)⁹⁸ using full quantum mechanical density matrix calculations for the semi-LASER sequence¹⁰⁷ including the actual excitation and adiabatic radio-frequency pulse shapes for all the TEs specified. The upfield metabolites were included in the basis set as described in Murali-Manohar et al.,³⁰ while simulating the ν_{ref} at 7.0 ppm. The simulated basis set consisted of following downfield (DF) peaks: N-acetyl aspartate (NAA)⁷, hCs¹¹⁴, and nicotinamide adenine dinucleotide (NAD⁺)¹²¹; and the simulated Voigt lines (CHSIMU) included: DF_{5.75} (5.75 ppm), DF_{5.97} (5.97 ppm), DF_{6.12} (6.12 ppm), DF_{6.83} (6.83 ppm), DF_{7.04} (7.04 ppm), DF_{7.30} (7.30 ppm), DF_{7.48} (7.48 ppm), DF_{8.18} (8.18 ppm), DF_{8.24} (8.24 ppm), DF_{8.37} (8.37 ppm),

NAA broad component (7.86 ppm), and DF_{8.49} (8.49 ppm). The chemical shifts were chosen based on the previous work by Fichtner et al.¹². These were further tailored by finding the maximum peak amplitudes in subject-wise summed spectra and matching the linewidths of LCModel to best describe the data of the TE series. After finding these settings from the across subjects summed spectra, these settings were used to fit all the per subject TE series. As most of the downfield peaks are unassigned, J-evolution effects were not considered. DKNTMN was set to 0.5 to enforce a flat spline baseline by LCModel. The fitting range was from 0.6 to 9.5 ppm to fit upfield and downfield metabolites simultaneously, and an LCModel ppm gap between 4.1 and 5.5 ppm was used to avoid baseline effects from the water residual. The upfield portion of spectra was used to constrain the LCModel software by providing metabolite lineshapes. None of the upfield and downfield components of the same metabolites were linked, they all were fitted independently: for instance the NAA aspartyl moiety was split into its upfield and downfield components due to very different T_2^{app} relaxation times and exchange effects. The chemical shifts, linewidth settings, and all other LCModel parameters are described in Appendix B.

Experimentally acquired TE-specific upfield macromolecular spectra³⁰ were included in the basis set, but the downfield part of the spectra was set to zero.

4.2.5 pH estimation

The chemical shift of most peaks in metabolite spectra are sensitive to pH changes, however, in ¹H-MRS only hCs and hist have been shown to have measurable sensitivities for physiological pH variations^{114,133}. The effects of pH in MRS are described by the derived form of the Henderson-Hasselbalch equation for fast exchanging acid/base systems, where the observed chemical shift (δ_{pH}) is a weighted average of the conjugated acid (δ_{acid}) and base (δ_{base}) endpoints, and pK_a is the logarithm of the acid dissociation constant:

$$pH = pK_a + \log \frac{\delta_{pH} - \delta_{acid}}{\delta_{base} - \delta_{pH}} \quad \text{Eq. 4.1}$$

Rewriting the equation, the chemical shift can be calculated for any given pH by:

$$\delta_{pH} = \frac{10^{pH-pK_a} * \delta_{base} + \delta_{acid}}{1 + 10^{pH-pK_a}} \quad \text{Eq. 4.2}$$

Table 4.1: Coefficients of the derived form of the Henderson-Hasselbalch equation for the two metabolites in ¹H-MRS sensitive to pH in the physiological range.

	hCs ¹¹⁴		hist ¹³³	
	Im C4 7.08 resonance	Im C2 8.08 resonance	Im C4 7.06 resonance	Im C2 7.79 resonance
pKa	6.86	6.86	6.127	6.114
δ_{acid} (ppm)	7.27	8.58	7.39	8.651
δ_{base} (ppm)	6.92	7.68	7.029	7.719

The coefficients of these equations for hCs and hist are summarized in Table 4.1. Basis sets of hCs were created using Eq. 4.2 for a pH sweep varying from 6.90 to 7.15 in steps of 0.01 (Figure 4.1). The plots show that the hCs_{Im-C2} peak at 8.08 ppm is the most sensitive to pH changes and that the imidazole peaks should be treated together accounting jointly for the pH value since the peaks are differently sensitive to pH changes. The previously described upfield and downfield metabolites, including the hCs imidazole peaks (ignoring the upfield GABA moiety of hCs), were used to create a combined upfield and downfield basis set specific to each pH value and TE.

Because pH differences between subjects are possible, each subject's set of spectra was fit with all basis sets of the pH sweep. LCModel was constrained to not shift the hCs peaks by using the following parameters: *nsdsh* = 1; *chsdsh*(1) = 'hCs'; *alsdsh*(1) = 0.0005. After this fitting iteration, the pH value for each subject (pH_y) was estimated by finding the pH value for which the concentration of hCs [*conc*_{hCs}(*y*, *pH*)] was maximal:

$$pH_y = \underset{pH=6.90,6.91,\dots,7.15}{\operatorname{argmax}} [conc_{hCs}(y, pH)], \text{ with } y = 1, \dots, 11 \quad \text{Eq. 4.3}$$

where *y* represents the individual subject.

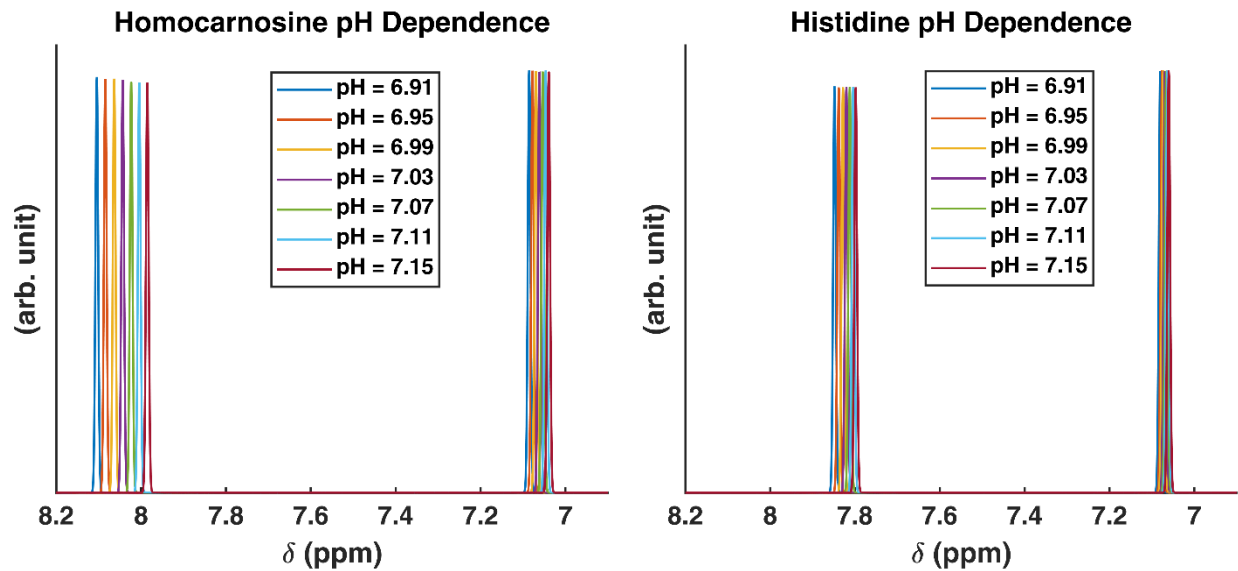


Figure 4.1: A sample of the pH sweep (steps of 0.04) of the homocarnosine (left) and histidine (right) basis sets. The δ symbol is used as the abbreviation for the chemical shift.

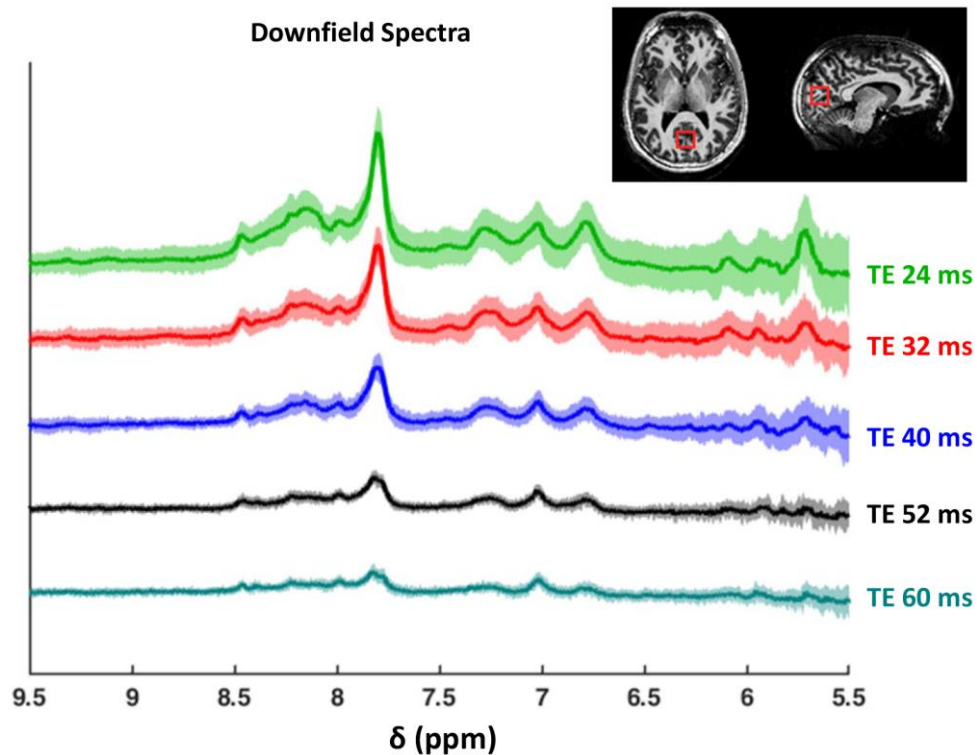


Figure 4.2: The downfield metabolite spectra are shown for the echo time (TE) series (TE = 24, 32, 40, 52 and 60 ms). The solid lines show the mean spectra and the shaded areas indicate the standard deviation between subjects. The inlay shows the voxel placement on the MRI image.

The hCs imidazole resonance at 7.08 ppm (hCs_{Im-C4}) has an overlap with a fast decaying component, named DF_{7.04}, observable both visually in spectra (Figure 4.2, Figure 4.3) and reported previously^{12,122}. To avoid the influence of this DF_{7.04} peak in the estimation of the pH, the peak was excluded from the basis set in the pH estimation step. TE = 40 ms was chosen for the estimation of the pH_y following visual analysis, observing the longer relaxation times of hCs compared to other peaks, as also reported previously¹²², but also considering the loss in SNR at later TEs.

After this pH estimation step, the entire TE series for each subject was refitted with the basis set using the calculated subject-specific pH_y, while also including the previously excluded DF_{7.04} peak.

4.2.6 T₂ relaxation

The LCModel fitted concentrations of the molecules resonating downfield were fit to a mono-exponential decay across the TE series to measure the T_2^{app} . The goodness of the exponential fits was evaluated by the mean coefficient of determination (R²). Relaxation time estimates with R² < 0.50 were discarded. Because some peaks exchange with water¹² at an exchange rate k , the T_2^{app} were corrected to get the exchange rate corrected T₂ relaxation time (T_2^{corr})¹³² such that:

$$\frac{1}{T_2^{corr}} = \frac{1}{T_2^{app}} - k \quad \text{Eq. 4.4}$$

4.2.7 Linewidth calculations

The full-width-half-maxima ($\Delta\nu_{1/2}$) were measured by extracting the fitted lineshapes of the peaks from the .coord files of the LCModel quantification. Contribution of T₂ relaxation and exchange to $\Delta\nu_{1/2}$ were calculated according to $(\pi T_2^{app})^{-1}$, using the calculated T_2^{app} values.

The residual linewidth was defined as:

$$\Delta\nu_{residual} = \Delta\nu_{1/2} - (\pi T_2^{app})^{-1} - \Delta\nu_{micro,macro} \quad \text{Eq. 4.5}$$

The B₀ component was calculated from the total creatine CH₃ resonance [tCr(CH₃)] as: $\Delta\nu_{micro,macro} = \Delta\nu_{1/2} - (\pi T_2^{app})^{-1} \approx \Delta\nu_{micro} + \Delta\nu_{macro}$ respectively. $\Delta\nu_{micro}$ and $\Delta\nu_{macro}$ represent the micro- and macro-susceptibility, respectively. Please find a more comprehensive discussion in subchapter 6.1.1.

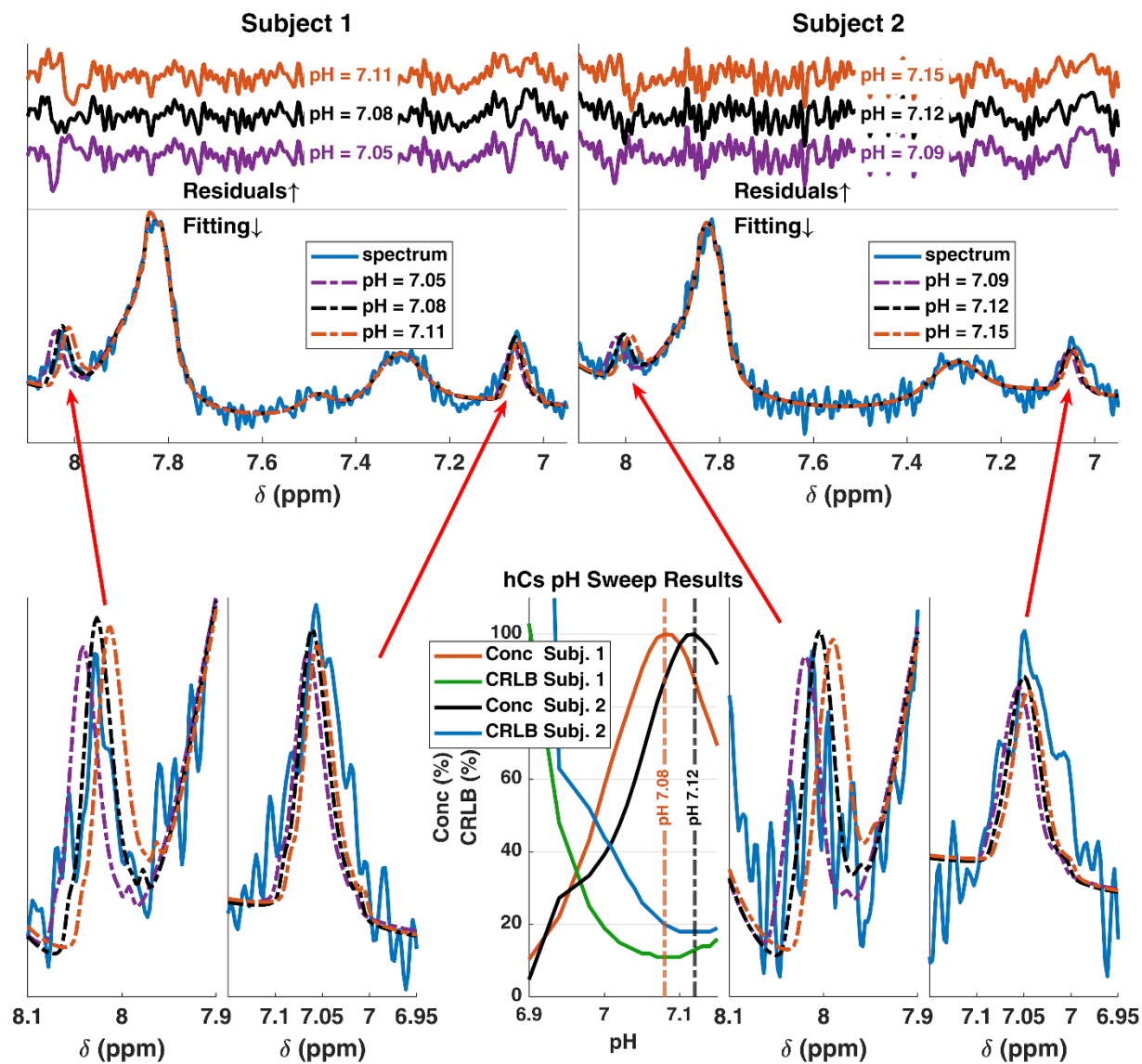


Figure 4.3: Two sample subjects are shown with the pH estimation fits, with the chosen $TE = 40$ ms spectra. The black dashed lines show the calculated pH value for the given subject, with the dashed purple and orange lines showing the fits for a pH value smaller and bigger by 0.03 respectively. The fit residuals for the three different pH fits are shown above. The imidazole peaks sensitive to pH are shown also zoomed in. The fitted concentrations over the pH sweep are also shown in the homocarnosine (hCs) pH Sweep Results. The concentrations show a parabolic curve, with the Cramer-Rao-Lower-Bounds (CRLBs) as calculated by LCMoDel decreasing accordingly. Concentrations are given in percent, being normalized to the maximal fitted value. Mind also the missing $DF_{7.04}$ peak under the hCs_{Im-C4} peak.

4.2.8 Concentrations

Quantification of the fitted concentrations was done as described in subchapter 1.6 using the TE 24 ms spectra. The obtained tissue compositions used for the quantification corrections were GM: 67.84 ± 5.14 %, WM: 27.96 ± 4.92 %, and CSF: 4.18 ± 2.49 %. Downfield resonances T_1 and T_2^{app} corrections were performed using the values from Fichtner et al.,¹² and from this work, respectively. Relaxation times of water in different tissue types at 9.4 T were taken from Hagberg et al.,⁵⁸ see Table 2.1. The concentrations for the unassigned peaks are reported as proton densities since the number of contributing protons is not known.

4.3 Results

Downfield spectra from all subjects displayed good spectral quality with the NAA downfield SNR = 59 ± 14 for TE = 24 ms; SNR = 12 ± 4 for TE = 60 ms, shimming achieved a linewidth of unsuppressed water of 17.9 ± 1.5 Hz.

Figure 4.2 shows the TE series of downfield spectra. The shaded area represents the standard deviation across all subjects indicating the reproducibility. No data sets were excluded from the study.

4.3.1 Fitting

Sweeping the pH from 6.90 to 7.15 yielded chemical shifts for hCs_{Im-C4} ranging from 7.087 to 7.039 ppm, and hCs_{Im-C2} ranging from 8.109 to 7.985 ppm (Figure 4.1).

Adjusting the pH value of hCs subject-wise resulted in improved spectral fitting (Figure 4.3). Visually notable differences were observed for pH changes of 0.03 and were especially pronounced on the more pH-sensitive hCs_{Im-C2} . Plotting the resulting concentrations across the pH range provided parabolic curves, with each subject having a well-defined maximum, defining the calculated pH value (pH_y), please see “hCs pH Sweep Results” (Figure 4.3). The Cramer-Rao-Lower-Bounds (CRLB) show the opposite trend, also because the noise in LCMoel was calculated from the fit residue.

The estimated pH_y values are reported for each subject in Table 4.2. While only the results of the TE = 40 ms were used in the further fitting, a good agreement was observed

between the calculated pH value per subject pH_y and the mean calculated pH value. All the estimated pH values are reported with a standard deviation of 0.02 or lower.

Table 4.2: pH values calculated in the pH estimation step, as described in the Methods under pH estimation section 4.2.5. The pH values are summarized for each subject and each TE. The chosen values for the follow-up fitting step were the values in the TE 40 ms column. The mean values across all the TEs for each subject are closely matching the chosen pH_y value.

Calculated pH value/Subject:	TE 24 ms	TE 32 ms	TE 40 ms (pH_y values)	TE 52 ms	TE 60 ms	mean \pm std estimated pH
Subject 1	7.10	7.09	7.09	7.07	7.12	7.09 \pm 0.02
Subject 2	7.08	7.08	7.10	7.10	7.09	7.09 \pm 0.01
Subject 3	7.09	7.07	7.09	7.11	7.10	7.09 \pm 0.01
Subject 4	7.09	7.08	7.11	7.12	7.12	7.10 \pm 0.02
Subject 5	7.12	7.08	7.11	7.11	7.10	7.10 \pm 0.02
Subject 6	7.13	7.12	7.12	7.14	7.15	7.13 \pm 0.01
Subject 7	7.10	7.08	7.07	7.10	7.11	7.09 \pm 0.02
Subject 8	7.08	7.07	7.10	7.09	7.08	7.08 \pm 0.01
Subject 9	7.10	7.10	7.07	7.10	7.09	7.09 \pm 0.01
Subject 10	7.07	7.09	7.07	7.07	7.07	7.07 \pm 0.01
Subject 11	7.08	7.08	7.08	7.07	7.03	7.07 \pm 0.02

Figure 4.4 shows a representative downfield spectrum acquired with TE = 24 ms from 5.5 to 9.5 ppm, with minimum fit residuals. A similar good quality fit of spectra was achieved for all subjects as seen in the representative TE series spectra (results not shown), however with some structured negative phase noise observed at later TEs, which could suggest some J-evolution effects. Figure 1.10 also shows the fit of the entire spectrum ranging from 0.5 to 9.5 ppm as the upfield and the downfield resonances were fit

simultaneously for all datasets. Mind, that the upfield metabolites were chosen by splitting them into moieties, where larger differences in T_2^{app} could be expected, as described in Murali-Manohar et al³⁰. None of the upfield metabolite basis vectors has peaks in the downfield: peaks of creatine, phosphocreatine, glutamine, glutathione were assumed to have decayed to allow a non-biased fitting. At the same time, the aspartate moiety of NAA was split into the upfield and downfield parts. Similarly, the upfield GABA moiety of hCs was not considered. The fitted upfield singlet metabolites showed Lorentzian-like lineshapes without distortions.

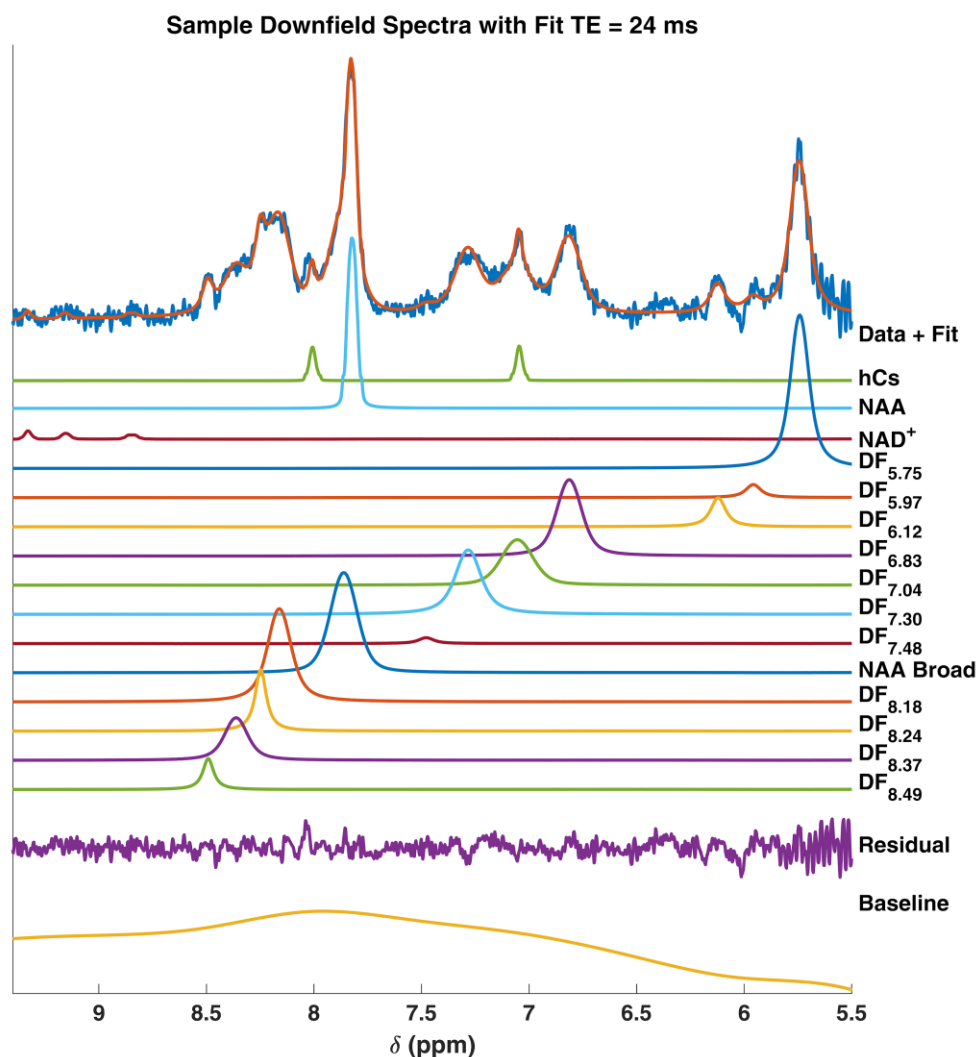


Figure 4.4: Sample spectra with the fitted molecules at TE = 24 ms are shown: hCs at the calculated pH value, N-acetyl aspartate (NAA), nicotinamide adenine dinucleotide (NAD⁺) and the simulated Voigt lines for the unassigned peaks.

4.3.2 T_2 relaxation

Figure 4.5 shows the exponential decay curves of the downfield metabolites. The calculated T_2^{app} of the downfield resonances in decreasing order are shown in the box plots of Figure 4.6. T_2^{app} of the downfield peaks were between ~16 and ~32 ms, except the T_2^{app} of hCs was measured to be ~50 ms.

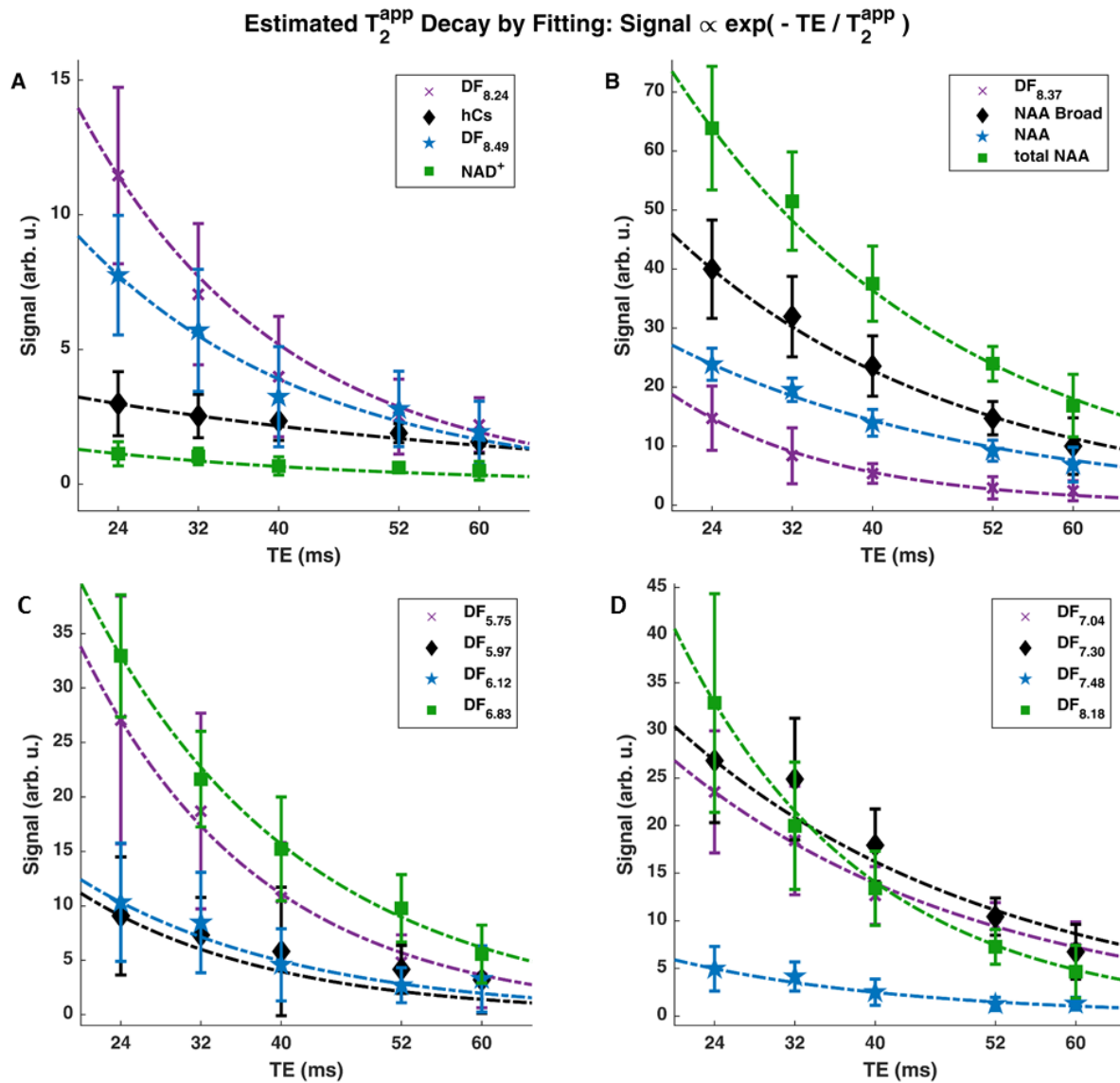


Figure 4.5: The estimated T_2^{app} decay curves are shown for eight of the fitted metabolite peaks. The error bars show the fitted concentrations in arbitrary units for the different subjects at all five TEs. The T_2^{app} were estimated by fitting the following signal equation: $\text{Signal} \propto \exp(-TE / T_2^{app})$. The dashed lines show the decay curve for the estimated mean T_2^{app} value (See also Table 4.3).

Table 4.3 gives the value of T_2^{app} with each R^2 (after the $R^2 < 0.50$ exclusion criterion). The R^2 values are all above 0.75 showing the goodness of the exponential fits to individual datasets. NAD⁺ fits were excluded due to low reliability; while from the across subjects summed spectra, the T_2^{app} of NAD⁺ was estimated as 30.3 ms ($R^2 = 0.86$). The calculated T_2^{corr} values are longer and closer to each other than T_2^{app} , and lie mostly between 21 and 30 ms (Table 4.3).

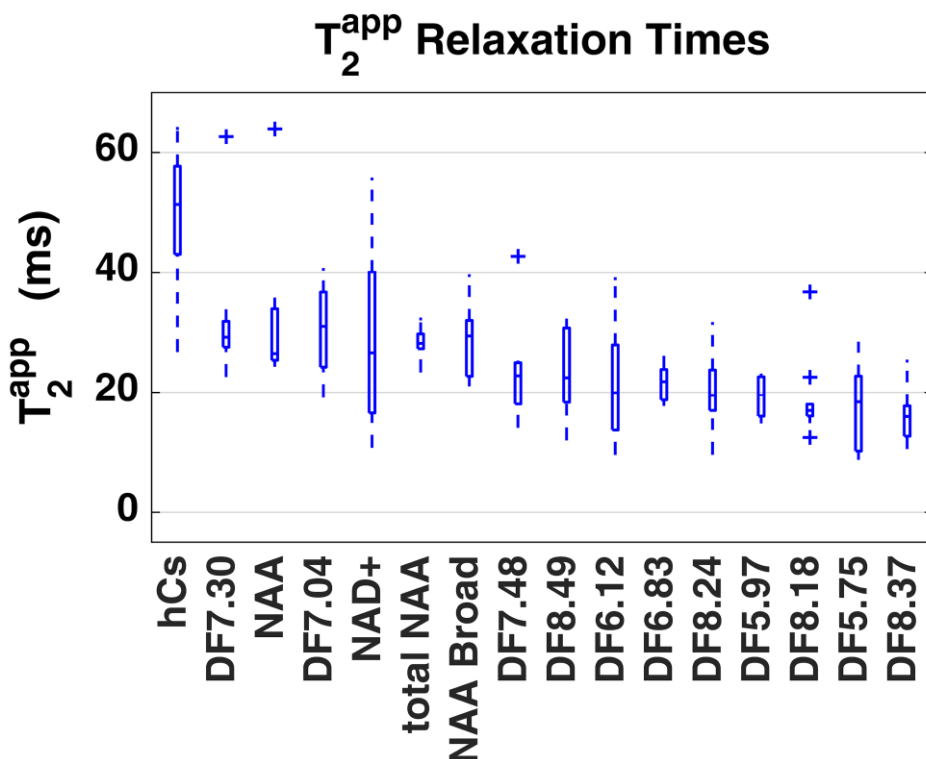


Figure 4.6: Box plots of the measured T_2^{app} relaxation times of the downfield peaks are shown in decreasing order. The longest relaxation time was measured for hCs of around 50 ms, followed by NAA with around 32 ms. In contrast, all other simulated Voigt line peaks have relaxation times between 30 and 15 ms.

4.3.3 Linewidth calculations

$\Delta\nu_{1/2}$ of the named downfield metabolites NAA and hCs were the lowest with 29.3 and 17.6 Hz, respectively (Table 4.3). Small $\Delta\nu_{1/2}$ were also measured for DF_{8.24} and DF_{8.49} with both being around 29.0 Hz, while all other resonances were found to be between approximately 40 and 80 Hz (Table 4.3). The T_2^{app} contributions to the linewidths $[(\pi T_2^{app})^{-1}]$ range between 6 and 19 Hz for the downfield peaks (Figure 4.7).

Table 4.3: Results for the downfield peaks, summarizing T_2^{app} , R^2 fit quality, calculated linewidth $\Delta\nu_{1/2}$, and mmol/kg concentrations with and without peak specific T_2^{app} correction. Exchange rate corrected T_2^{corr} values are reported only for resonances with measured exchange rates¹². Find concentrations in (mmol/L) in Table 4.4. Values are presented as mean \pm standard deviation.

	T_2^{app} (ms)	R^2	T_2^{corr} (ms)	k (s ⁻¹) [Fichtner et al. ¹²]	$\Delta\nu_{1/2}$ (Hz)	Conc. \pm std with T_2^{app} correction (mmol/kg)	Conc. \pm std w/o T_2^{app} correction (mmol/kg)
DF _{5.75}	17.9 \pm 6.7	0.85 \pm 0.13	20.4 \pm 6.7	6.76 \pm 1.59	52.5 \pm 4.0	9.83 \pm 5.60	3.06 \pm 1.74
DF _{5.97}	19.3 \pm 3.3 ^a	0.83 \pm 0.10	-	-	40.4 \pm 0.5	1.67 \pm 0.87	1.07 \pm 0.56
DF _{6.12}	20.4 \pm 9.9 ^a	0.90 \pm 0.11	-	-	40.5 \pm 0.5	2.36 \pm 0.89	0.98 \pm 0.37
DF _{6.83}	21.5 \pm 2.6	0.94 \pm 0.08	22.7 \pm 2.6	2.34 \pm 0.44	69.6 \pm 2.1	11.72 \pm 2.22	3.90 \pm 0.74
DF _{7.04}	30.8 \pm 7.1	0.85 \pm 0.07	-	-	81.2 \pm 0.7	6.08 \pm 1.86	2.80 \pm 0.86
DF _{7.30}	31.9 \pm 10.2	0.90 \pm 0.05	-	-	63.5 \pm 2.3	6.76 \pm 1.30	3.01 \pm 0.58
DF _{7.48}	23.6 \pm 7.6	0.84 \pm 0.13	-	-	40.9 \pm 0.7	1.24 \pm 0.48	0.44 \pm 0.17
DF _{8.18}	18.8 \pm 6.4	0.97 \pm 0.05	22.8 \pm 6.4	9.32 \pm 0.91	61.4 \pm 0.8	15.94 \pm 5.44	3.88 \pm 1.32
DF _{8.24}	20.1 \pm 5.7	0.94 \pm 0.04	24.8 \pm 5.7	9.32 \pm 0.91	29.0 \pm 0.3	4.91 \pm 0.57	1.45 \pm 0.17
DF _{8.37}	16.3 \pm 4.3	0.90 \pm 0.12	21.1 \pm 4.3	13.8 \pm 0.79	60.3 \pm 1.5	8.23 \pm 2.87	1.83 \pm 0.64
DF _{8.49}	23.3 \pm 6.2	0.81 \pm 0.08	25.2 \pm 6.2	3.31 \pm 0.06	28.6 \pm 0.2	2.43 \pm 0.47	0.83 \pm 0.16
hCs	48.9 \pm 11.0 ^b	0.78 \pm 0.14	-	-	17.6 \pm 2.0	0.58 \pm 0.31	0.38 \pm 0.20
NAA Broad	28.4 \pm 5.5	0.95 \pm 0.07	29.0 \pm 5.5	0.74 \pm 0.23	70.9 \pm 1.1	4.16 \pm 1.45	1.83 \pm 0.64
NAA	31.6 \pm 11.0	0.96 \pm 0.04	32.3 \pm 11.0	0.74 \pm 0.23	29.5 \pm 4.7	7.02 \pm 0.42	2.88 \pm 0.17
total NAA	28.4 \pm 2.5	0.98 \pm 0.02	29.0 \pm 2.5	0.74 \pm 0.23	-	17.47 \pm 2.25	7.45 \pm 0.96

^a While for most metabolites T_2^{app} of maximally two subjects were eliminated due to unreliable fits ($R^2 < 0.50$), measurement imprecisions were encountered for peaks denoted with a. The T_2^{app} of these peaks when averaging spectra across all subjects was: DF_{5.97} = 37.5 ms, DF_{6.12} = 23.9 ms.

^b hCs has some degree of uncertainty in terms of combined factor of high standard deviation in both T_2^{app} and R^2 . The worst two R^2 fits passing the $R^2 > 0.5$ criteria were: T_2^{app} = 64.2 ms and 52.5 ms with R^2 of 0.58 and 0.61, respectively.

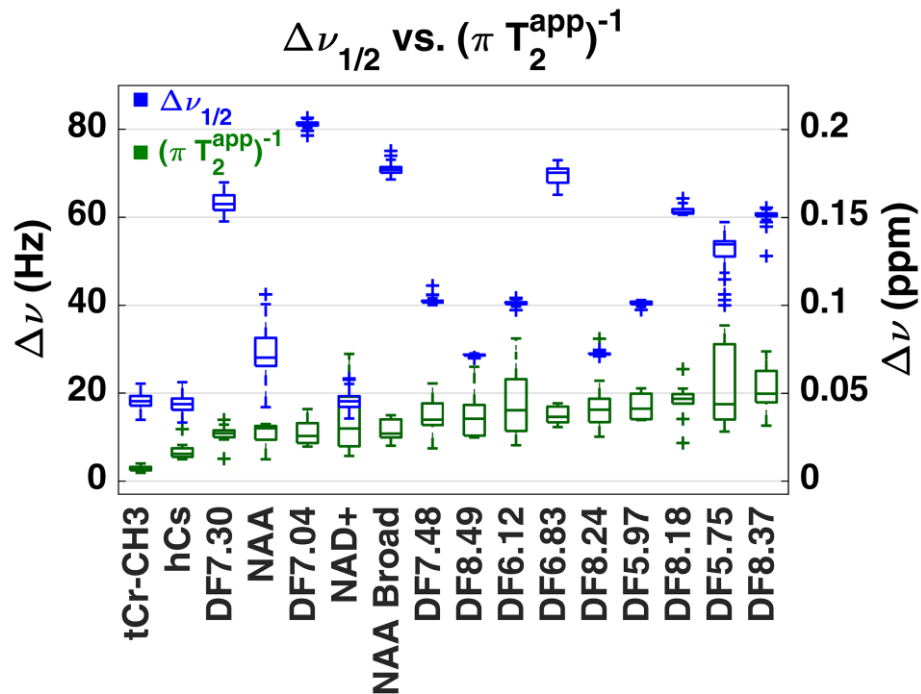


Figure 4.7: Box plots in blue show the measured $\Delta\nu_{1/2}$ of the downfield peaks and the $t\text{Cr}(\text{CH}_3)$ singlet. The $\Delta\nu_{1/2}$ of $t\text{Cr}(\text{CH}_3)$ was 18.2 ± 2.0 Hz. The $\Delta\nu_{1/2}$ of $h\text{Cs}$ is calculated on the $h\text{Cs}_{1m-C2}$ peak. Green boxplots show the $(\pi T_2^{\text{app}})^{-1}$, measuring 6.0 Hz for $h\text{Cs}$ up to 19.0 Hz for $\text{DF}_{8.37}$.

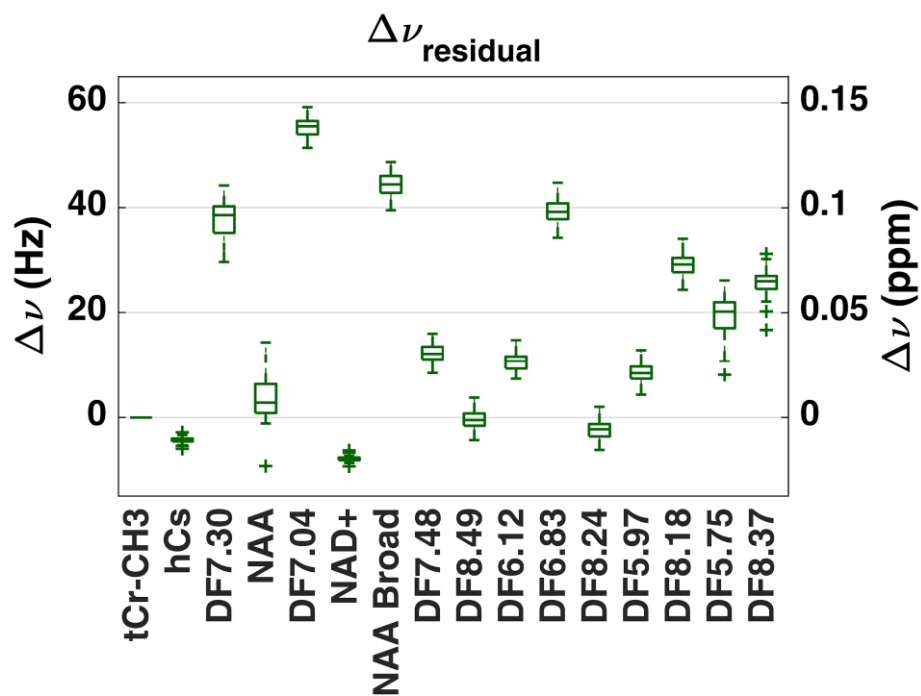


Figure 4.8: The $\Delta\nu_{\text{residual}}$ box plots are shown for all the downfield metabolites, where the $\Delta\nu_{\text{micro,macro}}$ was calculated from the $t\text{Cr}(\text{CH}_3)$ peak.

$\Delta\nu_{\text{residual}}$ is shown in Figure 4.8. This was calculated using $\Delta\nu_{\text{micro,macro}}$ from $t\text{Cr}(\text{CH}_3)$ as ~ 15.4 Hz. The simulated metabolite peaks have a $\Delta\nu_{\text{residual}}$ close to zero, with minor differences reflecting possible measurement errors or J-coupling effects, in particular: hCs = -3.7 Hz, NAA = 2.9 Hz. The simulated Voigt lines of DF_{8.49} and DF_{8.24} with $\Delta\nu_{\text{residual}}$ = -0.4 Hz, and -1.6 Hz, respectively suggests that these peaks originate from a single metabolite resonating at that frequency. Comparably small $\Delta\nu_{\text{residual}}$ are also observed for DF_{7.48}, DF_{6.12}, DF_{5.97} and are 10.0 – 12.0 Hz. Somewhat smaller $\Delta\nu_{\text{residual}}$ have DF_{5.75} with 20.0 Hz, DF_{8.37} with 26.0 Hz, whereas all other simulated downfield Voigt lines have $\Delta\nu_{\text{residual}}$ higher than 30.0 Hz.

4.3.4 Concentrations

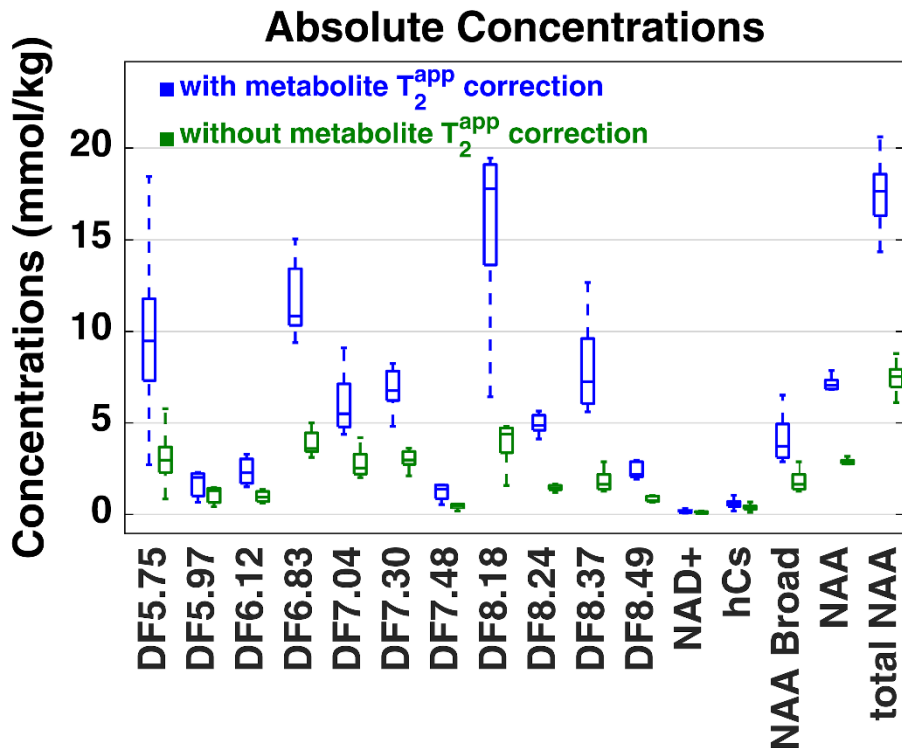


Figure 4.9: Box plots of the concentration in mmol/kg of the downfield metabolites. Concentrations are given both with and without correcting for metabolite T_2^{app} relaxation time.

The estimated tissue concentrations of the downfield metabolites and the proton density of the unassigned downfield peaks in millimolal are given in Figure 4.9 and Table 4.3 with and without T_2^{app} correction. All concentrations are corrected for tissue fractions, water relaxation times (T_1 and T_2) and downfield T_1 relaxation times (see subchapter 1.6 and

Table 2.1). For ease of comparison with the previous literature values, the estimated tissue concentration values in millimoles per tissue volume in a liter (mmol/L) are reported in Table 4.4. Note, the concentrations / proton densities were measured for only five out of the eleven volunteers, for which the anatomical images for tissue segmentation were also acquired.

Table 4.4: Concentrations of the downfield metabolites reported in mmol/L with and without metabolite specific T_2^{app} in comparison with previous literature. All concentrations are given as mean \pm standard deviation.

	Concentration with T_2^{app} correction (mmol/L)	Concentration w/o T_2^{app} correction (mmol/L)	Fichtner 9.4 T MRM 2018 ¹² (mmol/L)	Fichtner 7 T MRM 2017 ¹²² (mmol/L)	Other literature (mmol/L)
DF _{5.75}	7.25 \pm 4.14	2.26 \pm 1.29	4.58 \pm 1.12	0.53 \pm 0.43	-
DF _{5.97}	1.23 \pm 0.64	0.79 \pm 0.41	1.25 \pm 0.73	0.47 \pm 0.20	-
DF _{6.12}	1.74 \pm 0.63	0.72 \pm 0.26	1.21 \pm 0.74	0.47 \pm (N/A)	-
DF _{6.83}	8.64 \pm 1.67	2.88 \pm 0.56	2.87 \pm 0.68	3.72 \pm 0.36	-
DF _{7.04}	4.47 \pm 1.34	2.06 \pm 0.62	1.96 \pm 1.14	3.35 \pm 0.48	-
DF _{7.30}	4.98 \pm 0.98	2.22 \pm 0.44	1.94 \pm 0.28	4.81 \pm 0.69	-
DF _{7.48}	0.91 \pm 0.35	0.32 \pm 0.13	0.56 \pm 0.21	-	-
DF _{8.18}	11.73 \pm 3.97	2.86 \pm 0.97	4.16 \pm 0.45	-	-
DF _{8.24}	3.62 \pm 0.42	1.07 \pm 0.12	-	9.02 \pm 1.65	-
DF _{8.37}	6.07 \pm 2.13	1.35 \pm 0.47	0.92 \pm 0.32	-	-
DF _{8.49}	1.79 \pm 0.34	0.61 \pm 0.11	0.89 \pm 0.32	-	-
hCs	0.43 \pm 0.23	0.28 \pm 0.15	1.02 \pm 0.39	0.39 \pm 0.11	0.3-1.6 Petroff ¹⁴²
NAA Broad	3.06 \pm 1.08	1.35 \pm 0.47	4.91 \pm 0.79	3.02 \pm 0.59	10-13 Murali et al. ³⁰ Upfield NAA
NAA	5.17 \pm 0.28	2.12 \pm 0.12	10.52 \pm 1.16	10.5 \pm 1.0	
total NAA	12.87 \pm 1.64	5.49 \pm 0.70	15.43 \pm 1.16	13.52 \pm 1.0	

4.1 Discussion

T_2^{app} relaxation times and concentrations of downfield metabolites and proton density of downfield peaks are reported in the human brain at 9.4 T in this work. Also, $\Delta\nu_{1/2}$ of these peaks were quantitatively analyzed by calculating T_2^{app} relaxation time contributions and micro- and macro- susceptibility components. Characterizing these attributes help to understand the degree of overlap between components in the downfield proton spectrum. Furthermore, concentrations of the downfield molecules in the occipital lobe are reported both in mmol/kg and mmol/L.

4.1.1 Spectral Quality

A previous study at 9.4 T required a larger voxel size (2.0×2.0×3.0 cm³) for 96 averages in order to achieve good SNR since the study used MC-STEAM localization¹². However, the current study used an MC-semiLASER sequence, which resulted in good SNR from a smaller voxel (2×2×2 cm³). As expected, the SNR of the peaks in Figure 4.2 decreased as the signal decayed exponentially with increasing TEs. At TE = 60 ms, almost all of the peak signals had completely decayed except NAA and hCs. The shaded region in Figure 4.2 represents the standard deviation between all the subjects, which is larger closer to the water resonance, probably originating from water residuals. Using metabolite-cycling, which is a non-water saturation technique, made it possible to observe peaks such as DF_{5.75}, DF_{6.83}, DF_{8.18}, DF_{8.24}, DF_{8.37}, and DF_{8.49} with reported exchangeable protons¹².

4.1.2 Fitting

For fitting purposes, the decision was taken to fit the full upfield spectrum in addition to the downfield spectrum. The LCModel software uses “for initial referencing and phasing ... major landmarks”, especially singlets in the “Preliminary Analysis”¹⁵. To get this lineshape-information, in an initial trial, only an upfield singlet was used, but this information proved to be insufficient. One singlet from the upfield range was likely inadequate because all upfield singlets are overlapped to some extent with macromolecular contributions. The fitting results showed distorted lineshapes in some spectra (results not shown). Hence, the entire upfield spectrum was included to provide as much information as possible to improve LCModel quantification.

The residuals from spectral fitting were minimal with some structured noise and negative phase appearing at later TEs, which could suggest some J-evolution effects. Acquiring more averages for later TEs would have resulted not only in better fitting and therefore more certain T_2^{app} ; but also would have helped confirm potential J-evolution effects. However, to have feasible scan durations, a higher number of averages were not acquired for later TEs in this study.

4.1.3 pH estimation

Generally, a neutral pH value is assumed and used among all subjects. In this work, the estimation of pH for each subject proved useful in eliminating structured noise commonly present in fit residues. The estimated pH values were observed to be consistent among the different TEs for all subjects (Table 4.2). The reported pH values (pH = 7.07 to 7.12) are comparable to the pH = 7.06 of hCs reported by Rothman et al.,¹¹⁴ measured in epileptic patients under vigabatrin treatment. pH measurements using ^{31}P MRS estimate the pH value using the inorganic phosphate peak¹⁴³ and report intracellular pH values of 6.96 - 6.98 and extracellular pH values of 7.35 - 7.45. ^{31}P MRS imaging measurements indicate a spatially homogeneous pH of around 7.0 throughout the brain¹³⁴. As the CSF and extracellular concentrations of hCs are “several orders of magnitude below the level of detection using in vivo spectroscopy”¹¹⁴, the measured pH value of hCs primarily reflects the intracellular pH. The differences observed in the measured pH from ^{31}P MRS could originate from different compartments (neurons, glia) or a possibly imprecise pK_a value for either of the Henderson-Hasselbalch equations. Nevertheless, differences of the fit residual for changes of 0.03 in pH values were observable, and hence pH changes of up to 0.2 as reported for gliomas¹³⁴ could be quantifiable.

4.1.4 T_2 relaxation

The measured T_2^{app} follow the B_0 dependence, in comparison with the previous literature¹²². The T_2^{app} could be reliably estimated with the exclusion of at most two subjects per peak due to a poor fit ($R^2 < 0.50$), except for DF_{5.97}, DF_{6.12}, NAD⁺ and hCs. The DF_{5.97} and DF_{6.12} have low peak intensities and due to the close proximity of the water peak some residual artifacts disrupt a reliable T_2^{app} estimation. Hence, for both peaks the

T_2^{app} are also reported for the across subjects summed spectra in the Table 4.3 caption. The T_2^{app} of NAD⁺ estimated from the across subjects summed spectra was 30.3 ms, which is much shorter than the times reported by de Graaf and Behar¹²¹ (60 ± 13 ms) in the rat brain at 11.7 T. For the hCs peak, three subjects were excluded from the reported T_2^{app} values, however, no correlation was found between these excluded subjects and the estimated pH value or voxel GM content.

Of the measured T_2^{app} , the peaks reported previously to have a fast exchange with water¹² are also among the fastest T_2^{app} decaying peaks: DF_{5.75}, DF_{8.18}, DF_{8.37}. These same resonances also decayed the fastest in TE series spectra (starting at TE = 5 ms) acquired in the rat brain at 9.4 T¹⁴⁴. Furthermore, Liu et al.¹⁴⁵ reported a T₂ relaxation time of 22.7 ms and 28.5 ms in WM and GM, respectively at 7 T for the 3.5 ppm CEST peak. This 3.5 ppm CEST peak corresponds to the frequency range between 8.0 - 8.4 ppm in ¹H-MRS considering that the CEST saturation pulse had a bandwidth of 0.4 ppm. The calculated T₂ values by Liu et al., match closely the T_2^{corr} values of this study (21 to 30 ms), if the B₀ dependence is considered. T_2^{app} and T_2^{corr} of the unnamed downfield peaks from the current work have the same order of magnitude as the macromolecular peaks: 14 to 36 ms in the upfield spectrum³⁰.

The measured T_2^{app} values are specific to the occipital lobe at 9.4 T and the semiLASER sequence used. While the corrections applied for concentrations in this work are intrinsic to the semiLASER sequence, the contributions of the Carr-Purcell effect¹⁴⁶ to T_2^{app} should be investigated in future work.

4.1.5 Linewidth calculations

$\Delta\nu_{1/2}$ is composed of two components namely the static B₀ field inhomogeneity, which is composed of micro- and macro- susceptibility effects, and T_2^{app} . While the B₀ component is the same across all metabolites in a spectrum, the T_2^{app} contribution is specific to each peak depending on how quickly or slowly it decays¹²³. Figure 4.7 shows $\Delta\nu_{1/2}$ as well as the contribution to the linewidth from the T_2^{app} [$(\pi T_2^{app})^{-1}$] calculated specific to each peak. $\Delta\nu_{residual}$ in Figure 4.8 was calculated as described in the Methods section 4.2.7 considering the singlet linewidth from tCr(CH₃). $\Delta\nu_{residual}$ for hCs and NAA are close to

zero, indicating that there are either no or insignificant other components contributing to these peaks. The longer T_2^{app} indicates additionally that these are pure contributions from those metabolites. Similar assumptions of contributions from identical chemical shifts can also be made for DF_{8.49} and DF_{8.24}, while the relatively small $\Delta\nu_{residual}$ of DF_{7.48}, DF_{6.12}, DF_{5.97} may indicate J-coupling effects or resonances with minor chemical shift differences. On the other hand, all the remaining peaks have a considerable $\Delta\nu_{residual}$ ranging from 20 to 60 Hz. These $\Delta\nu_{residual}$ could denote the presence of multiple components with different chemical shifts or substantial contributions from J-evolving components. These non-zero $\Delta\nu_{residual}$ of the unassigned downfield peaks are similar to those in macromolecules as described in Murali-Manohar et al.,³⁰. An exchange induced line-broadening of a few Hz will occur as described in NMR for the protons exchanging with water¹⁴⁷. This line broadening effect, however, will mostly be equivalent to the difference between $(\pi T_2^{app})^{-1}$ and $(\pi T_2^{corr})^{-1}$.

4.1.6 Concentrations and Peak Assignments

The estimated tissue concentrations of the downfield metabolites and the proton densities of the unassigned resonances are reported in Figure 4.9 and Table 4.3 with and without T_2^{app} correction in mmol/kg. Table 4.4 gives concentration values in mmol/L with and without T_2^{app} correction for the ease of comparison with the previous literature. Since the T_2^{app} relaxation times of the downfield peaks are shorter compared to the upfield peaks, the T_2^{app} relaxation correction factor makes a significant impact on the concentrations as seen in the reported values. Concentrations reported here are within the range from previously reported values at 9.4 T and 7 T studies^{12,122} (Table 4.4). Specifically, the previous study at 9.4 T did not correct for T_2^{app} as the TE used in the study was only 10 ms. However, the current study used TE = 24 ms and a T_2^{app} correction was necessary. On the other hand, the study at 7 T used a water suppression method which resulted in a bias towards lower quantified concentrations for chemical compounds with exchangeable protons with water.

NAA has a resonance at 7.82 ppm as reported by Govindaraju et al.¹⁴ Recently de Graaf added N-acetylaspartylglutamate (NAAG) resonances at 7.95 and 8.26 ppm in the 3rd

edition of his book². Expected concentrations from upfield measurements³⁰ are 12 mmol/kg and 1.4 mmol/kg for NAA and NAAG, respectively. While the measured downfield NAA concentration (7 mmol/kg) of this study is lower than expected, the total NAA concentration (17.4 mmol/kg) is in line with literature¹². This high concentration value suggests that some other resonances are contributing to total NAA, possibly amides as seen for the DF_{8.18} and DF_{8.37}. The coupling constant (6.4 Hz) of NAA reported by Govindaraju et al¹⁴ was used in the current study, which fitted the observed spectral pattern. Although a concentration of ~10 mmol/kg could be achieved when using the coupling constant (7.9 Hz) from de Graaf², this J-splitting was broader than the splitting observed in the spectra (see also subchapter 5.2).

hCs concentration has been reported with concentrations from 0.3 – 1.6 mM^{12,122,142} with higher concentrations in cortical GM, which is in line with the reported value of ~0.43 mmol/L of this work.

We would like to remark, however, that all reported concentrations from this study should be considered with care since tissue fraction corrected concentration quantification was possible for only five subjects and hence, the sample size was too small to perform statistical tests.

Adenosine triphosphate (ATP) has three observable peaks at 6.126, 8.224, and 8.514 ppm. Initially, ATP was simulated as a basis set metabolite in this study; however, the chemical shift from Govindaraju et al.⁷ did not match the peaks present in 9.4 T human brain spectra. Simulating Voigt peaks as DF_{6.12}, DF_{8.24} and DF_{8.49} as shown in the final settings resulted in proton densities of 2.36, 4.95 and 2.41 mmol/kg, respectively. De Graaf et al.¹⁴⁸ reported 2.8 mmol/L as the reference concentration for ATP in ³¹P spectroscopy. The concentrations of DF_{8.49} and DF_{6.12} are close to the previously published literature value of ATP, while the DF_{8.24} concentration is close to the sum of ATP and NAAG (peak at 8.260 ppm) concentrations. It should be noted that the spline baseline is often positive from 7.7 to 8.4 ppm and this could also introduce a deviation from their actual concentrations. Therefore, DF_{8.49} and DF_{6.12} can be potentially assigned to ATP and DF_{8.24} to a combination of ATP and NAAG. The $\Delta v_{\text{residual}}$ equal almost 0 Hz (Figure 4.8) also suggests that the DF_{8.24} and DF_{8.49} peaks are indeed metabolite singlets. The DF_{6.12} peak was often contaminated with water sideband artifacts in our spectra,

which could be the ^{13}C resonance of the ATP ribose moiety. ATP measurements in ^{31}P MRS include potentially additional triphosphate resonances. In contrast the chemical shifts of the adenosine and ribose moieties of ATP in ^1H -MRS are similar to those of adenosine diphosphate¹⁴⁹ (measurements made in pH neutral D_2O solution at 35°C). The chemical shift for $\text{DF}_{8.49}$ peak, however, does not seem to match and the discrepancy with results from Govindaraju et al.,⁷ should be investigated.

Peaks between 8.0 and 8.4 ppm have been described by the literature as fast decaying amide resonances^{12,122,144,148}. The measured exchange times ($\sim 10\text{-}30\text{ s}^{-1}$) and resonance frequency (3.5 ppm in CEST) of these peaks closely match those of the amide proton transfer resonances measured with CEST^{12,120,144,150,151}. The quantification of these broad lines simultaneously with a pH estimation, could indeed complement CEST APT measurements for tumor tissues¹²⁶.

Watanabe et al.¹⁵², assigned the $\text{DF}_{5.75}$ peak to urea [$\text{CO}(\text{NH}_2)_2$], while Fichtner et al.¹²², speaks about a tentative assignment, since the concentration, not corrected for relaxation times was too low. The reported proton density of this study after T_2^{app} correction is 9.81 mmol/kg, which leads to a concentration of 2.45 ± 1.4 mmol/kg, if the four protons of urea are considered. This is very comparable to the concentration of 2.9 ± 0.4 mmol/kg measured in healthy human brain biopsies with high-performance liquid chromatography by Moats et al.¹⁵³ The $\text{DF}_{5.75} \Delta v_{\text{residual}}$ (~ 20.0 Hz) originates from the “scalar relaxation of the second kind caused by the fast quadrupolar relaxation of the most abundant nitrogen isotope ^{14}N ” as described in Stabinska et al.¹⁵⁴ and Finer et al.¹⁵⁵, and we therefore would assign the $\text{DF}_{5.75}$ peak to urea.

4.2 Conclusion

T_2^{app} relaxation times of 15 downfield resonances are reported for the first time in the human brain particularly in a GM-rich voxel in the occipital lobe at 9.4 T. They range from 30 to 50 ms for labeled metabolite peaks, which are typically longer than 16 to 30 ms for the other unassigned downfield peaks. The quantitative analysis of the contribution of T_2^{app} relaxation times and B_0 components to the linewidth of the downfield peaks lets one demarcate which of the peaks have a significant contribution from a single metabolite or which of them have significantly overlapped resonances. Furthermore, estimated tissue

concentrations of molecules resonating downfield are reported with and without T_2^{app} corrections both in mmol/kg and mmol/L. The feasibility of tissue pH estimation simultaneously with the quantification of amide resonances at around 8.30 ± 0.15 ppm, has also been demonstrated.

5 Novel spectral models – Downfield Peak assignments

MRS spectra include both resonances with lower and higher frequencies than those of water, referred to as upfield and downfield (DF) spectra. On the one hand, the metabolite peaks in the upfield spectrum have a higher SNR and contain many metabolites of interest used for clinical applications⁴. On the other hand, the downfield spectrum contains peaks with lower SNR, peaks with shorter T_2 relaxation times^{109,122} and protons exchanging with water^{12,120,121,144,148}.

While the downfield spectral peak appearances are comparable across the available literature^{12,109,120-122,133,144,148,156}, the assignment of the visible peaks to metabolites, compounds and macromolecules is not known. In an effort to summarize previous peak assignments of the downfield peaks, and to further characterize the downfield spectrum, this chapter discusses all metabolites reported to have downfield resonances and how peaks have been assigned thus far. Considering recently published chemical shifts, J-coupling constants, relaxation times and chemical exchange rates, we tentatively assign additional metabolites to their downfield resonances and critically evaluate some of the previous assignments.

Chemical shifts of in vivo detectable metabolites including their downfield peaks are summarized by the widely cited article (including corrigendum) of Govindaraju et al.^{7,14} (see Table 5.1). Further, de Graaf published in the 3rd edition of the book “In vivo NMR spectroscopy: principles and techniques”² some additional chemical shifts (see Table 5.1) and added for instance also a different J-coupling constant for the NH resonance of the aspartate moiety of NAA. All these chemical shifts and J-coupling constants were measured from in vitro solutions prepared with the individual metabolites and measured with NMR at a pH of 7.0 and a temperature of 37°C. These conditions mimic the in vivo healthy brain. Additionally, both publications highlight pH-sensitive resonances, resonances involved in chemical exchange with water and omit protons not measurable by MRS.

The recent measurements of the downfield spectrum were predominantly performed at ultra-high field-strengths, which benefits from a better spectral separation of the resonances^{12,109,121,122,144,148,156} (see also Figure 5.1). The recent downfield

measurements also explored multiple modalities to avoid the chemical exchange effects between the metabolite and the water protons, the methods including metabolite-cycling^{12,109,120,122} or excitation pulses selectively exciting only the downfield spectra^{121,144,148,156,157}.

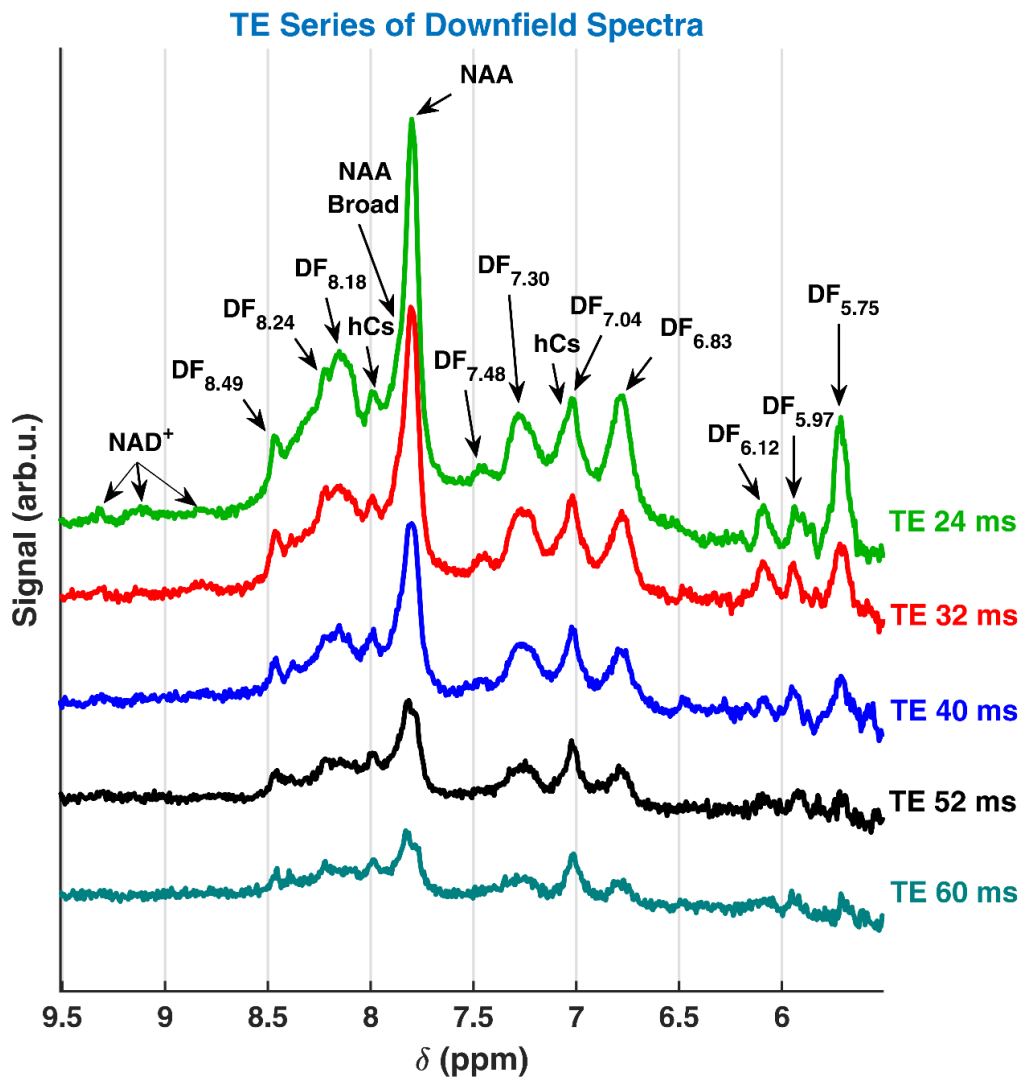


Figure 5.1: An echo-time (TE) series downfield spectrum measured in the human brain at 9.4 T is shown. The measured TEs were: 24, 32, 40, 52, and 60 ms. The spectra were acquired with a metabolite-cycling semiLASER sequence, avoiding water saturation. The arrows and labels point to the identified spectral peaks and metabolites used for fitting. Abbreviations: N-acetylaspartate (NAA), homocarnosine (hCs) and nicotinamide adenine dinucleotide (NAD⁺). DF_{x.xx} mark unassigned peaks at the chemical shift of x.xx.

In this chapter, possible assignments of the so far unassigned downfield resonances to metabolites and macromolecules are discussed. These assignment discussions are derived from the spectral appearance of the downfield peaks measured in the human brain at 9.4 T (see Figure 5.1). These assignments are initiated based on the matching chemical shifts listed in Table 5.1 and are consolidated after a detailed analysis of J-coupling, relaxation and exchange properties. These properties are extracted from chapter 4 of this work and by reviewing the literature of published results from other research groups investigating the downfield spectra.

Subchapter 5.1 starts with a theoretic introduction of chemical-exchange related line broadening effects. All following subchapters dedicate themselves to individual metabolites, analyzing the following properties (whenever appropriate): chemical shift, visibility in measured spectra, J-coupling, chemical exchange, relaxation times, and metabolite concentrations. Each of these subchapters is then concluding whether an assignment is possible. All these results are then summarized in subchapter 5.15 and Table 5.3.

Table 5.1: Chemical shifts (δ) and multiplicities are summarized for metabolites moieties with reported downfield resonances. The rightmost column lists the DF peaks from chapter 4, which could match the given chemical shifts.

Compound	Group & moiety	Govindaraju 2015 ⁷ δ (ppm)	de Graaf 2018 ² δ (ppm)	multiplicity	Possibly seen in the current study
NAA	Aspartate NH	7.8205 ^b	7.820	d	Yes
NAAG	Aspartyl NH	- ^b	8.260	-	Perhaps – DF _{8.24}
	Glutamate NH	- ^b	7.950	-	Perhaps – part of NAA Broad
ATP	Ribose ¹ CH	6.126	6.127	d	Yes – DF _{6.12}
	Adenosine ² CH	8.224	8.224	s	Yes – DF _{8.24}
	Adenosine ⁸ CH	8.514	8.514	s	Yes – DF _{8.49}
	Adenosine NH ₂	6.755	6.755	s	Unlikely – part of DF _{6.83}
Cr	NH	6.6490 ^b	6.65	s	No
D-Glucose	α -anomer ¹ CH	5.216	5.216	d	-
Gln	NH ₂	6.8160 ^b	-	s	Perhaps – part of DF _{6.83}
		7.5290 ^b	-	s	No
GSH	Glycine ⁹ NH	7.154	7.154	t	No
	Cysteine ⁶ NH	8.1770	8.177	d	Perhaps – part of DF _{8.18}
Histamine	Imidazole ² CH ^a	7.8520	-	s	Too low concentrations <0.1 mmol/kg ¹⁴
	Imidazole ⁵ CH ^a	7.0940	-	s	
Histidine	Imidazole ² CH ^a	7.791	7.79	s	Perhaps – part of NAA & DF _{7.04} (low concentration ^{14,133,142})
	Imidazole ⁵ CH ^a	7.058	7.06	s	
hCs	Imidazole ² CH ^a	7.075	8.08	s	Yes
	Imidazole ⁵ CH ^a	8.081	7.08	s	Yes
	GABA ⁴ CH ₂	7.899	-	d	Perhaps – part of NAA Broad
	GABA NH ₃	6.397	-	s	No

(Continues)

Table 5.1 (Continued)

Compound	Group & moiety	Govindaraju ⁷ δ (ppm)	de Graaf ² δ (ppm)	multiplicity	Possibly seen in the current study
NAD ⁺	Adenine ² CH	-	8.184	s	Low concentration ¹⁴⁸
	Adenine ⁸ CH	-	8.415	s	Low concentration ¹⁴⁸
	Nicotinamide ² CH	-	9.334	m	Yes
	Nicotinamide ⁴ CH	-	8.849	m	Yes
	Nicotinamide ⁵ CH	-	8.210	m	Low concentration ¹⁴⁸
	Nicotinamide ⁶ CH	-	9.158	m	Yes
	Ribose (adenine) ¹ 'CH	-	6.040	d	No
	Ribose (nicotinamide) ¹ 'CH	-	6.091	d	Low concentration ¹⁴⁸
Phenylalanine	Phenyl ² CH	7.3223	7.322	m	Perhaps – part of DF _{7.30}
	Phenyl ³ CH	7.4201	7.420	m	Unlikely – part of DF _{7.48}
	Phenyl ⁴ CH	7.3693	7.369	m	Perhaps – part of DF _{7.30}
	Phenyl ⁵ CH	7.4201	7.420	m	Unlikely – part of DF _{7.48}
	Phenyl ⁶ CH	7.3223	7.322	m	Perhaps – part of DF _{7.30}
PCr	NH	6.5810 ^b	6.58	s	No
	NH	7.2960 ^b	7.30	s	Perhaps – part of DF _{7.30}
Tryptophan	Indole ² CH	7.3120	7.312	s	Perhaps – part of DF _{7.30}
	Indole ⁴ CH	7.7260	7.726	d	No
	Indole ⁵ CH	7.2788	7.278	t	Perhaps – part of DF _{7.30}
	Indole ⁶ CH	7.1970	7.197	t	Perhaps – part of DF _{7.30}
	Indole ⁷ CH	7.5360	7.536	d	Unlikely – part of DF _{7.48}
Tyrosine	Phenyl ² CH	7.1852	7.186	m	No
	Phenyl ³ CH	6.8895	6.890	m	No
	Phenyl ⁵ CH	6.8895	6.890	m	No
	Phenyl ⁶ CH	7.1852	7.186	m	No

- Chemical shift not reported.

^a pH-dependent peaks.

^b exchangeable protons

5.1 Line broadening analysis due to chemical exchange rates

Sequences using water suppression techniques^{91-93,122,126} show decreased peak amplitudes of the peaks above 8.0 ppm, and low peak amplitudes of DF_{5.75}; all of which were reported by Fichtner et al.,¹²⁷ to have protons exchanging with water (recall Figure 1.5). In studies using sequences without water suppression, these peak amplitudes are significantly higher^{92,118,126,127}. This can be explained because the protons involved in a chemical exchange with water appear line broadened in MRS and NMR spectra, or their signal might even disappear from the acquired signal.

Chemical exchange is the transfer of a nucleus between different molecules. The exchange rates (also named reaction rates) k can be in the order of nanoseconds to seconds. Using the equations from Levitt “Spin dynamics”¹⁴⁷, we denote the chemical shifts of the two molecules A and B without the exchange effects as Ω_A^0 and Ω_B^0 . Depending on the difference between the chemical shifts of the molecules ($\Omega_\Delta = |\Omega_A^0 - \Omega_B^0|$) and the exchange rate k three different regimes of exchange are defined (see Figure 5.2A):

- Slow exchange ($k \ll \Omega_\Delta$), which leads to some line broadening of the peaks, while their resonance frequencies start to approach each other;
- Intermediate exchange ($k \approx \Omega_\Delta$), where the two resonances coalesce into one very broad peak;
- Fast exchange ($k \gg \Omega_\Delta$), where the coalesced peak starts to narrow.

To describe the spectral lineshape in the slow to the intermediate regime ($k < |\Omega_\Delta/2|$), we first define the Lorentzian function ($L(\Omega; \Omega_l, \lambda_L)$) as:

$$L(\Omega; \Omega_l, \lambda_L) = \frac{1}{\lambda_L + i(\Omega - \Omega_l)} \quad \text{Eq. 5.1a}$$

where Ω are the frequencies, Ω_l is the central frequency of the peak, and λ_L is the peak width parameter.

Using two Lorentzian functions from Eq. 5.1a, the spectral signal ($S(\Omega)$) in the slow to the intermediate regime of the two molecules A and B is described by the signal equation of Eq. 5.1b (λ is the inherent linewidth due to other effects than the exchange rate k).

$$S(\Omega) = \frac{1}{2} \left(1 - \frac{ik}{R} \right) \mathcal{L}(\Omega; \bar{\Omega} + R, \lambda + k) + \frac{1}{2} \left(1 + \frac{ik}{R} \right) \mathcal{L}(\Omega; \bar{\Omega} - R, \lambda + k) \quad \text{Eq. 5.1b}$$

with

$$\bar{\Omega} = \frac{1}{2} (\Omega_A^0 - \Omega_B^0) \quad \text{Eq. 5.1c}$$

$$R = \sqrt{|k^2 - (\Omega_\Delta/2)^2|}$$

The exchange regimes are field strength dependent, since Ω_Δ is field strength dependent.

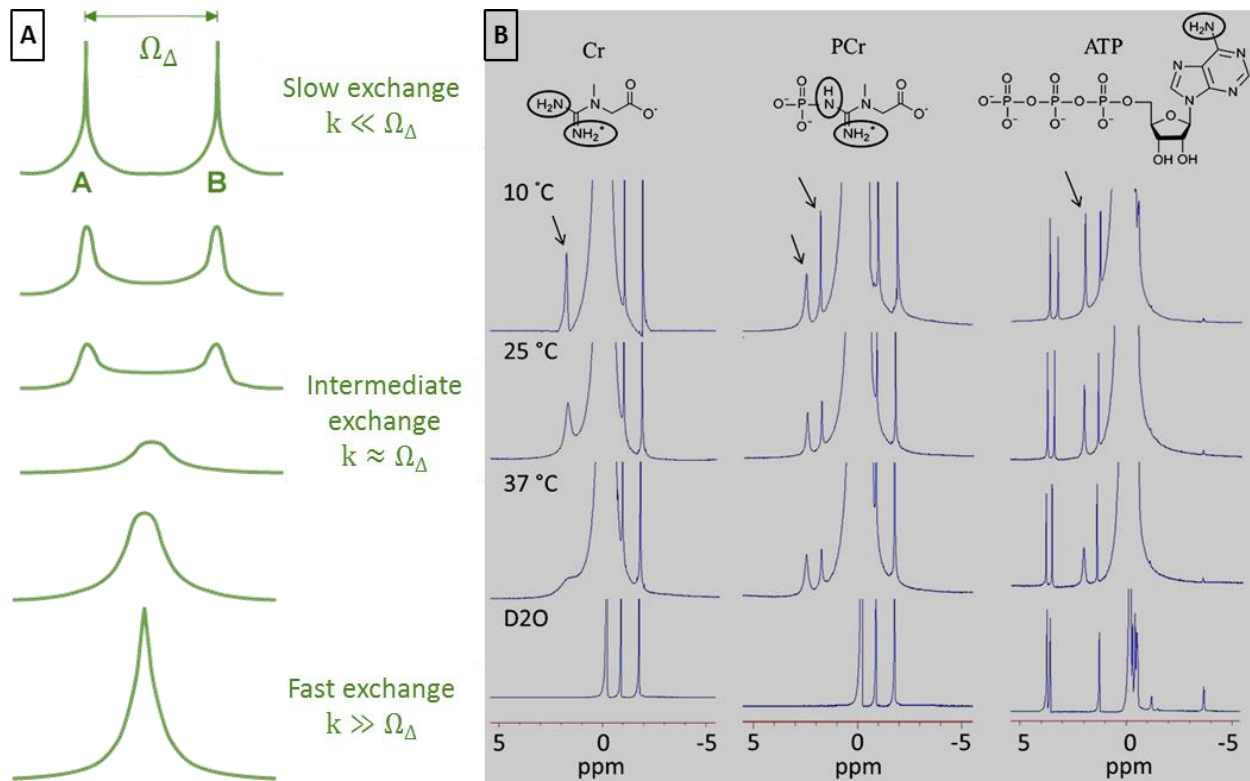


Figure 5.2 A: Depiction of the exchange regimes (slow, intermediate and fast) of two resonances A and B based on the exchange rate k . Courtesy of Allen D. Elster, MRIquestions.com. **B:** Behavior of the exchanging peaks of Cr, PCr and ATP, measured for *in vitro* solutions with NMR at different temperatures by Haris et al.¹⁵⁸. (Reproduced from M. Haris et al., *Exchange rates of creatine kinase metabolites: feasibility of imaging creatine by chemical exchange saturation transfer MRI*, *NMR Biomed.* 2012 25: 1305-1309 Copyright © 2012 John Wiley & Sons, Ltd. Reproduced with permission. All rights reserved).

At the field strength of 9.4 T downfield peaks with resonances between 5.75 ppm to 8.5 ppm and exchanging with water, will be in the slow exchange regime if the exchange

rates are slower than 150s^{-1} , whereas at around 950 s^{-1} we get to the intermediate exchange regime.

An example of metabolites with resonances downfield of water with exchange rates in the high-end slow exchange regime, and intermediate regime were measured using NMR by Haris et al.¹⁵⁸ (see Figure 5.2B). The calculated exchange rates of the four amide resonances at 9.4 T were: Cr at 6.65 ppm $k = 950\text{ s}^{-1}$; PCr at 6.58 ppm $k = 120\text{ s}^{-1}$, PCr at 7.30 ppm $k = 140\text{ s}^{-1}$; ATP at 6.76 ppm $k = 120\text{ s}^{-1}$ with the line broadening effects shown in Figure 5.2B. The apparent central frequency Ω_l of Cr becomes 6.32 ppm from 6.65 ppm, whereas the chemical shifts of the amines resonances of PCr and the ATP barely shift by 0.0025 ppm.

^1H -MRS measurements involve complex pulse sequences with multiple excitation or refocusing pulses to measure the spectra. Hence, numerous milliseconds pass from the first RF pulse affecting the water or metabolite signal until acquisition. For instance, MRS sequences tend to have longer TEs than 10 ms. Also, metabolite-cycling pulses may impact the water signal even before the excitation pulse. In consequence, exchange rates of $k > 100\text{ s}^{-1}$, meaning exchanges of protons within 10 ms, make these protons signal unmeasurable for the in vivo ^1H -MRS sequences used in this and other studies summarized in this chapter.

When determining exchange rates k of peaks through ^1H -MRS, the measurable exchange rates are also impacted by the pulse sequence. As mentioned in the paragraph above and described by Fichtner et al.¹², sequences with a TE of 10 ms or longer are limited in their “ability to measure exchange rates faster than 100 s^{-1} (corresponding to a lifetime of less than approximately 10 ms).”¹² Also, the long inversion pulses used to measure exchange rates in the inversion series spectra moderate the ability to quantify fast exchanging peaks. For the upper bound of quantifiable exchange rates Fichtner et al.¹² reports $k = 25\text{ s}^{-1}$, while MacMillan et al.¹²⁰ describe it as on the order of $k = 22\text{ s}^{-1}$. In the study of Fichtner et al.¹², exchange rates for several of the downfield peaks investigated in this thesis were measured (see Table 5.2). The exchange related line-broadening of these resonances with water was simulated using Eq. 5.1 and is depicted in Figure 5.3. The quantified line broadening effects denoted with $\Delta\nu_k$ are summarized in Table 5.2.

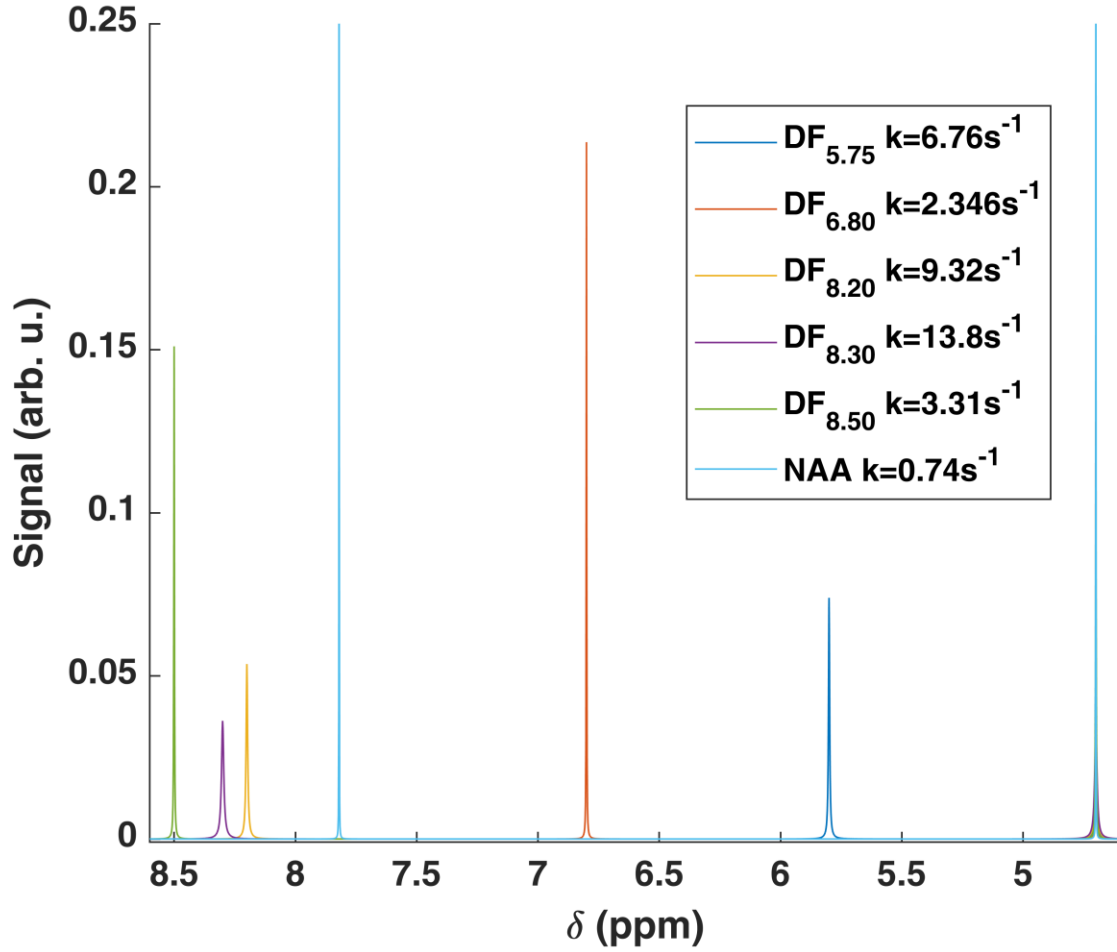


Figure 5.3: Simulations of the signal equation Eq. 5.1 for the downfield peaks with measured exchange rates in vivo in the human brain by Fichtner et al. ¹² These simulations depict the line broadening effects as well as the simultaneous drop in amplitude for identical concentrations simulated for these peaks.

Table 5.2 summarizes additionally the measured T_2^{app} and T_2^{corr} values from chapter 4, where T_2^{app} were the measured apparent relaxation times measured using a TE series spectra and T_2^{corr} were these T_2^{app} relaxation times corrected for the exchange rate according to $1/T_2^{corr} = 1/T_2^{app} - k$. Further, Table 5.2 reports the calculated line broadening effects $(\pi T_2^{app})^{-1}$ and $(\pi T_2^{corr})^{-1}$ related to these relaxation times.

In chapter 4, the $\Delta\nu_{residual}$ was defined according to Eq. 4.5 as the residual linewidth from the measured peak linewidth $\Delta\nu_{1/2}$ minus the contributions of the T_2^{app} linebroadening and micro- and macrosusceptibility effects ($\Delta\nu_{micro,macro}$). These were calculated for each downfield peak and summarized in Figure 4.7. A $\Delta\nu_{residual} \approx 0$ indicates, that likely only a single metabolite at that frequency contributes to the unassigned peak. $\Delta\nu_{residual} < 15 \text{ Hz}$ may indicate J-coupling effects of the metabolite, whereas $\Delta\nu_{residual} > 15 \text{ Hz}$ points toward multiple peak contributions, possibly macromolecules as shown in Murali-Manohar et al.³⁰

Table 5.2: Downfield peaks with measured exchange rates k in vivo at 9.4 T. Relaxation times, both apparent T_2^{app} and corrected for exchange rates T_2^{corr} are also given. The resulting T_2 related line broadening effects, as well as, with the difference between the two $(\pi T_2^{app})^{-1} - (\pi T_2^{corr})^{-1}$ are reported. The last column reports the measured line broadening effects $\Delta\nu_k$ as seen in Figure 5.3.

	$T_2^{app} \pm \text{std}$ (ms)	$T_2^{corr} \pm \text{std}$ (ms)	$k \pm \text{std}$ (s ⁻¹) [Fichtner et al. ¹⁵⁹]	$(\pi T_2^{app})^{-1}$ (Hz)	$(\pi T_2^{corr})^{-1}$ (Hz)	$(\pi T_2^{app})^{-1} - (\pi T_2^{corr})^{-1}$ (Hz)	$\Delta\nu_k$ (Hz)
DF _{5.75}	18.0 ± 6.7	20.4 ± 6.7	6.76 ± 1.59	17.68	15.60	2.08	2.17
DF _{6.83}	21.5 ± 2.6	22.6 ± 2.6	2.34 ± 0.44	14.80	14.08	0.72	0.76
DF _{8.18}	18.9 ± 6.3	22.9 ± 6.3	9.32 ± 0.91	16.84	13.90	2.94	2.95
DF _{8.24}	20.1 ± 5.6	24.8 ± 5.6	9.32 ± 0.91	15.84	12.84	3.00	2.95
DF _{8.37}	16.4 ± 4.3	21.2 ± 4.3	13.8 ± 0.79	19.41	15.01	4.39	4.39
DF _{8.49}	23.2 ± 6.2	25.1 ± 6.2	3.31 ± 0.06	13.72	12.68	1.04	1.04
NAA Broad	28.1 ± 5.3	28.7 ± 5.3	0.74 ± 0.23	11.33	11.09	0.24	0.24
NAA	32.4 ± 11.3	33.2 ± 11.3	0.74 ± 0.23	9.82	9.59	0.24	0.24
total NAA	28.6 ± 2.5	29.2 ± 2.5	0.74 ± 0.23	11.13	10.90	0.23	0.24

Since the chemical exchange also contributes to line broadening, the results from Table 5.2 serve as an indication, whether the exchange related line broadening effects impact the estimated $\Delta v_{residual}$ values. As visible from Table 5.2 the linewidth difference as quantified by $(\pi T_2^{app})^{-1} - (\pi T_2^{corr})^{-1}$ is very much comparable with the measured Δv_k , which was extracted from the signal Eq. 5.1 and Figure 5.3. Hence, the calculation of the $\Delta v_{residual}$ calculated using the T_2^{app} (see Eq. 4.5) is negligibly impacted by the linebroadening effect created by chemical exchange. This observation with $(\pi T_2^{app})^{-1} - (\pi T_2^{corr})^{-1} \approx \Delta v_k$ is only valid for these very slow exchange rates, measured for these peaks visible in the spectrum.

5.2 NAA and its J-coupling Analysis

Text and figures in this subchapter were adapted with minor modifications from our work previously published in the Supporting Information of:

Borbath T*, Murali-Manohar S*, Wright AM, Henning A. “In vivo characterization of downfield peaks at 9.4 T: T₂ relaxation times, quantification, pH estimation, and assignments.” *Magnetic resonance in medicine*, 2020

NAA has a downfield peak resonance at 7.820 ppm of its NH proton of the aspartyl moiety^{2,14}. A peak is consistently visible in all literature^{12,109,114,120-122,133,144,148,156,157} at this frequency and has been assigned accordingly. In the fitting of the peak beside a numerically modelled NAA basis set, an additional peak upfield of it at 7.86-7.87 ppm is used, which is named an NAA shoulder^{12,122} or NAA Broad¹⁰⁹.

For the NH downfield peak of the NAA aspartyl moiety at 7.82 ppm two different coupling constants have been published: 7.9 Hz by de Graaf in the 3rd edition of “In vivo NMR spectroscopy: principles and techniques”² and 6.4 Hz by Govindaraju et al.¹⁴. A detailed analysis of 9.4 T human brain downfield spectra lead to different results, and hence the following paragraphs and figures detail our findings.

Results of simulating the NAA peak in Vespa^{98,107} are shown in Figure 5.4 for different line broadening factors. The default settings to export basis sets from Vespa use a 3 Hz Gaussian broadening, while a 15 Hz line broadening is reflecting the linewidths measured for the singlets in the in-vivo spectra.

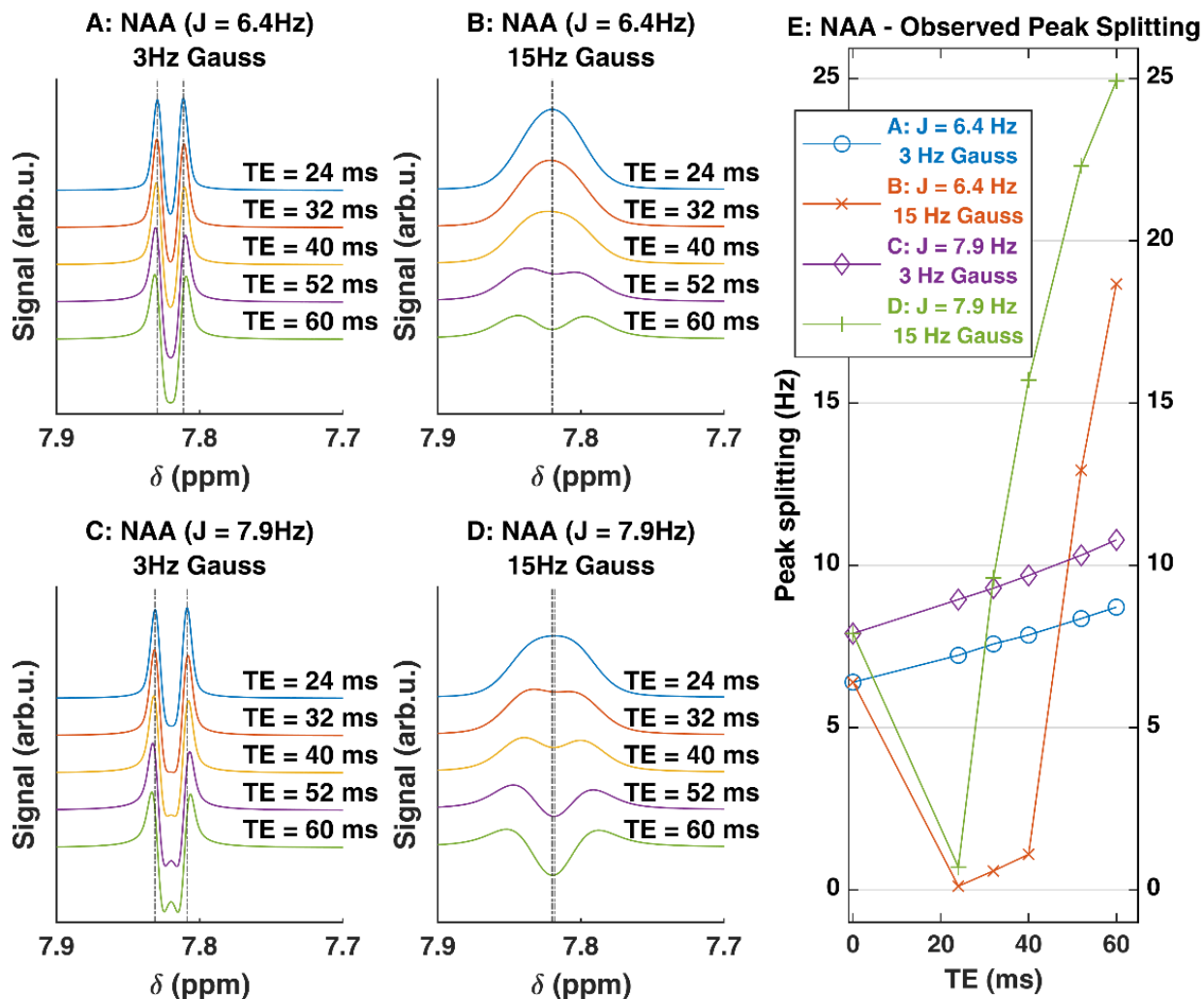


Figure 5.4: A-D: Display the spectra of the downfield NAA peak as simulated by the Vespa software for the semi-LASER sequence for the TE series (24, 32, 40, 52, and 60 ms). A and B show the simulation results for simulating a J-coupling of 6.4 Hz, whereas C and D show the spectra for a simulated J-coupling of 7.9 Hz. A and C show the spectra with the typical export setup of the basis set from Vespa with 3 Hz Gaussian broadening. On the other hand, for B and D, a 15 Hz broadening was applied, and the spectra were scaled by a factor of 3 for visualization purposes. In all subfigures A-D, the vertical lines reflect the measured peak amplitudes for TE = 24 ms. The E subfigure summarizes the measured peak splitting in Hz for the simulated spectra in subfigures A-D. It becomes apparent that the J-evolution in the longer TEs leads to a larger observed peak splitting. While the increase in peak splitting for a 3 Hz broadening is linear, the 15 Hz broadening leads to significantly higher peak splitting effects at longer TEs due to the combined effects of J-evolution and line broadening.

For the across subjects summed in vivo spectra, there was no observed peak splitting for the TEs = 24 ms and 32 ms, while for TE = 40 ms a small splitting of 2 Hz can be speculated. At TE = 52 ms and TE = 60 ms peak splitting of around 12 Hz and 20 Hz was observable, however, the measurements are highly affected by the low SNR at these longer TEs. This in vivo peak splitting behavior matches relatively closely the simulated results of the NAA with a J-coupling constant of 6.4 Hz.

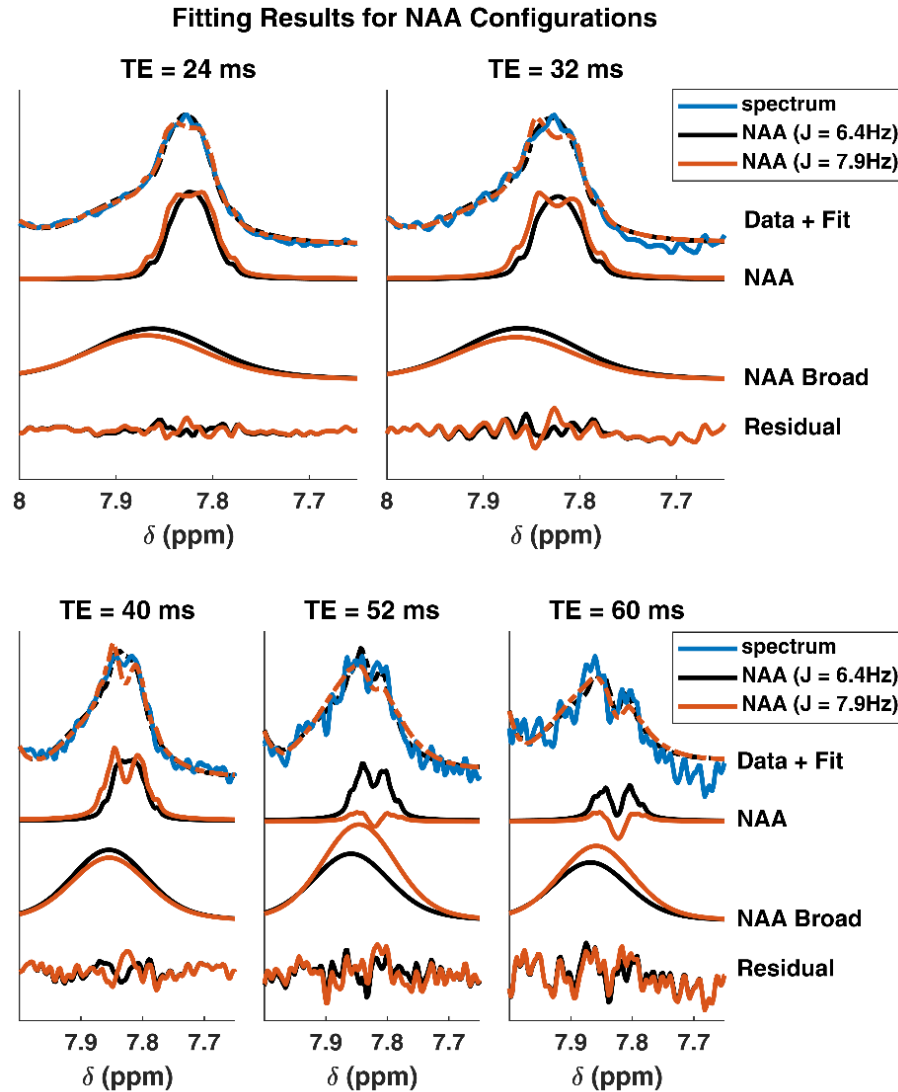


Figure 5.5: In vivo TE series sample spectra fitted with the different NAA basis sets simulated with the 6.4 Hz and 7.9 Hz coupling constants. The visualized spectra were rescaled for visualization purposes at each TE to the maximal peak amplitude of the 7.82 ppm peak. The baselines are not plotted, since these were identical in the two different fit settings.

The match between simulation and J-splittings measured in the in vivo spectra are also reflected by respective spectral fitting results (Figure 5.5). The fitted NAA resonance line assuming $J = 7.9$ Hz seems slightly broader than the actual spectra at TE 24, 32 and 40 ms. At the later TEs: 52 and 60 ms the in vivo peak is fitted mostly by the NAA Broad component, and the concentration drop in NAA does not seem to follow the exponential T_2^{app} of the metabolite.

While these observations suggest, that the NAA J-coupling of 6.4 Hz depicts the in vivo spectra best, this does not directly confirm the coupling constant. There could be other imprecisions involved, like an incomplete spectral model. For instance, resonance contributions of NAAG, additional peaks of hCs or hist were not considered.

The NH proton of NAA is reported to exchange with the water signal^{2,14}; however, the measured exchange rates^{12,120} were slow at around 0.8 s^{-1} .

The T_2 relaxation times^{109,122} were reported as 28 to 30 ms both at 7 T and 9.4 T, which are significantly shorter than those of the upfield resonances of NAA^{30,118}. While the determined concentrations of the NAA-NH peak were somewhat lower than for the upfield NAA, Fichtner et al.¹² proved that these correlate well.

In conclusion, the NAA peak is well quantifiable in the downfield, however, care has to be taken due to slow chemical exchange and short T_2 relaxation times.

5.3 Homocarnosine (hCs)

Homocarnosine has two proton resonances of its imidazole ring which are sensitive to neutral pH changes, resonating at around ~ 7.08 and ~ 8.08 ppm, respectively. The coefficients of the Henderson-Hasselbalch equations describing the chemical shifts of these peaks in dependence of pH were measured by Rothman et al.¹¹⁴

Additionally, the downfield chemical shifts of the GABA moiety of hCs are reported by Govindaraju et al.¹⁴, but omitted by de Graaf in the chemical shifts table in the book "In Vivo NMR Spectroscopy"². While the 7.899 ppm GABA moiety resonance of hCs would have a strong overlap with the NAA Broad peak and is overshadowed by the NAA peaks in other literature, the 6.397 ppm GABA moiety resonance is neither seen in the current study nor in other human studies. Rothman et al.¹¹⁴ measured patients under vigabatrin treatment and subtracted from their spectra those of healthy volunteers, and reports the

elevated hCs imidazole resonances and shows these in the difference spectrum. While this difference spectrum may allow some speculation about smaller peak contributions, Rothman et al.¹¹⁴ did not report either of these two GABA moiety peaks nor are these present in their hCs phantom spectra.

While in all human brain spectra, the hCs imidazole peaks are present, spectra acquired in rat or mice brain show missing, or hardly interpretable peaks at ~8.08 ppm for hCs^{121,152,160}. This is expected, since the concentration of hCs in rats and mice is (<0.07 mmol/kg¹⁴²) significantly lower when compared to the human brain (0.3-1.6 mmol/kg). The hCs peak amplitudes appear smaller, and lower concentrations are measured in parietal WM voxels compared to occipital GM rich voxels¹⁵⁹, confirming that it is more present in cortical gray matter¹⁴². The hCs peak was modelled in this study for different pH values according to the Henderson-Hasselbalch equation with the coefficients from Rothman et al.¹¹⁴ (Table 4.1). The pH sensitivity of hCs is shown in Figure 4.1, whereas the subject-specific pH assignments are summarized in Table 4.2.

None of the hCs peaks is J-coupled, nor has been a chemical exchange of these peaks reported. hCs has the longest T₂ relaxation times in the downfield spectrum at around 160 ms at 7 T¹²² and 50 ms at 9.4 T¹⁰⁹, however, both measurements were not very precise.

In clinical settings, significant concentrations increases of hCs have been observed for patients under vigabatrin, topiramate or gabapentin treatment, as summarized in the review by Petroff¹⁴². For healthy subjects, the concentrations of hCs vary between 0.3 to 1.6 mmol/kg, with higher concentrations in the subcortical gray matter¹⁴².

In conclusion, hCs has two well quantifiable pH-sensitive peaks visible in the human brain, whereas these peaks are not detectable in rodents.

5.4 Creatine (Cr) and Phosphocreatine (PCr)

Cr has an NH resonance at 6.65 ppm, while **PCr** has two NH resonances at 6.58 ppm and 7.30 ppm respectively. All being marked by Govindaraju et al.¹⁴ and de Graaf² as protons exchanging with water.

The Cr peak at 6.65 ppm and the PCr peak at 6.58 ppm might be seen in the TE = 5 ms non-water suppressed spectra of rat brain at 9.4 T by Gonçalves et al.¹⁶⁰, but this peak is

fully decayed at TE = 16 ms or when water suppression is used. Vermathen et al.¹³³, also assigns Cr and Gln in this region in their human brain spectra at 1.5 T. Compared with the other peaks, these peaks are among the fastest decaying ones, with no signal remaining at around TE = 55 ms. Similar decays are only visible for peaks above 8.0 ppm in their spectra.

The Cr resonance at 6.65 ppm is reported to have an exchange rate of 950 s⁻¹, in muscle by the CEST community¹⁵⁰, which is much faster than the exchange rates of the amide protons ≈ 8.2 ppm of 30 s⁻¹ (maximally reported as 280 s⁻¹). Exchange rates measured in phantoms using NMR at 9.4 T by Haris et al.¹⁵⁸ (see Figure 5.2B), were 950 s⁻¹ for Cr (6.65 ppm) and 120 s⁻¹ for PCr (6.58 ppm). These exchange rates could be the reason why the Cr and PCr peaks appear at very short TEs (without water suppression), but are absent or form a small shoulder of the DF_{6.83} peak in other studies^{120,122,152,159}. According to NMR an exchange rate on the same order of magnitude as the chemical shift between the exchanging peaks ($\frac{k_{ex}}{\Delta\omega} \approx 1$) implies that these peaks have intermediate (e.g. Cr peak with 950 s⁻¹) or close to intermediate (e.g. PCr with 120 s⁻¹) exchange rates a.k.a coalescence¹⁴⁷.

The NH amide proton of PCr at 7.30 ppm matches the observed DF_{7.30} resonance. However, the reported exchange rate of this peak in phantoms¹⁵⁸ measured at 9.4 T was 140 s⁻¹. Exchange rate measurements in the human brain of the DF_{7.30} peak report 1.3 s⁻¹ at 3 T¹²⁰ and report a “limited exchange”¹⁵⁹ at 9.4 T (likely < 4 s⁻¹). Hence, the overall measurable contribution of PCr to the DF_{7.30} peak remains likely insignificant.

In conclusion, the downfield resonances of PCr and Cr are generally not visible in downfield spectra, exceptions being non-water suppressed spectra with TEs significantly shorter than 10 ms.

5.5 Nicotinamide adenine dinucleotide (NAD⁺)

NAD⁺ was first reported in ¹H-MRS by de Graaf in 2014 in the rat brain¹²¹ at 11.7 T, the chemical shifts being also reproduced in the 3rd edition of “In vivo NMR spectroscopy: principles and techniques”² by the same author. The three non-overlapping resonances seen in the downfield spectra are at 9.334, 9.158 and 8.849 ppm, respectively (see Figure 5.6).

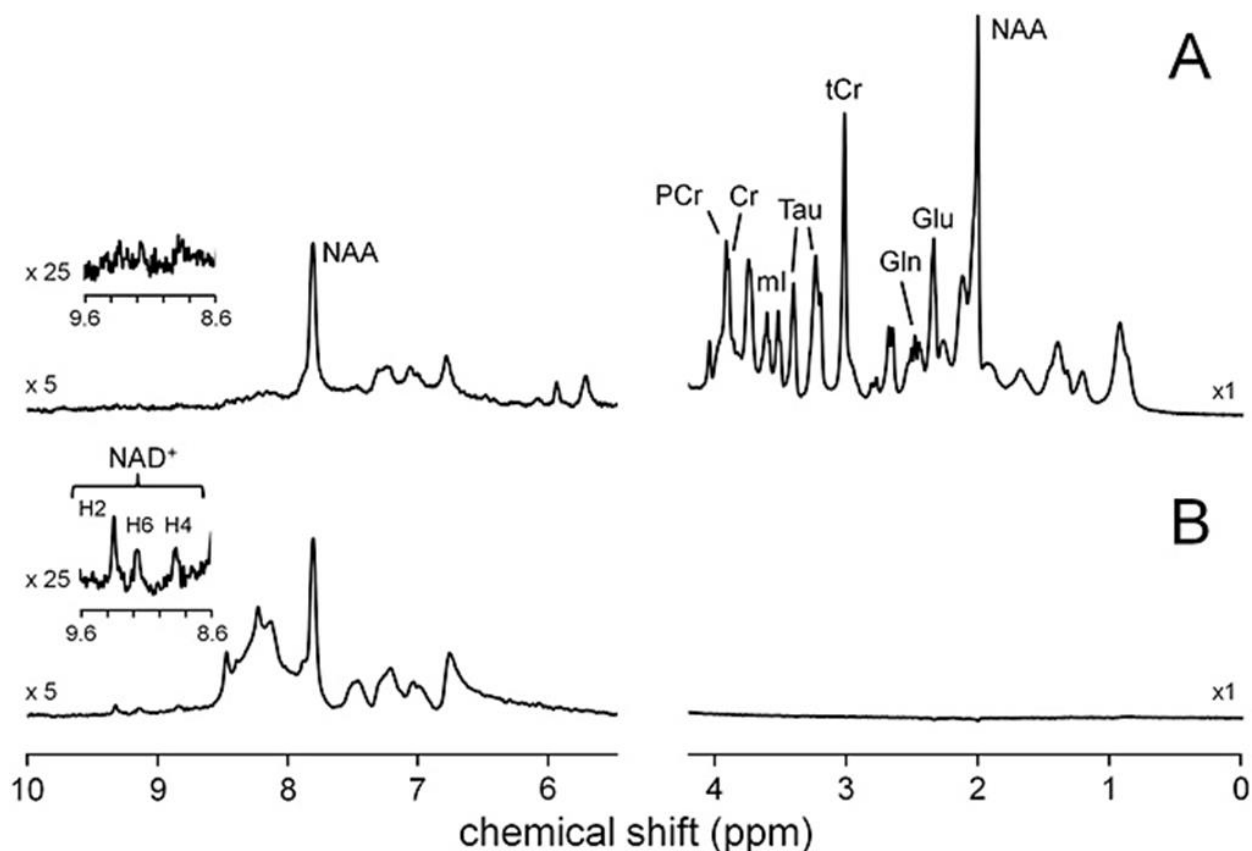


Figure 5.6: Spectrum showing the non-overlapping resonances of NAD^+ between 8.6 and 9.6 ppm. In the upper trace spectra (A), where the water is suppressed by saturating its signal, the NAD^+ peaks almost fully decay. Using selective excitation pulses (lower trace spectrum B) exciting only the downfield spectrum preserves better the magnetization of these peaks. (Reproduced from de Graaf et al., *Detection of cerebral NAD^+ by in vivo ^1H NMR spectroscopy*, *NMR Biomed.* 2014 27: 802-809 Copyright © 2014 John Wiley & Sons, Ltd. Reproduced with permission. All rights reserved).

The assigned peaks could be reproducibly shown in rats at 9.4 T¹⁶⁰ or in human studies at 7 T¹⁴⁸ and in the current study at 9.4 T¹⁰⁹. Other studies do not show/investigate the spectral range of these non-overlapping NAD^+ peaks.

In his seminal works^{121,148}, de Graaf reports all the chemical shifts, J-coupling constants of NAD^+ , and that due to an alcohol dehydrogenase (ADH) mediated interaction between water and NAD^+ , only 49% of the NAD^+ signal is ^1H -NMR visible even with selective excitation. As shown in Figure 5.6, the detection sensitivity is greatly improved by using selective excitation pulses, however, “the NAD^+ nicotinamide protons are non-exchangeable protons and as such the interaction with water is more complicated than

simple chemical exchange and probably involves cross-relaxation and interactions between NAD⁺ protons and immobilized macromolecular proton pools.”¹²¹. The measured T₂ relaxation times in the rat brain at 11.7 T were between 51 and 75 ms for the individual peaks.

NAD⁺ concentrations are low compared to other metabolite contributions at 0.1 to 0.3 mmol/L in rat and human brain^{121,148}. These concentrations also show a decrease with ageing (-1.24 μM/y) as reported by Bagga et al.¹⁵⁶

In conclusion, three non-overlapping proton resonances of NAD⁺ are measurable in the downfield spectrum. For accurate quantification, however, non-water suppressed sequences and good SNR are crucial.

5.6 Adenosine triphosphate (ATP)

ATP is reported^{2,14} with four downfield resonances, at 6.127, 8.224, 8.514, and 6.755 ppm in the downfield spectrum.

ATP resonances matching DF_{8.24} and DF_{8.49} were assigned by Vermathen et al.¹³³, de Graaf et al.¹⁴⁸, and visible in the spectra measured with frequency-selective pulses of Gonçalves et al.¹⁶⁰. Besides the DF_{8.24} and DF_{8.49} peaks, the DF_{6.12} is also visible in MacMillan et al.¹²⁰ at 3 T, Fichtner et al.¹²² at 7 T or Fichtner et al.¹⁵⁹ at 9.4 T. The ATP adenosine moiety NH₂ resonance at 6.755 ppm has, however, the same appearance issues like the above described Cr and PCr peaks, most likely it exchanges or relaxes too quickly to be measurable (see Figure 5.2B). The measured exchange rate of this amide peak in phantoms at 9.4 T¹⁵⁸ was 120 s⁻¹.

The DF_{8.24} and DF_{8.49} peaks are reported to exchange with water with exchange rates at 9.4 T¹² of ~3.5 s⁻¹ and ~10 s⁻¹, respectively and at 3 T¹²⁰ of ~9 s⁻¹ and ~7.5 s⁻¹, respectively. These exchange rates measurements, however, may be strongly impacted by the broader signals underneath. The signal decay of these two peaks is, however, also evident in all reports showing water-saturated spectra^{121,122,144}. No exchange rates were measurable for the DF_{6.12} in the aforementioned two publications^{12,120}. Theoretically, neither of the three resonances ATP at 8.514, 8224 and 6.127 ppm should chemically exchange with water^{2,14}. Nevertheless, a similar cross-relaxation interaction, as seen with NAD⁺, should be investigated in future.

The concentrations of ATP is used as a concentration reference in ^{31}P MRS and is set to 2.8 or 3 mmol/L. Concentrations of around 2.4 mmol/kg were estimated for the DF_{8.49} and DF_{6.12} at 9.4 T¹⁰⁹, while the increased concentration of 4.9 mmol/kg of the DF_{8.24} was attributed to additional NAAG contributions (see also subchapter 5.7).

In conclusion, ATP is measurable with ^1H -MRS, with the visible peaks attributed to DF_{8.49}, DF_{8.24}, and DF_{6.12}, however, the behavior of the chemical-exchange related behavior of the metabolite should be investigated in future. Further, the difference between the reported chemical shift of 8.514 ppm and the in vivo spectral peak appearance at 8.49 ppm should be clarified.

5.7 N-acetyl aspartyl glutamate (NAAG)

The downfield resonances of **NAAG** at 8.260 and 7.950 ppm, were first reported in the 3rd edition of the “In Vivo NMR Spectroscopy” book of de Graaf². Hence these have never been assigned to downfield in vivo spectra before. However, the 8.260 ppm resonance matches perfectly DF_{8.24} assigned only to ATP in the previous publications^{133,148}, Borbath et al.¹⁰⁹ are first to attribute the DF_{8.24} peaks contribution to both ATP and NAAG. The 7.950 ppm resonance, on the other hand, is severely overlapped by NAA and the broader amide resonances. It could also form the 8.0 ppm resonance observed by Vermathen et al.¹³³: “at least three resonances contribute to the peak at 7.9 ppm”.

Both amide resonances of NAAG are reported to exchange with water¹⁴, their exchange rate, however, was not explicitly determined. The measured exchange rates of matching resonances in the in vivo spectra were 9.32 s⁻¹ and 0.74 s⁻¹, respectively.

NAAG concentrations in the upfield are measured at 1.4 mmol/kg³⁰, which is smaller than the concentrations of the peaks NAAG possibly contributes to in the downfield spectra: DF_{8.24} at 4.9 mmol/kg and NAA Broad at 4.16 mmol/kg.

In conclusion, NAAG contributions to the downfield spectral peaks are likely, however, further investigations are needed.

5.8 Glucose, α -anomer (Glc)

The **α -Glucose** has a peak at 5.216 ppm. This peak has been accurately quantified from upfield spectra in combination with excellent water suppression^{11,161} or during glucose infusion⁴³.

From studies focused measuring only the downfield spectrum, only Fichtner et al.¹²² successfully quantified this Glc peak. All other publication either had significant water contaminations in that ppm region, or their selective excitation pulses did not excite this resonance in the proximity of water.

5.9 Glutamine (Gln)

The downfield chemical shifts of **Gln** at 6.816 ppm (Hz) and 7.529 ppm (H_E) are reported by Govindaraju et al.⁷ but omitted by de Graaf in the chemical shifts table in the book “In Vivo NMR Spectroscopy”².

Contributions of Gln to the downfield spectra are most intensively investigated by Watanabe et al.¹⁵² at 9.4 T in the rat brain. The resonance at 6.816 ppm (Hz) is exchanging slower with water than the resonance at 7.529 ppm (H_E)^{152,162}. The Hz resonance is visible in the anesthetized mice brain also under normal physiological conditions (37 °C). The H_E resonance, however, was measurable only at hypothermia (22 °C), when the exchange rate with water decreases. Both H_E and Hz resonance signals increase with the “addition of 15% CO₂ to the inspiratory gas”, which corresponds to a reduction in intracellular pH¹⁵². Vermathen et al.¹³³, also label the resonance at 6.83 ppm as Gln, whereas other literature instead speaks about possible contributions¹⁶⁰. While there could be visible contributions in the non-water-suppressed spectra of de Graaf et al.^{121,148}, Gonçalves et al.¹⁶⁰ and Dziadosz et al.¹⁵⁷ of the 7.529 ppm peak, this peak is absent in spectra of the current study¹⁰⁹.

The DF_{6.83} peak, on the other hand, is visible in all cited literature and the current study, hence a Gln Hz contribution is possible.

The measured exchange rates of the DF_{6.83} peak are around 5 s⁻¹ at 3 T¹²⁰ and 2.4 s⁻¹ at 9.4 T¹². The T_2^{app} relaxation times of this peak were measured as ~25 ms at 7 T and as ~22 ms at 9.4 T. Estimated concentrations average between 2.8 to 3 mmol/kg without correction for relaxation times^{12,109,122}, and at 11.7 mmol/kg correcting for T_2^{app} relaxation effects¹⁰⁹; both are permitting a contribution of Gln to this peak.

In conclusion, Gln constitutes a significant proportion of the DF_{6.83} peaks signal, which peak was measurable in all literature. The in vivo measured DF peak at 7.5 ppm may also

contain Gln signal contributions; however, this peak is only visible when selective excitation pulses are used.

5.10 Histidine (Hist)

Hist has two proton resonances of its imidazole ring which are sensitive to neutral pH changes, resonating at around ~7.06 and ~7.79 ppm, respectively. The coefficients of the Henderson-Hasselbalch equations describing the chemical shifts of these peaks in dependence of pH were measured by Vermathen et al.¹³³ (Table 4.1)

Hist concentrations in the human brain were extensively investigated by Vermathen et al.¹³³ at 1.5 T, by the administration of histidine, measuring its uptake, pH, and T_2 relaxation. Considering the chemical shifts alone, all literature has resonances at the frequencies of histidine; the two resonances are either characterized as $DF_{7.04}$ or overlapped significantly by the NAA signal.

Modelling the peak with the Henderson-Hasselbalch equation shows that it is less sensitive to pH than hCs (Figure 4.1). Vermathen et al.¹³³ report hist concentrations of around 0.09 mM as a base concentration, which is significantly lower than the reported hCs concentrations of 0.3 - 1.6¹⁴². In a fitting trial of this study, histidine was included as a pH-sensitive metabolite in the basis set. The resulting concentrations were quantified to be around five times smaller than those of hCs, and short T_2^{app} relaxation times of around 27 ms were estimated. All of these would be in agreement with the previous literature¹³³, especially, since the hist resonances could partially originate from the histidine amino acid, which should have a short relaxation time. However, the histidine fits were unreliable due to the strong spectral overlap with hCs, NAA and $DF_{7.04}$. Since the inclusion of hist in the basis set negatively influenced the quantification of the before mentioned metabolites, it was excluded from the basis set and hence not shown in the reported results.

In conclusion, in healthy brains, the histidine contributions are hardly quantifiable due to severe overlap with other larger resonances. However, for other metabolic conditions, such as histidine uptake, the resonances should be considered including their pH sensitivity.

5.11 Histamine

Histamine, while included in the list of metabolites by Govindaraju, it is not quantified in any literature, since the concentration of this metabolite is $< 0.1\text{mmol/kg}^{14}$.

5.12 Urea

Urea, with the chemical formula $\text{CO}(\text{NH}_2)_2$, has four protons in an identical chemical environment. The protons are reported to resonate at 5.75 ppm by Watanabe et al.¹⁵², while Stabinska et al.¹⁵⁴ measured the peak in the WEX spectra at 5.73 ppm at pH 6.96 and $T = 37.0^\circ\text{C}$ with a 600MHz NMR spectrometer. Furthermore, Stabinska et al.¹⁵⁴ quantified that all the four protons of urea are exchanging with water. Both the pH and temperature dependence of the exchange rates were quantified, the exchange rates being between $2\text{-}4\text{ s}^{-1}$ for a neutral pH at $T = 37.0^\circ\text{C}$. The urea peak was reported both by Stabinska et al.¹⁵⁴ and Finer et al.¹⁵⁵ to be broader than the broadening effect created by proton exchange or T_2 relaxation time. The broader linewidth was attributed to the “scalar relaxation of the second kind caused by the fast quadrupolar relaxation of the most abundant nitrogen isotope ^{14}N ”. More precisely Finer et al.¹⁵⁵ explains, that “the breadth of the line arises from the scalar (^{14}N , ^1H) coupling, which gives a 1:1:1 triplet which is only partly washed out by the rapid quadrupolar relaxation of the nitrogen”. The coupling constant of $J_{^{14}\text{N}}$ is 63.5 Hz ($J_{^{15}\text{N}} = 89\text{ Hz}$). The typical $\Delta\nu_{1/2}$ of urea measured by Finer et al.¹⁵⁵ in NMR at 220MHz (negligible micro- and macro-susceptibility effects) was 40 Hz.

Watanabe et al.¹⁵², assigned this $\text{DF}_{5.75}$ peak measured in the mouse brain at 9.4 T to urea, while Fichtner et al.¹²² and Fichtner et al.¹² speak more of tentative assignments for their $\text{DF}_{5.75}$ peak measured in the human brain at 7 T and 9.4 T respectively.

Since an exchange with water of 7.4 s^{-1} was measured for the $\text{DF}_{5.75}$ peak at 9.4 T¹², an exchange induced line-broadening of a few Herz will occur as described in NMR¹⁴⁷, but these are about equivalent to $(\pi T_2^{\text{app}})^{-1} - (\pi T_2^{\text{corr}})^{-1}$ (see Table 5.2). The measured $\Delta\nu_{\text{residual}}$ of the $\text{DF}_{5.75}$ peak was around 20 Hz, a line-broadening, which is originating from the scalar coupling of the second kind as described by Stabinska et al.¹⁵⁴ and Finer et al.¹⁵⁵ The $\Delta\nu_{1/2}$ of the $\text{DF}_{5.75}$ peak was $52.5 \pm 4.0\text{ Hz}$, with an estimated microscopic and macroscopic susceptibility component $\Delta\nu_{\text{singlet}}$ from $\text{tCr}(\text{CH}_3)$ of $\sim 15.1\text{ Hz}$, leading to

the $\Delta v_{\text{residual}} + (\pi T_2^{\text{app}})^{-1} \approx 37.4 \text{ Hz}$. This linewidth is comparable to the $\Delta v_{1/2}$ of 40 Hz measured by Finer et al.¹⁵⁵ at 220 MHz in NMR.

The increase in peak intensity of the DF_{5.75} peak during hypercapnia or hypothermia was demonstrated by Watanabe et al.¹⁵² on the mouse brain. Both phenomenon are related to the sensitivity of exchange rates to temperature or pH.

Urea was measured in post mortem biopsy samples by Moats et al.¹⁵³ using high-performance liquid chromatography. The study reported concentrations of 2.9 ± 0.4 mmol/kg in healthy human brains (16.9 ± 5.1 mmol/kg in hepatic coma patient; and 2.6 ± 0.5 mmol/kg in rat brains). The reported concentration of this study after T_2 correction is 9.81 mmol/kg, which taken the four protons of urea into account leads to a concentration of 2.45 ± 1.4 mmol/kg. This concentration is very comparable to the concentration reported by Watanabe et al.¹⁵², and the aforementioned study by Moats et al.¹⁵³.

A higher certainty in the peak assignment could be through a study of patients with liver conditions since the urea cycle primarily occurs in the liver. Urea is a protein catabolism product, and an around 1.5 fold increase of the metabolite was shown in Huntington's disease by Handley et al.¹⁶³, using biochemical assay (urea assay kit) for in vitro brain samples. While DF_{5.75} is an exchanging peak with water, the relatively slow exchange rate¹⁵⁹ of $< 10 \text{ s}^{-1}$, the concentration of only 2.45 mmol/kg and the closeness of ~ 1 ppm to water poses difficulties to image this peak with CEST.

In conclusion, the full signal intensity of the DF_{5.75} peak is attributable to urea alone. To measure this resonance frequency non-water-saturated sequences should be used since selective excitation pulses tend to suppress this peak due to the transition bandwidths^{121,144,148,156,157}.

5.13 Glutathione (GSH),

Measuring solutions with **GSH** Grande et al.¹⁶⁴ identified the amide of the glycine moiety of GSH showing a resonance at 8.27 ppm at a pH of 7, temperature unknown. In the measured solutions, the resonances in the downfield of the cysteine moiety fully decayed at pH = 7, whereas the resonance is present at lower pH values. In the COSY spectra of the solutions, cross-peaks between the amide resonance of the glycine moiety (8.27 ppm) and the CH₂ protons of the glycine moiety (3.78 ppm) were observed. It seems that the

Govindaraju et al.¹⁴, and de Graaf² erroneously attribute the resonance at 8.177 ppm to the cysteine moiety. These cross-peaks at (8.2 ppm, 3.7 ppm) are also reported in spectra of brain phantom solutions containing GSH as well as in human brain spectra measured at 3 T by Nagarajan et al.¹⁶⁵. Both NH resonances of GSH are marked as exchangeable protons, and a signal decay with increasing pH is found by Grande et al.¹⁶⁴

DF_{8.37}, DF_{8.18}, and NAA Broad are widely attributed to **amide** resonances of peptides and proteins and to contributions from GSH in various literature^{120,121,159,160,166}. Increased signal intensities of the 8.27 ppm resonance, attributed to GSH, was reported in tumor cell cultures by Grande et al.¹⁶⁴

In conclusion, the accurate chemical shifts of GSH should be reinvestigated. With both amide protons of GSH exchanging with water and overlapping with significant other signal contributions between 8.0 and 8.5 ppm, these resonances will likely remain not quantifiable by 1D-MRS.

5.14 Other amides and Amino Acids of Macromolecules

While DF_{6.83}, DF_{7.04}, DF_{7.30}, and DF_{7.48} peaks have been variously assigned, or contributions of Gln, hCs, hist, phenylalanine, tyrosine and tryptophan speculated^{133,152}, these assignments became less confident recently^{159,160}. Moreover, while the assignments are possible, the concentrations of these peaks seem too small to explain the full amplitude of these peaks. For example, Kreis¹⁶⁷ showed that the measurement of phenylalanine concentrations of 0.6 to 1.5 mmol/kg in patients with phenylketonuria was possible. However, he also concluded that the “brain phenylalanine concentration is only some 50 μM in healthy subjects and ...cannot be measured”¹⁶⁷. Recently, de Graaf et al.,¹⁴⁸ instead reported these peaks as macromolecules, and one could speculate, that due to the short T₂ relaxation times, their broad linewidths and matching chemical shifts, these could belong to amino acids of proteins. The possible contributors could be amino acids like tyrosine, phenylalanine as summarized in the Biological Magnetic Resonance Bank (BMRB) amino acid database^{168,169}. See also discussion in chapter 6.

Tyrosine and phenylalanine contributions, in the form of free metabolites or as amino acids part of a protein chain, are also supported by measured cross-peaks in vivo using COSY spectra by Nagarajan et al.¹⁶⁵ and Waisbren et al.¹⁷⁰. Nagarajan et al.¹⁶⁵ reports

these cross peak at (7.1 ppm, 6.8 ppm) and attributes them to the non-exchangeable protons of the phenyl ring of tyrosine, whereas the spectra of Waisbren et al.¹⁷⁰ shows more bulky peaks in the ppm range between 6.8 and 7.5 ppm.

The sum of broad resonances between 8.0 and 8.5 ppm is assumed to be **amide** resonances of peptides and proteins^{120,121,159,160,166}. Their measured exchange rates between 8 to 14 s⁻¹ both at 3 T¹²⁰ and 9.4 T¹² (both measurements potentially being limited to measure significantly faster exchange rates), and the loss in signal intensity when saturating the water signal^{121,122,144,157} also support this thesis. The broad linewidths of these downfield peaks also match those described in the BMRB database^{168,169} for amide resonances (see discussion in chapter 6).

The measured T₂ relaxation times of the unassigned peaks: DF_{6.83}, DF_{7.04}, DF_{7.30}, DF_{7.48}, DF_{8.18}, DF_{8.37} and NAA Broad were between 24 and 40 ms at 7 T¹²², and between 20 at 30 ms at 9.4 T¹⁰⁹. These are indeed more similar to the relaxation times of macromolecules^{27,30} than metabolites^{30,71} quantified in the upfield spectra. These type of similarity is also observed when comparing T₁ relaxation times^{12,27,120,171-173}.

While for most visible peaks, either an assignment can be made, or some speculated, the **DF_{5.97}** peak remains completely unassigned. No reported metabolite by Govindaraju et al.⁷, or by de Graaf² has a resonance at this frequency, nor does any amino acid from the BMRB¹⁶⁸ have any matching resonance.

5.15 Summary of downfield peak assignments

In the previous subchapters, all the metabolites with reported resonances in the downfield were discussed individually. Properties such as chemical shift, exchange rates and concentrations were elucidated, and their appearances in both literature spectra and spectra from the current thesis (see chapter 4) extensively discussed.

Concluding, the possible metabolite contributions measured in the spectra at 9.4 T from the current study (chapter 4), are summarized in Table 5.3. This thesis contributes to the novel assignments of the following metabolites: urea, ATP, and NAAG. Additionally, a more elucidated assignment discussion for NAA, hCs, PCr and Gln, as well as macromolecular contributions, was provided.

Table 5.3: A summary of the downfield peaks and their possible metabolite contributions. The right columns compare the reported concentration values from literature (¹H-MRS where not marked otherwise) and those measured in subchapter 4.3.4.

	Possible contributions		Concentration expected from Metabolites (mmol/kg)	Conc. ± std with T ₂ ^{app} correction (mmol/kg)
	Metabolites	Macro-molecules ^a		
DF _{5.75}	Urea		2.9 ¹⁵³ (four protons) ^d	9.81 ± 5.62
DF _{5.97}	-		-	1.66 ± 0.87
DF _{6.12}	ATP		2.0-4.0 ²	2.36 ± 0.89
DF _{6.83}	Gln	TYR	2.5 (lit.), 7 (9.4 T results) ³⁰	11.77 ± 2.23 ^c
DF _{7.04}	hist	TYR, PHE	0.1 ¹³³	6.05 ± 1.82 ^c
DF _{7.30}	Phenylalanine; PCr; Trp	PHE, TRP	0.2 ² ; 3.0-5.5 ² ; 0.03 ²	6.84 ± 1.31 ^b
DF _{7.48}	Phenylalanine	PHE, TRP	0.2 ²	1.24 ± 0.50 ^c
DF _{8.18}	GSH	Amides	1.5-3.0 ²	15.79 ± 5.41 _c
DF _{8.24}	NAAG; ATP		1.0-1.4 ² ; 2.0-4.0 ²	5.00 ± 0.58
DF _{8.37}	-	Amides	-	8.21 ± 2.85 ^c
DF _{8.49}	ATP		2.0-4.0 ^{2 e}	2.41 ± 0.47
NAD ⁺	NAD ⁺		0.11 ²	0.19 ± 0.11
hCs	hCs		0.3-1.6 ¹⁴²	0.60 ± 0.31
NAA Broad	NAA; NAAG; hCs	Amides	10-12 ³⁰ ; 1.0-1.4 ² ; 0.3-1.6 ¹⁴²	4.16 ± 1.44
NAA	NAA; hist		10-12 ³⁰ ; 0.1 ¹³³	7.02 ± 0.41
total NAA	NAA; NAAG; hCs; hist		10-12 ³⁰ ; 1.0-1.4 ² ; 0.3-1.6 ¹⁴² ; 0.1 ¹³³	17.44 ± 2.24 _b

^aConcentrations of macromolecules measurable with MRS is unknown

^b Concentrations are a bit higher than expected when considering only the suggested metabolite concentration contributions, but could be still plausible.

^c Concentrations are significantly higher than expected when considering only the suggested metabolite concentration contributions.

^d Measured in biopsies by Moats et al.¹⁵³ using high-performance liquid chromatography

^e Measured with ³¹P MRS.

6 Novel spectral models – Amino acid model

Parts of the text and figures in subchapters 6.2 to 6.2 of this chapter previously published in:

Borbath T, Murali Manohar S, Henning A. “Towards a Fitting Model of Macromolecular Spectra: Amino Acids.” *Proc. of the 27th Annual Meeting of the International Society for Magnetic Resonance in Medicine*, 2019, Montréal, QC,

In chapter 2, the effects of the MM spectrum on the metabolite quantification were extensively discussed. This MM spectrum is described as containing the proton resonances of proteins and peptides and forming broad peaks. This chapter presents a fitting model to fit the MM spectrum to the contributions of individual amino acids (AA), where the chemical shifts of these AAs are extracted from a protein database.

As the first step in this chapter, the motivation of a new model is introduced, which is based on the broad linewidth appearance of the MM peaks and previous NMR measurements of cytosol from brain biopsies. Then the newly developed fitting model and results are presented and interpreted in the perspective of existing literature.

6.1 Motivation

The MM spectrum is the broad signal underlying the narrower spectral lines of the metabolite spectrum. Depending on how the MM spectrum is handled significant effects on the quantified metabolite concentrations were observed^{27,36,104} (see also chapter 2). To achieve the most accurate metabolite concentrations, the MM spectrum is treated similarly to a single metabolite: a single basis set for it being included into the fitting software^{27,36,103,174}. Such an MM spectrum basis set is generally created from a previously acquired metabolite nulled MM spectrum.

The usage of such acquired MM spectra in spectral fitting became increasingly important at ultra-high-field (UHF) strengths^{27,103} since the difference in T_2 relaxation times between metabolites and macromolecules decreases with increasing B_0 ²⁸⁻³⁰. On the other hand, recent UHF measurements allowed a better separation and characterization of the peaks of the MM spectrum. These MM peak characterizations include both T_1 , T_2 relaxation times, and peak linewidths^{25,30,171}.

In the following two subchapters, the broad linewidth appearance of the MM peaks (see Figure 2.1) is discussed. The MM peaks seem to have broader linewidths than what can be attributed to line broadening effects caused by T_2 relaxation and B_0 effects alone. Subchapter 6.1.1 verifies the general assumption of this thesis, whether the linewidth ($\Delta\nu_{1/2}$) of singlet metabolites can be characterized as composed of T_2 relaxation broadening ($(\pi T_2^{app})^{-1}$) and micro- and macrosusceptibility linebroadening ($\Delta\nu_{micro,macro}$) effects alone. This should mean a close to zero $\Delta\nu_{residual} = \Delta\nu_{1/2} - (\pi T_2^{app})^{-1} - \Delta\nu_{micro,macro}$ (see Eq. 4.5) for all metabolites. The following two subchapters 6.1.2 and 6.1.3, show the results from other literature, summing up the motivation for the AA fit model.

6.1.1 Linewidth analysis of upfield singlets and effects of the B_0 shimming

Text and figures in this subchapter were adapted with minor modifications from our work previously published in the Supporting Information of:

Borbath T*, Murali-Manohar S*, Wright AM, Henning A. “In vivo characterization of downfield peaks at 9.4 T: T_2 relaxation times, quantification, pH estimation, and assignments.” *Magnetic resonance in medicine*, 2020

To verify, whether the linewidth information is accurate enough to derive conclusions on other effects than T_2 relaxation and B_0 effects alone, a linewidth analysis on the metabolite singlet peak is performed.

Indeed, multiple metabolites with very similar resonance frequencies contribute also to the singlet peaks. To assess the contributions to the linewidth of different metabolites contributing to the same resonance we define $\Delta\nu_{diff}$. $\Delta\nu_{diff}$ describes the difference between the chemical shifts of the protons of metabolites taken from Govindaraju et al.^{7,14}, which contributed to the measured singlets (e.g. for tCr(CH₃) $\Delta\nu_{diff} = |3.027 - 3.029| = 0.002$ (ppm) . The contributions are as follows:

- tCr(CH₃) is attributed to Cr(CH₃) at 3.027 ppm and PCr(CH₃) at 3.029 ppm
- tCr(CH₂) is attributed to Cr(CH₂) at 3.913 ppm and PCr(CH₂) at 3.930 ppm
- tCho(CH₃)₃ is attributed mostly to GPC(CH₃)₃ at 3.212 ppm and PCh(CH₃)₃ at 3.208 ppm

- *NAA(CH₃) resonates at 2.008 ppm, but NAAG with the CH₃ peak at 2.042 could also have some almost negligible contributions.

Abbreviations: Creatine (Cr), Phosphocreatine (PCr), Glycerophosphocholine (GPC), Phosphocholine (PCh)

To assess whether the $\Delta v_{\text{micro,macro}}$ effects are still identical for the measured singlets the different linewidth contributions of the singlets were assessed as described in the subchapter 4.2.7. The results are summarized in Table 6.1 and Figure 6.1.

The $\Delta v_{\text{residual}}$ linewidths (see Table 6.1) are smaller than <1.0 Hz, except for tCr(CH₂), where the Δv_{diff} is a stronger factor. These ~0 ppm residual linewidths, which also match the Δv_{diff} indicates, that the differences of the $\Delta v_{\text{micro,macro}}$ effects between the singlets are negligible.

Lastly, the tCr(CH₃) singlet was chosen as a reference for the determination of $\Delta v_{\text{micro,macro}}$ because of the following factors: prominence in the spectrum, smallest Δv_{diff} , less overlap with the macromolecular baseline or other metabolites, and closer in proximity to the downfield spectrum than NAA(CH₃). Nevertheless, for MM spectra, where this tCr(CH₃) peak is fully suppressed, other peaks, such as tCr(CH₂) can also serve to estimate the line broadening effects of the micro- and macro-susceptibility ($\Delta v_{\text{micro,macro}}$).

Table 6.1: Linewidth components of upfield singlets given as mean \pm standard deviation.

	$\Delta v_{1/2}$		$(\pi T_2^{\text{app}})^{-1}$		$\Delta v_{\text{residual}}$		Δv_{diff}
	(ppm)	(Hz)	(ppm)	(Hz)	(ppm)	(Hz)	(ppm)
tCr(CH ₃)	0.046 \pm	18.2 \pm	0.007 \pm	2.9 \pm	0.000 \pm	0.0 \pm	0.002
	0.005	2.0	0.002	0.6	0.000	0.0	
tCr(CH ₂)	0.049 \pm	19.7 \pm	0.008 \pm	3.2 \pm	0.003 \pm	1.2 \pm	0.017
	0.004	1.6	0.002	0.8	0.002	0.9	
NAA(CH ₃)	0.045 \pm	18.1 \pm	0.006 \pm	2.5 \pm	0.001 \pm	0.5 \pm	0.034 ^a
	0.006	2.4	0.002	0.7	0.002	0.7	
tCho(CH ₃) ₃	0.048 \pm	19.0 \pm	0.009 \pm	3.4 \pm	0.001 \pm	0.6 \pm	0.004
	0.005	1.9	0.003	1.1	0.002	0.7	

^a The contributions of NAAG should be negligible.

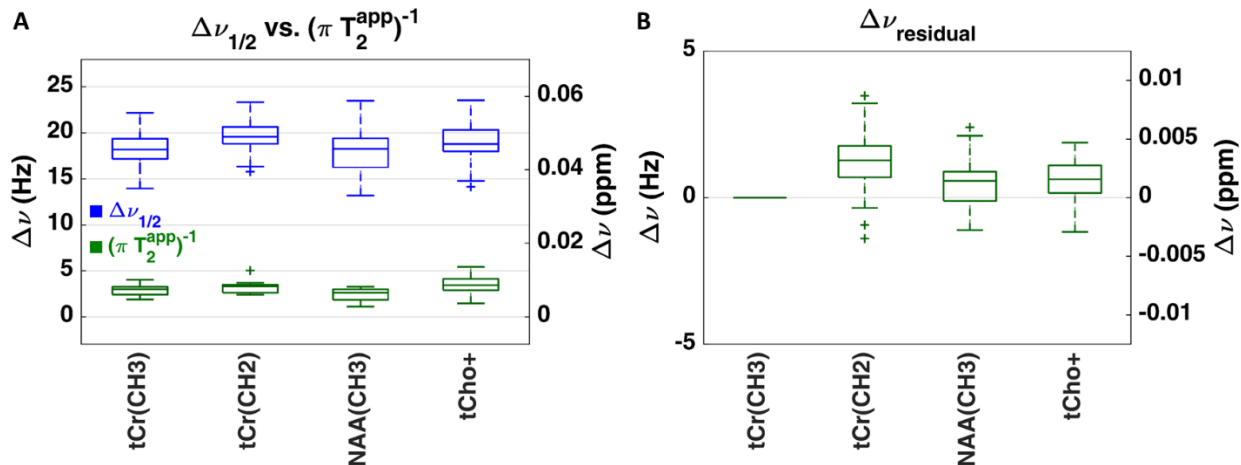


Figure 6.1: A. Box plots of the measured $\Delta\nu_{1/2}$ of the upfield singlets are shown in blue measuring 14.0 to 23.0 Hz. The green boxplots show the $(\pi T_2^{app})^{-1}$, measuring 1.5 to 5.0 Hz. B. Display the $\Delta\nu_{residual}$ box plots, where the $\Delta\nu_{micro,macro}$ was calculated from the tCr(CH₃) peak. All $\Delta\nu_{residual}$ are close to zero, which reflects partially the slight difference in the chemical shift of the metabolites contributing to each singlet resonance, but also that the $\Delta\nu_{micro,macro}$ effects are comparable between these peaks.

6.1.2 The residual linewidth of the macromolecular peaks

Similarly, to the $\Delta\nu_{residual}$ residuals calculated in subchapter 4.2.7 and Figure 4.8, $\Delta\nu_{residual}$ values were also measured for the MM peaks by Murali-Manohar et al.³⁰ Since the MM spectra used in that study, suppressed all the residual signals of the tCr(CH₃) through DIR, the tCr(CH₂) residual singlet linewidth was used to estimate the micro- and macro-susceptibility ($\Delta\nu_{micro,macro}$) effects. Nevertheless, as described in the previous subchapter 6.1.1, the linewidth of this peak tCr(CH₂) is also precise enough to determine $\Delta\nu_{residual}$.

Previously it was believed, that the short T_2^{app} relaxation times are the main contributors to the MMs broad appearance. Observing the $\Delta\nu_{residual}$ values in Figure 6.2, the linewidths ($\Delta\nu_{1/2}$) of the macromolecular peaks is larger than the $\Delta\nu_{micro,macro}$ and the T_2^{app} linebroadening effects. As seen in Table 6.1, the linewidth of singlets reflects the T_2^{app} relaxation and micro- and macrosusceptibility caused line broadening (almost zero $\Delta\nu_{residual}$). However, the non zero $\Delta\nu_{residual}$ of the macromolecules indicates that the broad linewidths of these peaks can not be explained by shorter T_2^{app} relaxation times

alone, as it was concluded also by Murali-Manohar et al.³⁰. The individual MM peaks were named by the terminology of $M_{x.xx}$, where $x.xx$ denotes the chemical shift of the peak in ppm.

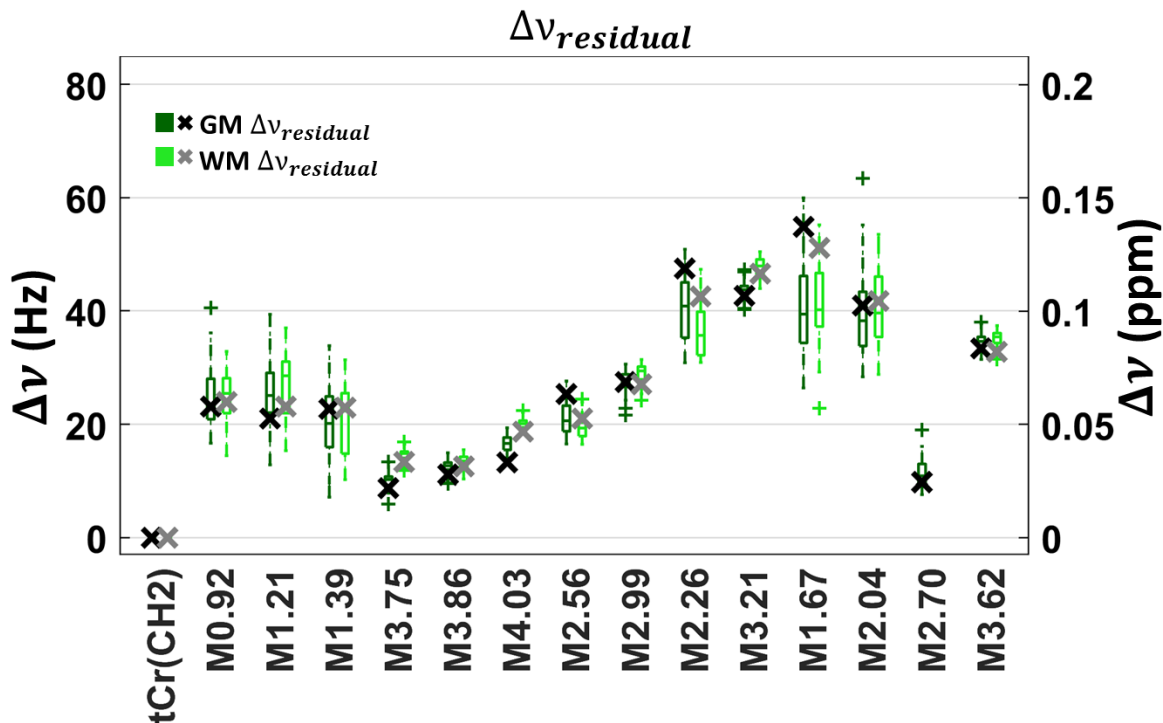


Figure 6.2: $\Delta\nu_{residual}$ calculated for the MM peaks. (Adapted from Murali-Manohar et al., *T₂ relaxation times of macromolecules and metabolites in the human brain at 9.4 T*, *Magn. Reson. Med.* 2020; 84:542-558 Copyright © 2020 The Authors. *Magnetic Resonance in Medicine* published by Wiley Periodicals, Inc., Creative Commons Attribution License).

6.1.3 NMR spectra of cytosol

Broad signals underlying in vivo ^1H MRS spectra are referred to in the literature as macromolecules. While most work refers to them as resonances of amino acids (AA), proteins and lipids³⁸, Behar et al.^{31,32} had assigned them to AAs. Behar et al. created these assignments comparing metabolite nulled in vivo spectra with brain extracts after dialysis from both rat³¹ and human³² brain; verifying cross-peaks with COSY spectra and J-couplings with J-resolved spectra. The chemical shifts, the cross-peaks in the COSY spectra, the J-coupling constants, and the tentative assignments of these MM peaks were also summarized and discussed in the recent “Contribution of macromolecules to brain ^1H MR spectra: Experts' consensus recommendations”²⁷ paper (see Figure 6.3).

Recommended nomenclature	Previous nomenclature ^{4,8}	ppm ^a	Cross-peaks in 2D spectra ^b	J, Hz ^c	Tentative assignment
M _{0.94}	M1	0.94 0.88	0.94, 2.05	7.7(d)	Leucine, isoleucine, valine
M _{1.22}	M2	1.22	1.24, 4.24	6.6(d)	Threonine
M _{1.43}	M3	1.43	1.43, 1.70 1.43, 4.32	7.7(d)	Alanine
M _{1.70}	M4	1.70	1.70, 1.43 1.70, 3.00	m 7.8(t)	Lysine, arginine, leucine

Figure 6.3 Sample of the MM peaks, with their measured chemical shifts, cross-peaks in the COSY spectra, the J-coupling constants, and the tentative assignments, as reported in a recent Experts' consensus recommendations paper²⁷. (Adapted from C Cudalbu, KL Behar, PK Bhattacharyya, W Bogner, T Borbath, RA de Graaf, R Gruetter, A Henning, C Juchem, R Kreis, P Lee, H Lei, M Marjanska, R Mekte, S Murali-Manohar, M Považan, V Rackayova, AM Wright, D Simicic, J Slotboom, Z Starčuk, J Starčukova, BJ Soher, I Tkáč, S Williams, M Wilson, L Xin, V Mlynárik. Contribution of macromolecules to brain 1H MR spectra: Experts' consensus recommendations. *NMR Biomed.* 2020; e4393 Copyright © 2020 The Authors. *Magnetic Resonance in Medicine* published by Wiley Periodicals, Inc., Creative Commons Attribution License)

Proteins have different lengths and hence different molecular weights. The presence of the peaks assigned to AAs in the brain has been verified for different molecular weight cytosolic macromolecule fractions by Behar et al.³¹: “The spectra of brain cytosolic proteins span a molecular weight range between 25 kDa to >100 kDa” (see Figure 6.4). Proteins are composed of chains of AAs. The chemical environment of the protein chain creates distinct chemical shifts of the respective resonances for the composing AAs. For instance, neighbouring AAs or the way the protein is folded changes the electron shielding of a given proton. These slight changes in shielding make the protons of the same amino acid have a resonance frequency in the proximity of the same amino acid but in a different protein or at a different position in a protein. The chemical shifts of protons of the same AAs in various proteins and located at different positions within the protein have been very well documented and stored in the Biological Magnetic Resonance Data Bank (BMRB)¹⁶⁸. Plotting all these resonance frequencies in a histogram, broad peaks appear. This work aims to create a spectral fitting model for macromolecules using the published chemical shifts of amino acids bound at different positions in a large number of cytosolic proteins from the BMRB¹⁶⁸.

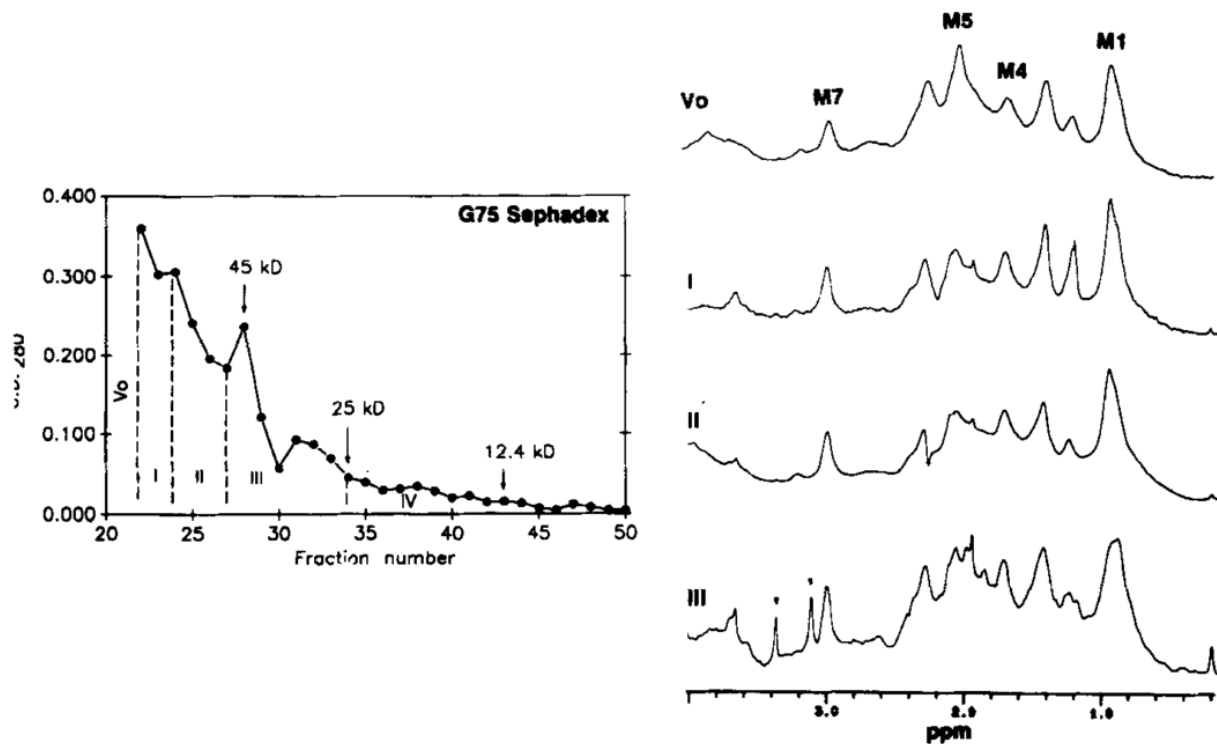


Figure 6.4: Chromatographic separation of the cytosolic macromolecule fraction of a rat brain biopsy. The right column shows the ^1H NMR spectra the following pooled fractions separated by chromatography (see left column): fraction $V_0 > 110\text{kDa}$; fraction I, 63 to 110 kDa; fraction II, 48 to 63 kDa; fraction III, 25 to 48 kDa. (Reproduced from K Behar and T Ogino. *Characterization of Macromolecule Resonances in the ^1H NMR Spectrum of Rat Brain*. *Mag. Res. in Med.* 1993; 30:38-44 Copyright © 1993 by Williams & Wink Reproduced with permission. All rights reserved).

6.2 Methods

To evaluate the macromolecular fit model ^1H -MRS metabolite-cycled (MC) double-inversion-recovery (DIR) semi-LASER spectra were acquired (TR 10 s / TE 24 ms / NEX = 64). The inversion times ($T_{\text{Inv}1}$ 2360 ms / $T_{\text{Inv}2}$ 625 ms) were chosen such that metabolite signals could be efficiently nulled while preserving the macromolecular signal. Additionally, to compare the effects of double-inversion-recovery on the spectral peaks in the downfield with the results of the macromolecular fit model, non-inverted MC-semiLASER spectra were acquired (TR 10 s / TE 24 ms / NEX = 64). The MRS voxels were positioned in the occipital lobe of the human brain at 9.4 T in 11 volunteers. Spectra were preprocessed and averaged across subjects according to Murali-Manohar et al.³⁰

The reported proton resonances in BMRB¹⁶⁸ were extracted into .csv tables using the provided routines in the R programming language by Ulrich et al.¹⁶⁸ The database contains more than 120 thousand measured proteins using NMR spectroscopy, hence for each proton resonance in each amino acid, several ten-thousand chemical shifts were reported: for example the $H^{\beta 2}$ resonance of glutamic acid (GLU) at 2.05 ppm has 51047 reported chemical shifts. While the chemical shifts are centered around a main frequency, like 2.05 ppm in the example above, depending on the protein structure, these can become slightly shifted. The distribution of the chemical shifts of the same resonance line belonging to the same amino acid becomes apparent, when histograms are plotted.

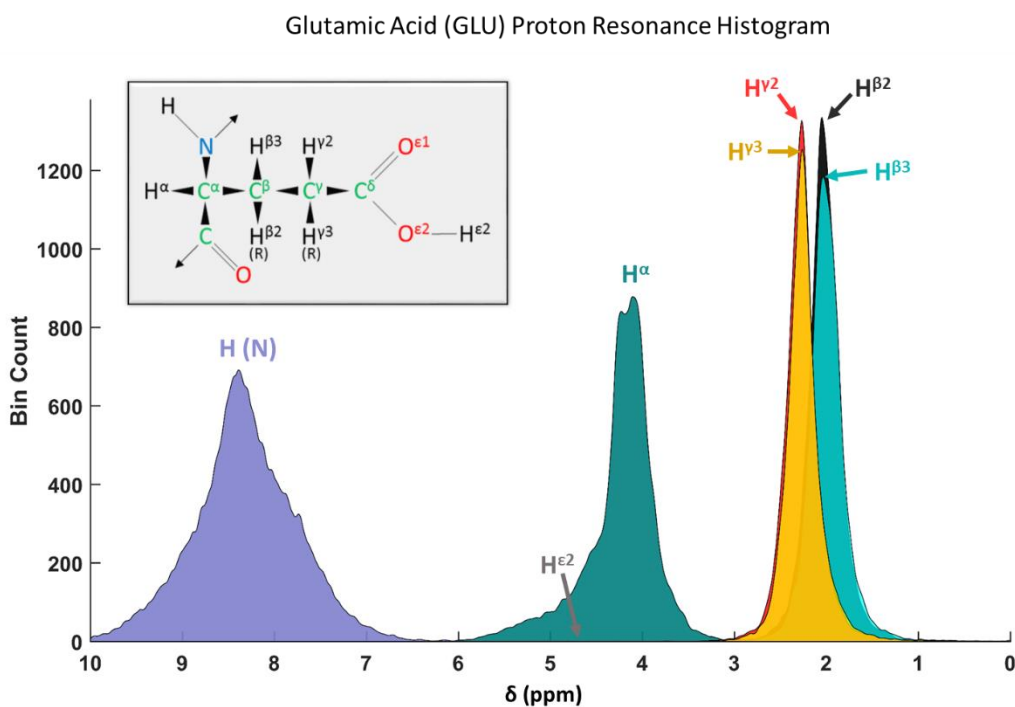


Figure 6.5: Histogram of the measured proton resonances in chemical shifts of the glutamic acid (GLU) extracted from the BMRB data bank¹⁶⁸. Depending on the position of Glu inside a protein chain and the respective 3 dimensional structure of the protein, different chemical shifts have been measured for the same spins. The histogram bins are 0.01 ppm wide. The inlay shows the chemical structure of GLU; arrows indicate bonds to chemical compounds in the protein chain. Enumerating the resonances, central resonance frequency, #total counts of measured chemical shifts found in the BMRB for GLU: $H(N)$ – at 8.39 ppm – #78312; H^{α} – at 4.11 ppm – #56215; $H^{\beta 2}$ – at 2.05 ppm – #51047; $H^{\beta 3}$ – at 2.04 ppm – #48024; $H^{\gamma 2}$ – at 2.27 ppm – #47238; $H^{\gamma 3}$ – at 2.26 ppm – #43957; $H^{\epsilon 2}$ – at 4.81 ppm – #15.

Using the extracted .csv tables histograms with the bin width of 0.01 ppm were created in Matlab for all 20 amino acids. See the example histogram for GLU in Figure 6.5. We can observe, that protons with a similar chemical environment have comparable appearances, like $H^{\beta 2}$ and $H^{\beta 3}$, or $H^{\gamma 2}$ and $H^{\gamma 3}$. For all protons, the histograms show the distribution of the reported chemical shifts around the central frequency. Protons which are more influenced by the other adjacent amino acids in the protein chains, like $H(N)$ or H^{α} have an even broader appearance than the other peaks. Also, these histograms show that the resulting broad peaks that reflect the envelop of the chemical shift histograms are not perfectly symmetric, as it could also be observed in the measured MM spectra.

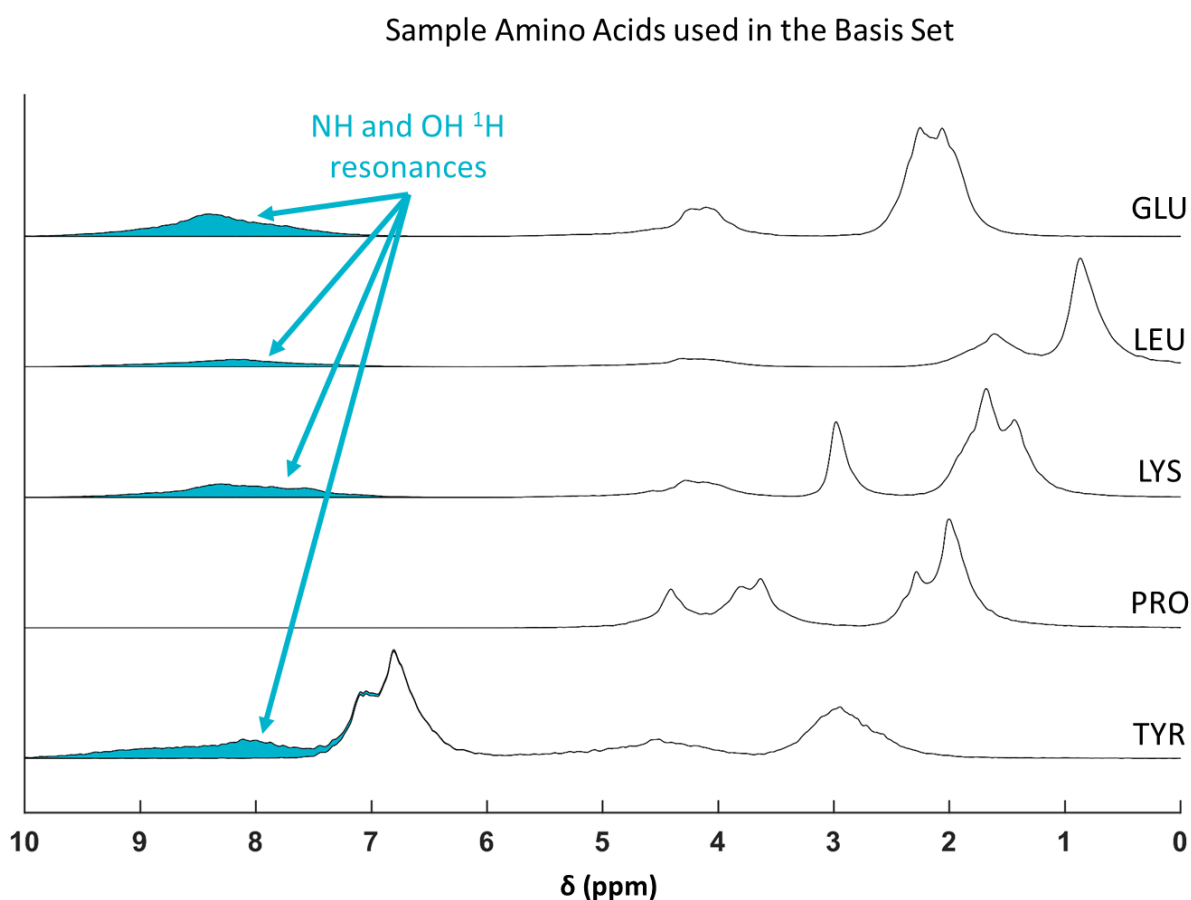


Figure 6.6: A sample of the created basis sets for the amino acids after summarizing the chemical shifts from the BMRB data bank¹⁶⁸. The blue shaded areas highlight the contribution to the spectra from the amide protons found in NH and OH groups. Two basis sets were created with and without the resonances of the NH and the OH groups. Abbreviations of the amino acids: GLU: glutamic acid, LEU: leucine, LYS: lysine, PRO: proline and TYR: tyrosine.

Schanda P.¹⁶⁶ reports rapidly exchanging peaks of “oxygen- and nitrogen-bound sidechain protons”. “Some of the oxygen- or nitrogen-bound sidechain protons in proteins, as well as backbone amide protons, can exchange with water, i.e. the bond to the O or N atom in the protein can be broken, and a water proton takes the place instead.”¹⁶⁶ Hence, out of the proton resonances of the amino acids two basis sets were created: 1. including all resonances, 2. all resonances except the NH and OH proton resonances of the amino acids (see Figure 6.6). The smoothness of the histograms was ensured by fitting a spline to the summed histograms of each amino acid.

The MC-DIR-semi-LASER spectra were fit using LCMoDel-v6.3¹⁵ with the aforementioned basis sets containing 20 amino acids and residual singlets for total creatine [tCr(CH₂)] singlet at 3.92 ppm and the N-acetyl-aspartate [NAA(NH)] at 7.82 ppm. A good fit was ensured by setting a flat spline baseline in LCMoDel.

6.3 Results

The across subjects summed spectra showed a high SNR quality (see Figure 6.7). Comparing downfield spectra of MC-semi-LASER and MC-DIR-semi-LASER, the relaxation of the resonances above 8.0 ppm, can be seen. Multiple studies have assigned the peaks at 8.2-8.3 ppm to fast exchanging amide protons^{12,120}. The used DIR sequence was optimized to suppress the signals of metabolites with T₁ relaxation times longer than 1200 ms. Since the T₁ relaxation times of water⁵⁸ are longer than 1400 ms (see also Table 2.1), the water signal is also largely suppressed. Suppressing the water signal with the DIR sequence also suppresses the resonances of the amide protons exchanging with water, as predicted by de Graaf et al.¹²¹

The metabolite nulled spectrum shows a decent fit using amino acids as basis set (see Figure 6.7B), but is significantly improved if the NH and OH protons are not included (see Figure 6.7A). Visually the overfit of the amino acids above 8.0 ppm (see Figure 6.7B) match the MC-semi-LASER spectrum without double inversion (see Figure 6.7C).

The full fit with all the individual components is shown in Figure 6.8. The model shows a decent fit both upfield and downfield of the water peak. Unfortunately, minor lineshape distortions created by LCMoDel can be seen on the right-hand side of the individual amino acid components.

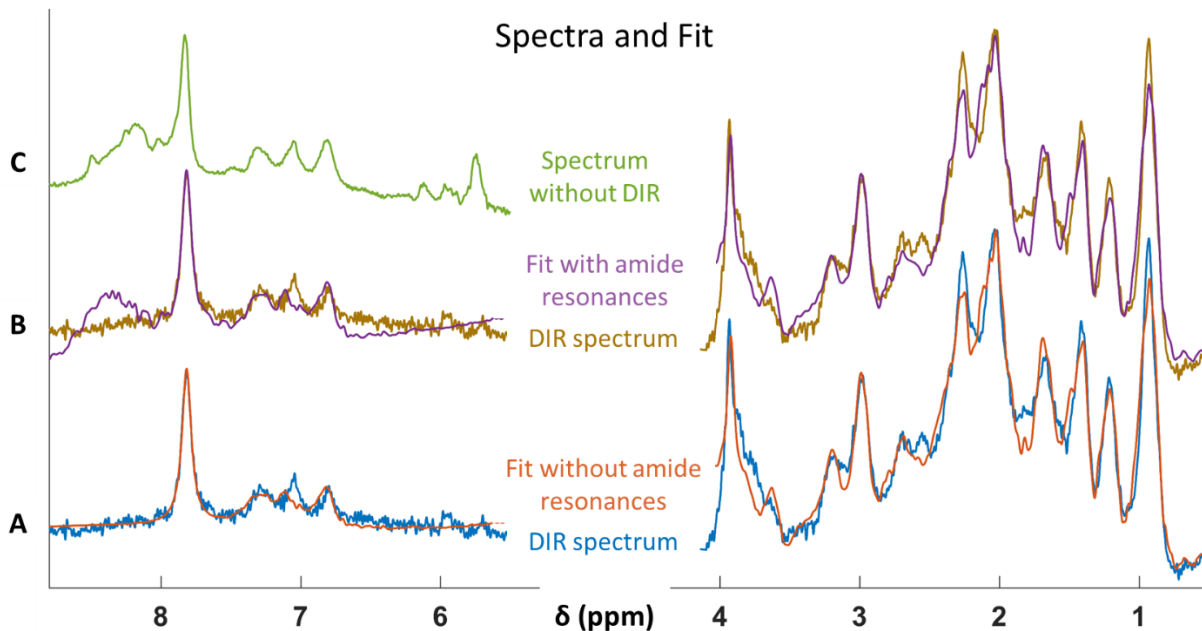


Figure 6.7: Double inversion recovery (DIR) spectrum with the fit for the compiled amino acid basis set (A, B). In (B) all the resonances of the amino acids were used for fitting. The fit is improved significantly if the NH and OH and resonances are removed from the basis set (A). The same spectrum acquired without double inversion is shown in C. The region between 4.1 and 5.5 ppm is not shown, since it was set as a ppm gap for fitting.

6.1 Discussion

This work attempts for the first time to create a fitting model for the in vivo human brain macromolecular spectra using published chemical shift ranges of amino acid resonances bound to thousands of different cytosolic proteins.

The exchange effects with water of the peaks above 8.0 ppm have been reported in previous in vivo studies^{12,120,121}. These could also correspond to the amide resonances of the amino acids¹⁶⁶ (Figure 6.6), hence the improved fit (Figure 6.7), when omitting these resonances for fitting the DIR sequence spectra. The used DIR sequence suppresses also the water signal due to its long T_1 relaxation times, producing a signal loss of the peaks exchanging with water. Hence, the peaks above 8.0 ppm may correspond to the amide protons of amino acids¹⁶⁶, as also described in subchapter 5.13. The only downfield resonance potentially also suppressed by the DIR sequence is homocarnosine¹²², since all other peaks have shorter T_1 relaxation times than 700 ms at 9.4 T¹².

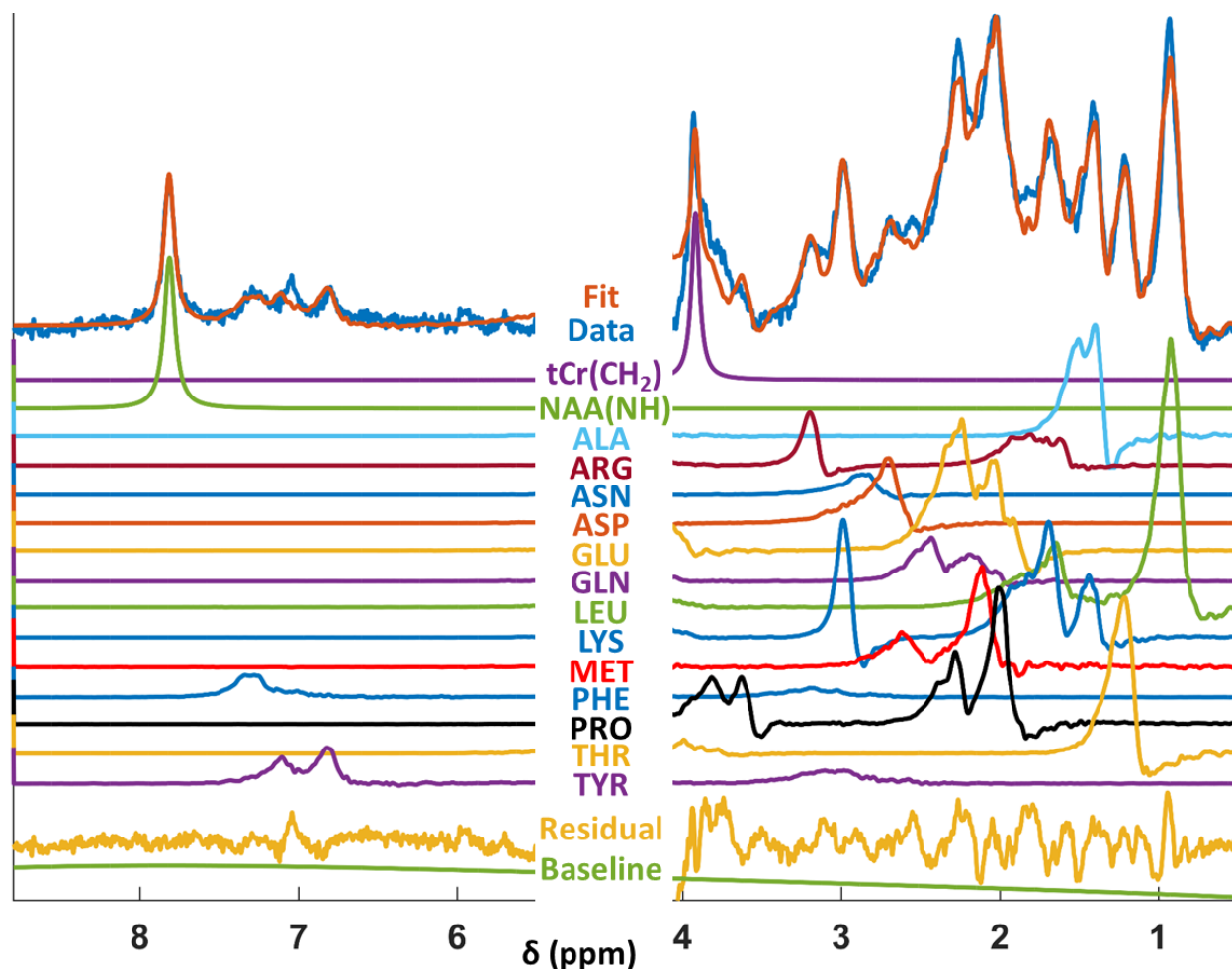


Figure 6.8: Spectrum, fit, residual, flat baseline and amino acid contributions to the fit are shown. The basis set without the NH and OH groups was used. Residual singlets for $tCr(CH_2)$ at 3.92 ppm and $NAA(NH)$ at 7.82 ppm have also been added to the fit model. The region between 4.1 and 5.5 ppm is not shown, since it was set as a ppm gap for fitting.

The assignment of the peaks above 8.0 ppm to amides of amino acids would be in agreement with both CEST measurements^{128,150,175} and also the downfield MRS measurements (see chapter 4 and subchapter 5.13).

The contributions of the different amino acids, contributing to the broad in vivo macromolecular resonances are in agreement with the assignments by Behar et al.^{31,32} for example alanine (ALA), leucine (LEU), glutamic acid (GLU), glutamine (GLN), lysine (LYS), methionine (MET). Additionally, not assigned cross-peaks and resonances seen in that work of Behar et al.^{31,32} would match those of proline (PRO) from this fit.

The fits of tyrosine (TYR) and phenylalanine (PHE) are in agreement with the cross-peaks seen in the downfield COSY spectra of Nagarajan et al.,¹⁶⁵ and Waisbren et al.¹⁷⁰

There is a substantial spectral overlap between GLU and GLN and hence per subject fits weighted these contributions differently. Similarly, the overlaps between LEU, isoleucine (ILE), and valine (VAL) are neither distinguishable, the main contribution being assigned to LEU for most fits.

Povazan et al.⁷⁸ presented the spatial distribution of the macromolecular peaks by using MRSI. These trends are matching well with this AA fitting model. Macromolecular peaks at 2.04, 2.26, 3.77 ppm, which have shown similar trends of increased concentrations in GM, were assigned by this model to coupled GLU, GLN, and PRO peaks. Mostly homogeneous distribution of macromolecular peaks at 1.43, 1.67 and 2.99 ppm are fit with ALA and LYS. The peak at 3.2 ppm with a higher white matter content is fit in our model with arginine (ARG), which has minor contributions at 1.9 ppm. Furthermore, a supposed dominant GM content of the GLU and GLN amino acids also matches the high GM contents of the free-floating metabolites glutamate and glutamine^{77,78}.

The measured T_2^{app} of the downfield peaks: DF_{6.83}, DF_{7.04}, DF_{7.30}, and DF_{7.48}, namely 20 to 32 ms (see table Table 4.3) are in the same range as those of the upfield macromolecules³⁰. Hence, the assignment of these peaks to AAs, similarly to the upfield MM spectra is plausible. The same range of relaxation times was also found for DF_{8.18}, DF_{8.37}, and NAA Broad, which could indeed form the amide resonances of the amino acids, considering their exchange behavior with water, and hence decay, as described above.

While all the macromolecular peaks have the short T_2^{eff} (16 to 35 ms), the peaks at 0.92, 1.21, and 1.39 have the longest relaxation times of 30 to 35 ms. These peaks are fitted in our model by ALA, threonine (THR), and the very similar resonances of LEU, ILE, and VAL. None of these amino acids has a significant resonance in other parts of the spectrum. The MM peak with the shortest T_2^{eff} on the other hand, is at 2.70 ppm, which was assigned by our model to aspartic acid (ASP), which neither has a significant contribution in other parts of the spectra.

While the DIR MM spectra are known to have contributions of residual tCr(CH₂), this metabolite probably overfits both the glycine (GLY) and serine (SER) AA peaks. The only

non-amide peak of GLY is from $H^{\alpha 2}$ and $H^{\alpha 3}$ with the chemical shift centered at 3.95 ppm. SER has a resonance overlapped by water, and an amide peak exchanging with water, leaving only its $H^{\beta 2}$ and $H^{\beta 3}$ peaks visible in our MM spectra. Both $H^{\beta 2}$ and $H^{\beta 3}$ are resonating at 3.89 ppm. Because of this severe overlap, LCModel did not fit these two AAs, although both are reported with relatively high concentrations in the human brain. In the fit residual there is an apparent peak at 7.04 ppm not fitted by the AA model, which likely belongs to homocarnosine (see chapter 4) since the used DIR pulse sequence would not affect this metabolite.

The fitting model at the moment is far from being finished. There is still a significant fit residual in the upfield region partly due to the inability of the spectral fitting software LCModel to correctly describe the unusual histogram lineshapes while introducing a lineshape distortion on individual AAs (see right-hand side of the fitted peaks of ALA, LYS, PRO, or THR in Figure 6.8). The lineshape problems arise both from the LCModel software's inability to work with broad asymmetric basis set peaks, but also due to the AA histograms are having broader peaks than actually occurring in the measured brain spectra. These broad histograms originate from the BMRB data bank, which includes paramagnetic protein measurements, or measurements at different pH or temperature than in vivo. These should be excluded from the .csv tables used for the creation of the basis sets, or they should be corrected for the pH as described by the measurements of Platzer et al.¹⁷⁶ The lineshape distortions created by LCModel could be eliminated in future by using another fitting software. For instance, ProFit-v3 could be developed to fit the MMs to the AA fit model in future (see chapter 3).

Because of these necessary improvements and missing cross-validations, quantitative results are not reported in this study. Also, all the different fitted AA concentrations should be corrected for their T_2 relaxation time. Assuming the reported T_2^{eff} values, an AA with a T_2^{eff} of 35 ms will retain 50% of its magnetization at $TE = 24$ ms, whereas, an AA with a T_2^{eff} of 15 ms will retain only 20% of its magnetization. Due to the multiple resonances of each AA, using the correct factors for the relaxation correction is difficult. Hence, the AA concentrations should be evaluated first on a very short TE sequence or even directly on FIDs using sequences, such as ISIS.

Nevertheless, the AA fitting model is in agreement with literature by not fitting cystathionine (CYS), histidine (HIS), and tryptophan (TRP), since these AAs have the lowest natural abundance. These are often at detection limit and have the lowest reported concentrations in the human brain as measured using quantitative paper chromatography in biopsies or post mortem^{177,178}. The AAs fitted in this work, which have the lowest concentrations were ARG and PHE, in agreement with the paper chromatography studies^{177,178}. All other AAs have higher concentrations, but there are several variations between GM and WM, proteolipid protein and residual protein, or compartmentalization (nucleus, mitochondria, microsoma, etc.). Unfortunately, at the moment, the origin of the MM signals measured by ¹H-MRS is not known²⁷. Neither were T_2^{eff} corrections performed on this data, and hence, no conclusions on the agreement or disagreement in the fitted concentrations can be drawn.

6.2 Conclusion

Broad signals underlying in vivo ¹H MRS spectra are referred to in the literature as macromolecules and have been assigned to AAs by Behar et al.^{31,32} These amino acids are linked through chemical bonds into chains of AAs forming together peptides and proteins. Depending on the three-dimensional protein structure, AAs have different chemical shifts as published in the protein databases, like BMRB¹⁶⁸. This work used these published chemical shifts of AAs to create for the first time a fitting model for the in vivo brain detectable macromolecular signals. The used AA histogram model reflected overall well the MM spectra, and several agreements throughout the literature were found to the fitted model. Nevertheless, the fitting model will need more improvements to allow appropriate quantification of the AAs from the MM spectra. This could prove useful both in order to determine the origin of these MM signals but also to provide clinical markers for observed changes in the MM spectra in pathologies^{179,180}.

7 Conclusion and Outlook

This thesis presents both work on MRS fitting algorithm and fit model development and new peak assignments for macromolecules and downfield resonances, which were possible due to the ultra-high-field (9.4 T MR scanner) measurements with advanced MRS sequences, which do not perturb the water signal (metabolite-cycling), as introduced in chapter 1.

In chapter 2, we have shown the role of spline baselines and macromolecular baselines on the fitting of metabolites. Based on this knowledge, the newly developed ProFit-v3 fitting algorithm (chapter 3), includes both an adaptive baseline handling and prior-knowledge on macromolecules and metabolites to handle the very ill-posed problem of metabolite fitting.

Chapter 4 and 5 focus on the downfield spectra. The novelty in chapter 4 is the pH estimation through the fitting, followed by the calculation of T_2^{app} relaxation times, concentrations and linewidth properties of these peaks. These values, together with chemical shifts, and the analysis of exchange behavior, are used in chapter 5 to assign the unknown peaks to metabolite and macromolecular contributions. These peak assignments are discussed not only in the context of the results from this work but also in the context of other measurements of the downfield spectra.

Finally, chapter 6 presents the novel work on creating a fitting model using amino acids to characterize the macromolecular spectra.

Since the newly developed fitting algorithm ProFit-v3 was not fully developed at the time of the investigations performed in chapters 4 to 6, the LCModel software was used for fitting those spectra. In chapter 4, the commercial LCModel software was adopted to quantify the not assigned downfield peaks, to evaluate T_2 relaxation times, and to estimate pH values. In chapter 6, LCModel was tuned to the novel modelling of the MM spectrum as individual amino acid contributions. However, these solutions were somewhat challenging to achieve with LCModel and show capabilities, which should be included in the ProFit-v3 software in future to handle this type of data.

While the work from chapters 2, 3, and 4 show potential problems and software solutions to quantify MRS spectra, the peak assignments from chapter 5 and 6 expand the potential clinical biomarkers significantly.

8 Abbreviations

$\Delta\nu_{1/2}$: linewidth (equivalent to FWHM)	DFx.xx: DF peak at the chemical shift of x.xx ppm
$\Delta\nu_{micro,macro}$: linewidth due to micro- and macro-susceptibility effects	DIR: double-inversion-recovery
$\Delta\nu_{residual}$: linewidth without T2 and $\Delta\nu_{micro,macro}$ effects	FDR: False Discovery Rate
1H-MRS: proton MRS	FID: free-induction-decay
31P MRS: phosphorus MRS	FQN: fit-quality-number
AA: amino acid	FWHM: Full-width half maximum or $\Delta\nu_{1/2}$
ALA: alanine (AA)	GABA: γ -aminobutyric acid
APT: amide proton transfer	GLU: glutamic acid (AA)
ARG: arginine (AA)	Glu: glutamate
ASN: asparagine (AA)	Gln: glutamine
Asp: aspartate	GLN: glutamine (AA)
ASP: aspartic acid (AA)	GM: grey-matter
ATP: adenosine triphosphate	GPC: glycerophosphocholine
BMRB: Biological Magnetic Resonance Bank	GSH: glutathione
CEST: chemical exchange saturation transfer	Gly: glycine
Cr: creatine	GLY: glycine (AA)
CRLB: Cramer Rao Lower Bound	hCs: homocarnosine
CSDE: chemical shift displacement error	hist: histidine
CSF: cerebrospinal fluid	HIS: histidine (AA)
CYS: cystathionine (AA)	HSVD: Hankel singular value decomposition
DKNTMN: spline stiffness parameter of LCModel software	ILE: isoleucine (AA)
DF: downfield	k: chemical exchange rate
	Lac: lactate
	LEU: leucine (AA)
	IPL: left parietal lobe
	LYS: lysine (AA)

MC: metabolite-cycling
MET: methionine (AA)
mI: myo-inositol
MM: macromolecule or macromolecular
Mx.xx: MM peak at the chemical shift of
x.xx ppm
MMB: macromolecular basis set
MR: magnetic resonance
MRI: magnetic resonance imaging
MRS: magnetic resonance spectroscopy
MRSI: magnetic resonance spectroscopic
imaging
NAA: N-acetylaspartate
NAA(CH₂): CH₂ resonances of aspartyl
moiety of NAA
NAA(CH₃): acetyl moiety of NAA
NAAG: N-acetylaspartylglutamate
NAD⁺: nicotinamide adenine
dinucleotide
NEX: number of excitations
NMR: nuclear magnetic resonance
OccL: occipital lobe
OVS: outer volume suppression
PCho: phosphocholine
PCr: phosphocreatine
PE: phosphoethanolamine
PHE: phenylalanine (AA)
PRO: proline (AA)
RF: radio-frequency
ROI: region of interest
SD: standard deviation

SER: serine (AA)
sI: scyllo-inositol
SNR: signal-to-noise ratio
STEAM: stimulated echo acquisition mode
Tau: taurine
T1: longitudinal relaxation time
T2: transverse (spin-spin) relaxation time
 T_2^{eff} : T2 relaxation time including also
unknown J-coupling effects (used for
MM peaks)
 T_2^{app} : T2 relaxation time including both
unknown J-coupling effects and
chemical exchange (used for DF peaks)
 T_2^{corr} : T_2^{app} relaxation times corrected for
exchange rates k
tCho: total choline composed of GPC and
PCho
tCho+: total choline and PE
tCr: total creatine composed of Cr and PCr
tCr(CH₃): methyl moiety of tCr
tCr(CH₂): methylene moiety of tCr
TE: echo time
THR: threonine (AA)
TR: repetition time
TRP: tryptophan (AA)
TYR: tyrosine (AA)
UHF: ultra-high field
VAL: valine (AA)
WM: white matter
WS: water pre-saturation

9 Curriculum Vitae

Tamás Borbáth

Address: Im Winkelrain. 56, 72076 Tübingen
Mobile: +49157 70305400
E-Mail: tamas.borbath@outlook.com
Date of birth: 18.11.1989
Nationalities: EU citizen: Romanian, Hungarian, German



EDUCATION

- 02/2016 – now **PhD Student**, *Eberhard Karls Universität Tübingen*, Bioinformatics
Thesis: “Magnetic Resonance Spectroscopy: Quantitative Analysis of Brain Metabolites and Macromolecules”
- 10/2013 – 11/2015 **Master of Science with honours**, *Technical University of Munich*,
Computational Science and Engineering (Cumulative grade: 1.4)
Thesis: “Enhancing Software Tools in Magnetic Resonance Spectroscopy”
- 10/2009 – 07/2013 **Bachelor of Science**, *Transilvania University of Braşov*
Computer Engineering (Cumulative grade: 9.75 from 10)
Thesis: “Speed control using image processing on an embedded system”
- 10/2011 – 08/2012 **Erasmus exchange year**, *Ruhr University Bochum*
Majors in information technology, cryptography and embedded systems
(Cumulative grade: 93.58%)
- 09/2005 – 07/2009 **Baccalaureate**, *Áprily Lajos High School* (Cum. Grade: 9.68 from 10)

WORK EXPERIENCE

- 02/2016 – now **Computational Science / M.R. Engineer PhD Student**,
Max Planck Institute of Biological Cybernetics
Software development for a magnetic resonance spectroscopy
Module and engineering of a clinical decision support system
- 05/2014 – 12/2015 **Student Project + Intern Software Developer (8 + 8 months)**, *General
Electric Research Center*
Engineering of the software framework, development of graphical user
interface and software back-end of a magnetic resonance spectroscopy
tool
- 10/2014 – 02/2015 **Academic Course Tutor**, *Technical University of Munich*
Tutoring of the graduate course Advanced Programming (C++).

- 06/2014 – 09/2014 **Research Assistant, Technical University of Munich**
Development of image processing algorithms for 3D endoscopy images
- 03/2014 – 05/2014 **Research Assistant, Technical University of Munich**
Programming BLAS routines for FPGAs.

PROJECTS

- 05/2014 – 02/2015 **Code optimization for High Performance Computing**, team of two
Parallelization with MPI
- 09/2014 – 10/2014 **Ferienakademie Project**, Team leader of 16 students
Image processing, Kinect camera, simulations, visualizations
- 01/2013 – 02/2013 **Texture detection in a painting (competition)**, image processing
- 10/2011 – 01/2012 **Cryptographic cyphers on embedded systems**
- 11/2010 – 03/2011 **Autonomous Drive of a model car**, team of five
Command and control of GPIOs on an embedded system

VOLUNTEERING AND SECONDARY ACTIVITIES

- 05/2016 – now **DAAD Freundeskreis**, organizing events for international students
- 03/2014 – 06/2014 **TEDxTUM**, Event organization
- 05/2010 – 09/2013 **Tour guide**, *World Synergy Travel and Active Holidays agencies*
- 10/2009 – 03/2011 **AIESEC Braşov**, international student organization
leadership, internationalism, project management
- 12/2006 – 02/2013 **Ski instructor**, *Ana Hotels*

COMPUTER SKILLS

- Programming *Advanced: C/C++, Matlab, UML, SW-patterns, optimization algorithms*
Intermediate: Python, Java, R, Assembly, MPI, OpenMP
- Applications *Advanced: MS Office, LibreOffice, LaTeX*
- Operating Systems *Advanced: Microsoft Windows, Linux*

LANGUAGES

- Hungarian Mother language (C2)
- Romanian Second language (C2)
- German Full professional proficiency (C2)
Deutsches Sprachdiplom – Level C1– 05/2009
7 years study at the “**Johannes Honterus**“ **German School**
- English Full professional proficiency (C2)
Cambridge Advanced English – Level C1– 06/2010
- Spanish Elementary proficiency (A2)

10 List of publications

10.1 Publications included in this doctoral thesis

Journal Articles - first or shared-first author:

1. Giapitzakis IA*, **Borbath T***, Murali-Manohar S, Avdievich N, Henning A. “Investigation of the influence of macromolecules and spline baseline in the fitting model of human brain spectra at 9.4 T”. *Magnetic resonance in medicine*, 2019;81(2):746-758. DOI: [mrm.27467](#)
2. **Borbath T***, Murali-Manohar S*, Wright AM, Henning A. “In vivo characterization of downfield peaks at 9.4 T: T₂ relaxation times, quantification, pH estimation, and assignments.” *Magnetic resonance in medicine*, 2020. DOI: [mrm.28442](#)
3. **Borbath T**, Dorst J, Murali-Manohar S, Wright AM, Henning A. “ProFit-v3 - a 1-D fitting software and open-source validation datasets.” [Submitted](#)
4. **Borbath T**, Murali-Manohar S, Henning A. “Human brain downfield peak assignments – a review from 9.4 T measurements perspective.” [In preparation](#)

*Equal contributions to the publication

Conference talks:

1. **Borbath T**, Murali Manohar S, Henning A. “Towards a Fitting Model of Macromolecular Spectra: Amino Acids.” Proc. of the 27th Annual Meeting of the International Society for Magnetic Resonance in Medicine, 2019, Montréal, QC, Canada.
2. **Borbath T**, Giapitzakis IA, Henning A. “The influence of the macromolecular and spline baselines on quantification results at 9.4 T”, University Hospital

Tuebingen's Workshop on Proton MR Spectroscopy in Neuroradiological Diagnostics, 2018, Tuebingen, Germany

Conference posters:

1. Murali Manohar S, **Borbath T**, Wright A, Henning A. "Characterization of Downfield Resonances and their T_2 Relaxation Times in Human Brain at 9.4 T." Proc. of the 27th Annual Meeting of the International Society for Magnetic Resonance in Medicine, 2019, Montréal, QC, Canada.
2. Murali Manohar S, **Borbath T**, Fichtner N, Giapitzakis I, Zaldivar D, Kreis R, Henning A. "Estimation of T_2 Relaxation Times of Downfield Peaks in Human Brain at 9.4 T." Proc. of the 26th Annual Meeting of the International Society for Magnetic Resonance in Medicine, 2018, Paris, France
3. **Borbath T**, Giapitzakis I, Murali Manohar S, Henning A. "Do macromolecular and spline baselines affect the metabolite quantification at 9.4T?", Proc. of the 34th Annual Meeting of the European Society for Magnetic Resonance in Medicine and Biology, 2017, Barcelona, Spain.

10.2 Publications not included in this thesis

Journal Articles - shared-first author:

1. Murali-Manohar S*, **Borbath T***, Wright AM, Soher B, Mekte R, Henning A. "T₂ relaxation times of macromolecules and metabolites in the human brain at 9.4 T." Magnetic resonance in medicine, 2020;84:542–558. DOI: [mrm.28174](https://doi.org/10.1002/mrm.28174)

Journal Articles - co-authored:

1. Cudalbu C, Behar K, Bhattacharyya P, Bogner W, **Borbath T**, de Graaf R, Gruetter R, Henning A, Juchem C, Kreis R, Lee P, Lei H, Marjańska M, Mekte R, Murali-Manohar S, Považan M, Rackayová V, Simicic D, Slotboom J, Soher B, Starcuk Z, Starcukova J, Tkáč I, Williams S, Wilson M, Wright AM, Xin L,

- Mlynárik V. "Contribution of macromolecules to brain ^1H MR spectra: Experts' consensus recommendations.", NMR in Biomedicine, 2020 DOI: [nbm.4393](#)
2. Murali-Manohar S*, Wright AM*, **Borbath T**, Avdievich NI, Henning A. "A novel method to measure T_1 -relaxation times of macromolecules and quantification of the macromolecular resonances." Magnetic Resonance in Medicine, 2020. DOI: [mrm.28484](#)
 3. Avdievich N, Giapitzakis I, Pfrommer A, **Borbath T**, Henning A. "Combination of surface and 'vertical' loop elements improves receive performance of a human head transceiver array at 9.4 T." NMR in Biomedicine 2018;31(2):e3878. DOI: [nbm.3878](#)
 4. Murali-Manohar S*, Wright AM*, **Borbath T**, Avdievich NI, Henning A. "Relaxation corrected macromolecular model enables accurate determination of ^1H longitudinal T_1 -relaxation times and concentrations of human brain metabolites at 9.4 T." [Submitted](#)
 5. Simicic D, Rackayova V, Xin L, Tkac I, **Borbath T**, Starcuk Z, Starcukova J, Lanz B, Cudalbu C. "Macromolecule signals in Rat Brain ^1H MR Spectra at 9.4T: parametrization, spline baseline estimation and T_2 relaxation times." [Submitted](#)
 6. Dorst J, **Borbath T**, Ruhm L, Avdievich N, Henning A. "Simultaneous Detection of Metabolite Concentration Changes, Water BOLD Signal and pH Changes during Visual Stimulation in the Human Brain at 9.4T" [In preparation](#)

Conference talks:

1. **Borbath T**, Giapitzakis IA, Murali Manohar SV, Henning A. "Fitting comparison for 9.4T 1D semi-LASER and 2D-J-resolved semi-LASER data", Proc. of the 25th Annual Meeting of the International Society for Magnetic Resonance in Medicine, 2017, Honolulu, HI, USA

Conference posters:

1. Dorst J, **Borbath T**, Ruhm L, Avdievich N, Henning A. " ^{31}P Transversal Relaxation Times in the Human Brain at 9.4T", Proc. of the 28th Annual Meeting of the International Society for Magnetic Resonance in Medicine, 2020

2. Murali-Manohar S., **Borbath T.**, Henning A.: Estimation of T_2 Relaxation Times and Absolute Quantification of Metabolites in the Human Brain at 9.4 T." Proc. of the 36th Annual Meeting of the European Society for Magnetic Resonance in Medicine and Biology, 2019, Rotterdam, Netherlands.
3. Murali Manohar S, Wright A, **Borbath T**, Henning A. "Longitudinal Relaxation times of Macromolecular Resonances at 9.4 T in Human Brain", Proc. of the 27th Annual Meeting of the International Society for Magnetic Resonance in Medicine, 2019, Montréal, QC, Canada.
4. Wright A, Murali Manohar S, **Borbath T**, Henning A. "Longitudinal Relaxation Times of Metabolites in vivo at 9.4 T.", Proc. of the 27th Annual Meeting of the International Society for Magnetic Resonance in Medicine, 2019, Montréal, QC, Canada.
5. **Borbath T**, Murali Manohar S, Henning A. "Estimation of T_{p2} Relaxation Times of Macromolecules in Human Brain Spectra at 9.4 T." MRS Workshop 2018 Metabolic Imaging, Utrecht, The Netherlands
6. Murali Manohar S, Giapitzakis I, **Borbáth T**, Gaertner M, Henning A. "Qualitative Comparison between In Vivo J-Resolved Semi-LASER at 3 T and 9.4 T.", Proc. of the 25th Annual Meeting of the International Society for Magnetic Resonance in Medicine, 2017, Honolulu, HI, USA
7. Coello E, Janich M, Schirmer T, Noeske R, **Borbáth T**, Haase A, Schulte R. "Overdiscrete Reconstruction in Echo-Planar Spectroscopic Imaging with Auto Calibrated B_0 Field Map Estimation." Proc. of the 24th Annual Meeting of the International Society for Magnetic Resonance in Medicine, 2016, Singapore, Singapore

11 Statement of Contributions

Journal Articles - first or shared-first author:

1. *Investigation of the influence of macromolecules and spline baseline in the fitting model of human brain spectra at 9.4 T*

In this study, the effects of the origin of the macromolecular baseline and the stiffness of the spline baseline on metabolite fitting were investigated. It was found that a macromolecular baseline acquired from a different brain location, with significantly different tissue composition impacted the metabolite quantification to a small extent. On the other hand, it was observed that the used stiffness of the spline baseline had a significantly higher impact on the metabolite quantification, multiple metabolite concentrations being altered considerably from the assumed ground truth. Lastly, simulated macromolecular spectra with a flexible spline baseline lead to significantly altered metabolite concentrations for almost all metabolites.

- **Borbath T** – Had the scientific idea of evaluating the spline baseline contributions to the fitting with the LCModel software. Performed the post-processing of the spectra, set up the LCModel analysis and analyzed the data. Had minor contributions in data acquisition (data originates from another publication). Wrote the major part of the manuscript.
- **Giapitzakis IA** – Had the scientific idea of investigating the effects of the origin of the macromolecular baseline on fitting. Was responsible for the data acquisition and gave advice and some code for the post-processing and analysis of the data. Wrote parts of the manuscript.
- **Murali-Manohar S** – Contributed to data acquisition and proofread the manuscript.
- **Avdievich N** – Provided the RF coil for 9.4T
- **Henning A** – Supervised project and advised on the manuscript

2. *In vivo* characterization of downfield peaks at 9.4 T: T_2 relaxation times, quantification, pH estimation, and assignments.

In this study, the downfield spectra of the human brain at 9.4 T was investigated. Using the homocarnosine peak pH values for the individual subjects were estimated. For the different downfield peaks T_2 relaxation times, concentrations and linewidth properties were derived. These characteristics were used for the discussion of possible peak assignments.

- **Borbath T** – Had the scientific idea of pH estimation, linewidth analysis and peak assignments. Performed the post-processing of the spectra, set up the LCModel analysis and analyzed the data. Had minor contributions in data acquisition. Wrote the major part of the manuscript.
- **Murali-Manohar S** – Had the scientific idea of measuring T_2 relaxation times of downfield spectra. Was responsible for the data acquisition and gave extensive advice for the post-processing and analysis of the data. Wrote parts of the manuscript.
- **Wright AM** – Contributed to data acquisition and proofread the manuscript.
- **Henning A** – Supervised project and advised on the manuscript

3. *ProFit-v3 - a 1-D fitting software and open-source validation datasets.*

In this study, a new open-source fitting algorithm, named ProFit-v3, was developed. ProFit-v3 includes an adaptive spline baseline determination and an advanced cost function. The fitting results of ProFit-v3 were extensively evaluated, both on simulated and in vivo data. The fitting results are also compared to the commercial LCModel software.

- **Borbath T** – Had the scientific ideas of the developments of the fitting algorithm and its validation. Developed the software, created the simulated and in vivo data for the precision and accuracy analysis. In vivo data were reused from previous acquisitions performed for another publication. Wrote the manuscript.

- **Dorst J** – Supported the data analysis with extensive discussions and proofread the manuscript.
- **Murali-Manohar S** – Supported the data analysis with extensive discussions and proofread the manuscript.
- **Wright AM** – Supported the data analysis with extensive discussions and proofread the manuscript.
- **Henning A** – Supervised project and advised on the manuscript

4. *Human brain downfield peak assignments – a review from 9.4 T measurements perspective.*

In this study, a comprehensive discussion on the downfield peaks is given. All metabolites with reported resonances in the downfield spectrum are analyzed on whether their resonances can appear in the downfield spectrum. While the discussion focusses on the in vivo measurements of the human brain at 9.4 T, the results include most publications reporting downfield spectra measurements.

- **Borbath T** – Had the scientific idea of reviewing the literature on downfield spectra and deriving the peak assignments. Performed the data analysis to permit further conclusions, beyond the results existing in the previous literature. Wrote the manuscript.
- **Murali-Manohar S** – Supported the literature analysis with extensive discussions and proofread the manuscript.
- **Henning A** – Supervised project and advised on the manuscript

Conference talks:

1. *Towards a Fitting Model of Macromolecular Spectra: Amino Acids*

In this study, a new fitting model to fit the macromolecular spectra is presented. Histograms of the proton resonances of 20 amino acids were extracted from a protein data bank, and basis sets for each amino acid were created. The fit results are finally interpreted in the context of other existing literature.

- **Borbath T** – Had the scientific idea of modelling the macromolecular spectrum as a combination of amino acids. Performed the post-processing of the spectra, created the fit model based on the histograms of the protein data bank and analyzed the data. Wrote the manuscript.
- **Murali-Manohar S** – Was responsible for the in vivo data acquisition and proofread the manuscript.
- **Henning A** – Supervised project and advised on the manuscript

2. *The influence of the macromolecular and spline baselines on quantification results at 9.4 T*

In this study, the first results from journal article 1 ([mrm.27467](#)) were presented at a workshop.

- **Borbath T** – Had the scientific idea of evaluating the spline baseline contributions to the fitting with the LCModel software. Performed the post-processing of the spectra, set up the LCModel analysis and analyzed the data. Had minor contributions in data acquisition (data originates from another publication). Wrote the manuscript.
- **Giapitzakis IA** – Had the scientific idea of investigating the effects of the origin of the macromolecular baseline on fitting. Was responsible for the data acquisition and gave advice and some code for the post-processing and analysis of the data.
- **Henning A** – Supervised project and advised on the manuscript

Bibliography

1. Gasparovic C, Song T, Devier D, et al. Use of tissue water as a concentration reference for proton spectroscopic imaging. *Magnetic resonance in medicine*. 2006;55(6):1219-1226.
2. De Graaf RA. *In vivo NMR spectroscopy: principles and techniques*. John Wiley & Sons; 2019.
3. Keeler J. *Understanding NMR spectroscopy*. John Wiley & Sons; 2011.
4. Öz G, Alger JR, Barker PB, et al. Clinical proton MR spectroscopy in central nervous system disorders. *Radiology*. 2014;270(3):658-679.
5. Proctor W, Yu F. The dependence of a nuclear magnetic resonance frequency upon chemical compound. *Physical Review*. 1950;77(5):717.
6. Harris RK, Becker ED, De Menezes SMC, Goodfellow R, Granger P. NMR nomenclature. Nuclear spin properties and conventions for chemical shifts (IUPAC Recommendations 2001). *Pure and Applied Chemistry*. 2001;73(11):1795-1818.
7. Govind V, Young K, Maudsley AA. Corrigendum: Proton NMR chemical shifts and coupling constants for brain metabolites. Govindaraju V, Young K, Maudsley AA, *NMR Biomed*. 2000; 13: 129–153. *NMR in Biomedicine*. 2015;28(7):923-924.
8. Chavhan GB, Babyn PS, Thomas B, Shroff MM, Haacke EM. Principles, techniques, and applications of T2*-based MR imaging and its special applications. *Radiographics*. 2009;29(5):1433-1449.
9. Giapitzakis I-A, Shao T, Avdievich N, Mekle R, Kreis R, Henning A. Metabolite-cycled STEAM and semi-LASER localization for MR spectroscopy of the human brain at 9.4T. *Magn Reson Med*. 2017.
10. de Graaf RA. Single Volume Localization and Water Suppression. *In Vivo NMR Spectroscopy*. John Wiley & Sons, Ltd; 2007:297-348.
11. Tkáč I, Gruetter R. Methodology of 1 H NMR spectroscopy of the human brain at very high magnetic fields. *Applied magnetic resonance*. 2005;29(1):139.
12. Fichtner ND, Giapitzakis IA, Avdievich N, et al. In vivo characterization of the downfield part of 1 H MR spectra of human brain at 9.4 T: Magnetization exchange with water and relation to conventionally determined metabolite content. *Magnetic resonance in medicine*. 2018;79(6):2863-2873.
13. de Graaf RA. In Vivo NMR Spectroscopy – Static Aspects. *In Vivo NMR Spectroscopy*. John Wiley & Sons, Ltd; 2007:43-110.

14. Govindaraju V, Young K, Maudsley AA. Proton NMR chemical shifts and coupling constants for brain metabolites. *NMR in Biomedicine*. 2000;13(3):129-153.
15. Provencher S. LCMModel & LCMgui user's manual. *Stephen W Provencher*. 2005.
16. Provencher SW. Estimation of metabolite concentrations from localized in vivo proton NMR spectra. *Magnetic resonance in medicine*. 1993;30(6):672-679.
17. Provencher SW. Automatic quantitation of localized in vivo ¹H spectra with LCMModel. *NMR in Biomedicine*. 2001;14(4):260-264.
18. Barker PB, Lin DD. In vivo proton MR spectroscopy of the human brain. *Progress in Nuclear Magnetic Resonance Spectroscopy*. 2006;49(2):99-128.
19. Mangia S, Tkáč I, Gruetter R, et al. Sensitivity of single-voxel ¹H-MRS in investigating the metabolism of the activated human visual cortex at 7 T. *Magnetic resonance imaging*. 2006;24(4):343-348.
20. Mangia S, Tkáč I, Logothetis NK, Gruetter R, de Moortele V, Uğurbil K. Dynamics of lactate concentration and blood oxygen level-dependent effect in the human visual cortex during repeated identical stimuli. *Journal of neuroscience research*. 2007;85(15):3340-3346.
21. Just N. Proton functional magnetic resonance spectroscopy in rodents. *NMR in Biomedicine*. 2020:e4254.
22. Ligneul C, Fernandes FF, Shemesh N. Functional Magnetic Resonance Spectroscopy in the mouse. *arXiv preprint arXiv:200108505*. 2020.
23. Bogner W, Gruber S, Trattnig S, Chmelik M. High-resolution mapping of human brain metabolites by free induction decay ¹H MRSI at 7 T. *NMR in Biomedicine*. 2012;25(6):873-882.
24. Deelchand DK, Van de Moortele PF, Adriany G, et al. In vivo ¹H NMR spectroscopy of the human brain at 9.4 T: initial results. *J Magn Reson*. 2010;206(1):74-80.
25. Lopez-Kolkovsky AL, Mériaux S, Boumezbeur F. Metabolite and macromolecule T1 and T2 relaxation times in the rat brain in vivo at 17.2 T. *Magnetic resonance in medicine*. 2016;75(2):503-514.
26. Redpath TW. Signal-to-noise ratio in MRI. *The British Journal of Radiology*. 1998;71(847):704-707.
27. Cudalbu C, Behar KL, Bhattacharyya PK, et al. Contribution of macromolecules to brain ¹H MR spectra: Experts' consensus recommendations. *NMR in biomedicine*. 2020:e4393.
28. Wyss PO, Bianchini C, Scheidegger M, et al. In vivo estimation of transverse relaxation time constant (T2) of 17 human brain metabolites at 3T. *Magnetic resonance in medicine*. 2018.

29. Landheer K, Gajdošík M, Treacy M, Juchem C. Concentration and effective T2 relaxation times of macromolecules at 3T. *Magnetic Resonance in Medicine*. 2020.
30. Murali-Manohar S, Borbath T, Wright AM, Soher B, Mekte R, Henning A. T2 relaxation times of macromolecules and metabolites in the human brain at 9.4 T. *Magnetic resonance in medicine*. 2020;84:542–558.
31. Behar KL, Ogino T. Characterization of macromolecule resonances in the 1H NMR spectrum of rat brain. *Magnetic resonance in medicine*. 1993;30(1):38-44.
32. Behar KL, Rothman DL, Spencer DD, Petroff OA. Analysis of macromolecule resonances in 1H NMR spectra of human brain. *Magnetic Resonance in Medicine*. 1994;32(3):294-302.
33. Avdievich NI, Hoffmann J, Shajan G, et al. Evaluation of transmit efficiency and SAR for a tight fit transceiver human head phased array at 9.4 T. *NMR Biomed*. 2017;30(2):1-12.
34. Pohmann R, Speck O, Scheffler K. Signal-to-noise ratio and MR tissue parameters in human brain imaging at 3, 7, and 9.4 tesla using current receive coil arrays. *Magnetic Resonance in Medicine*. 2016;75(2):801-809.
35. Giapitzakis I-A, Avdievich N, Henning A. Characterization of macromolecular baseline of human brain using metabolite cycled semi-LASER at 9.4 T. *Magn Reson Med*. 2018.
36. Schaller B, Xin L, Gruetter R. Is the macromolecule signal tissue-specific in healthy human brain? A 1H MRS study at 7 tesla in the occipital lobe. *Magnetic Resonance in Medicine*. 2014;72(4):934-940.
37. Snoussi K, Gillen JS, Horska A, et al. Comparison of brain gray and white matter macromolecule resonances at 3 and 7 Tesla. *Magn Reson Med*. 2015;74(3):607-613.
38. Cudalbu C, Mlynarik V, Gruetter R. Handling macromolecule signals in the quantification of the neurochemical profile. *J Alzheimers Dis*. 2012;31 Suppl 3:S101-115.
39. Behar KL, Rothman DL, Spencer DD, Petroff OA. Analysis of macromolecule resonances in 1H NMR spectra of human brain. *Magn Reson Med*. 1994;32(3):294-302.
40. Fuchs A, Luttje M, Boesiger P, Henning A. SPECIAL semi-LASER with lipid artifact compensation for 1H MRS at 7 T. *Magn Reson Med*. 2013;69(3):603-612.
41. Schaller B, Xin L, Cudalbu C, Gruetter R. Quantification of the neurochemical profile using simulated macromolecule resonances at 3 T. *NMR Biomed*. 2013;26(5):593-599.
42. Provencher SW. Automatic quantitation of localized in vivo 1H spectra with LCModel. *NMR Biomed*. 2001;14(4):260-264.

43. Pfeuffer J, Tkáč I, Provencher SW, Gruetter R. Toward an in vivo neurochemical profile: quantification of 18 metabolites in short-echo-time ¹H NMR spectra of the rat brain. *Journal of magnetic resonance*. 1999;141(1):104-120.
44. Avdievich N, Giapitzakis IA, Henning A. Optimization of the receive performance of a tight-fit receiver phased array for human brain imaging at 9.4T. Paper presented at: 25th Annual Meeting of the ISMRM2017; Honolulu, USA.
45. Hoffmann J, Henning A, Giapitzakis IA, et al. Safety testing and operational procedures for self-developed radiofrequency coils. *NMR Biomed*. 2016;29(9):1131-1144.
46. Mugler JP, 3rd, Brookeman JR. Three-dimensional magnetization-prepared rapid gradient-echo imaging (3D MP RAGE). *Magn Reson Med*. 1990;15(1):152-157.
47. Gruetter R, Tkac I. Field mapping without reference scan using asymmetric echo-planar techniques. *Magn Reson Med*. 2000;43(2):319-323.
48. Versluis MJ, Kan HE, van Buchem MA, Webb AG. Improved signal to noise in proton spectroscopy of the human calf muscle at 7 T using localized B1 calibration. *Magn Reson Med*. 2010;63(1):207-211.
49. Vanhamme L, Sundin T, Hecke PV, Huffel SV. MR spectroscopy quantitation: a review of time-domain methods. *NMR Biomed*. 2001;14(4):233-246.
50. Smith SA, Levante TO, Meier BH, Ernst RR. Computer Simulations in Magnetic Resonance. An Object-Oriented Programming Approach. *J Magn Reson, Series A*. 1994;106(1):75-105.
51. Govindaraju V, Young K, Maudsley AA. Proton NMR chemical shifts and coupling constants for brain metabolites. *NMR Biomed*. 2000;13(3):129-153.
52. Kreis R, Bolliger CS. The need for updates of spin system parameters, illustrated for the case of gamma-aminobutyric acid. *NMR Biomed*. 2012;25(12):1401-1403.
53. Steinke J, Gaser C, Langbein K, et al. Hippocampal metabolism and prefrontal brain structure: A combined ¹H-MR spectroscopy, neuropsychological, and voxel-based morphometry (VBM) study. *Brain Research*. 2017;1677:14-19.
54. Chadzynski GL, Pohmann R, Shajan G, et al. In vivo proton magnetic resonance spectroscopic imaging of the healthy human brain at 9.4 T: initial experience. *Magnetic Resonance Materials in Physics, Biology and Medicine*. 2015;28(3):239-249.
55. Terpstra M, Ugurbil K, Tkac I. Noninvasive quantification of human brain ascorbate concentration using ¹H NMR spectroscopy at 7 T. *NMR in Biomedicine*. 2010;23(3):227-232.

56. Tkac I, Oz G, Adriany G, Ugurbil K, Gruetter R. In vivo ¹H NMR spectroscopy of the human brain at high magnetic fields: metabolite quantification at 4T vs. 7T. *Magn Reson Med.* 2009;62(4):868-879.
57. Gasparovic C, Song T, Devier D, et al. Use of tissue water as a concentration reference for proton spectroscopic imaging. *Magn Reson Med.* 2006;55(6):1219-1226.
58. Hagberg GE, Bause J, Ethofer T, et al. Whole brain MP2RAGE-based mapping of the longitudinal relaxation time at 9.4 T. *NeuroImage.* 2017;144:203-216.
59. Wyss M, Kirchner T, Ringenbach A, Prüssmann KH, Anke. Relaxation Parameter Mapping Adapted for 7T and Validation against Optimized Single Voxel MRS. *In: Proceedings of the 21st Annual Meeting of the ISMRM, Salt Lake City, USA.* 2013:2464.
60. Kreis R. The trouble with quality filtering based on relative Cramér-Rao lower bounds. *Magn Reson Med.* 2016;75(1):15-18.
61. Benjamini Y, Yekutieli D. The control of the false discovery rate in multiple testing under dependency. *Annals of statistics.* 2001:1165-1188.
62. Sawilowsky SS. New effect size rules of thumb. 2009.
63. Lakens D. Calculating and reporting effect sizes to facilitate cumulative science: a practical primer for t-tests and ANOVAs. *Frontiers in Psychology.* 2013;4(863).
64. Avdievich NI, Giapitzakis IA, Pfrommer A, Borbath T, Henning A. Combination of surface and 'vertical' loop elements improves receive performance of a human head transceiver array at 9.4 T. *NMR Biomed.*e3878-n/a.
65. Scheenen TW, Klomp DW, Wijnen JP, Heerschap A. Short echo time 1H-MRSI of the human brain at 3T with minimal chemical shift displacement errors using adiabatic refocusing pulses. *Magn Reson Med.* 2008;59(1):1-6.
66. Pouwels PJW, Frahm J. Differential distribution of NAA and NAAG in human brain as determined by quantitative localized proton MRS. *NMR Biomed.* 1997;10(2):73-78.
67. Gasparovic CM. Adjusting Concentrations for Tissue Composition in Brain: Assumptions & Conundrums. ISMRM Workshop on MR Spectroscopy: From Current Best Practice to Latest Frontiers; 2016; Lake Constance, Germany.
68. Penner J, Bartha R. Semi-LASER 1 H MR spectroscopy at 7 Tesla in human brain: Metabolite quantification incorporating subject-specific macromolecule removal. *Magn Reson Med.* 2014;74(1):4-12.
69. Mekte R, Mlynarik V, Gambarota G, Hergt M, Krueger G, Gruetter R. MR spectroscopy of the human brain with enhanced signal intensity at ultrashort echo times on a clinical platform at 3T and 7T. *Magn Reson Med.* 2009;61(6):1279-1285.

70. Knight-Scott J, Haley AP, Rossmiller SR, et al. Molality as a unit of measure for expressing ¹H MRS brain metabolite concentrations in vivo. *Magn Reson Imaging*. 2003;21(7):787-797.
71. Marjanska M, Auerbach EJ, Valabregue R, Van de Moortele PF, Adriany G, Garwood M. Localized ¹H NMR spectroscopy in different regions of human brain in vivo at 7 T: T2 relaxation times and concentrations of cerebral metabolites. *NMR Biomed*. 2012;25(2):332-339.
72. de Graaf RA, Brown PB, McIntyre S, Nixon TW, Behar KL, Rothman DL. High magnetic field water and metabolite proton T1 and T2 relaxation in rat brain in vivo. *Magn Reson Med*. 2006;56(2):386-394.
73. Allerhand A, Thiele E. Analysis of Carr—Purcell Spin-Echo NMR Experiments on Multiple-Spin Systems. II. The Effect of Chemical Exchange. *The Journal of Chemical Physics*. 1966;45(3):902-916.
74. Michaeli S, Garwood M, Zhu XH, et al. Proton T2 relaxation study of water, N-acetylaspartate, and creatine in human brain using Hahn and Carr-Purcell spin echoes at 4T and 7T. *Magn Reson Med*. 2002;47(4):629-633.
75. Deelchand DK, Henry PG, Marjanska M. Effect of Carr-Purcell refocusing pulse trains on transverse relaxation times of metabolites in rat brain at 9.4 Tesla. *Magn Reson Med*. 2015;73(1):13-20.
76. Öz G, Tkáč I. Short-echo, single-shot, full-intensity proton magnetic resonance spectroscopy for neurochemical profiling at 4 T: Validation in the cerebellum and brainstem. *Magnetic Resonance in Medicine*. 2011;65(4):901-910.
77. Nassirpour S, Chang P, Henning A. High and ultra-high resolution metabolite mapping of the human brain using ¹H FID MRSI at 9.4 T. *Neuroimage*. 2016.
78. Považan M, Strasser B, Hangel G, et al. Simultaneous mapping of metabolites and individual macromolecular components via ultra-short acquisition delay ¹H MRSI in the brain at 7T. *Magnetic resonance in medicine*. 2018;79(3):1231-1240.
79. Cudalbu C, Mlynarik V, Xin L, Gruetter R. Quantification of in vivo short echo-time proton magnetic resonance spectra at 14.1 T using two different approaches of modelling the macromolecule spectrum. *Measurement Science and Technology*. 2009;20(10):104034.
80. Hofmann L, Slotboom J, Jung B, Maloca P, Boesch C, Kreis R. Quantitative ¹H-magnetic resonance spectroscopy of human brain: influence of composition and parameterization of the basis set in linear combination model-fitting. *Magnetic resonance in medicine*. 2002;48(3):440-453.

81. Sibson NR, Dhankhar A, Mason G, Behar K, Rothman D, Shulman R. In vivo ¹³C NMR measurements of cerebral glutamine synthesis as evidence for glutamate–glutamine cycling. *Proceedings of the National Academy of Sciences*. 1997;94(6):2699-2704.
82. Sibson NR, Dhankhar A, Mason GF, Rothman DL, Behar KL, Shulman RG. Stoichiometric coupling of brain glucose metabolism and glutamatergic neuronal activity. *Proceedings of the National Academy of Sciences*. 1998;95(1):316-321.
83. Lu M, Zhu X-H, Zhang Y, Mateescu G, Chen W. Quantitative assessment of brain glucose metabolic rates using in vivo deuterium magnetic resonance spectroscopy. *Journal of Cerebral Blood Flow & Metabolism*. 2017;37(11):3518-3530.
84. Ren J, Sherry AD, Malloy CR. ³¹P-MRS of healthy human brain: ATP synthesis, metabolite concentrations, pH, and T1 relaxation times. *NMR in Biomedicine*. 2015;28(11):1455-1462.
85. Lanz B, Duarte JM, Kunz N, Mlynárik V, Gruetter R, Cudalbu C. Which prior knowledge? Quantification of in vivo brain ¹³C MR spectra following ¹³C glucose infusion using AMARES. *Magnetic Resonance in Medicine*. 2013;69(6):1512-1522.
86. van Ormondt D, Graveron-Demilly D, Sima DM, Van Huffel S, Williams SR. Time-Domain Methods for Quantifying MR Spectra. *eMagRes*: John Wiley & Sons, Ltd; 2007.
87. Pouillet J-B, Sima DM, Van Huffel S. MRS signal quantitation: a review of time-and frequency-domain methods. *Journal of Magnetic Resonance*. 2008;195(2):134-144.
88. Henning A. Advanced Spectral Quantification: Parameter Handling, Nonparametric Pattern Modeling, and Multidimensional Fitting. *eMagRes*. 2016.
89. Das D, Coello E, Schulte RF, Menze BH. Quantification of metabolites in magnetic resonance spectroscopic imaging using machine learning. Paper presented at: International Conference on Medical Image Computing and Computer-Assisted Intervention2017.
90. Vanhamme L, van den Boogaart A, Van Huffel S. Improved method for accurate and efficient quantification of MRS data with use of prior knowledge. *Journal of magnetic resonance*. 1997;129(1):35-43.
91. Ratiney H, Sdika M, Coenradie Y, Cavassila S, Ormondt Dv, Graveron-Demilly D. Time-domain semi-parametric estimation based on a metabolite basis set. *NMR in Biomedicine: An International Journal Devoted to the Development and Application of Magnetic Resonance In vivo*. 2005;18(1):1-13.

92. Wilson M, Reynolds G, Kauppinen RA, Arvanitis TN, Peet AC. A constrained least-squares approach to the automated quantitation of in vivo ¹H magnetic resonance spectroscopy data. *Magnetic resonance in medicine*. 2011;65(1):1-12.
93. Pouillet JB, Sima DM, Simonetti AW, et al. An automated quantitation of short echo time MRS spectra in an open source software environment: AQSES. *NMR in Biomedicine: An International Journal Devoted to the Development and Application of Magnetic Resonance In vivo*. 2007;20(5):493-504.
94. Soher BJ, Young K, Govindaraju V, Maudsley AA. Automated spectral analysis III: application to in vivo proton MR spectroscopy and spectroscopic imaging. *Magnetic Resonance in Medicine*. 1998;40(6):822-831.
95. Young K, Soher BJ, Maudsley AA. Automated spectral analysis II: application of wavelet shrinkage for characterization of non-parameterized signals. *Magnetic resonance in medicine*. 1998;40(6):816-821.
96. Fuchs A, Boesiger P, Schulte RF, Henning A. ProFit revisited. *Magnetic Resonance in Medicine*. 2014;71(2):458-468.
97. Schulte RF, Boesiger P. ProFit: two-dimensional prior-knowledge fitting of J-resolved spectra. *NMR in Biomedicine: An International Journal Devoted to the Development and Application of Magnetic Resonance In vivo*. 2006;19(2):255-263.
98. Soher B, Semanchuk P, Todd D, Steinberg J, Young K. VeSPA: integrated applications for RF pulse design, spectral simulation and MRS data analysis. Paper presented at: Proc Int Soc Magn Reson Med2011.
99. Chong DG, Kreis R, Bolliger CS, Boesch C, Slotboom J. Two-dimensional linear-combination model fitting of magnetic resonance spectra to define the macromolecule baseline using FiTAID, a Fitting Tool for Arrays of Interrelated Datasets. *Magnetic Resonance Materials in Physics, Biology and Medicine*. 2011;24(3):147-164.
100. Wilson M. Adaptive Baseline Fitting for ¹H MR Spectroscopy Analysis. *bioRxiv*. 2020.
101. Oeltzschner G, Zöllner HJ, Hui SC, et al. Osprey: Open-Source Processing, Reconstruction & Estimation of Magnetic Resonance Spectroscopy Data. *bioRxiv*. 2020.
102. Marjańska M, Terpstra M. Influence of fitting approaches in LCModel on MRS quantification focusing on age-specific macromolecules and the spline baseline. *NMR in Biomedicine*. 2019:e4197.
103. Giapitzakis IA, Borbath T, Murali-Manohar S, Avdievich N, Henning A. Investigation of the influence of macromolecules and spline baseline in the fitting model of human brain spectra at 9.4 T. *Magnetic resonance in medicine*. 2019;81(2):746-758.

104. Schaller B, Xin L, Cudalbu C, Gruetter R. Quantification of the neurochemical profile using simulated macromolecule resonances at 3 T. *NMR in Biomedicine*. 2013;26(5):593-599.
105. Wright A, Murali Manohar S, Henning A. Relaxation corrected and Sequence-dependent Macromolecule Baseline Model Paper presented at: 27th Annual Meeting and Exhibition of the International Society for Magnetic Resonance in Medicine (ISMRM 2019)2019.
106. Giapitzakis IA, Shao T, Avdievich N, Mekle R, Kreis R, Henning A. Metabolite-cycled STEAM and semi-LASER localization for MR spectroscopy of the human brain at 9.4 T. *Magnetic resonance in medicine*. 2018;79(4):1841-1850.
107. *Vespa: Versatile Simulation Pulses and Analysis. User Code Contributions – semi-LASER* [computer program]. <https://scion.duhs.duke.edu/vespa/contrib/wiki/1f03e57e-1d27-4d36-8b31-db9e5e2f73e82013>.
108. Near J, Evans CJ, Puts NA, Barker PB, Edden RA. J-difference editing of gamma-aminobutyric acid (GABA): Simulated and experimental multiplet patterns. *Magnetic resonance in medicine*. 2013;70(5):1183-1191.
109. Borbath T, Murali-Manohar S, Wright AM, Henning A. In vivo characterization of downfield peaks at 9.4 T: T2 relaxation times, quantification, pH estimation, and assignments. *Magnetic resonance in medicine*. 2020.
110. Bland JM, Altman D. Statistical methods for assessing agreement between two methods of clinical measurement. *The lancet*. 1986;327(8476):307-310.
111. Kreis R, Boer V, Choi IY, et al. Terminology and concepts for the characterization of in vivo MR spectroscopy methods and MR spectra: Background and experts' consensus recommendations. *NMR in Biomedicine*. 2020:e4347.
112. Slotboom J, Nirkkko A, Brekenfeld C, Van Ormondt D. Reliability testing of in vivo magnetic resonance spectroscopy (MRS) signals and signal artifact reduction by order statistic filtering. *Measurement Science and Technology*. 2009;20(10):104030.
113. Wermter FC, Mitschke N, Bock C, Dreher W. Temperature dependence of 1 H NMR chemical shifts and its influence on estimated metabolite concentrations. *Magnetic Resonance Materials in Physics, Biology and Medicine*. 2017;30(6):579-590.
114. Rothman DL, Behar KL, Prichard JW, Petroff OA. Homocarnosine and the measurement of neuronal pH in patients with epilepsy. *Magnetic resonance in medicine*. 1997;38(6):924-929.
115. Zhang Y, Shen J. Effects of noise and linewidth on in vivo analysis of glutamate at 3 Tesla. *Journal of Magnetic Resonance*. 2020:106732.

116. Henry PG, Öz G, Provencher S, Gruetter R. Toward dynamic isotopomer analysis in the rat brain in vivo: automatic quantitation of ¹³C NMR spectra using LCMoDel. *NMR in Biomedicine: An International Journal Devoted to the Development and Application of Magnetic Resonance In Vivo*. 2003;16(6-7):400-412.
117. Deelchand DK, Nguyen TM, Zhu XH, Mochel F, Henry PG. Quantification of in vivo ³¹P NMR brain spectra using LCMoDel. *NMR in Biomedicine*. 2015;28(6):633-641.
118. Marjańska M, Auerbach EJ, Valabrègue R, Van de Moortele PF, Adriany G, Garwood M. Localized ¹H NMR spectroscopy in different regions of human brain in vivo at 7 T: T2 relaxation times and concentrations of cerebral metabolites. *NMR in Biomedicine*. 2012;25(2):332-339.
119. Dreher W, Leibfritz D. New method for the simultaneous detection of metabolites and water in localized in vivo ¹H nuclear magnetic resonance spectroscopy. *Magnetic resonance in medicine*. 2005;54(1):190-195.
120. MacMillan EL, Chong DG, Dreher W, Henning A, Boesch C, Kreis R. Magnetization exchange with water and T1 relaxation of the downfield resonances in human brain spectra at 3.0 T. *Magnetic resonance in medicine*. 2011;65(5):1239-1246.
121. de Graaf RA, Behar KL. Detection of cerebral NAD⁺ by in vivo ¹H NMR spectroscopy. *NMR in biomedicine*. 2014;27(7):802-809.
122. Fichtner ND, Henning A, Zoelch N, Boesch C, Kreis R. Elucidation of the downfield spectrum of human brain at 7 T using multiple inversion recovery delays and echo times. *Magnetic resonance in medicine*. 2017;78(1):11-19.
123. Deelchand DK, Van de Moortele P-F, Adriany G, et al. In vivo ¹H NMR spectroscopy of the human brain at 9.4 T: initial results. *Journal of Magnetic Resonance*. 2010;206(1):74-80.
124. Kogan F, Hariharan H, Reddy R. Chemical exchange saturation transfer (CEST) imaging: description of technique and potential clinical applications. *Current radiology reports*. 2013;1(2):102-114.
125. Krikken E, van der Kemp WJ, Khlebnikov V, et al. Contradiction between amide-CEST signal and pH in breast cancer explained with metabolic MRI. *NMR in Biomedicine*. 2019:e4110.
126. Zaiss M, Windschuh J, Goerke S, et al. Downfield-NOE-suppressed amide-CEST-MRI at 7 Tesla provides a unique contrast in human glioblastoma. *Magnetic resonance in medicine*. 2017;77(1):196-208.

127. Goerke S, Milde KS, Bukowiecki R, et al. Aggregation-induced changes in the chemical exchange saturation transfer (CEST) signals of proteins. *NMR in Biomedicine*. 2017;30(1):e3665.
128. Ray KJ, Simard MA, Larkin JR, et al. Tumor pH and Protein Concentration Contribute to the Signal of Amide Proton Transfer Magnetic Resonance Imaging. *Cancer research*. 2019;79(7):1343-1352.
129. Zaiss M, Schuppert M, Deshmane A, et al. Chemical exchange saturation transfer MRI contrast in the human brain at 9.4 T. *NeuroImage*. 2018;179:144-155.
130. Cohen O, Huang S, McMahon MT, Rosen MS, Farrar CT. Rapid and quantitative chemical exchange saturation transfer (CEST) imaging with magnetic resonance fingerprinting (MRF). *Magnetic resonance in medicine*. 2018;80(6):2449-2463.
131. Perlman O, Ito H, Herz K, et al. AI boosted molecular MRI for apoptosis detection in oncolytic virotherapy. *bioRxiv*. 2020.
132. Woessner DE, Zhang S, Merritt ME, Sherry AD. Numerical solution of the Bloch equations provides insights into the optimum design of PARACEST agents for MRI. *Magnetic Resonance in Medicine: An Official Journal of the International Society for Magnetic Resonance in Medicine*. 2005;53(4):790-799.
133. Vermathen P, Capizzano AA, Maudsley AA. Administration and ¹H MRS detection of histidine in human brain: application to in vivo pH measurement. *Magnetic Resonance in Medicine: An Official Journal of the International Society for Magnetic Resonance in Medicine*. 2000;43(5):665-675.
134. Mirkes C, Shajan G, Chadzynski G, Buckenmaier K, Bender B, Scheffler K. 31 P CSI of the human brain in healthy subjects and tumor patients at 9.4 T with a three-layered multi-nuclear coil: initial results. *Magnetic Resonance Materials in Physics, Biology and Medicine*. 2016;29(3):579-589.
135. Avdievich NI, Giapitzakis IA, Pfrommer A, Henning A. Decoupling of a tight-fit transceiver phased array for human brain imaging at 9.4 T: Loop overlapping rediscovered. *Magnetic resonance in medicine*. 2018;79(2):1200-1211.
136. Gruetter R, Tkáč I. Field mapping without reference scan using asymmetric echo-planar techniques. *Magnetic resonance in medicine*. 2000;43(2):319-323.
137. Versluis MJ, Kan HE, van Buchem MA, Webb AG. Improved signal to noise in proton spectroscopy of the human calf muscle at 7 T using localized B1 calibration. *Magnetic Resonance in Medicine: An Official Journal of the International Society for Magnetic Resonance in Medicine*. 2010;63(1):207-211.

138. Mekle R, Mlynárik V, Gambarota G, Hergt M, Krueger G, Gruetter R. MR spectroscopy of the human brain with enhanced signal intensity at ultrashort echo times on a clinical platform at 3T and 7T. *Magnetic Resonance in Medicine*. 2009;61(6):1279-1285.
139. Boer V, van Lier A, Hoogduin J, Wijnen J, Luijten P, Klomp D. 7-T 1H MRS with adiabatic refocusing at short TE using radiofrequency focusing with a dual-channel volume transmit coil. *NMR in Biomedicine*. 2011;24(9):1038-1046.
140. Ashburner J, Barnes G, Chen C, et al. SPM12 manual. *Wellcome Trust Centre for Neuroimaging, London, UK*. 2014:2464.
141. Giapitzakis IA, Avdievich N, Henning A. Characterization of macromolecular baseline of human brain using metabolite cycled semi-LASER at 9.4 T. *Magnetic resonance in medicine*. 2018;80(2):462-473.
142. Petroff OA. Book review: GABA and glutamate in the human brain. *The Neuroscientist*. 2002;8(6):562-573.
143. Ren J, Shang T, Sherry AD, Malloy CR. Unveiling a hidden 31P signal coresonating with extracellular inorganic phosphate by outer-volume-suppression and localized 31P MRS in the human brain at 7T. *Magnetic resonance in medicine*. 2018;80(4):1289-1297.
144. Gonçalves SI, Ligneul C, Shemesh N. Short echo time relaxation-enhanced MR spectroscopy reveals broad downfield resonances. *Magnetic resonance in medicine*. 2019;82(4):1266-1277.
145. Liu D, Zhou J, Xue R, Zuo Z, An J, Wang DJ. Quantitative characterization of nuclear overhauser enhancement and amide proton transfer effects in the human brain at 7 tesla. *Magnetic resonance in medicine*. 2013;70(4):1070-1081.
146. Michaeli S, Garwood M, Zhu XH, et al. Proton T2 relaxation study of water, N-acetylaspartate, and creatine in human brain using Hahn and Carr-Purcell spin echoes at 4T and 7T. *Magnetic Resonance in Medicine: An Official Journal of the International Society for Magnetic Resonance in Medicine*. 2002;47(4):629-633.
147. Levitt MH. *Spin dynamics: basics of nuclear magnetic resonance*. John Wiley & Sons; 2001.
148. de Graaf RA, De Feyter HM, Brown PB, Nixon TW, Rothman DL, Behar KL. Detection of cerebral NAD+ in humans at 7T. *Magnetic resonance in medicine*. 2017;78(3):828-835.
149. Son T-D, Chachaty C. Proton NMR and spin lattice relaxation study of nucleoside di- and triphosphates in neutral aqueous solutions. *Biochimica et Biophysica Acta (BBA)-General Subjects*. 1977;500(2):405-418.

150. Zaiss M, Bachert P. Chemical exchange saturation transfer (CEST) and MR Z-spectroscopy in vivo: a review of theoretical approaches and methods. *Physics in Medicine & Biology*. 2013;58(22):R221.
151. Xu J, Yadav NN, Bar-Shir A, et al. Variable delay multi-pulse train for fast chemical exchange saturation transfer and relayed-nuclear overhauser enhancement MRI. *Magnetic resonance in medicine*. 2014;71(5):1798-1812.
152. Watanabe T, Frahm J, Michaelis T. Amide proton signals as pH indicator for in vivo MRS and MRI of the brain—Responses to hypercapnia and hypothermia. *Neuroimage*. 2016;133:390-398.
153. Moats R, Lien Y, Filippi D, Ross B. Decrease in cerebral inositols in rats and humans. *Biochemical Journal*. 1993;295(Pt 1):15.
154. Stabinska J, Neudecker P, Ljimini A, Wittsack HJ, Lanzman RS, Müller-Lutz A. Proton exchange in aqueous urea solutions measured by water-exchange (WEX) NMR spectroscopy and chemical exchange saturation transfer (CEST) imaging in vitro. *Magnetic resonance in medicine*. 2019;82(3):935-947.
155. Finer E, Franks F, Tait M. Nuclear magnetic resonance studies of aqueous urea solutions. *Journal of the American Chemical Society*. 1972;94(13):4424-4429.
156. Bagga P, Hariharan H, Wilson NE, et al. Single-Voxel 1H MR spectroscopy of cerebral nicotinamide adenine dinucleotide (NAD⁺) in humans at 7T using a 32-channel volume coil. *Magnetic Resonance in Medicine*. 2020;83(3):806-814.
157. Dziadosz M, Bogner W, Kreis R. Non-water-excitation MR spectroscopy techniques to explore exchanging protons in human brain at 3 T. *Magnetic resonance in medicine*. 2020;84(5):2352-2363.
158. Haris M, Nanga RPR, Singh A, et al. Exchange rates of creatine kinase metabolites: feasibility of imaging creatine by chemical exchange saturation transfer MRI. *NMR in Biomedicine*. 2012;25(11):1305-1309.
159. Fichtner ND, Giapitzakis IA, Avdievich N, et al. In vivo characterization of the downfield part of 1H MR spectra of human brain at 9.4 T: Magnetization exchange with water and relation to conventionally determined metabolite content. *Magnetic Resonance in Medicine*. 2017.
160. Gonçalves SI, Ligneul C, Shemesh N. Short echo time relaxation-enhanced MR spectroscopy reveals broad downfield resonances. *Magnetic resonance in medicine*. 2019.

161. Tkáč I, Öz G, Adriany G, Uğurbil K, Gruetter R. In vivo ¹H NMR spectroscopy of the human brain at high magnetic fields: metabolite quantification at 4T vs. 7T. *Magnetic Resonance in Medicine*. 2009;62(4):868-879.
162. Kanamori K, Ross BD. Glial alkalization detected in vivo by ¹H-¹⁵N heteronuclear multiple-quantum coherence-transfer NMR in severely hyperammonemic rat. *Journal of neurochemistry*. 1997;68(3):1209-1220.
163. Handley RR, Reid SJ, Brauning R, et al. Brain urea increase is an early Huntington's disease pathogenic event observed in a prodromal transgenic sheep model and HD cases. *Proceedings of the National Academy of Sciences*. 2017;114(52):E11293-E11302.
164. Grande S, Luciani AM, Rosi A, Guidoni L, Viti V. Identification of amide protons of glutathione in MR spectra of tumour cells. *NMR in Biomedicine: An International Journal Devoted to the Development and Application of Magnetic Resonance In vivo*. 2008;21(10):1057-1065.
165. Nagarajan R, Ramadan S, Thomas MA. Detection of amide and aromatic proton resonances of human brain metabolites using localized correlated spectroscopy combined with two different water suppression schemes. *Magnetic resonance insights*. 2010;4:MRI.S4739.
166. Schanda P. Fast-pulsing longitudinal relaxation optimized techniques: enriching the toolbox of fast biomolecular NMR spectroscopy. *Progress in Nuclear Magnetic Resonance Spectroscopy*. 2009;55(3):238-265.
167. Kreis R. ¹H-Magnetic Resonance Spectroscopy of Cerebral Phenylalanine Content and its Transport at the Blood-Brain Barrier. *Neural Metabolism In Vivo*: Springer; 2012:1117-1134.
168. Ulrich EL, Akutsu H, Doreleijers JF, et al. BioMagResBank. *Nucleic acids research*. 2007;36(suppl_1):D402-D408.
169. Borbath T, Murali Manohar S, Henning A. Towards a Fitting Model of Macromolecular Spectra: Amino Acids. Paper presented at: 27th Annual Meeting & Exhibition, 1068. 27th Annual Meeting and Exhibition of the International Society for Magnetic Resonance in Medicine (ISMRM 2019)2019; Montréal, QC, Canada.
170. Waisbren SE, Prabhu SP, Greenstein P, et al. Improved measurement of brain phenylalanine and tyrosine related to neuropsychological functioning in phenylketonuria. *JIMD Reports, Volume 34*: Springer; 2016:77-86.

171. Murali-Manohar S, Wright AM, Borbath T, Avdievich NI, Henning A. A novel method to measure T1-relaxation times of macromolecules and quantification of the macromolecular resonances. *Magnetic Resonance in Medicine*. 2020.
172. Xin L, Schaller B, Mlynarik V, Lu H, Gruetter R. Proton T1 relaxation times of metabolites in human occipital white and gray matter at 7 T. *Magnetic resonance in medicine*. 2013;69(4):931-936.
173. Wright A, Murali Manohar S, Borbath T, Henning A. Longitudinal Relaxation Times of Metabolites in vivo at 9.4 T. Paper presented at: 27th Annual Meeting and Exhibition of the International Society for Magnetic Resonance in Medicine (ISMRM 2019)2019.
174. Near J, Harris AD, Juchem C, et al. Preprocessing, analysis and quantification in single-voxel magnetic resonance spectroscopy: experts' consensus recommendations. *NMR in Biomedicine*. 2020:e4257.
175. Zhou J, Wilson DA, Sun PZ, Klaus JA, van Zijl PC. Quantitative description of proton exchange processes between water and endogenous and exogenous agents for WEX, CEST, and APT experiments. *Magnetic Resonance in Medicine: An Official Journal of the International Society for Magnetic Resonance in Medicine*. 2004;51(5):945-952.
176. Platzer G, Okon M, McIntosh LP. pH-dependent random coil ¹H, ¹³C, and ¹⁵N chemical shifts of the ionizable amino acids: a guide for protein pK_a measurements. *Journal of biomolecular NMR*. 2014;60(2-3):109-129.
177. Robinson N. Proteolipids and proteins in subcellular particles of human brain. *Clinica Chimica Acta*. 1966;13(5):541-545.
178. Robinson N, Williams C. Amino acids in human brain. *Clinica Chimica Acta*. 1965;12(3):311-317.
179. Mader I, Seeger U, Weissert R, et al. Proton MR spectroscopy with metabolite-nulling reveals elevated macromolecules in acute multiple sclerosis. *Brain*. 2001;124(5):953-961.
180. García-Gómez JM, Luts J, Julià-Sapé M, et al. Multiproject–multicenter evaluation of automatic brain tumor classification by magnetic resonance spectroscopy. *Magnetic Resonance Materials in Physics, Biology and Medicine*. 2009;22(1):5.

Appendix A

Text in this chapter was adapted with minor modifications from our work previously published in the Supporting Information of:

Giapitzakis IA*, **Borbath T***, Murali-Manohar S, Avdievich N, Henning A. "Investigation of the influence of macromolecules and spline baseline in the fitting model of human brain spectra at 9.4 T". *Magnetic resonance in medicine*, 2019;81(2):746-758.

Sample LCMODL .control files used for the quantification of the occipital lobe spectra for the different processing protocols: (a), (b), (c) and (d). The "FILBAS" parameter sets the included basis set, which includes besides the metabolites also a macromolecular baseline from the occipital lobe ((a) and (c)) or the left parietal lobe (b). For the processing protocol (d) on the other hand, the simulated macromolecules are not excluded with "CHNOT". Note: the parameters "WCONC" and "ATTH20" which account for the water concentration and water relaxation, respectively, are not those used for the calculation of the concentration levels, since additional corrections were applied as described in the quantification section 2.2.5.

Processing protocol (a)

```
$LCMODL                                hzpppm= 399.719
OWNER='MPI biological Cybernetics'      neach= 50
TITLE='Occl_spec_with_Occl_MMB_dkntmn_1' nunfil= 4096
FILBAS='~/BasisSets/Basis_with_Occl_MMB.basis' ppmend= 0.2
FILRAW='~/data/occl_signal.RAW'        ppmst= 4.1
FILH2O='~/data/occl_water.RAW'        sddegp= 5
FILPS='~/Output/occl_sample.ps'       sddegz= 15
FILTAB='~/Output/occl_sample.table'    wconc= 40873
FILCSV='~/Output/occl_sample.csv'      nnot2 = 9
FILC00='~/Output/occl_sample.coord'    chnot2(1) = 'Lip09'
LTABLE=7                                chnot2(2) = 'MM09'
LCOORD=9                                chnot2(3) = 'Glyc'
LCSV=11                                  chnot2(4) = '-CrCH2'
atth2o= 1                                chnot2(5) = 'Scyllo'
deltat= 1.2500e-04                       chnot2(6) = 'MM20'
dkntmn= 1                                chnot2(7) = 'MM12'
doecc= F                                  chnot2(8) = 'MM14'
dows= T                                  chnot2(9) = 'MM17'
                                           $END
```

Processing protocol (b)

```
$LCMODL
OWNER='Max Planck Institute biological
Cybernetics'
TITLE='Occl_spec_w_lPL_MMB_dkntmn_1'
FILBAS='~/BasisSets/Basis_with_lPL_MMB.basis'
FILRAW='~/data/occl_signal.RAW'
FILH2O='~/data/occl_water.RAW'
FILPS='~/Output/occl_sample.ps'
FILTAB='~/Output/occl_sample.table'
FILCSV='~/Output/occl_sample.csv'
FILCOO='~/Output/occl_sample.coord'
LTABLE=7
LCOORD=9
LCSV=11
atth2o= 1
deltat= 1.2500e-04
dkntmn= 1
doecc= F
dows= T

hzpppm= 399.719
neach= 50
nunfil= 4096
ppmend= 0.2
ppmst= 4.1
sddegp= 5
sddegz= 15
wconc= 40873
nnot2 = 9
chnot2(1) = 'Lip09'
chnot2(2) = 'MM09'
chnot2(3) = 'Glyc'
chnot2(4) = '-CrCH2'
chnot2(5) = 'Scyllo'
chnot2(6) = 'MM20'
chnot2(7) = 'MM12'
chnot2(8) = 'MM14'
chnot2(9) = 'MM17'
$END
```

Processing protocol (c)

```
$LCMODL
OWNER='MPI biological Cybernetics'
TITLE='Occl_spec_w_Occl_MMB_dkntmn_0.15'
FILBAS='~/BasisSets/Basis_with_Occl_MMB.basis'
FILRAW='~/data/occl_signal.RAW'
FILH2O='~/data/occl_water.RAW'
FILPS='~/Output/occl_sample.ps'
FILTAB='~/Output/occl_sample.table'
FILCSV='~/Output/occl_sample.csv'
FILCOO='~/Output/occl_sample.coord'
LTABLE=7
LCOORD=9
LCSV=11
atth2o= 1
deltat= 1.2500e-04
dkntmn= 0.15
doecc= F
dows= T

hzpppm= 399.719
neach= 50
nunfil= 4096
ppmend= 0.2
ppmst= 4.1
sddegp= 5
sddegz= 15
wconc= 40873
nnot2 = 9
chnot2(1) = 'Lip09'
chnot2(2) = 'MM09'
chnot2(3) = 'Glyc'
chnot2(4) = '-CrCH2'
chnot2(5) = 'Scyllo'
chnot2(6) = 'MM20'
chnot2(7) = 'MM12'
chnot2(8) = 'MM14'
chnot2(9) = 'MM17'
$END
```

Processing protocol (d)

```
$LCMODL
OWNER='MPI biological Cybernetics'
TITLE='Occl_spec_w/o_experimental_MMB_dkntmn_0.15'
FILBAS='~/BasisSets/Basis_without_MMB.basis'
FILRAW='~/data/occl_signal.RAW'
FILH2O='~/data/occl_water.RAW'
FILPS='~/Output/occl_sample.ps'
FILTAB='~/Output/occl_sample.table'
FILCSV='~/Output/occl_sample.csv'
FILCOO='~/Output/occl_sample.coord'
LTABLE=7
LCOORD=9
LCSV=11
atth2o= 1
deltat= 1.2500e-04
doecc= F
dows= T
hzpppm= 399.719
neach= 50
nunfil= 4096
ppmend= 0.2
ppmst= 4.1
sddegp= 5
sddegz= 15
wconc= 40873
$END
```

Appendix B

Sample LCModel.control files used for the quantification of the downfield metabolite spectra. The calculated pH value will be replaced (pH_XXX with for e.g. pH_7.07) selecting hence the basis set with the corresponding pH shifts of the hCs imidazole ring. The RFWHM parameter was left at its default value of 1.8.

```
$LCMODL
OWNER='Max Planck Institute biological Cybernetics'
TITLE='XXXX_TE24_DF'
FILBAS='/PATH/sLASER_7ppm_moiety_imidazole_pH_XXX_basis_TE24.basis'
FILRAW='/ PATH /XXXX/XXXX_TE24.RAW'
FILH2O='/ PATH /XXXX/XXXX_water.RAW'
FILPS='/ PATH /Output/XXXX/XXXX_pH_XXX_TE24.ps'
FILTAB='/ PATH /Output/XXXX/XXXX_pH_XXX_TE24.table'
FILCSV='/ PATH /Output/XXXX/XXXX_pH_XXX_TE24.csv'
FILCOO='/ PATH /Output/XXXX/XXXX_pH_XXX_TE24.coord'
LTABLE=7
LPS = 8
LCOORD=9
LCSV=11
atth2o= 1
deltat= 1.2500e-04
dkntmn= 0.5
doecc= F
dows= T
hzpppm= 399.719
neach= 50
nunfil= 4096
ppmend= 0.6
```

```
ppmst= 9.5
ppmgap(1,1)=5.5
ppmgap(2,1)=4.1
fwhmba=0.0075
sddegp= 0
sddegz= 0
nsdsh=1
chsdsh(1)='hCs'
alsdsh(1)=0.0005
wconc= 40873
nratio= 0
nsimul= 12
chsimu(1)= 'DF5.75 @ 5.75 +- 0.01 FWHM= .06 < .10 +- .01 AMP= 1.'
chsimu(2)= 'DF5.97 @ 5.97 +- 0.01 FWHM= .03 < .08 +- .005 AMP= 1.'
chsimu(3)= 'DF6.12 @ 6.12 +- 0.01 FWHM= .03 < .08 +- .005 AMP= 1.'
chsimu(4)= 'DF6.83 @ 6.83 +- 0.01 FWHM= .10 < .13 +- .01 AMP= 1.'
chsimu(5)= 'DF7.30 @ 7.30 +- 0.01 FWHM= .08 < .11 +- .01 AMP= 1.'
chsimu(6)= 'DF7.48 @ 7.48 +- 0.01 FWHM= .03 < .08 +- .01 AMP= 1.'
chsimu(7)= 'NAAB @ 7.86 +- 0.01 FWHM= .12 < .13 +- .005 AMP= 1.'
chsimu(8)= 'DF8.18 @ 8.18 +- 0.01 FWHM= .08 < .11 +- .005 AMP= 1.'
chsimu(9)= 'DF8.24 @ 8.24 +- 0.01 FWHM= .01 < .06 +- .005 AMP= 1.'
chsimu(10)= 'DF8.37 @ 8.37 +- 0.01 FWHM= .08 < .11 +- .01 AMP= 1.'
chsimu(11)= 'DF8.49 @ 8.49 +- 0.01 FWHM= .01 < .06 +- .005 AMP= 1.'
chsimu(12)= 'DF7.04 @ 7.04 +- 0.01 FWHM= .14 < .15 +- .005 AMP= 1.'
ncombi= 17
chcomb(17)='NAAB+NAA_DF'
$END
```